UNIVERSIDAD DE CHILE
FACULTAD DE CIENCIAS FÍSICAS Y MATEMÁTICAS
DEPARTAMENTO DE ASTRONOMÍA

MASSIVE AND DENSE CLUMPS: PHYSICAL PROPERTIES AND EVOLUTION

TESIS PARA OPTAR AL GRADO DE
DOCTOR EN CIENCIAS, MENCIÓN ASTRONOMÍA

SUDEEP NEUPANE

PROFESOR GUÍA:
GUIDO GARAY BRIGNARDELLO

PROFESORA CO-GUÍA:
YANETT CONTRERAS MORALES

MIEMBROS DE LA COMISIÓN:
LARS-ÅKE NYMAN
AMELIA MARIE STUTZ
RICARDO MUÑOZ VIDAL

SANTIAGO DE CHILE
2020

RESUMEN DE LA MEMORIA PARA OPTAR
AL TÍTULO DE DOCTOR EN CIENCIAS, MENCIÓN ASTRONOMÍA
POR: SUDEEP NEUPANE
FECHA: 2020
PROF. GUÍA: GUIDO GARAY BRIGNARDELLO
PROF. CO. GUÍA: YANETT CONTRERAS MORALES

MASSIVE AND DENSE CLUMPS: PHYSICAL PROPERTIES AND EVOLUTION

En esta Tesis se estudian las propiedades física, químicas de nubes moleculares densas y masivas (MDCs), que corresponden a las maternidades de estrellas de alta masa, que se encuentran en diferentes etapas evolutivas como tambien las características de su fragmentación. El objetivo principal es proveer, a traves de observaciones, una perspectiva sobre los procesos de formación de estrellas de alta masa. Primero observamos, utilizando el telescopio APEX con una resolución angular de 20" ($\sim$ 0.3 pc), la emisión molecular en lineas con alta excitación ($J = 3 \rightarrow 2$, $4 \rightarrow 3$ de HCO^+, $H^{13}CO^+$, HCN, HNC and N_2H^+) hacia 73 MDCs en diferentes etapas evolutivas. El objetivo de este estudio, llamado SuperMALT, es investigar el tamaño, morfología, intensidad, ancho y asimetrías de la emisión en las diferentes lineas a escalas de los MDCs. Encontramos que la morfología, de la emisión en las líneas son similares a la de la emisión del polvo a 870 μm. La intensidad y el ancho de las lineas aumenta al pasar de pre-estelar, protoestelar y nubes H II. El movimiento de colapso, indicadas por las asimetrías en el corrimiento al azul en lineas gruesas en el óptico, son más comunes en etapas tempranas mientras que el movimíento de expansión indicadas por asimetrías el corrimiento al rojo, son más comunes en etapas más evolucionadas. Segundo observamos, utilizando el telescopio APEX con una resolución angular de 8", la emisión en 350 μm hacia 23 MDCs en diferentes etapas evolutivas, con el fin de investigar las propiedades de fragmentación a escalas de 0.1pc. Encontramos que, en promedio, las MDCs muestran 2 a 3 núcleos ("cores"), con el mas masivo usualmente localizado cerca del centro de la nube. Tercero observamos, utilizando el radiotescopio ALMA con una resolución angular de 2" ($\sim$ 0.02 pc), la emisión en continuo y líneas moleculares hacia 2 MDCs, uno en etapa previa a la formación estelar (AGAL333) y otro en etapa protoestelar (AGAL239). El objetivo es estudiar las propiedades de fragmentación y la cinemática del gas de las MDCs en etapas tempranas. Encontramos que ambas nubes tienen 10 núcleos, sin embargo, los núcleos en la nube protoestelar son más masivos, la mayoría se encuentran virializados, y, presentan líneas más anchas y temperatura más altas comparados con los núcleos en la nube pre-estelar. En la MDC protoestelar detectamos un núcleo central y masivo, con 119 M$\odot$, el que exhibe *outflows* y que está colapsando con una alta tasa de acreción de masa. La fracción de masa en la forma de núcleos en la MDC pre-formación estelar es 6%, mientras que en la MDC protoestelar es 23%. Finalmente, proponemos un escenario de evolución para MDC en el cual las nubes se fragmentan en etapas tempranas y los núcleos acumulan masa a partir del entorno en la nube, a medida que evolucionan. La fracción de masa en la forma de núcleos relativo a la masa total del MDC aumenta desde la fase pre-estelar a la protoestelar. Las propiedades físicas y químicas de las nubes evolucionan reflejandose en el ancho de líneas y su temperatura, como tambien en el intensidad de las líneas moleculares. MDCs en etapas tempranas de evolución exhiben señales de colapsos de gran escala más a menudo comparado con loa MDC en etapas más evolucionadas. Los núcleos ubicados en el pozo del potencial gravitatorio de la nube acumulan más masa a partir del gas que colapsa por lo que son capaces de formar estrellas masivas.

Abstract

MASSIVE AND DENSE CLUMPS: PHYSICAL PROPERTIES AND EVOLUTION

In this thesis, I investigate the physical, chemical and fragmentation characteristics of massive and dense clumps (MDCs), which are the maternities of high-mass stars, in different evolutionary stages (from quiescent to protostellar to HII clumps). My goal is to provide an important observational perspective about high-mass star formation processes.

First, I made a survey of the emission in high excitation molecular lines (HCO^+, $H^{13}CO^+$, HCN, HNC and N_2H^+ in $J = 3 \rightarrow 2$ and $4 \rightarrow 3$) towards 73 MDCs in different evolutionary stages, called the SuperMALT survey conducted from APEX telescope, to investigate their morphologies, sizes, line intensities, line widths, line ratios and line asymmetries with an angular resolution of 20" (typically 0.3 pc at the distances of the MDCs). I found that the morphologies of the line emission are similar to that of the dust emission at 870 μm. The intensities in all molecular lines species and the line widths increase from prestellar to protostellar and HII clumps. Infall motions, indicated by a blueshifted asymmetry in optically thick lines, are more common in early stage clumps while expansion motions, indicated by a redshifted asymmetry, are more common in evolved stage clumps.

Second, to investigate the fragmentation properties at the scale of 0.1 pc, I observed the 350 μm emission from 23 MDCs in different evolutionary stages, a subset drawn from the SuperMALT, using the Artemis camera mounted on the APEX telescope. On average, the MDCs reveal 2 to 3 cores, with the most massive one usually found near the center of the clump. I found no significant correlations between fragmentation level and the parent clump properties such as temperature, density, line width and virial parameter.

Third, to study the fragmentation properties and gas kinematics within early stage clumps, I observed two MDCs, one in the prestellar stage (AGAL333) and the other in the protostellar stage (AGAL329), using ALMA (3mm) in continuum and molecular lines (HCO^+, $H^{13}CO^+$, N_2H^+ $J = 1 \rightarrow 0$ and CH_3CN $5 \rightarrow 4$). I found that both clumps contain $\sim$10 cores, however, cores in the protostellar clump are more massive. The central massive core (119 $M_\odot$) in the protostellar clump exhibit an outflow and infall signatures with a high mass accretion rate. The cores within the prestellar clump have smaller line widths and temperatures than those in the protostellar clump, they are in a sub-virial state while most cores in protostellar clump are virialized. The fraction of the mass in the form of cores in the prestellar clump is 6%, while in the protostellar clump is 23%. These above results indicate that clumps fragment at early stages and that the fragmented cores gather more mass as they evolve.

Finally, I present an observational model of MDC evolution, in which, clumps fragment at early stages and the cores gather more mass from the clump environment. The fraction of mass in the form of cores relative to the clump mass increases from prestellar to protostellar stage. The physical and chemical properties of clumps evolve. This is seen in the increase in the line widths and temperature, as well as the increase in brightness of molecular line emissions with evolution. Clumps at early evolutionary stages exhibit signature of large scale infall more often than clumps at evolved stages that show more often expansion motions. The cores located at the bottom of the clump gravitational potential gather more mass from the globally infalling gas and hence are able to form high-mass star/s.

Dedicated to my parents, Binod and Saraswati.

Agradecimientos

I would like to express my sincere gratitude to my thesis advisor Prof. Dr. Guido Garay and co-advisor Dr. Yanett Contreras, without whom this thesis work would not have been possible. I am indebted to them. I am deeply grateful to Prof. Garay who always provided me the necessary support, convincingly guided me, encouraged me, pushed me forward till the end of the program. Besides my advisors, I would like to thank my thesis committee members who have provided valuable comments and suggestions to improve the quality of the thesis work.

I wish to thank all the faculty members, administrative staffs and functionaries at Calan Observatory. Calan family was helpful and supportive to me. My particular regards to Prof. Diego Mardones and Prof. Leo Broffmann who always provided the opportunity to discuss my research and encouraged me.

At different stages of this thesis work I collaborated and received support from many researchers. Among them I am delighted to mention Dr. Andres Guzman and Dr. Fabien Louvet who have provided me the necessary mentorship when needed. Among the helpful others, I appreciate my friends and collaborators Dr. Victor S. Magalhães and Dr. Riwaj Pokhrel. I also want to remember my early career mentors Prof Dr. Binil Aryal and Dr. Rishi Shah back in Nepal. I feel indebted to all the teachers and mentors from my school days to the university level. In one way or another, they have contributed to make me a person who I am today.

I have been lucky to have many friends in Chile, Nepal and from other countries. I can not write all of their names. Friends who are reading this shall know that I appreciate them from the bottom of my heart. Having said that I could not leave it without mentioning Calan colleagues and friends Luciano, Srini, Tomas, Julian, Marchi, Elise, Valentin, Paula, Maritza, Ricardo, Blake, Jorge, Matias, Greco, JuanP, Nathen, Govanina, Pineda, Arce, Pablo, Armin et al. and Nepalese friends Sitaram, Ram, Deep, Panthee, Rishi, Jaydev, Suresh, Suman, Manoj, Sunita, Taya, Amrit, Sudip J., Rijendra, et al. My friends have made my past memories and present life beautiful.

Finally, I would like to profess my love and sincere gratitude to my family members back in Nepal. I feel enormously grateful to my late grandmother, my parents, my brother and my two sisters who have been continuously sending love and support from thousands of miles away. Their good wishes, love and encouragement always gave me the courage to survive the PhD program and live through the difficult times.

Contents

List of Tables

List of Figures

List of Acronyms

ACA	Atacama Compact Array
ALMA	Atacama Large Millimeter Array
APEX	Atacama Pathfinder EXperiment
ATLASGAL	APEX Telescope Large Area Survey of the Galaxy
CASA	Common Astronomy Software Applications package
FWHM	Full Width Half Maximum
GLIMPSE	Galactic Legacy Infrared Mid-Plane Survey Extraordinaire
GMC	Giant Molecular Cloud
HWHM	Half Width Half Maximum
IMF	Initial Mass Function
ISM	Interstellar Medium
LAMBDA	Leiden Atomic and Molecular Database
LTE	Local Thermodynamic Equilibrium
MALT90	Millimeter Astronomy Legacy Team 90 GHz
MDC	Massive and Dense Clump
MIPS	Multiband Imaging Photometer
MIPSGAL	MIPS Galactic Plane Survey
PDR	Photodissociation region
SED	Spectral Energy Distribution

Chapter 1

Introduction

The main components of the galaxies are stars, gas, dust and invisible dark matter. Galaxies contain hundreds of billions of stars most of which are low mass stars (<8 $M_\odot$). However, the dominant stars that inject energy back to the intestellar medium (ISM) are the high-mass stars (≥ 8 $M_\odot$). They regulate the energy input in the galaxies in the form of stellar winds, H II regions and supernova explosions. Hence to understand the formation of galaxies it is necessary to understand the formation and evolution of massive stars.

The gas in galaxies can be found in ionized, neutral or molecular form. It is in the regions of molecular gas, which also contains small amounts of dust, that star formation takes place. In the night sky, the star forming regions are visible as dark patches in the plane of our galaxy. These dark regions, first noted by Herschel 1785, are produced by the blocking of visible light by dust although their main component is molecular hydrogen. Molecular clouds are not homogeneous in density but contain over-density structures where stars form.

The formation and evolution of low mass stars in the molecular clouds is relatively well understood (e.g., Shu et al. 1987 Andre et al. 2000). In the case of high-mass stars, their formation and evolutionary mechanisms are less understood despite the fact that they dominate the energy balance of the ISM.

In this thesis, I investigate the evolutionary properties of molecular structures that can form high-mass stars and their early-stage fragmentation processes. In this introductory section I describe general properties of molecular clouds and the processes leading to star formation within them. The fundamental issues that are not understood well in the formation of high-mass stars will be briefly discussed to emphasize the relevance of this thesis work.

1.1 Giant Molecular clouds

Giant molecular clouds (GMCs) are the main sites of star formation in the galaxies. They contain mostly hydrogen (H_2) molecules, have sizes extending over a few tens of parsecs and masses of $\sim 10^5$ $M_\odot$. The internal structure of GMCs are filamentary and exhibit non-

homogeneous density regions (see Fig. 1.1).

The formation of GMCs in the galaxy is not clearly understood. Mechanisms such as converging flows driven by feedback or turbulence, agglomeration of smaller clouds, gravitational instability has been proposed. Computer simulations of colliding flows of warm neutral gas in the ISM show the production of filamentary structures with properties consistent with those determined from observational studies (e.g., Heitsch et al. 2007).

Fragmentation of the GMCs leads to the formation of smaller over-density units known as "clumps" (mass $\sim 10^3$ $M_\odot$ and size $\sim$1 pc). Molecular clumps appear to follow *size versus line width* and *density versus size* relations, known as Larson relations (Larson 1981), which are thought to indicate that clouds are in approximate virial equilibrium. The size versus line width relation, even though it is found to vary with surface density of the cloud (e.g., Heyer et al. 2009; Miville-Deschênes et al. 2017), implies that larger clouds are more turbulent. One important implication of the scaling relations is that most of the clumps are marginally gravitationally bound with turbulence playing key role in preventing them to undergo collapse. Studies of magnetic field in the molecular clouds have hinted that magnetic fields play a crucial role in shaping molecular clouds and perhaps also in their fragmentation processes. Clumps subsequently fragment into smaller units defined as "cores" (mass $\sim$1 to $\leq 10^2$ $M_\odot$ and size $\sim$0.1 pc) which are the precursors of a single star or multiple stellar system. A massive clump of thousand solar masses can form tens to hundreds of stars in a clustered environment.

1.2 Star formation

Star formation takes place via collapse of a cloud core typically located in the densest part of molecular structures that are filamentary in nature. A simplified theoretical view of a prestellar core is that of a truncated isothermal (Bonnor-Ebert) sphere which exhibits a flat density profile in the central region and a power law outside. In the inner part of the core the gas and dust are well coupled and hence have same temperature while on the outer regions they are not, and therefore different temperatures are expected. To determine the physical properties of cores observations in infrared, millimeter and radio wavelenghts are an absolute requirement. Continuum observations provide information of the properties of the dust while molecular line observations provide information about the kinematics and density structure of the gas.

Several observations have shown that low mass star forming cores follow an evolutionary sequence (e.g., Andre et al. 2000) from prestellar to protostellar to a new born star on the main sequence. The spectral energy distribution is used to classify the young stellar objects in Class 0, Class I, Class II and Class III (e.g., Lada 1987, Wilking et al. 1989). The Class 0 objects are only visible in (sub)millimetre continuum, Class I objects are visible in the near-infrared but not in the optical, Class II objects are optically visible and show infrared excess, and finally Class III objects have spectral energy distributions (SED) similar to normal stellar photo-spheres.

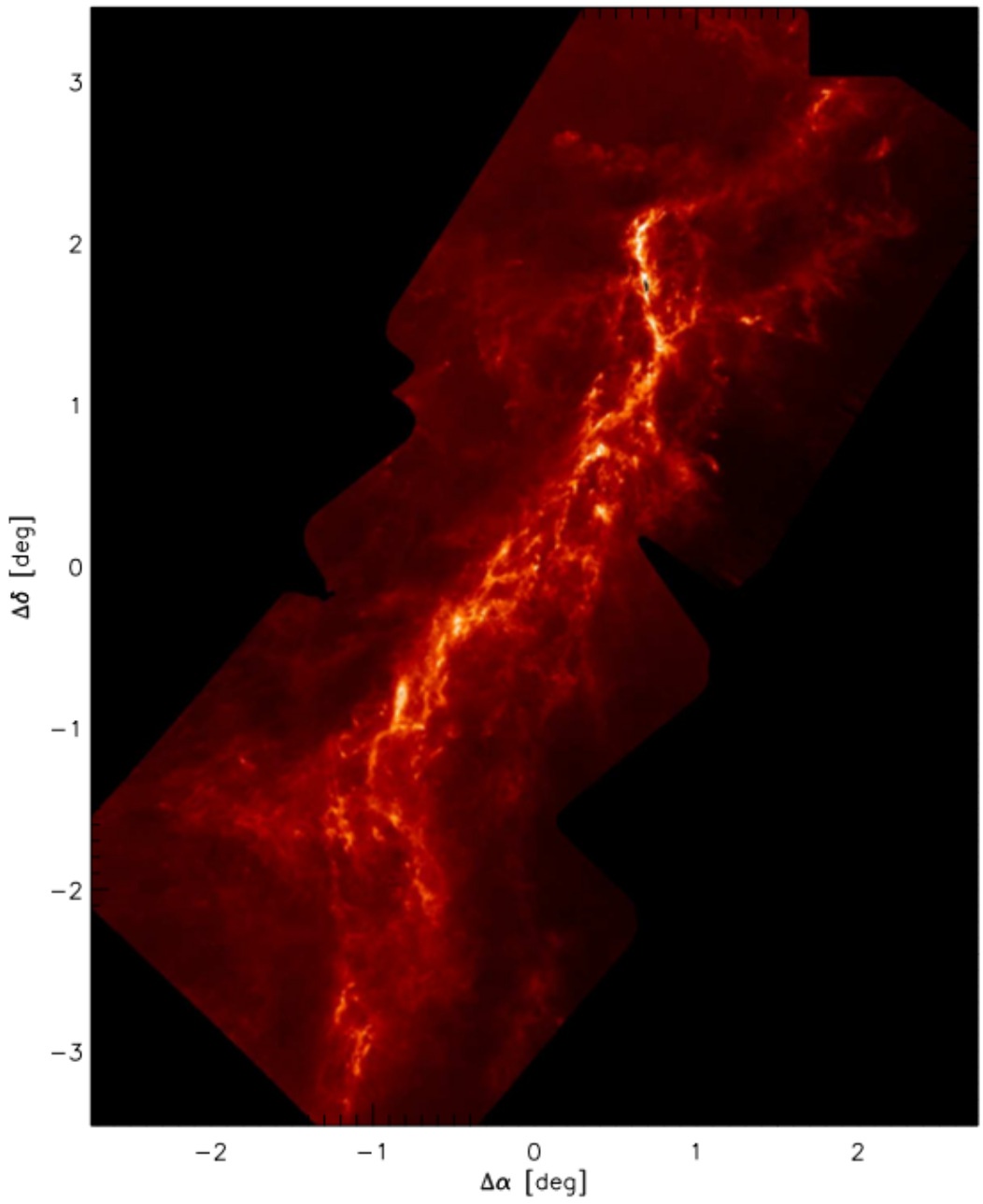

Figure 1.1: Orion-A column density (N(H)) map (Adopted from Stutz & Kainulainen 2015).

High-mass ($M \geq 8 M_\odot$) star formation, on the other hand, is still not well understood. Since high-mass stars form in a clustered environment, mostly embedded in giant molecular clouds, it is difficult to study their formation mechanism and evolutionary properties.

Time-scales

The collapse of a spherical, uniform density, pressure-free cloud occurs on a free-fall time, t_{ff}, given by,

$$t_{ff} = (\frac{3\pi}{32G\rho})^{1/2}, \tag{1.1}$$

where G is the gravitational constant and ρ is the initial mass density. In convenient units,

$$t_{ff} = 3.1 \times 10^5 \times (\frac{n_{H_2}}{10^4\ cm^{-3}})^{-1/2}\ yrs, \tag{1.2}$$

where, $n_{H_2} = \rho/\mu$ is the particle density of hydrogen molecule and μ=2.8 is the mean molecular weight per hydrogen molecule. For a cloud with a density of $n_{H_2} \sim 10^4$ cm^{-3}, the free-fall time is $\sim 3.1 \times 10^5$ years. If gravity alone is at work, star formation happens within one free-fall timescale. This also means that all dense gas collapses to form stars. However, the total gas mass in Galactic molecular clouds with density $\geq 10^3$ cm^{-3} is $\sim 10^9$ $M_\odot$, and without support against gravity star formation rate would be $\sim$ 200 $M_\odot$/yr. This is much higher than the galactic star formation rate inferred from the observations of $\sim$ 1-3 $M_\odot$/yr. Interpretation of the result is that not all the dense gas is undergoing free-fall collapse to form stars. The observed star formation efficiency is lower possibly due to the role of turbulence, magnetic field, rotation, feedback etc.

1.2.1 High-mass star formation

High-mass stars ($M \geq 8$ $M_\odot$) are OB type stars (B3 type and earlier) and have luminosities $\geq 10^3$ $L_\odot$. They are mainly responsible for heating up the surrounding gas and dust via radiation and winds, and enrich the interstellar medium via other feedback events (e.g., outflow, supernova etc).

High-mass stars are mostly found at the center of young open clusters. A large fraction ($> 50\%$) of them are found in binaries (Sana et al. 2013). In the stellar mass distribution (also known as initial mass function, IMF), high-mass stars represent less than 1% of the stars (e.g., Kroupa 2001), therefore observing a statistically significant sample of high-mass protostellar objects and their predecessors is difficult.

The high-mass star forming regions are highly obscured by circumstellar dust with extinctions $A_V \gtrsim 100$. Due to their much lower opacities, observations in infrared and radio/mm domain are used to observe such regions of high extinction in the optical domain. A wealth of observations have revealed that high-mass stars are formed within massive ($M \sim 10^3 M_\odot$)

and dense (n$\sim 10^5$ cm^{-3}) clumps (e.g., Faúndez et al. 2004, Contreras et al. 2016, also see review by Motte et al. 2018a) in a cluster environment.

On the theoretical side, it is still not well understood how high-mass protostars accrete mass in spite of the radiation pressure. A massive star ionizes the surrounding gas and dust forming H II regions that expands within the cloud. When the protostar becomes $\geq$8 M$_\odot$, its radiation pressure is enough to stop the accretion process. In addition to the accretion problem, the way in which molecular clouds fragment to give rise to the observed mass distribution of newly born stars is not yet clear.

The pre-main sequence life time of a high-mass star before it reaches zero age main sequence (ZAMS), known as the Kelvin-Helmholtz time scale ($t_{KH} = \frac{GM^2}{R_p L}$), is typically of the order of $\sim 10^4$ years. On average, this timescale correspond to $\sim$1% of the main sequence lifetime. On the other hand, the clumps that form high-mass stars have high densities ($n\sim 10^4$ cm^{-3}) and their free-fall timescale are of the order of $\sim 10^5$ years. Clumps/cores with higher densities have even shorter free-fall timescales. Unlike for low-mass stars, the free-fall timescale is greater than the Kelvin-Helmholtz timescale for high-mass stars. In particular, for a protostar of mass $\sim$15 M$_\odot$ the free-fall time scale is an order of magnitude larger than the Kelvin-Helmholtz time-scale implying that the protostar has already started nuclear fusion while it is still accreting (e.g., Keto & Wood 2006). How does the accretion process continue despite the radiation pressure from the protostar? This is still debated and is being studied.

Understanding a full picture of high-mass star formation not only requires to explain the accretion process in high-mass star formation, but also how the massive dense clump fragmentation leads to forming high-mass star/s along with low and intermediate mass stars in a clustered environment.

1.2.2 High-mass star formation theories

A handful of models have been proposed to explain high-mass star formation in a clustered environment: (i) Turbulent core accretion (e.g., McKee & Tan 2002; Padoan & Nordlund 2002); (ii) Competitive accretion (e.g., Bonnell & Bate 2006) and (iii) Global hierarchical collapse (e.g., Vázquez-Semadeni et al. 2009, 2017, 2019). These models primarily differ on how the gas is accreted onto the protostars. In addition, the former two models mostly ignore the role of large scale structure while the latter ignores the role of magnetic field in their simulations.

In the turbulent accretion (or core accretion) model the fragmentation of a high mass star forming clump (0.1 - 1 pc scale) leads to cores (0.03 to 0.1 pc scale) with a broad range of masses due to the high degree of turbulence. Each fragmented cores form one or multiple system of stars from the available mass in the core. The competitive accretion model proposes that the clump fragments at early-stages into multiple low mass cores which compete for the mass assembly in a dynamical process. Central cores are at favorable locations to accrete more mass from the clump environment and to become massive and be able to form a massive protostar. Both of these models assume as initial condition a somewhat isolated quasi-static

molecular clump that fragments to form cores and then stars. However the clumps are part of giant molecular clouds (GMCs) that are massive and large in size, hence they are unlikely to be disconnected from their environment. This implies that to understand the process of star formation within clumps, we must understand clump formation itself.

The third model emerges from the proposition that gravity dominates in shaping the cloud structures and their fragmentation. The local versus global gravitational potential play key roles in fragmentation. Theoretical framework of a global hierarchical collapse model has been forwarded by Vazquez-Semadeni et al. (2009, 2017, 2019). This scenario resembles the competitive accretion model in the sense that the clump-fragmentation is not predicted to generate isolated cores. Instead, the cores take part in a dynamical accretion process as they progress toward star formation.

1.2.3 Massive and dense clumps

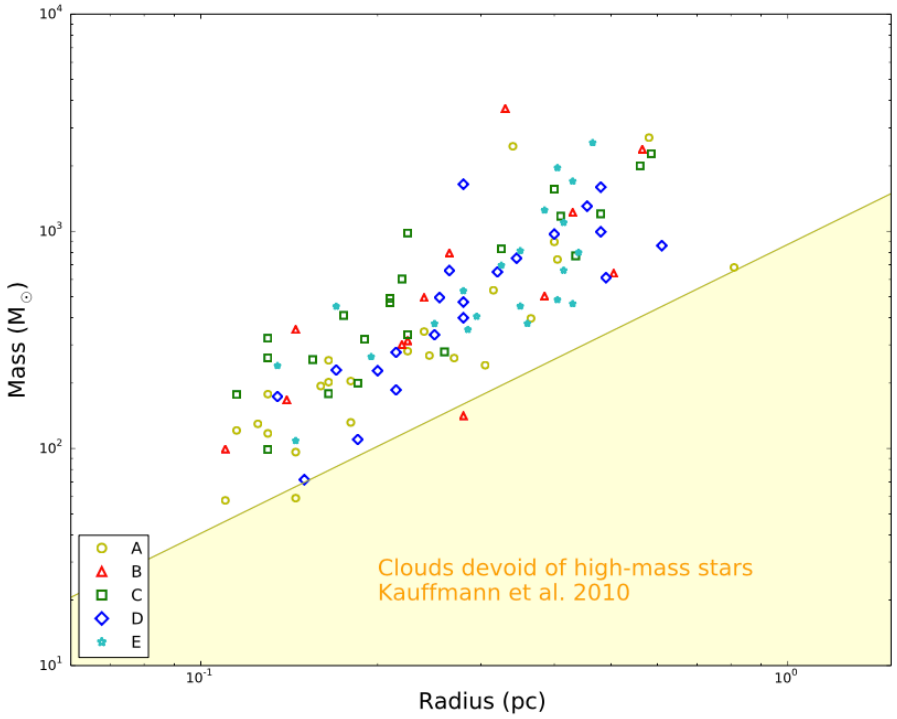

Figure 1.2: Mass verses size relationship of the clumps in five filamentary clouds in Milky-way galaxy. (Adopted from Contreras et al. 2017).

Massive and dense clumps (MDCs) (mass $\sim 10^3$ M$_\odot$, size $\leq$ 1pc, density $\sim 10^5$ cm^{-3}) are the maternities of high-mass stars (e.g., Faúndez et al. 2004; Contreras et al. 2017; Motte et al. 2018a). They are located within giant molecular clouds (GMCs). Herschel multi-wavelength observations (5 bands: 70, 160, 250, 350 and 500 μm) of galactic molecular clouds first revealed that GMCs exhibit filamentary structures. Contreras et al. (2017) studied filamentary molecular clouds harboring several clumps and showed that filaments fragment into clumps (M $\sim$ 20 - 2500 M$_\odot$, R $\sim$ 0.2 - 1.6 pc and n $\sim$ 10^3 - 10^5 cm^{-3})

and most of them have enough mass to form at least one high-mass star as implied by the empirical mass–size relationship (Kauffmann et al. 2010) (see Figure 1.2).

1.2.4 Properties of massive and dense clumps

Evolutionary stages of clumps

Spitzer (3.6, 4.5, 8 and 24 μm) observations (GLIMPSE; Churchwell et al. 2009, MIPSGAL; Carey et al. 2009) toward massive and dense clumps allowed to characterize their evolutionary stages. During the early-stages, clumps are infrared dark, lacking 24 μm emission (Prestellar/Quiescent stage) while in the later stages clumps are infrared bright, exhibiting 24 μm emission along with 3.6-8 μm emission (Protostellar and H II clumps). A summary of the classification scheme using the *Spitzer* observations is listed below:

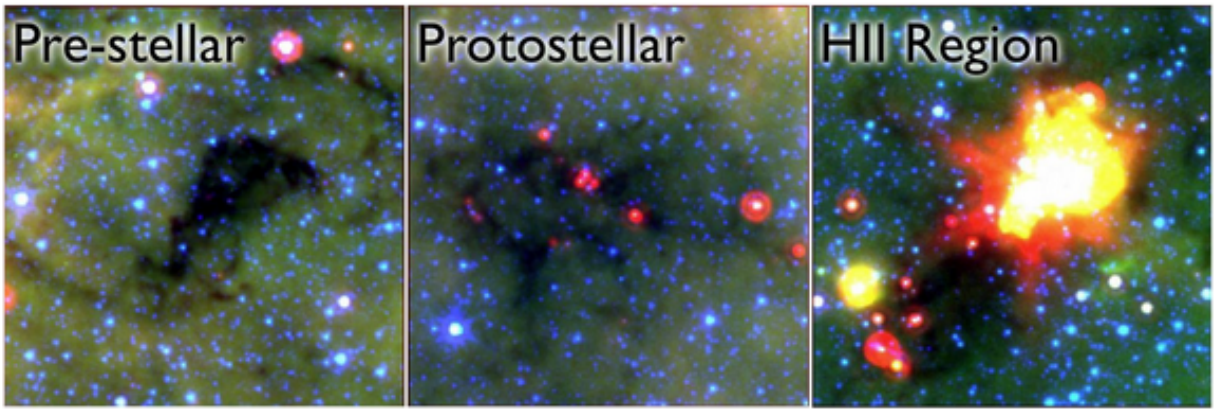

Figure 1.3: Three color image (GLIMPSE 3.6, 8.0 μm, MIPSGAL 24 μm) of different types of clumps. (Left) Pre-stellar: appears as infrared dark, (Middle) Proto-stellar: shows embedded 24 μm point source, (Right) H II: shows extended MIPSGAL and GLIMPSE emission.

- **Quiescent or Prestellar clumps** have no embedded high-mass protostellar object and they do not show 24 μm emission.
- **Protostellar clumps** contain at least a high-mass protostellar object. The birth of protostar/s initiate the heating of the surrounding gas and dust. These clumps show 24 μm emission but have not yet developed H II regions. Additional sign of an embedded protostellar object may be seen as 4.5 μm "green fuzzy" emission.
- **H II clumps** are evolved stages where protostellar objects have started to ionize the surrounding dust and gas and form a compact H II region. These clumps show emission in 3.6 to 24 μm (both GLIMPSE and MIPSGAL). The morphologies of the emission can be compact or extended bubble like structure.

Complementary information is provided by *Herschel* (70, 160, 250, 350 and 500 μm) observations of the massive and dense clumps. The spectral energy distribution of clumps shows an increase in the dust temperature from early to late evolutionary stages (Guzmán

et al. 2015). Early-stage clumps (prestellar or quiescent) are cold (18.6 K) while protostellar and H II clumps show higher temperatures, with average values of 23.6 K and 28.1 K, respectively.

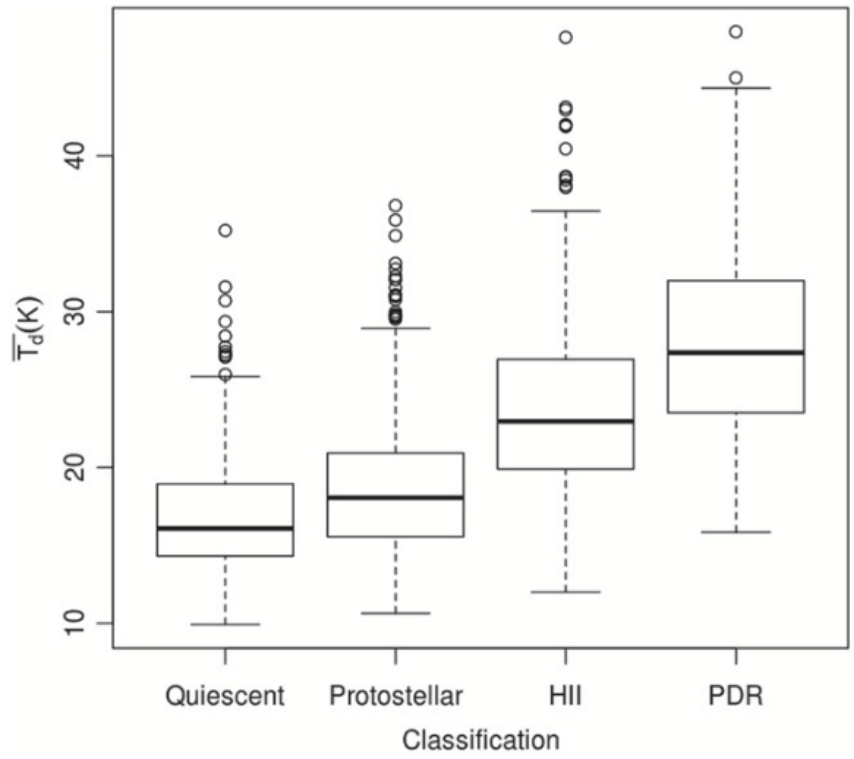

Figure 1.4: Distribution of average dust temperature from clumps in different evolutionary stages. The boxes represent interquartile range of 50% of the distribution. (Adopted from Guzmán et al. 2015)

Various molecular line surveys have been conducted to determine the properties of massive and dense clumps. One of the largest surveys, the Millimeter Astronomy Legacy Team 90 GHz (MALT90) survey (Foster et al. 2011; Jackson et al. 2013; Rathborne et al. 2016), conducted observations towards ∼3200 molecular clumps using the Mopra telescope (40"). The kinematic distances toward the sample are reported by Whitaker et al. (2017). The survey revealed chemical differences of clumps in different evolutionary stages (Rathborne et al. 2016).

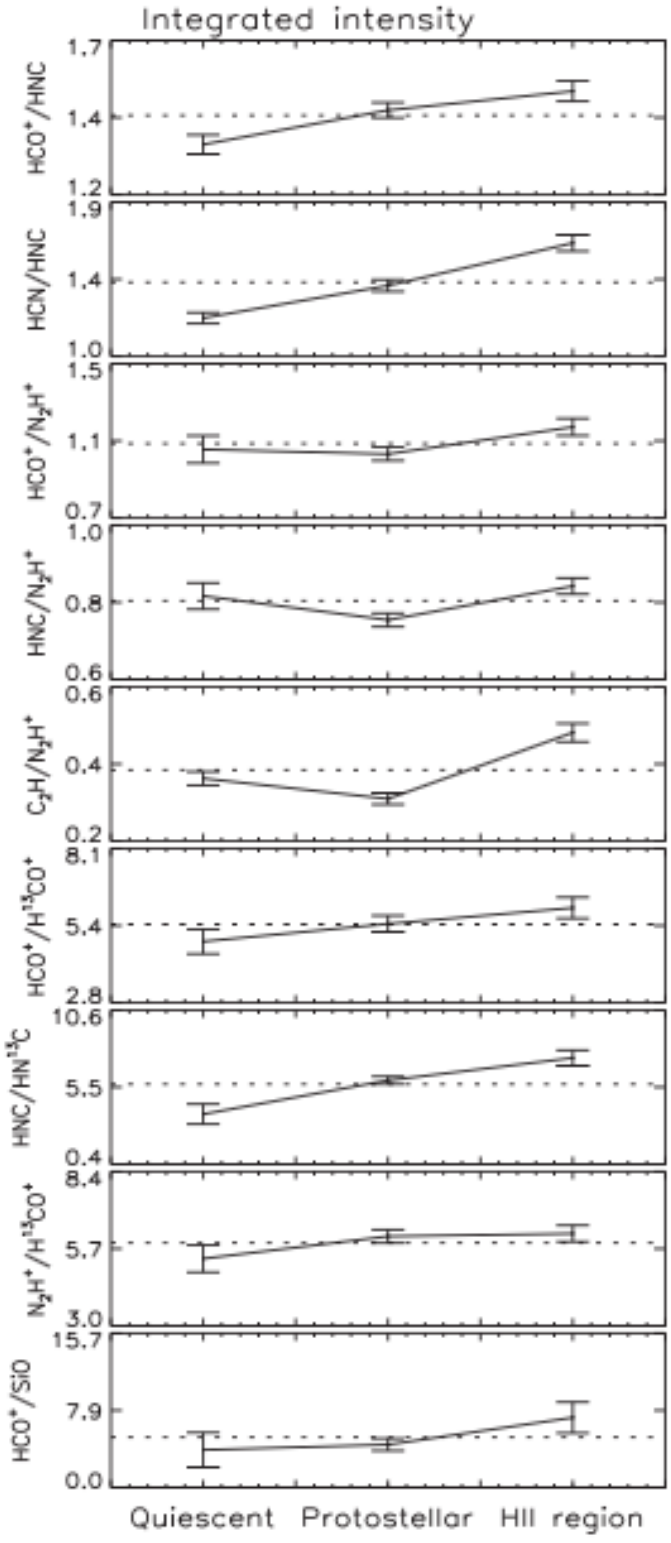

Figure 1.5: Average line ratios of MALT90 clumps at different evolutionary stages. (Adopted from Rathborne et al. 2016)

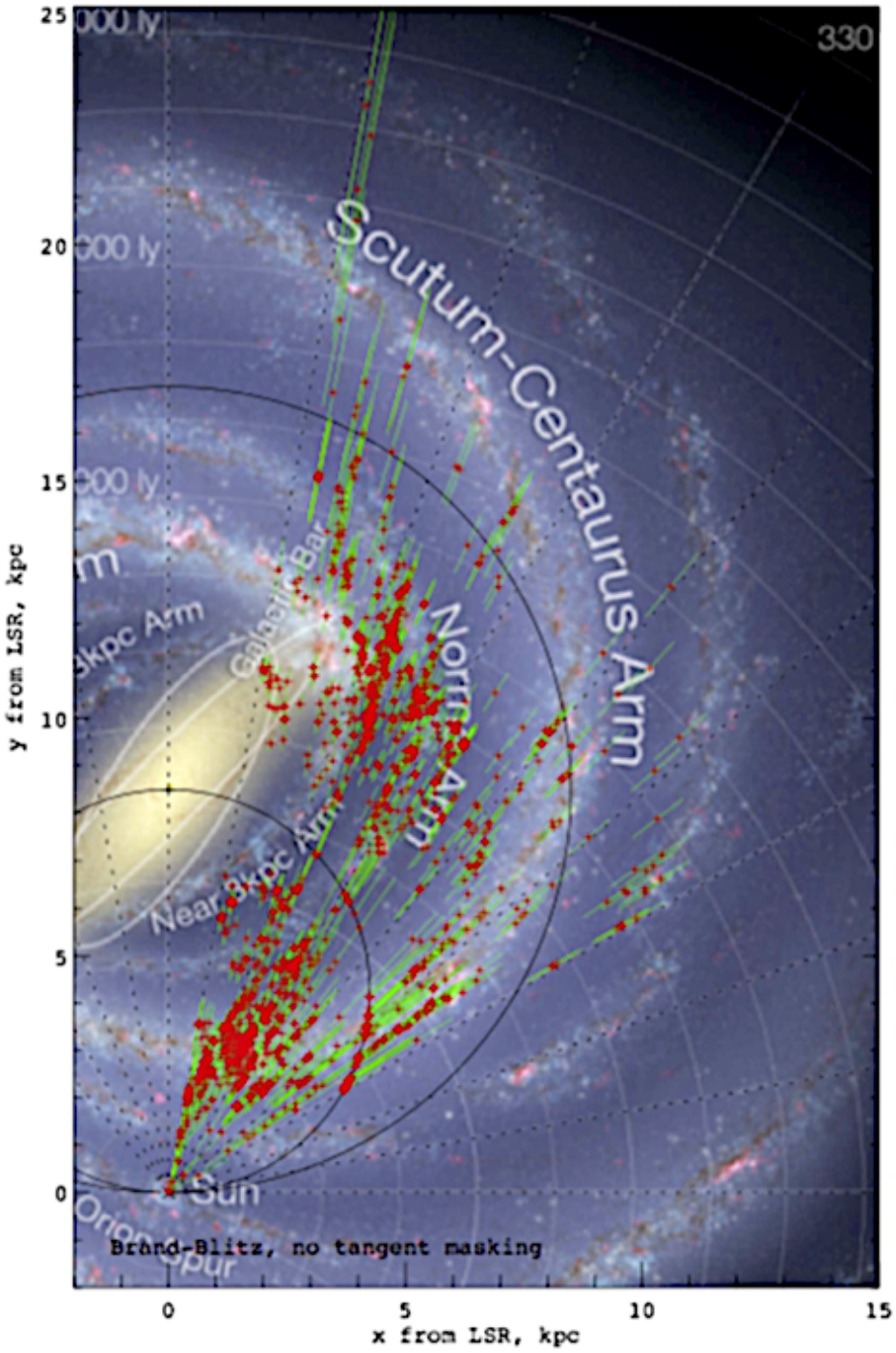

Figure 1.6: MALT90 sources with kinematic distances superposed on iconic Milky Way representation. (Adopted from Whitaker et al. 2017)

1.2.5 Fragmentation of clumps

Jeans fragmentation

The gravitational fragmentation of a cloud is characterized by its Jeans mass. The Jeans mass is derived from the balance between gravitational potential energy (U) and kinetic energy (K). In equilibrium 2K + U = 0, condition referred as virial equilibrium. From this condition, the Jeans mass and radius of a spherical molecular cloud can be expressed in terms of the temperature T and uniform density ρ_o as, respectively,

$$M_J = (\frac{5kT}{G\mu m_H})^{3/2} \quad (\frac{3}{4\pi\rho_o})^{1/2} \ , \tag{1.3}$$

and,

$$R_J = \sqrt{\frac{5kT}{4\pi G\mu m_H \rho_o}} \ , \tag{1.4}$$

where, $\mu = 2.37$ is the molecular weight per free particle, k is the Boltzmann constant, and m_H is the mass of the hydrogen atom.

In convenient units,

$$M_J = 14.7 \ M_\odot \ (\frac{T}{20K})^{3/2} \ (\frac{10^4 cm^{-3}}{n})^{1/2}, \tag{1.5}$$

and,

$$R_J = 0.18 \ pc \ (\frac{T}{20K})^{1/2} \ (\frac{10^4 \ cm^{-3}}{n})^{1/2} \ , \tag{1.6}$$

where, n is the average particle density ($=\rho_o/\mu m_H$).

Molecular clouds with masses higher than the Jeans mass can not be supported by the thermal pressure against the gravity. We note, however, that clouds/cores are unlikely to be in thermodynamic equilibrium, thus the assumption of single temperature and constant density is merely an approximation to simplify the problem. For a clump with a constant density of 10^5 cm^{-3} and a constant temperature of 20 K, the thermal Jeans mass is $\sim$ 3.5 $M_\odot$. This means that a constant density and temperature clump with a mass $\sim 10^3$ $M_\odot$ is expected to fragment, under the Jeans criteria, into $\sim$300 cores with Jeans masses.

One important inference from the Jeans analysis is that to form a massive clump without undergoing fragmentation requires additional support, likely provided by turbulence and/or magnetic fields. Thus the physical properties of massive and dense clumps in terms of turbulence, magnetic fields, and feedback processes are important for understanding which mechanisms provide support against fragmentation. Observations of optically thin molecular lines toward high-mass star forming clumps show considerable broader line widths than in low-mass star forming clumps, indicating higher levels of turbulence which could provide support against the fragmentation (e.g., Zhang et al. 2015). Similarly, magnetic field could play important role in shaping the cloud structure and fragmentation (e.g., Fontani et al. 2016).

Fragmentation of clumps into substructures therefore is not a straight forward physical process. High spectral and spatial resolution observations, for example from ALMA, are crucial to study fragmentation properties of clumps at early-stages from which high-mass star formation process begins.

1.3 Clump physical parameters

1.3.1 Dust emission, mass and column density

Molecular clumps contain mostly molecular hydrogen (H_2) which is relatively hard to observe because its detectable emission lines are produced only at temperatures exceeding $\sim 10^3$ K. Molecular clumps are cold ($\sim$10 - 20 K), hence their hydrogen molecules are invisible. However emission in other molecular species (e.g., CO) and dust are detectable. Observations at infrared, far-infrared, millimeter and radio frequencies are widely used to derive the physical parameters of the molecular clumps. In the following we present a derivation of the mass and column density of a molecular clump using the observed dust continuum emission.

The interstellar dust emission is thermal. The intensity of the radiation emitted by a thermal source of temperature T, optical depth τ_ν at frequency ν can be expressed as,

$$I_\nu = B_\nu(T)(1 - \mathrm{e}^{-\tau_\nu}), \tag{1.7}$$

where $B_\nu(T)$ is the intensity of radiation of a blackbody of temperature T at frequency ν,

$$B_\nu(T) = \frac{2h\nu^3}{c^2}\frac{1}{\mathrm{e}^{h\nu/kT} - 1}, \tag{1.8}$$

where h is the Planck constant, c is the speed of light and k is the Boltzmann constant.

The optical depth τ_ν of the dust emission can be expressed in terms of the mass absorption coefficient or opacity (per mass) k_ν of the dust grains as,

$$\tau_\nu = \int k_\nu \rho \mathrm{d}l \ , \tag{1.9}$$

where ρ is the density of the medium. The column density of molecular hydrogen, N_{H_2} ($= \int n(H_2)\mathrm{d}l$), is related to the opacity as,

$$N_{H_2} = \int \frac{\rho}{\mu m_H}\mathrm{d}l \ , \tag{1.10}$$

where μ is the molecular weight per hydrogen molecule, m_H is the mass of the hydrogen atom. Therefore the column density of hydrogen molecule can be expressed in terms of the dust optical depth as,

$$N_{H_2} = \frac{\tau_\nu}{\mu m_H k_\nu}. \tag{1.11}$$

In the optically thin regime, the optical depth can be written, using the eqn. (1.7), as,

$$\tau_\nu = \frac{I_\nu}{B_\nu(T)} \ , \tag{1.12}$$

and the column density as,

$$N_{H_2} = \frac{I_\nu}{\mu m_H k_\nu B_\nu(T)} \ . \tag{1.13}$$

The observed flux density per beam solid angle is,

$$S_\nu^{beam} = \int_{\Omega_b} I_\nu P \mathrm{d}\Omega \ , \tag{1.14}$$

where P is the power pattern of the telescope, normalized to unity at its most sensitive direction, and $\Omega_b = \int P \mathrm{d}\Omega$ is the beam solid angle. Then, the beam averaged intensity can be written as, $< I_\nu >= S_\nu^{beam}/\Omega_b$. Using this relation, we can write the beam averaged column density as,

$$N_{H_2} = \frac{S_\nu^{beam}}{\Omega_b \mu m_H k_\nu B_\nu(T)} \ . \tag{1.15}$$

The mass of the clump can be derived by integrating the column density across the source, hence

$$M = \mu m_H \int\int n(H_2) \mathrm{d}l \mathrm{d}A = \mu m_H \int N_{H_2} \mathrm{d}A \tag{1.16}$$

where dA is the surface element related to the solid angle element $\mathrm{d}\Omega$ by $\mathrm{d}A = D^2 \mathrm{d}\Omega$, where D is the distance to the source. Using eqn. (1.13) for the column density, the mass of a clump can then be written as,

$$M = \frac{S_\nu D^2 R_{g\mathrm{d}}}{k_\nu B_\nu(T)}, \tag{1.17}$$

where S_ν is the integrated flux density, k_ν the dust mass absorption coefficient and $R_{g\mathrm{d}}$ the gas-to-dust ratio.

1.3.2 Molecular line emission

Molecular transitions can be classified into three categories depending on the motions of their electrons and nuclei: electronic, vibrational and rotational. Electronic states have the higher energies and the radiation emitted in electronic transitions usually fall in the visible to UV frequency ranges. Vibrational transitions occur between levels of the same electronic state and the emitted radiation usually fall in the infrared frequency range. The rotational energies of the nuclei are considerably smaller than the electron energies and rotational transitions give rise to emission at millimeter and microwave wavelengths. These are the most commonly observed transitions from molecular clumps in order to determine their physical and chemical properties.

The rotational angular momentum is quantized and transitions between levels are permitted only when $\Delta J = \pm 1$, where J is the rotational quantum number. The rotational energy is given by,

$$E_{rot} = J(J+1)\frac{h}{8\pi^2 m r_{\rm e}^2}, \tag{1.18}$$

and the frequency of photon emitted in the rotational transition $J \rightarrow J-1$ is given by,

$$\nu = \frac{\Delta E_{rot}}{h} = \frac{hJ}{4\pi m r_{\rm e}^2} \quad J = 1, 2, 3, 4... \tag{1.19}$$

where m is the reduced mass and $\rm r_e$ is the nuclear separation.

The ratio of the populations in upper and lower energy levels, n_l and n_u, respectively, in thermal equilibrium is given by the Boltzmann distribution,

$$\frac{n_l}{n_u} = \frac{g_u}{g_l} {\rm e}^{-h\nu/kT_K} \tag{1.20}$$

where T_K is the thermal or kinetic temperature and $\rm g_l$ and $\rm g_u$ are, respectively, the degeneracy in the lower and upper levels. In general, the level population is determined by both collisions and radiation, and we may write

$$\frac{n_l}{n_u} = \frac{g_u}{g_l} {\rm e}^{-h\nu/kT_{\rm ex}} \tag{1.21}$$

where T_{ex} is the excitation temperature. The excitation temperature is equal to the kinetic temperature when collisions dominate and equal to the radiation temperature when radiation dominates. The regime in which collisions plays a role but thermalizaton has not yet been achieved is refered as sub-thermal excitation.

Critical density

The critical density of a molecular transition can be defined as the density at which spontaneous downward transitions, collisional excitations and de-excitations in a two level populations are balanced, and can be written as,

$$n_{crit} \approx A_{\rm ij}/\gamma_{\rm ij} \ , \tag{1.22}$$

where $\rm A_{ij}$ is the Einstein's coefficient and $\gamma_{\rm ij}$ is the collision rate. The Einstein's coefficient depends on the frequency of the transition and the dipole moment of the molecule. The collision rate depends on the kinetic temperature. Molecular species such as HCO^+, HCN, HNC, N_2H^+ have critical densities $\geq 10^4$ cm^{-3} at kinetic temperature of 20 K. Thus, they are referred as high density tracers. Table 1.1 lists the critical densities for different transitions of the commonly observed molecular species adopted from Shirley (2015).

Table 1.1: Critical densities of dense gas tracers.

Molecule	$J \rightarrow J-1$	ν (GHz)	E_J/k (K)	n_{crit} (at 20 K) (cm^{-3})
HCO^+	1→0	89.189	4.28	4.5×10^4
	2→1	178.375	12.84	4.2×10^5
	3→2	267.558	25.68	1.4×10^6
	4→3	356.734	42.80	3.2×10^6
$H^{13}CO^+$	1→0	86.754	4.16	4.1×10^4
	2→1	173.507	12.49	3.8×10^5
	3→2	260.255	24.98	1.3×10^6
	4→3	346.998	41.63	2.9×10^6
HCN	1→0	88.632	4.25	3.0×10^5
	2→1	177.261	12.76	2.8×10^6
	3→2	265.886	25.52	1.0×10^7
	4→3	354.505	42.53	2.3×10^7
HNC	1→0	90.664	4.35	1.1×10^5
	2→1	181.325	13.05	1.0×10^6
	3→2	271.981	26.11	4.0×10^6
	4→3	362.630	43.51	1.0×10^7
N_2H^+	1→0	93.174	4.47	4.1×10^4
	2→1	186.345	13.41	3.7×10^5
	3→2	279.512	26.83	1.2×10^6
	4→3	372.673	44.71	2.8×10^6

Degeneracies

For rotational lines, the degeneracy of level g_u is given by,

$$g_u = g_J g_K g_I \ ,$$

$$where,$$

$$g_J = 2J_u + 1 \ \ , \tag{1.23}$$

$$g_K = 1 \quad for \quad K = 0 \ \ and \ \ 2 \quad for \quad K \neq 0 \ \ ,$$

$$g_I = g_{nuclear}/g_n \ ,$$

where g_J and g_K are the degeneracy due to rotational quantum numbers J and K associated with symmetric and asymmetric top molecules and g_I is the nuclear spin degeneracy in rotational states due to identical nuclei in non linear molecule with symmetry (e.g., H in CH_3CN), g_n and $g_{nuclear}$ can be calculated as:

$$g_n = (2I+1)^\sigma$$

$$g_{nuclear} = \tfrac{1}{3}(2I+1)(4I^2+4I+3) \quad for \quad K = 3n \tag{1.24}$$

$$= \tfrac{1}{3}(2I+1)(4I^2+4I) \quad for \quad K \neq 3n,$$

where σ is the number of identical nuclei and $I = 1/2$ is the spin number, and n is a non-negative integer value.

Line strength

For a linear molecular transition from $J \rightarrow J-1$, the line strength is given by,

$$S = \frac{J}{(2J+1)} \ . \tag{1.25}$$

For a symmetric top transition from $J, K \rightarrow J-1, K$, the line strength can be written as:

$$S = \frac{J^2 - K^2}{J(2J+1)} \ . \tag{1.26}$$

Finally, for $J, K \rightarrow J, K$ or Q-branch transitions,

$$S = \frac{K^2}{J(J+1)} \ . \tag{1.27}$$

Rotational partition function

The partition function (Q_{rot}) of a molecule is a function of its electronic, rotational, vibrational and spin state of its nuclei. This quantity gives the statistical sum of population levels and can be expressed as:

$$Q_{rot} = \sum_{\rm i} g_{\rm i}\ exp(-E_{\rm i}/kT)\ . \tag{1.28}$$

The partition function for linear polyatomic molecules can be written as (McDowell 1988):

$$Q_{rot} \simeq \frac{kT}{hB_o}\ exp(\frac{hB}{3kT})\ . \tag{1.29}$$

The first order approximation of this equation yields,

$$Q_{rot} \simeq \frac{kT}{hB_o} + \frac{1}{3}\ . \tag{1.30}$$

Observations: brightness temperature and flux density

From the observations of molecular lines it is possible to determine or constrain various physical parameters of the emiting region. At millimeter wavelengths, the intensity of radiation from a clump falls in the Rayleigh-Jeans regime i.e. hν <<kT. The exponential $e^{h\nu/kT}$ in the Planck equation (1.8) becomes ≈1+hν/kT, and the Planck function reduces to,

$$B_\nu = \tfrac{2\nu^2}{c^2} kT\ . \tag{1.31}$$

The brightness temperature, T_b, of radiation with intensity I_ν is defined as the temperature of a black body that emits the same intensity at that frequency, namely,

$$I_\nu = \frac{2h\nu^3}{c^2}\ \frac{1}{(e^{h\nu/kT_b} - 1)}\ . \tag{1.32}$$

In the Rayleigh-Jeans regime,

$$I_\nu = \frac{2k\nu^2}{c^2}\ T_b\ . \tag{1.33}$$

One frequently defines the radiation temperature $J(T)$ at frequency ν as,

$$J_\nu(T) = \frac{c^2}{2k\nu^2} I_\nu = \frac{h\nu}{k} \frac{1}{e^{h\nu/kT_b} - 1}\ . \tag{1.34}$$

Hence, in the Rayleigh-Jeans regime the radiation temperature is equal to the black body temperature that reproduces the brightness of the source.

For a line with an optical depth τ and excitation temperature T_{ex}, the main beam brightness temperature T_{mb} can be written as,

$$T_{mb} = f[J(T_{\rm ex}) - J(T_{bg})](1 - {\rm e}^{\tau}), \tag{1.35}$$

where T_{bg} is the background temperature and f is the beam filling factor.

The quantity measured from the observations is the antenna temperature, T_A, which is related to the main beam brightness temperature (T_{mb}) by,

$$T_{mb} = T_A/\eta_{mb} \ , \tag{1.36}$$

where η_{mb} is the main beam efficiency.

The flux density from a source subtending a solid angle Ω_s can be expressed in terms of the main beam brightness temperature as,

$$S_\nu = \frac{2kT_{mb}\nu^2}{c^2}\Omega_s \ . \tag{1.37}$$

Column density

The column density of a molecule can be expressed in terms of the excitation temperature, T_{ex}, and optical depth, τ_ν, of a single line as (e.g., Garden et al. 1991),

$$N_{tot} = \frac{3h}{8\pi^3|\mu_{lu}|^2}\frac{Q_{rot}}{g_u} \quad ({\rm e}^{E_u/kT_{\rm ex}})[{\rm e}^{h\nu/kT} - 1]^{-1} \int \tau_\nu {\rm d}v \ , \tag{1.38}$$

where Q_{rot} is the partition function, E_u is the upper level energy, $\int \tau {\rm d}v$ is the integrated optical depth of the line and $|\mu_{lu}|$ is the dipole matrix element related to the line strength S and dipole moment μ as $|\mu_{lu}| = S\mu^2$. Both the excitation temperature and optical depth can be constrained from observations of molecular transition lines.

In optically thin regime, the main beam brightness temperature can be written as

$$T_{mb} = f[J(T_{\rm ex}) - J(T_b)]\tau. \tag{1.39}$$

Using this equation and substituting the partition function in eqn. (1.38), we can express the column density in terms of the observed integrated line intensity ($\int T_{mb}{\rm d}v$) as,

$$N_{tot} = \frac{3k}{8\pi^3\mu^2 B}\frac{(T_{\rm ex} + hB/3k)}{J_u R_{\rm i}}\frac{exp(\frac{E_u}{kT_{\rm ex}})}{exp(h\nu/kT_{\rm ex}) - 1}\frac{1}{f[J(T_{\rm ex}) - J(T_{bg})]}\int T_{mb}{\rm d}v, \tag{1.40}$$

where $R_{\rm i}$ is the relative line strength of an hyperfine transition.

Rotational diagram analysis

The detection of emission in at least two rotational transitions of a molecule allows to determine the rotational temperature. The standard rotational diagram analysis assumes that the lines are optically thin and that the population levels are characterized by a single excitation temperature (LTE assumption).

The upper level population density, N_u, of a transition can be expressed in terms of the observed line flux density as,

$$\frac{N_u}{g_u} = \frac{3c^2}{16\pi^3\nu^3 S_{lu}\mu^2\Omega_s}\int S_\nu \mathrm{d}v \tag{1.41}$$

where ν is the frequency of the transition, Ω_S the source size, S_{lu} the line strength, μ the dipole moment, g_u the degeneracy of the upper level and $S_\nu \mathrm{d}v$ the velocity integrated line flux density.

The total population density and upper level population density are related as,

$$ln\frac{N_u}{g_u} = ln(N_t) - lnQ(T_{rot}) - \frac{E_u}{kT_{rot}}\ . \tag{1.42}$$

Combining the above two equations yields,

$$ln\Big[\frac{3c^2}{16\Omega_s\pi^3\nu^3\mu^2 S_{lu}}\int S_\nu \mathrm{d}V\Big] = ln\Big[\frac{N_t}{Q(T_{rot})}\Big] - \Big[\frac{E_u}{kT_{rot}}\Big]\ . \tag{1.43}$$

When two or more transition lines of a molecule are observable this analysis provides the rotational temperature and column density of the molecule.

1.4 Outline of the thesis

This thesis is primarily based on the work done in three individual research projects, all of which have a common goal: determining the physical properties of massive and dense clumps and their fragmentation properties. Chapter 2 briefly outlines the objectives of the thesis. Chapter 3 presents the SuperMalt project which aims to determine the properties of large sample of massive and dense clumps using multi-level molecular transition line data obtained using the APEX telescope with an angular resolution of ∼20". Chapter 4 presents the fragmentation properties of a subsample of clumps derived from observations made at angular resolution of ∼8" using the Artemis camera at the APEX telescope. Chapter 5 presents high angular resolution (∼1.5") study of two clumps made using the ALMA telescope with the goals of studying the dynamical and kinematical properties of the fragmented substructures. Chapters 3 to 5 were written in a self-sufficient way for easy reading. Finally, chapter 6 combines a summary of this work together with future prospects.

Chapter 2

Thesis objectives

The first aim of my thesis was to observe, using the APEX telescope with an angular resolution of ∼20", a large sample of massive and dense clumps in different molecular line transitions, mainly high-density tracers, to investigate their physical and chemical properties. Thereafter, I observed a sub-sample of these clumps, also using APEX but with an angular resolution of ∼8", with the goal of investigating their fragmentation characteristics at the scale of 0.1 pc. Finally, I performed ALMA observations, with an angular resolution of ∼1.5", in order to investigate the mass distribution at the scale of cores (0.02 pc) and their kinematical properties. Each of the projects included in this thesis are presented in detail in separate chapters, hence only a brief account of the project objectives is presented here.

2.1 SuperMALT: physical and chemical properties of massive and dense clumps

The Millimeter Astronomy Legacy Team 90 GHz (MALT90) Survey used the 22 m Mopra Telescope to observe 15 low excitation molecular lines and one recombination line, near 90 GHz, towards ∼3200 dense molecular clumps in different evolutionary stages (from pre-stellar to proto-stellar and H II regions) (Foster et al. 2011; Jackson et al. 2013; Rathborne et al. 2016). This survey was made with an angular resolution ∼40" and a velocity resolution of ∼ 0.1 km/s. The main molecular lines detected toward these clumps in the MALT90 survey correspond to dense gas tracers, such as HNC, HCN, HCO^+ and N_2H^+. This survey revealed wealth of information about morphology, chemistry and kinematics of the clumps. However the results were constrained by the observation of low excitation molecular lines and the coarse spatial resolution, of ∼40", of the survey. Single excitation line observations alone are not sufficient to determine the physical properties of clumps, such as gas column/volume density, kinetic temperatures etc. Multi-level molecular excitation line information are needed to understand physical and chemical properties of the clumps. In addition, high excitation molecular maps can provide better spatial resolution revealing the substructures.

The SuperMALT Survey is designed as a follow up of the MALT90 survey with the goal of observing a sub-sample of 73 MALT90 clumps in high excitation molecular lines and key isotopomers from APEX 12 m Telescope (see Table 1). The sample is selected by using the following criteria: [1] reliable detection ($\geq 5\sigma$) in key molecular transitions (i.e. N_2H^+, HCN, HNC, HCO^+(1-0) in MALT90, [2] masses $\geq$ 200 $M_\odot$, [3] distance $\sim$ 4 kpc and [4] representative of various evolutionary stages [pre-stellar or quiescent, proto-stellar, H II clumps]. The sample size is statistically robust to characterize the detailed gas kinematics, temperature, and density structure of the high-mass star forming clumps with their evolutionary stages.

The observational goals of the SuperMALT survey are (i) to map high-mass star forming dense clumps in $J = 3 \rightarrow 2$ and $4 \rightarrow 3$ transition lines of key high density tracers (eg. HCO^+, N_2H^+, HCN, HNC) within a region of size $2'$x$2'$ with an angular resolution ($\sim$ 20") and (ii) to obtain spectra of key isotopomer $H^{13}CO^+$ $J = 3 \rightarrow 2$ toward the peak position of the clumps.

Among the various science goals of the survey, the following are the key science objectives investigated in this thesis work.

- To investigate the emission line morphologies of the clumps at different evolutionary stages.
- To study the line emission properties (profiles/asymmetries, intensities and line widths etc) to determine properties, such as collapse/expansion motions, role of turbulence, and chemical characteristics and assess changes with the evolutionary stages.
- To determine the physical properties of the clumps (kinetic temperatures, densities and column densities) and provide a statistically robust physical and chemical characteristics of massive and dense clumps at different evolutionary stages.

I also incorporate the MALT90 survey data to characterize the physical and chemical properties of high-mass star forming clumps at different evolutionary stages. The analysis and result of the multi-level molecular transition lines from the SuperMALT survey are presented in chapter 3.

2.2 Artemis survey: fragmentation properties of massive dense clumps at 0.1 pc scale

I selected massive and dense clumps from the SuperMALT survey, likely to give birth to massive stars, to study the fragmentation characteristics from $\sim$0.5-1 pc to $\sim$0.1 pc scales. The sample consists of 23 massive dense clumps covering four different evolutionary stages: prestellar (5), protostellar (10), H II (6), PDR (1) and 'Unknown' classification (1). The MDCs are at similar distances of 3.3–3.9 kpc, have sizes of $\sim$0.5 pc and masses of the order $\geq$200$M_\odot$, therefore the sample provide homogeneous physical scale and different evolutionary stage clumps to study the link between fragmentation, evolutionary stage and other physical properties. The objective of this work is to study the level of fragmentation within massive and dense clumps at the scale of 0.1 pc.

2.3 ALMA observations of two massive and dense clumps

High-mass stars (≥ 8 $M_\odot$) form in massive ($\sim 10^3$ $M_\odot$) and dense ($\sim 10^4$ cm^3) over-densities in the large molecular structures in the galaxies, which is referred as massive and dense clumps (or MDCs) (Faúndez et al. 2004; Contreras et al. 2017) in this work. However, the early evolution of MDCs and the ensuing fragmentation leading to the formation of cores is not well understood. The relative importance of primordial clump fragmentation versus large-scale accretion in determining the distribution of core masses still remains to be assessed. Determining the physical and kinematical properties of the molecular gas in MDCs at both, the large clump scale ($\sim$1 pc) and small core scale (5000 AU), will permit to investigate the presence of global or localized collapse and the characteristics of the primordial fragmentation.

With these goals in mind we identified several clumps in MALT90 program that are in the pre-stellar and protostellar phase of evolution showing the unambiguous presence of large-scale collapse motions, namely line profiles in optically thick tracers showing blueshifted asymmetries with respect to the observed profiles in optically thin gas tracers. They represent the best candidates in which to test theories. We selected two clumps (AGAL333.014-00.521 (quiescent) and AGAL329.184-00.314 (protostellar)) which fulfilled the following criteria: (i) in early evolutionary stages, either quiescent or protostellar; (ii) with line profiles exhibiting the blue asymmetry signature of global collapse; (iii) with total masses derived from dust in excess of 500 $M_\odot$; and (iv) isolated, namely far away from extended H II and PDR regions.

The following are the scientific objectives of this study:

- Determination of the mass distribution (core mass function), physical properties and kinematics of the individual dense cores within the pre-stellar and protostellar clumps.

- Determination of the characteristics of the velocity field and shape of the line profiles in order to assess the role of turbulence in the clumps and its possible evolution with time.

- Determination of the physical properties, in particular the density profile, and map the velocity field of the large scale clump (envelop) as a function of radius.

We undertook ALMA band 3 ($\sim$90 GHz) observations of four molecular species (HCO^+, $H^{13}CO^+$, N_2H^+ J 1 $\rightarrow$ 0 and CH_3CN J 5 $\rightarrow$ 4) along with the continuum emission. The observations provide a spatial resolution of $\sim$1.5" and spectral resolution of $\sim$0.2-0.4 km s^{-1}. Each molecular species were chosen to fulfill certain science goal. For example the pair of optically thick HCO^+ and optically thin $H^{13}CO^+$ lines allows us to study the infall motions, the N_2H^+ traces the cold dense gas and CH_3CN traces the temperature of the gas.

2.4 Data reduction tools and methods

Data reduction tools

I used GILDAS (Class & Greg package) to reduce the single dish data. Data reduction process includes baseline fitting, re-gridding and smoothing the spectra to obtain desired signal to noise ratio for the maps. I fitted Gaussian line profile to extract the line parameters where possible. For interferometric data, I used CASA software package which is a dedicated software for ALMA data reduction and analysis.

Radiative transfer models

To constrain the physical parameters, I used integrated line intensities and line ratios of the peak spectra in multi transition line data. I used RADEX for the 1-D radiative transfer models to constrain the physical parameters (e.g., density, kinetic temperatures, column densities) of the clumps.

Statistical study

For statistical study of the observed and derived parameters e.g., noise, line width, temperature, densities etc., I used multiple statistical tools. For presentation of the results, I used bar, scatter, histogram and Whisker plots. I will mainly use various python packages (e.g., numpy, scipy, astropy, matplotlib, aplpy, etc) for this purpose. Some advanced statistical test has been performed where required.

Chapter 3

SuperMALT: A survey of massive and dense clumps in high excitation molecular lines

The early report of the SuperMALT survey is published in Neupane et al. (2018) and full report is in submission process (Neupane et al. in *prep.)*

In this paper we present the SuperMALT survey, a follow-up of the MALT90 survey, carried out from the APEX telescope with the goal of observing emission in the $J = 3 \rightarrow 2$ and $J = 4 \rightarrow 3$ rotational transitions of HCO^+, HNC, HCN, and N_2H^+ toward a sample of high-mass star forming clumps. The targets were selected from the MALT90 catalog by that exhibited strong emission in the $J = 1 \rightarrow 0$ transition of the above species and that spanned the whole range of early evolutionary stages (from quiescent to H II clumps). The observational strategy was to map the emission in the above transitions in regions of $2' \times 2'$ in size, and in addition to obtain a single spectra in the $J = 3 \rightarrow 2$ line of $H^{13}CO^+$ toward the emission peak of each clump. The aim of the SuperMALT survey is to provide an important new legacy database to characterize the physical and chemical evolution of high-mass star-forming clumps. We detected all lines toward the observed clumps. We analyzed the line emission profiles, morphologies, sizes, line intensities and line ratios for clumps at different evolutionary phases. The results demonstrate that properties of clumps evolve which are seen in changes in the molecular line emissions and their profiles, as well as the increase in the line widths and temperature. Analysis of line asymmetry in optical thick lines show that large scale infall motions are more common towards clumps at earlier evolutionary stages while expansion motions become more common at later stages.

3.1 Introduction

Molecular clouds exhibit long filamentary structures which display smaller over-density regions where star formation takes place (e.g., Takahashi et al. 2013; Teixeira et al. 2016; Contreras et al. 2016). Observations have demonstrated that high-mass stars (with masses

$>8\,M_\odot$) form in the most massive ($\sim10^3$ $M_\odot$) and dense ($\sim10^4$ cm^{-3}) over-densities (Garay et al. 2004, Faúndez et al. 2004; Contreras et al. 2017), which we refer as 'clumps'. However, how high-mass protostars acquire mass during their formation process is not understood well. The current models of high-mass star formation, such as competitive accretion (e.g., Bonnell & Bate 2006), turbulent core accretion (e.g., Padoan & Nordlund 2002), hierarchical gravitational fragmentation (e.g., Vázquez-Semadeni et al. 2009, 2017), differ primarily in the fragmentation process of the clumps and the ensuing mass accretion process.

All theories assume that a high-mass star begins its life in a dense clump, which collapses and fragments to form cold pre-stellar cores, which evolve into high-mass protostars. Once the high-mass protostar enters the main sequence phase, feedback processes such as ionization and outflows/stellar winds are likely to terminate further star formation. This phase is observable as ultra-compact H II regions and hot molecular cores. Despite the theoretical expectations, the clump evolutionary phases remain poorly understood, mainly because the processes involved are difficult to observe. Clearly, new observational studies to characterize the clumps physical and chemical evolutionary properties are sorely needed.

Recent Galactic plane surveys of dust continuum emission (e.g. ATLASGAL - Schuller et al. 2009; BGPS - Dunham et al. 2010; Hi-GAL - Molinari et al. 2010) and molecular line emission (e.g., MALT90 - Foster et al. 2011; Jackson et al. 2013; Rathborne et al. 2016) have provided a rich database of massive and dense clumps in the Galactic plane. In particular the Millimetre Astronomy Legacy Team 90 GHz (MALT90) survey, a large molecular line survey conducted with the Mopra telescope, has been a key first step into systematically determining the physical characteristics of high-mass star forming clumps (e.g., Jackson et al. 2013; Hoq et al. 2013; Guzmán et al. 2015; Rathborne et al. 2016). MALT90 obtained $3' \times 3'$ maps in 16 spectral lines in the 3mm atmospheric spectral window toward more than 3500 ATLASGAL clumps. While MALT90 provides the global morphology, chemistry, and kinematics of the dense star-forming gas within each of these clumps (at an angular resolution of $\sim$38" - 0.7 pc at distance of $\sim$4 kpc) it cannot, alone, provide a robust measurement of the gas temperatures and column/volume densities. Only with a multi-level excitation analysis, a reliable determination of clump temperatures, densities, and column densities can be obtained, parameters which are crucial to ascertain the physical and chemical differences among clumps in different evolutionary stages.

In this paper we present the SuperMALT survey[1], a follow up of the MALT90 survey. The paper is organized as follows: in Section 3.2 we describe the motivation of the survey, the sources targeted, and the molecular lines observed; in Section 3.3 we describe the observations made with the APEX telescope and the data reduction; Section 3.4 presents the observational results, including the characteristics of the line profiles and the morphology of the emission in the different lines. In Section 3.5 we discuss the analysis of the data, including the derivation of the physical parameters, kinematics and chemistry of the clumps. The main conclusions of this work are summarized in Section 3.6.

[1]http://www.yanettcontreras.com/supermalt.html

3.2 The survey

The aim of the SuperMALT survey is to provide a new legacy database to characterize the evolution of high-mass star forming clumps. In order to do this, we observed a sample of 73 high-mass star forming clumps in the Galactic plane in a range of evolutionary stages in key molecular species and high excitation lines, with the intention to be complementary to the MALT90 survey which observed these molecular species in the $J = 1 \rightarrow 0$ transition.

3.2.1 Targets

Table 3.1: List of sources observed by SuperMALT

Name[a]	Map center RA	DEC	Dist. (kpc)	Dust Temp. (K)	R_{eff} (pc)	Mass (10^3 $M_\odot$)	Virial Mass (10^3 $M_\odot$)	n(H_2) (10^4 cm^{-3})	L_{bol} (10^3 $L_\odot$)
Prestellar									
AGAL331.639+00.501_S	16:10:07.8	-50:56:56.9	3.6	14^{+2}_{-2}	0.86±0.09	1.44±0.30	0.63±0.10	0.9±0.1	1.0±0.3
AGAL332.737-00.621_S	16:20:06.7	-50:59:53.9	3.5	20^{+3}_{-3}	0.27±0.03	0.41±0.09	0.31±0.04	8.6±1.0	0.4±0.1
AGAL332.892-00.569_S	16:20:33.9	-50:51:23.9	3.9	19^{+4}_{-6}	0.24±0.02	0.33±0.06	0.22±0.04	10.2±1.1	0.2±0.1
AGAL333.014-00.521_S	16:20:54.1	-50:44:10.0	3.7	22^{+2}_{-2}	0.49±0.05	1.07±0.30	0.99±0.21	3.2±0.7	9.0±4.0
AGAL333.016-00.751_S	16:21:56.7	-50:53:50.2	3.8	$17.6^{+0.4}_{-0.6}$	0.68±0.06	0.69±0.13	1.99±0.41	0.9±0.1	1.2±0.3
AGAL333.071-00.399_S	16:20:37.5	-50:36:30.2	3.7	18^{+2}_{-2}	0.84±0.08	2.11±0.41	1.70±0.17	1.5±0.2	5.3±1.5
AGAL333.179-00.396_S	16:21:05.9	-50:31:40.9	11.6	20^{+1}_{-2}	1.32±0.04	5.37±0.44	1.11±0.06	1.0±0.1	9.4±2.0
AGAL333.198-00.352_A	16:20:59.6	-50:29:13.1	3.5	19^{+1}_{-1}	0.18±0.02	0.29±0.06	0.14±0.03	22.1±2.7	0.07±0.02
AGAL333.449-00.182_S	16:21:20.6	-50:11:19.3	3.3	17^{+2}_{-2}	0.54±0.06	0.39±0.09	1.52±0.22	1.0±0.1	1.0±0.3
AGAL333.481-00.224_S	16:21:39.9	-50:11:47.5	3.5	19^{+1}_{-1}	0.50±0.05	0.59±0.13	0.53±0.07	1.9±0.3	1.4±0.4
AGAL333.566-00.296_S	16:22:21.6	-50:11:22.2	3.4	20^{+1}_{-1}	0.71±0.08	0.87±0.20	0.50±0.06	1.0±0.1	4.4±1.3
AGAL333.669-00.349_S	16:23:04.7	-50:09:06.2	11.8	19^{+1}_{-1}	1.94±0.07	3.04±0.22	2.82±0.32	0.17±0.01	9.8±2.1
AGAL335.592+00.184_S	16:28:55.4	-48:24:03.5	3.6	$15.1^{+0.4}_{-0.5}$	0.22±0.02	0.30±0.06	0.23±0.06	11.6±1.4	0.06±0.02
AGAL340.179-00.242_S	16:48:41.9	-45:15:45.6	4.1	14^{+2}_{-3}	0.85±0.07	1.47±0.27	1.52±0.19	1.0±0.1	0.9±0.3
AGAL340.232-00.146_S	16:48:26.2	-45:09:49.4	12.1	14^{+2}_{-2}	0.66±0.02	6.68±0.44	0.81±0.18	9.4±0.5	0.7±0.1
AGAL340.301-00.402_S	16:49:48.5	-45:16:30.4	12.1	$14.6^{+0.3}_{-0.5}$	1.46±0.05	11.0±0.9	1.88±0.26	1.5±0.1	3.8±0.8
AGAL340.304-00.376_S	16:49:44.1	-45:15:15.8	4.0	17^{+1}_{-1}	0.61±0.05	1.13±0.21	0.78±0.09	2.1±0.2	0.7±0.2
AGAL340.398-00.396_S	16:50:09.0	-45:11:48.1	3.7	14^{+1}_{-1}	0.45±0.04	1.69±0.34	0.81±0.17	7.9±0.9	0.3±0.1
AGAL341.039-00.114_S	16:51:13.1	-44:31:38.1	3.6	14^{+1}_{-1}	0.75±0.08	1.07±0.23	0.58±0.12	1.1±0.1	0.8±0.2
AGAL341.181-00.277_S	16:52:26.8	-44:30:54.1	3.7	13^{+1}_{-1}	0.50±0.05	0.37±0.08	0.39±0.07	1.3±0.2	0.2±0.1
AGAL341.196-00.221_S	16:52:15.9	-44:28:03.2	3.7	17^{+1}_{-1}	0.43±0.05	0.89±0.19	0.92±0.40	4.5±0.5	1.3±0.4
Protostellar									
AGAL304.886+00.636_S	13:08:11.1	-62:10:27.2	4.0	22^{+2}_{-2}	0.55±0.14	0.27±0.14	0.28±0.08	0.7±0.2	2.2±1.2
AGAL309.154-00.349_S	13:45:51.1	-62:33:41.6	3.7	18^{+1}_{-1}	0.53±0.18	0.36±0.24	0.87±0.31	1.0±0.4	1.4±1.0
AGAL309.236-00.457_S	13:46:44.4	-62:39:03.6	3.6	21^{+5}_{-7}	0.40±0.13	0.66±0.44	0.29±0.10	4.4±1.5	1.3±0.9
AGAL318.049+00.086_S	14:53:42.7	-59:08:51.9	3.6	28^{+1}_{-1}	0.76±0.11	1.50±0.45	0.95±0.17	1.4±0.2	18.5±6.7

Continued on next page

Table 3.1 – Continued from previous page

Name	Map center		Dist.	Dust Temp.	R_{eff}	Mass	Virial Mass	$n(H_2)$	L_{bol}
	RA	DEC	(kpc)	(K)	(pc)	(10^3 $M_\odot$)	(10^3 $M_\odot$)	(10^4 cm^{-3})	(10^3 $L_\odot$)
AGAL322.158+00.636_S	15:18:34.7	-56:38:21.2	3.9	26^{+1}_{-1}	1.59±0.19	5.52±1.37	6.97±0.97	0.6±0.1	161±51
AGAL331.724-00.204_S	16:13:35.5	-51:24:16.1	3.4	18^{+2}_{-2}	0.50±0.06	0.49±0.11	0.72±0.11	1.7±0.2	0.8±0.3
AGAL332.226-00.536_S	16:17:23.2	-51:17:52.4	11.4	21^{+3}_{-4}	2.05±0.07	4.46±0.32	1.70±0.19	0.21±0.01	25.2±5.3
AGAL332.281-00.547_S	16:17:40.7	-51:16:07.9	11.4	18^{+2}_{-3}	1.97±0.07	7.70±0.55	2.56±0.24	0.42±0.02	16.9±3.6
AGAL332.559-00.147_S	16:17:13.4	-50:46:58.6	3.3	22^{+1}_{-1}	0.50±0.05	0.69±0.18	0.56±0.11	1.9±0.4	6.1±2.2
AGAL332.559-00.591_S	16:19:09.7	-51:06:20.6	3.5	20^{+1}_{-1}	0.41±0.04	0.43±0.09	0.57±0.10	2.5±0.3	0.6±0.2
AGAL332.604-00.167_S	16:17:29.4	-50:46:14.1	3.3	20^{+2}_{-3}	1.11±0.13	1.12±0.26	1.64±0.21	0.34±0.04	4.2±1.3
AGAL332.726-00.621_S	16:20:06.7	-50:59:53.9	3.5	27^{+1}_{-1}	0.29±0.03	0.22±0.06	0.32±0.06	3.1±0.6	6.3±2.2
AGAL332.812-00.701_S	16:20:49.3	-51:00:06.0	11.4	24^{+2}_{-2}	1.52±0.05	3.49±0.25	1.19±0.16	0.41±0.02	22.0±4.6
AGAL332.942-00.686_S	16:21:19.3	-50:54:02.7	3.5	25^{+1}_{-1}	0.26±0.03	0.63±0.14	0.48±0.09	14.4±1.7	1.6±0.5
AGAL332.986-00.489_S	16:20:38.9	-50:44:03.4	3.7	$25.7^{+0.4}_{-0.6}$	1.43±0.14	3.21±0.66	1.68±0.17	0.45±0.05	52.2±14.8
AGAL332.999-00.639_S	16:21:22.6	-50:49:32.2	3.5	27^{+2}_{-2}	0.23±0.03	0.20±0.05	0.22±0.04	6.5±0.8	0.6±0.2
AGAL333.076-00.559_S	16:21:20.9	-50:42:43.3	11.3	17^{+3}_{-4}	1.82±0.06	11.3±1.1	3.10±0.28	0.8±0.1	10.0±2.1
AGAL333.314+00.106_S	16:19:28.8	-50:04:44.6	3.3	23^{+1}_{-1}	0.65±0.08	0.92±0.21	1.03±0.12	1.4±0.2	3.8±1.2
AGAL333.721-00.207_S	16:22:40.3	-50:00:35.9	3.4	19^{+1}_{-1}	0.71±0.08	1.09±0.26	0.73±0.09	1.3±0.2	3.9±1.2
AGAL335.284-00.132_S	16:29:02.0	-48:50:33.4	12.1	16^{+1}_{-1}	2.38±0.08	13.0±0.9	3.47±0.26	0.40±0.02	8.8±1.9
AGAL335.586-00.291_S	16:30:58.6	-48:43:47.1	12.0	$22.5^{+0.4}_{-0.5}$	3.94±0.13	42.1±3.4	7.53±0.30	0.28±0.02	202±42
AGAL336.018-00.827_S	16:35:05.6	-48:46:10.1	3.5	22^{+1}_{-1}	1.40±0.14	3.00±0.80	3.82±0.70	0.38±0.07	27±10
AGAL336.958-00.977_S	16:39:37.3	-48:10:55.2	3.4	17^{+2}_{-2}	0.49±0.06	0.97±0.23	0.75±0.10	3.4±0.4	0.6±0.2
AGAL337.098-00.929_S	16:39:58.1	-48:02:43.5	12.4	24^{+1}_{-1}	0.99±0.03	4.70±0.33	1.11±0.11	2.0±0.1	10.5±2.2
AGAL337.612-00.059_S	16:38:10.3	-47:04:49.8	12.0	27^{+1}_{-1}	2.54±0.08	13.7±0.9	5.39±0.63	0.35±0.02	171±36
AGAL337.761-00.339_S	16:39:58.3	-47:09:20.9	3.3	$14.8^{+0.4}_{-0.6}$	0.84±0.10	2.12±0.51	1.52±0.19	1.5±0.2	1.3±0.4
AGAL339.924-00.084_S	16:47:03.9	-45:21:22.5	4.1	20^{+1}_{-1}	0.87±0.09	1.34±0.35	2.10±0.40	0.7±0.1	6.9±2.7
AGAL340.054-00.244_S	16:48:14.0	-45:21:39.7	4.0	28^{+1}_{-1}	1.38±0.14	3.00±0.80	3.80±0.70	0.4±0.1	1.1±0.4
AGAL341.216-00.236_S	16:52:23.5	-44:27:54.9	3.7	24^{+1}_{-2}	0.86±0.09	1.48±0.31	0.81±0.09	1.0±0.1	12.2±3.5
AGAL341.217-00.212_S	16:52:18.2	-44:26:54.0	3.6	24^{+1}_{-1}	0.46±0.05	1.07±0.23	0.70±0.08	4.4±0.5	4.7±1.4
AGAL341.219-00.259_S	16:52:31.5	-44:28:32.4	3.7	18^{+2}_{-2}	0.50±0.05	1.48±0.31	0.70±0.08	4.9±0.5	1.4±0.4
AGAL343.133-00.482_S	17:00:07.2	-43:07:25.4	3.3	$15.2^{+0.4}_{-0.5}$	0.38±0.05	0.20±0.05	0.64±0.10	1.5±0.2	0.23±0.08
AGAL343.521-00.519_S	17:01:34.1	-42:50:16.9	3.3	16^{+1}_{-1}	0.88±0.09	1.60±0.40	1.80±0.40	0.8±0.2	2.3±1.0

Continued on next page

Table 3.1 – Continued from previous page

Name	Map center		Dist.	Dust Temp.	R_{eff}	Mass	Virial Mass	n(H_2)	L_{bol}
	RA	DEC	(kpc)	(K)	(pc)	(10^3 $M_\odot$)	(10^3 $M_\odot$)	(10^4 cm^{-3})	(10^3 $L_\odot$)
AGAL343.528-00.507_S	17:01:34.1	-42:50:16.9	3.3	16^{+1}_{-1}	0.35±0.04	0.50±0.13	0.71±0.16	3.9±0.8	0.7±0.3
HII Clumps									
AGAL310.014+00.387_S	13:51:38.0	-61:39:04.5	3.6	28^{+1}_{-2}	0.68±0.18	1.12±0.58	0.75±0.20	1.4±0.4	11.5±6.4
AGAL312.108+00.309_S	14:08:39.0	-61:10:53.9	7.3	31^{+3}_{-4}	1.24±0.20	3.96±1.29	1.73±0.30	0.9±0.1	75.8±28.8
AGAL314.264+00.091_S	14:26:04.3	-60:40:53.8	4.2	20^{+2}_{-2}	0.82±0.17	2.18±0.91	1.23±0.28	1.6±0.3	5.2±2.4
AGAL320.676+00.244_S	15:10:44.8	-57:44:55.2	4.3	22^{+1}_{-1}	0.90±0.12	1.25±0.33	2.02±0.44	0.7±0.1	6.6±2.1
AGAL331.418-00.356_S	16:12:51.6	-51:43:28.9	4.2	23^{+5}_{-7}	1.31±0.11	2.91±0.54	1.45±0.20	0.5±0.1	16.5±4.3
AGAL332.094-00.421_S	16:16:16.6	-51:18:25.2	3.8	27^{+1}_{-1}	1.00±0.09	1.56±0.29	1.22±0.12	0.6±0.1	37.0±10.2
AGAL332.584-00.559_S	16:19:08.2	-51:03:55.7	3.6	25^{+2}_{-2}	0.92±0.10	0.82±0.19	0.87±0.19	0.4±0.1	11.1±3.2
AGAL333.053+00.029_S	16:18:38.4	-50:18:57.9	3.2	27^{+2}_{-2}	0.88±0.11	0.55±0.13	0.58±0.10	0.34±0.04	16.5±5.2
AGAL333.068-00.447_S	16:20:49.1	-50:38:40.5	3.7	26^{+1}_{-1}	1.55±0.15	4.65±0.92	2.28±0.24	0.5±0.1	120±34
AGAL335.687-00.812_S	16:33:43.7	-49:00:45.5	3.6	21^{+1}_{-1}	1.07±0.11	1.36±0.28	0.98±0.12	0.5±0.1	5.7±1.6
AGAL336.020-00.816_S	16:35:05.6	-48:46:10.1	3.5	24^{+1}_{-1}	0.28±0.03	0.26±0.06	0.40±0.05	5.1±0.6	3.0±0.9
AGAL337.284-00.159_S	16:37:18.3	-47:23:38.7	11.8	25^{+1}_{-1}	0.82±0.03	3.10±0.24	1.04±0.27	2.3±0.2	9.5±2.0
AGAL340.248-00.374_S	16:49:31.0	-45:17:56.5	3.9	22^{+1}_{-2}	1.65±0.15	6.27±1.15	3.13±0.29	0.6±0.1	30.4±8.2
AGAL340.401-00.381_S	16:50:04.9	-45:10:56.1	12.3	15^{+1}_{-1}	2.45±0.08	24.0±2.0	3.67±0.39	0.68±0.04	13.4±2.8
AGAL343.689-00.017_S	16:59:59.3	-42:23:49.5	3.4	22^{+2}_{-2}	0.55±0.07	0.23±0.06	0.62±0.11	0.6±0.1	1.9±0.6
PDR									
AGAL340.319-00.227_S	16:49:07.4	-45:08:34.1	3.7	23^{+1}_{-1}	0.75±0.08	0.87±0.18	0.84±0.14	0.9±0.1	6.8±1.9
Uncertain type									
AGAL333.103-00.502_S	16:21:15.0	-50:39:22.9	3.8	25^{+3}_{-4}	1.22±0.11	1.70±0.32	1.37±0.14	0.39±0.04	44.6±12.2
AGAL338.402+00.032_S	16:40:49.6	-46:25:54.9	12.5	27^{+1}_{-1}	1.27±0.04	4.77±0.39	4.03±0.39	1.0±0.1	51.9±10.9

[a]Clump names appended with "S" correspond to clumps with no second line of sight velocity component identified in MALT90 survey (Rathborne et al. 2016). In the case of two line of sight velocity components identified from two physically separate clumps, source names are appended by "A" and "B".

The SuperMALT targets comprise of 73 clumps, taken from the MALT90 sample (Foster et al. 2011; Jackson et al. 2013; Rathborne et al. 2016), selected by having bright dust continuum emission at 870 μm ($>$ 250 mJy/beam), significant emission (signal-to-noise ratio $>$ 5) in the main four molecular lines detected in MALT90: HCO^+ $J = 1 \rightarrow 0$, HNC $J = 1 \rightarrow 0$, HCN $J = 1 \rightarrow 0$ and N_2H^+ $J = 1 \rightarrow 0$, and by covering a wide range of evolutionary stages determined by mid-infrared *Spitzer* emissions (Foster et al. 2011; Jackson et al. 2013).

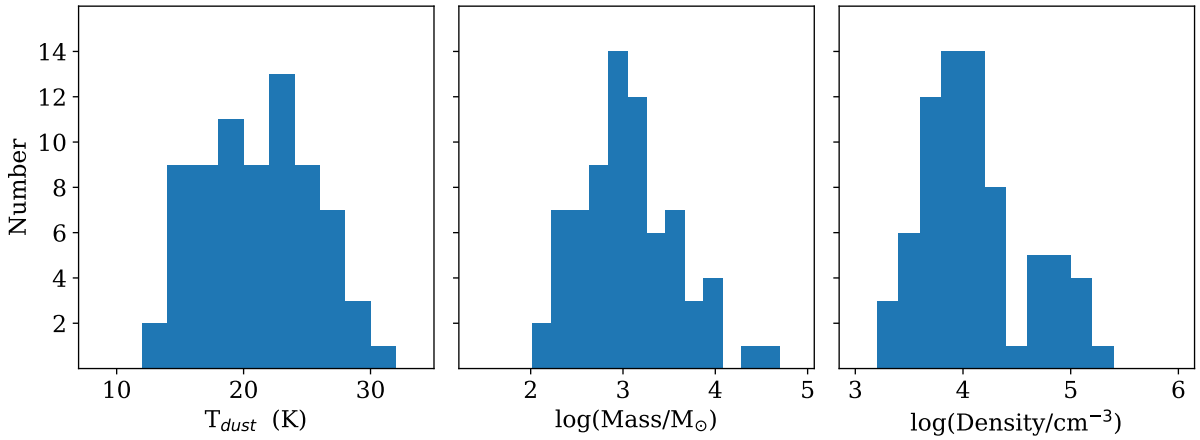

Figure 3.1: Distribution in temperature (left panel), mass (middle panel) and density (right panel) of the SuperMALT clumps.

The SuperMALT targets span a wide range of early evolutionary states in high-mass star formation. Twenty one objects correspond to 'Quiescent' or 'Pre-stellar' clumps, which represent the earliest stage of clump evolution. These clumps are characterized as having little or no emission in the infrared *Spitzer* GLIMPSE (3.6 to 8 μm; e.g., Churchwell et al. 2009) images and MIPSGAL 24 μm (Carey et al. 2009) image, suggesting that star formation has not yet begun within them. Thirty-four objects correspond to 'Proto-stellar' clumps, which represent clumps in an intermediate stage where star formation activity has just begun. These clumps are characterized by the presence of infrared emission in the GLIMPSE and MIPSGAL images. Typically the infrared emission seen toward these clumps is in the form of 4.5 μm extended emission, 8 μm bright emission or 24 μm point like emission. The 4.5 μm extended emission is commonly associated with shocks (e.g., Cyganowski et al. 2008), produced by the outflows of newly formed high-mass proto-stellar objects, whereas the 8 μm and 24 μm emissions are from warm dust grains heated by the radiation from newly formed embedded stars. Fifteen objects correspond to 'H II region' clumps, which represent the latest stage of evolution, in which the high-mass proto-stars start to ionize their surroundings. These clumps are characterized by bright diffuse infrared emission at 8 and 24 μm in the GLIMPSE and MIPSGAL images. Of the remaining 3 objects, one corresponds to a PDR and two have uncertain classification.

Table 3.1 summarizes the known characteristics of each clump. The MALT90 name of the observed clumps is given in col. 1 of Table 3.1. Cols. 4 to 10 list, respectively, the kinematic distance (Whitaker et al., 2017), average dust temperature, effective radius, mass, virial mass, average volume density and bolometric luminosity (Contreras et al., 2016; Guzmán et al., 2015). The distributions in mass, density and dust temperature are presented in Figure 3.1.

Table 3.2: Parameters of the observed molecular lines.

Molecule	Transition	Rest Freq. (GHz)	Res. (MHz)	E_u/k (K)	n_{crit}[a] (cm^{-3})	Observation mode	Beam (")	n_{mb}
HCO^+	$J = 3 \rightarrow 2$	267.557	0.076	25.68	1.4×10^6	$2' \times 2'$ Map	23.3	0.67
	$J = 4 \rightarrow 3$	356.734	0.076	42.80	3.2×10^6	$2' \times 2'$ Map	17.5	0.59
HNC	$J = 3 \rightarrow 2$	271.981	0.076	26.11	4.0×10^6	$2' \times 2'$ Map	22.9	0.67
	$J = 4 \rightarrow 3$	362.630	0.076	43.51	1.0×10^7	$2' \times 2'$ Map	17.2	0.59
HCN	$J = 3 \rightarrow 2$	265.886	0.076	25.52	1.0×10^7	$2' \times 2'$ Map	23.5	0.67
	$J = 4 \rightarrow 3$	354.505	0.076	42.53	2.3×10^7	$2' \times 2'$ Map	17.6	0.59
N_2H^+	$J = 3 \rightarrow 2$	279.512	0.076	26.82	1.2×10^6	$2' \times 2'$ Map	22.3	0.67
	$J = 4 \rightarrow 3$	372.673	0.076	44.71	2.8×10^6	$2' \times 2'$ Map	16.7	0.59
$H^{13}CO^+$	$J = 3 \rightarrow 2$	260.255	0.076	24.98	1.3×10^6	Single pointing	24.0	0.67

[a] Critical densities derived by Shirley (2015), calculated using a gas kinetic temperature of 20 K.

The masses range from 200 to 4200 $M_\odot$, the densities from $1.6{\times}10^3$ to $2.2{\times}10^5$ cm^{-3} and the dust temperatures from 13 to 31 K. The later range from 13 to 20 K for prestellar clumps, from 15 to 28 K for protostellar clumps and from 15 to 31 K for H II clumps. The average dust temperature steadily increases from prestellar to H II clumps (c.f., Guzmán et al. 2015)

3.2.2 Molecular lines

SuperMALT targeted the emission in the $J = 3 \rightarrow 2$ and $J = 4 \rightarrow 3$ rotational transitions of the four main molecular species detected in MALT90 in $J = 1 \rightarrow 0$ transition: HCO^+, HNC, HCN and N_2H^+. In addition, it also targeted the emission in the $J = 3 \rightarrow 2$ transition of $H^{13}CO^+$. Table 3.2 lists the parameters of the molecular lines observed in this survey.

3.3 Observations and data reduction

The observations were carried out using the Atacama Pathfinder EXperiment (APEX) 12-m single dish telescope, located at Llano de Chajnantor in the Chilean Atacama desert. The observing runs took place in the austral winter and spring seasons from 2013 to 2017. We used the Swedish Heterodyne Facility Instrument (SHeFI) receivers Apex-1 (213-275 GHZ) and Apex-2 (267-378 GHz). The system temperatures were typically in the range of 300-400 K and the precipitable water vapour (PWV) between 0.5 to 1.5 mm.

We mapped the emission in the $J = 3 \rightarrow 2$ lines of HCO^+, HNC, HCN and N_2H^+ toward 73 clumps and the emission in the $J = 4 \rightarrow 3$ lines toward 15 clumps. The observations were made using the On-The-Fly (OTF) mode, covering a region of $2'$ by $2'$ in size, centred at the position of the peak of the continuum emission in ATLASGAL given in columns 2 and 3 of Table 3.1. To avoid striping, all maps were observed in both longitude and latitude scanning directions.

The root mean square (rms in T_A^*) noise level achieved in the $J = 3 \rightarrow 2$ maps at the velocity resolution of 0.08 km s^{-1} is 0.17 K and in the $J = 4 \rightarrow 3$ maps at the velocity

resolution of 0.06 km s^{-1} is 0.23 K. The single point observations of the $J = 3 \rightarrow 2$ transition of $H^{13}CO^+$ were made in the On-Off mode, integrating until an *rms* sensitivity of 0.07 K at a velocity resolution of 0.08 km s^{-1} was achieved. For all the sources the OFF position was chosen to be 1 degree below their galactic latitude and at the same galactic longitude.

Cols. 3 to 9 of Table 3.2 list the rest frequency, spectral resolution, upper level energy, critical density, observing mode, FWHM beam diameter and main beam efficiency for each of the observed molecular transition.

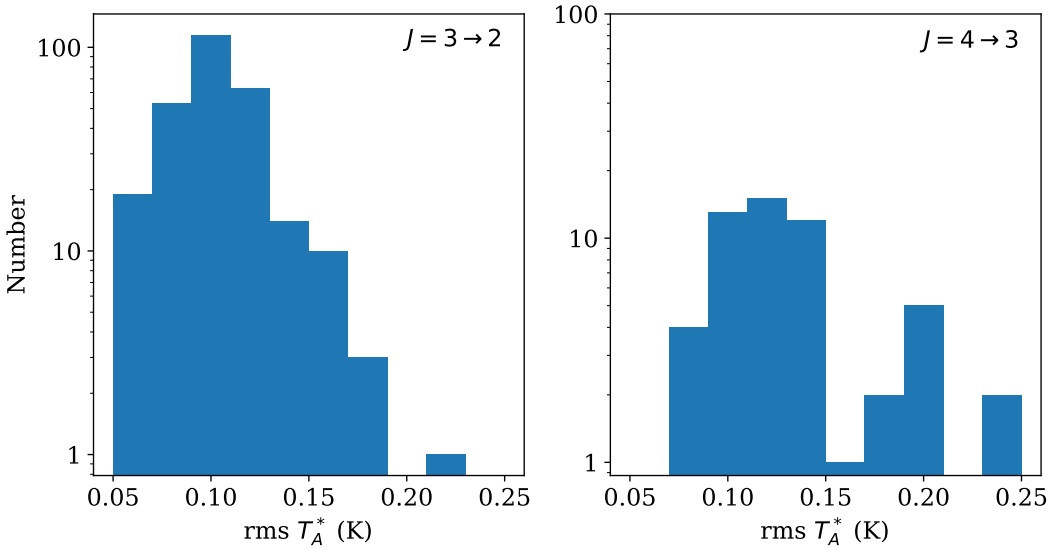

Figure 3.2: Histogram of the *rms* noise in T_A^* (K) achieved in the HCO^+, HNC, HCN, and N_2H^+ $J = 3 \rightarrow 2$ and $J = 4 \rightarrow 3$ observations. At 0.2 km/s spectral resolution, the typical *rms* noise in T_A^* (K) is ∼0.10 K and ∼0.14 K in $J = 3 \rightarrow 2$ and $J = 4 \rightarrow 3$ observations, respectively.

We used the GILDAS[2] (Pety 2005; Gildas Team 2013) software packages to reduce and analyse the data. The CLASS and GREG packages were utilised to produce the spectra, subtract baselines, fit profiles, and make maps. For a uniform analysis of the emission in the different transitions, we produced final spectra at a velocity resolution 0.2 km s^{-1} in 12×12 pixel maps with a pixel size of 10" × 10". At 0.2 km/s spectral resolution, the typical *rms* noise in T_A^* (K) achieved in the HCO^+, HNC, HCN, and N_2H^+ $J = 3 \rightarrow 2$ is ∼0.1 K and and $J = 4 \rightarrow 3$ is ∼0.14 K (see Figure 3.2).

In what follows we refer to the "Central spectra" as those obtained toward the emission peak of the clumps in 870 μm ATLASGAL images and averaged over a circular region of 20" in diameter (similar to the beam size of the $J = 3 \rightarrow 2$ observations).

[2]http://www.iram.fr/IRAMFR/GILDAS

3.4 Results

3.4.1 Line detection

Emission in the $J = 3 \rightarrow 2$ lines of HCO^+, HCN, HNC, N_2H^+ and $H^{13}CO^+$ was detected, when observed, toward all clumps, except HCN in one clump. Emission in the $J = 4 \rightarrow 3$ lines of HCO^+, HCN, HNC and N_2H^+ was detected toward most of the observed clumps. Table 3.3 summarizes the number of observed clumps in a given molecular line and the detection rate.

Table 3.3: Line detection rate.

Species	$J = 3 \rightarrow 2$		$J = 4 \rightarrow 3$	
	Observed clumps	Detection rate	Observed clumps	Detection rate
HCO^+	72	100%	15	100%
HCN	72	99%	14	93%
HNC	73	100%	13	100%
N_2H^+	70	100%	15	80%
$H^{13}CO^+$	68	100%	–	–

3.4.2 Spectra

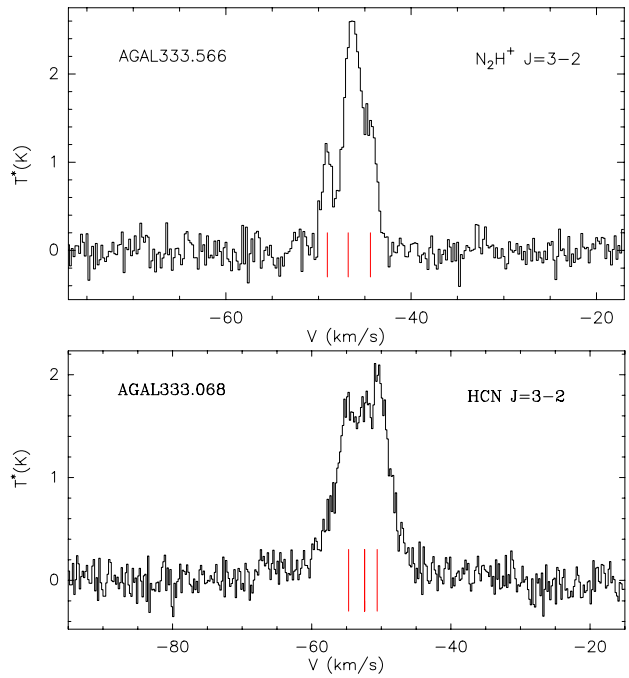

Figure 3.3: Top: Spectra of the N_2H^+ $J = 3 \rightarrow 2$ emission observed toward the prestellar clump AGAL333.566. The red marks at the bottom indicate the velocities of the three HF components. Bottom: Spectra of the HCN $J = 3 \rightarrow 2$ emission observed toward the prestellar clump AGAL333.068. The red marks at the bottom indicate the velocities of three distinct hyperfine transitions.

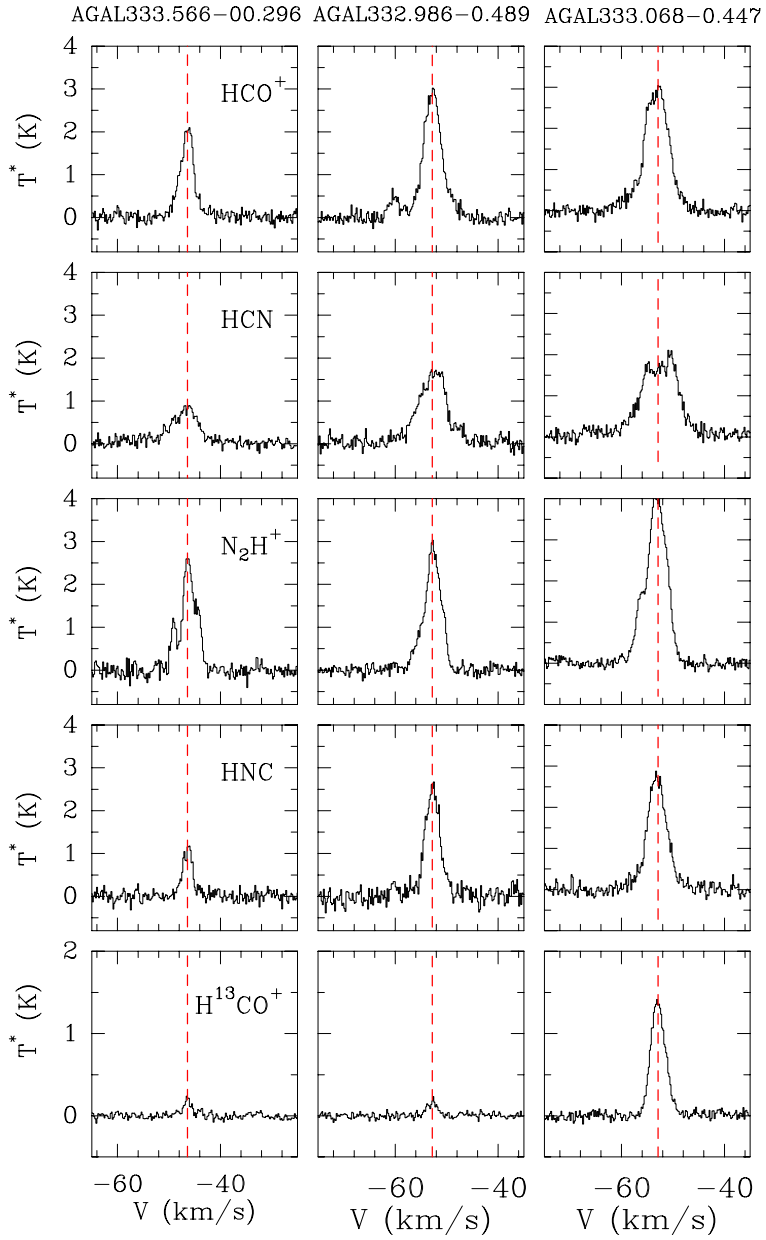

Figure 3.4: Central spectra of the $J = 3 \rightarrow 2$ emission from clumps in different evolutionary stages. Left: AGAL333.566-0.296_S pre-stellar clump; Middle: AGAL332.986-0.489_S proto-stellar clump; Right: AGAL333.068-0.447_S H II clump. Rest frame source velocities are shown in dotted red lines.

Figures A1, A2 and A3 of the Appendix 3.7.1 show the Central spectra in the $J = 3 \rightarrow 2$ lines of HCO^+, HCN, HNC, N_2H^+ and $H^{13}CO^+$ from, respectively, prestellar, protostellar and H II clumps. The profiles of the HCO^+ and HCN lines show a wide range of features, such as self-absorption, red and blue skewness, and wings. The line asymmetric features are seen more often toward the evolved (protostellar and H II) clumps. On the other hand, the profiles of the HNC and $H^{13}CO^+$ lines from most clumps are typically Gaussian, indicating that they are optically thin. In addition, the profiles of the N_2H^+ and HCN emission show complex shape due to their hyperfine (HF) structure. The N_2H^+ $J = 3 \rightarrow 2$ transition consists of 16 HF components (Caselli et al. 2002), however, due to the overlap of closely spaced HF

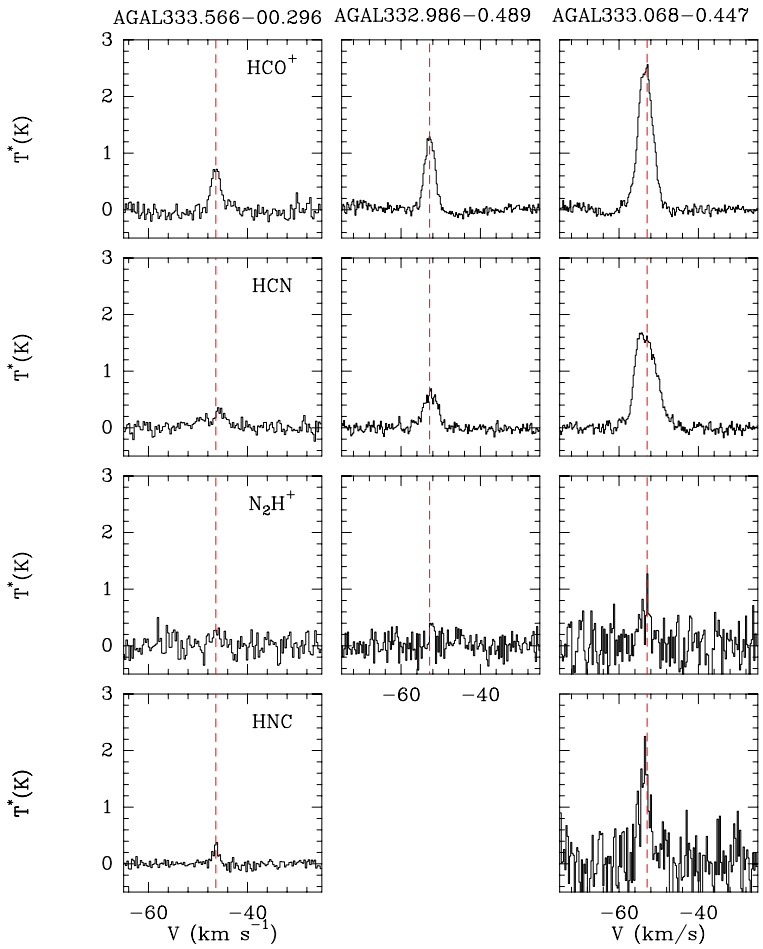

Figure 3.5: Central spectra of $J = 4 \rightarrow 3$ the emission from clumps in different evolutionary stages: Left: AGAL333.566-0.296_S pre-stellar clump; Middle: AGAL332.986-0.489_S proto-stellar clump; Right: AGAL333.068-0.447_S H II clump. Rest frame source velocities are shown in dotted red lines.

components (rest frequencies from 279.509 to 279.514 GHz), only three distinct components are observed (see Figure 3.3). The HCN $J = 3 \rightarrow 2$ line consists of six hyperfine components (rest frequencies from 265.884 to 265.888 GHz) (Ahrens et al. 2002). The blending of the HCN hyperfine lines typically produces a single broad component which is noticeably broader than the HCO^+ and HNC lines (see Figs. A1 to A3 of the Appendix 3.7.1). However, in some cases we are able to see three components (see Figure 3.3) illustrating hyperfine line anomalies (e.g., Loughnane et al. 2012).

In general the strength of the line emission increases from early to late evolutionary stages. This is illustrated in Figure 3.4 which plots the $J = 3 \rightarrow 2$ spectra, in all five observed species, from three clumps in different evolutionary stages, showing that the intensity is lower at the quiescent stage (left panel) and increases toward later stages (middle and right panels). We analyze the increment in line emission with evolutionary stage more quantitatively in Section 3.5.1. The HF structure of the N_2H^+ $J = 3 \rightarrow 2$ line is most easily discerned in the spectra of the quiescent clump.

Figures B1 to B4 of the Appendix 3.7.2 show the central spectra of the $J = 4 \rightarrow 3$ lines of HCO^+, HCN, HNC and N_2H^+ toward all 15 observed clumps. The $J = 4 \rightarrow 3$ lines are typically weaker than the $J = 3 \rightarrow 2$ lines of the same species. This is illustrated in Figure 3.5 which plots the profiles of the $J = 4 \rightarrow 3$ emission from the same clumps as in Figure 3.4.

3.4.3 Velocities and line widths

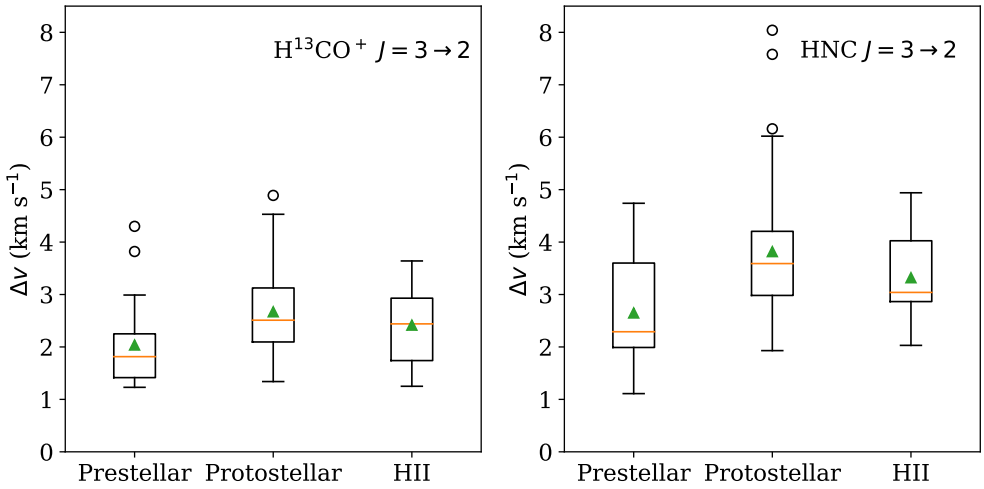

Figure 3.6: Whisker plot of the $J = 3 \rightarrow 2$ line widths of clumps in different evolutionary stages. Left: $H^{13}CO^+$. Right: HNC. The boxes show interquartile range and the horizontal orange lines inside the boxes show median values and the green triangles show mean values. The open circles show outliers that are outside 1.5 times the interquartile range from the boxes' limit.

To determine the systemic velocity and line width of the clumps, we fitted Gaussian profiles to the observed spectra in the optically thin $H^{13}CO^+$ and in the HNC $J = 3 \rightarrow 2$ lines. The fitted parameters are listed in Table 5.6. As illustrated in Figure 3.6, which presents whisker plots of the line widths (FWHM) in HNC and $H^{13}CO^+$ for the three type of clumps, the line widths of the emission from quiescent clumps are significantly narrower than those of protostellar and H II clumps. The K-S test p-value associated with the null hypothesis that the distribution of line widths in prestellar versus ptotostellar and H II are same, is 2×10^{-4}. The average widths in the $H^{13}CO^+$ $J = 3 \rightarrow 2$ line are 2.04±0.82, 2.67±0.87 and 2.42±0.71 km/s for, respectively, prestellar, protostellar and H II clumps and 2.65±1.08, 3.82±1.39 and 3.32±0.81 km/s in the HNC $J = 3 \rightarrow 2$ line. The explanation for the larger line widths observed toward protostellar and H II clumps is not straightforward. Possible reasons for the larger line widths are an increase in turbulence due to star formation activities e.g., outflows/jets and shocks, or an increase in the gas motions due to the gravitational collapse of the clumps.

Figure 3.7 shows a comparison of the line widths and velocities determined from both lines for all clumps. Whereas the velocities are similar, the HNC $J = 3 \rightarrow 2$ line widths are larger than the $H^{13}CO^+$ $J = 3 \rightarrow 2$ line widths for most clumps. This suggests that the HNC

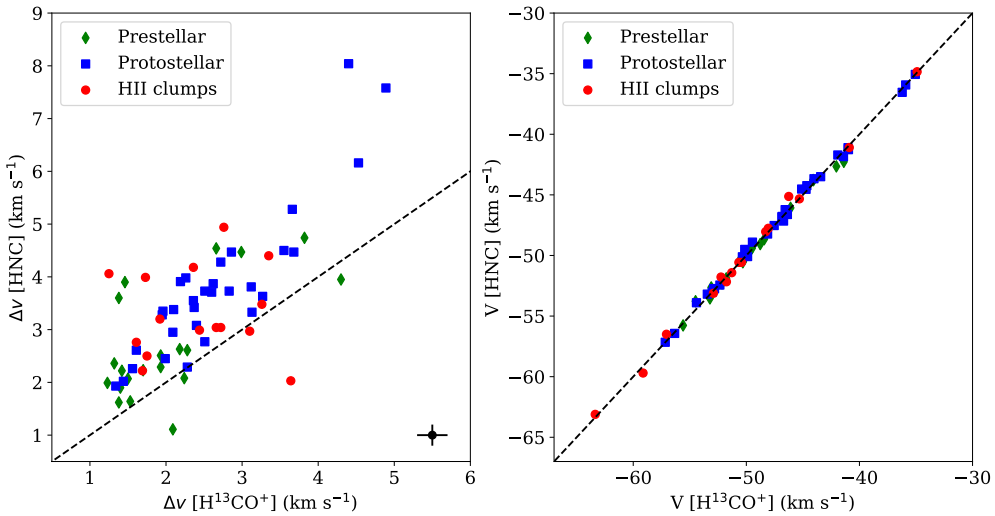

Figure 3.7: Left: Comparison of line widths of prestellar, protostellar and H II clumps determined from Gaussian fits to the central spectra of optically thin $H^{13}CO^+$ $J = 3 \rightarrow 2$ and HNC $J = 3 \rightarrow 2$ lines. Typical error in line widths is shown on the bottom right corner. Right: Comparison of source velocities determined from $H^{13}CO^+$ and HNC $J = 3 \rightarrow 2$ lines.

$J = 3 \rightarrow 2$ line emission may not be optically thin, the larger line widths being possibly due to optical depth effects.

Table 3.4: Gaussian fit parameters.

Name	$H^{13}CO^+$ ($J = 3 \rightarrow 2$)			HNC ($J = 3 \rightarrow 2$)		
	A (K km s^{-1})	V_{lsr} (km s^{-1})	Δv (km s^{-1})	A (K km s^{-1})	V_{lsr} (km s^{-1})	Δv (km s^{-1})
Quiescent/Prestellar clumps						
AGAL331.639+00.501_S	0.33±0.06	-52.15±0.19	2.28±0.50	1.55±0.11	-52.30±0.09	2.61±0.19
AGAL332.737-00.621_S	0.30±0.02	-50.14±0.07	1.93±0.16	2.94±0.10	-50.24±0.04	2.51±0.09
AGAL332.892-00.569_S	–	–	–	0.48±0.09	-56.91±0.10	1.15±0.29
AGAL333.014-00.521_S	0.46±0.03	-53.22±0.06	2.18±0.15	3.74±0.12	-53.54±0.04	2.63±0.10
AGAL333.016-00.751_S	0.33±0.04	-55.59±0.26	3.82±0.57	1.19±0.14	-55.77±0.27	4.74±0.64
AGAL333.071-00.399_S	0.51±0.04	-54.49±0.11	2.99±0.24	5.13±0.17	-53.78±0.07	4.47±0.16
AGAL333.179-00.396_S	0.32±0.03	-50.31±0.11	2.24±0.28	2.21±0.09	-50.56±0.04	2.08±0.10
AGAL333.198-00.352_A	0.21±0.03	-49.49±0.11	1.53±0.21	1.53±0.14	-49.39±0.08	1.64±0.16
AGAL333.449-00.182_S	0.43±0.04	-44.06±0.22	4.30±0.52	2.00±0.18	-43.78±0.17	3.95±0.40
AGAL333.481-00.224_S	0.27±0.03	-48.77±0.07	1.50±0.17	0.78±0.09	-49.06±0.12	2.07±0.31
AGAL333.566-00.296_S	0.37±0.04	-46.40±0.08	1.70±0.25	2.65±0.11	-46.37±0.05	2.23±0.11
AGAL333.669-00.349_S	0.12±0.03	-48.42±0.23	1.93±0.53	1.14±0.14	-48.66±0.14	2.29±0.30
AGAL335.592+00.184_S	0.22±0.02	-49.71±0.06	1.23±0.14	1.46±0.11	-49.69±0.07	1.99±0.17
AGAL340.179-00.242_S	0.12±0.02	-53.10±0.15	1.46±0.26	1.09±0.18	-52.64±0.27	3.90±0.98
AGAL340.232-00.146_S	0.13±0.02	-50.47±0.10	1.40±0.19	1.20±0.11	-50.42±0.09	1.90±0.22
AGAL340.301-00.402_S	0.09±0.02	-50.54±0.17	1.38±0.32	1.11±0.08	-50.34±0.05	1.62±0.15
AGAL340.304-00.376_S	0.28±0.03	-51.77±0.06	1.38±0.16	2.22±0.11	-51.89±0.09	3.60±0.21
AGAL340.398-00.396_S	0.13±0.02	-46.09±0.12	1.42±0.34	0.87±0.09	-46.07±0.12	2.22±0.27
AGAL341.039-00.114_S	0.10±0.03	-42.04±0.34	2.09±0.66	0.81±0.09	-42.65±0.06	1.11±0.13
AGAL341.181-00.277_S	0.15±0.02	-44.10±0.11	1.32±0.25	1.53±0.11	-43.78±0.08	2.36±0.20
AGAL341.196-00.221_S	0.23±0.06	-41.38±0.40	2.66±1.07	2.29±0.19	-42.27±0.19	4.54±0.43
Protostellar clumps						
AGAL304.886+00.636_S	0.41±0.03	-36.22±0.05	1.34±0.12	2.72±0.16	-36.54±0.05	1.93±0.15
AGAL309.154-00.349_S	0.37±0.01	-40.97±0.05	2.51±0.12	1.52±0.11	-41.27±0.10	2.77±0.25
AGAL309.236-00.457_S	0.97±0.02	-41.01±0.02	1.99±0.05	2.67±0.08	-41.11±0.04	2.45±0.09
AGAL318.049+00.086_S	4.51±0.04	-49.89±0.01	2.83±0.03	9.21±0.13	-50.09±0.03	3.73±0.07

AGAL322.158+00.636_S	9.19±0.06	-57.17±0.01	4.53±0.03	26.50±0.20	-57.16±0.02	6.16±0.05
AGAL331.724-00.204_S	0.58±0.05	-47.54±0.12	3.13±0.28	3.48±0.13	-47.53±0.06	3.33±0.14
AGAL332.226-00.536_S	0.44±0.03	-52.34±0.05	1.56±0.12	2.26±0.11	-52.44±0.05	2.26±0.13
AGAL332.281-00.547_S	0.97±0.04	-52.89±0.04	2.10±0.09	6.18±0.10	-52.73±0.02	3.38±0.07
AGAL332.559-00.147_S	0.16±0.03	-46.85±0.13	1.44±0.30	2.59±0.12	-46.83±0.04	2.02±0.12
AGAL332.559-00.591_S	0.27±0.03	-50.35±0.10	1.96±0.25	1.76±0.21	-50.11±0.20	3.35±0.45
AGAL332.604-00.167_S	0.68±0.04	-46.37±0.09	3.27±0.23	3.82±0.11	-46.62±0.05	3.63±0.13
AGAL332.726-00.621_S	–	–	-	2.44±0.08	-50.30±0.04	2.81±0.12
AGAL332.812-00.701_S	0.47±0.04	-53.45±0.07	1.95±0.17	3.73±0.10	-53.19±0.04	3.28±0.11
AGAL332.942-00.686_S	1.96±0.04	-49.46±0.04	3.66±0.10	7.21±0.29	-48.90±0.10	5.28±0.27
AGAL332.986-00.489_S	0.43±0.04	-52.81±0.10	2.37±0.22	9.16±0.22	-52.75±0.04	3.42±0.10
AGAL332.999-00.639_S	0.26±0.03	-48.12±0.14	2.28±0.34	1.63±0.09	-48.23±0.06	2.29±0.16
AGAL333.076-00.559_S	0.21±0.03	-56.34±0.22	2.62±0.39	2.34±0.14	-56.43±0.11	3.87±0.27
AGAL333.314+00.106_S	2.34±0.03	-46.57±0.02	3.55±0.05	8.23±0.15	-46.22±0.04	4.50±0.10
AGAL333.721-00.207_S	0.20±0.03	-46.84±0.12	1.61±0.23	2.90±0.12	-46.78±0.05	2.61±0.13
AGAL335.284-00.132_S	0.57±0.02	-45.11±0.05	2.36±0.12	4.37±0.12	-44.52±0.05	3.55±0.13
AGAL335.586-00.291_S	5.64±0.06	-46.71±0.02	3.68±0.04	15.81±0.20	-47.16±0.03	4.47±0.08
AGAL336.018-00.827_S	–	–	-	8.85±0.19	-47.82±0.06	6.02±0.17
AGAL336.958-00.977_S	0.89±0.04	-44.65±0.05	2.40±0.12	3.63±0.13	-44.24±0.05	3.08±0.13
AGAL337.098-00.929_S	0.67±0.04	-41.91±0.06	2.09±0.14	2.29±0.12	-41.71±0.08	2.95±0.17
AGAL337.612-00.059_S	1.15±0.04	-50.14±0.08	4.40±0.19	5.85±0.17	-49.50±0.11	8.04±0.27
AGAL337.761-00.339_S	0.58±0.03	-41.41±0.06	2.19±0.15	5.05±0.20	-41.84±0.08	3.91±0.18
AGAL339.924-00.084_S	1.47±0.04	-53.02±0.04	2.86±0.09	4.10±0.14	-53.03±0.07	4.47±0.20
AGAL340.054-00.244_S	7.53±0.08	-54.41±0.03	4.89±0.06	16.01±0.25	-53.90±0.06	7.58±0.15
AGAL341.216-00.236_S	1.43±0.04	-44.02±0.04	3.12±0.09	7.38±0.16	-43.67±0.04	3.81±0.10
AGAL341.217-00.212_S	2.72±0.03	-43.43±0.02	2.72±0.04	7.27±0.17	-43.50±0.05	4.28±0.12
AGAL341.219-00.259_S	0.73±0.03	-44.72±0.06	2.60±0.15	6.71±0.13	-44.54±0.03	3.71±0.08
AGAL343.133-00.482_S	0.59±0.03	-35.91±0.04	2.26±0.13	3.32±0.11	-35.93±0.06	3.98±0.17
AGAL343.521-00.519_S	–	–	-	1.75±0.15	-34.20±0.14	3.16±0.31
AGAL343.528-00.507_S	1.32±0.03	-35.06±0.03	2.51±0.06	5.04±0.17	-35.06±0.06	3.73±0.13
HII clumps						
AGAL310.014+00.387_S	3.43±0.03	-40.90±0.01	2.44±0.03	7.35±0.12	-41.09±0.02	2.99±0.06

AGAL312.108+00.309_S	0.28±0.03	-48.29±0.08	1.73±0.19	5.50±0.12	-48.04±0.04	3.99±0.10
AGAL314.264+00.091_S	1.24±0.02	-51.76±0.03	3.10±0.07	3.52±0.12	-52.17±0.05	2.97±0.14
AGAL320.676+00.244_S	0.73±0.03	-59.13±0.08	3.64±0.21	2.84±0.10	-59.70±0.03	2.03±0.10
AGAL331.418-00.356_S	0.64±0.04	-63.36±0.07	2.66±0.19	5.65±0.13	-63.11±0.03	3.04±0.09
AGAL332.094-00.421_S	3.68±0.04	-57.06±0.02	3.26±0.04	8.58±0.12	-56.50±0.02	3.48±0.06
AGAL332.584-00.559_S	0.32±0.02	-51.29±0.05	1.69±0.10	1.98±0.11	-51.42±0.06	2.22±0.13
AGAL333.053+00.029_S	0.78±0.03	-45.31±0.03	1.75±0.08	2.40±0.11	-45.33±0.06	2.50±0.14
AGAL333.068-00.447_S	4.93±0.05	-52.91±0.02	3.35±0.04	12.74±0.17	-53.12±0.03	4.40±0.07
AGAL335.687-00.812_S	0.50±0.02	-50.43±0.04	1.61±0.10	1.88±0.15	-50.57±0.11	2.76±0.26
AGAL336.020-00.816_S	0.95±0.04	-48.06±0.05	2.72±0.14	6.09±0.12	-47.76±0.03	3.04±0.07
AGAL337.284-00.159_S	0.25±0.02	-52.24±0.11	2.36±0.23	2.05±0.13	-51.78±0.12	4.18±0.32
AGAL340.248-00.374_S	1.71±0.04	-50.66±0.03	2.76±0.07	11.16±0.16	-50.57±0.04	4.94±0.08
AGAL340.401-00.381_S	0.14±0.04	-46.25±0.17	1.25±0.45	2.87±0.14	-45.13±0.09	4.06±0.22
AGAL343.689-00.017_S	0.71±0.02	-34.90±0.03	1.92±0.08	3.89±0.11	-34.84±0.04	3.20±0.11
PDR clump						
AGAL340.319-00.227_S	–	–	–	1.07±0.11	-46.06±0.12	2.37±0.31
Uncertain clumps						
AGAL333.103-00.502_S	0.86±0.03	-57.06±0.06	3.48±0.12	5.57±0.15	-56.33±0.03	2.64±0.08
AGAL338.402+00.032_S	0.43±0.03	-41.40±0.21	5.14±0.47	4.48±0.12	-40.94±0.06	4.89±0.17

3.4.4 Morphologies

To investigate the morphology of the clumps in the different molecular lines we made maps of the velocity integrated emission using, for a given clump, the same velocity interval for all lines. Figures 3.32 to 3.55 in the Appendix 3.7.3 present contour maps of the $J = 3 \rightarrow 2$ velocity integrated emission (moment zero maps) in HCO^+, HCN, HNC and N_2H^+ for all clumps. While most of the clumps as seen with the Mopra telescope (38" angular resolution) show a single structure in the $J = 1 \rightarrow 0$ lines, the morphology of the $J = 3 \rightarrow 2$ emission as seen with APEX (angular resolution of 20") is generally more complex, typically exhibiting the presence of more than one component. Of the 73 clumps, 34 exhibit a single component, 13 show two components, 2 show three components and the rest of the clumps show either arc-like, filamentary or complex morphologies.

To compare the morphologies of the molecular and dust emissions, observed with similar angular resolutions, we retrieved the 870 μm images from the ATLASGAL survey (Schuller et al. 2009). This survey was made with an angular resolution of ∼19.2", similar to that of the molecular line observations. From the visual inspection, the spatial distribution of the $J = 3 \rightarrow 2$ emission in all four mapped molecular species is similar to that of the 870 μm dust continuum, with HCO^+ and N_2H^+ exhibiting the best agreement with the dust continuum morphology. This is illustrated in Figure 3.8 which shows contour maps of the velocity integrated line emission in all four mapped $J = 3 \rightarrow 2$ transitions, superimposed on grey scale images of the 870μm continuum emission, for the same clumps of which the spectra are presented in Figure 3.4.

Contour maps of the velocity integrated $J = 4 \rightarrow 3$ emission in HCO^+, HCN, and HNC for all observed clumps, except the PDR clump, are presented in Figures 3.56 to 3.59 of the Appendix 3.7.4. Not shown are the HCN and N_2H^+ maps toward a few clumps (e.g., AGAL3410.401) for which no or very weak emission was detected. The extent of the emission in the $J = 4 \rightarrow 3$ lines is always smaller than that in the $J = 3 \rightarrow 2$ lines, a result consistent with the clumps being centrally condensed, the $J = 4 \rightarrow 3$ emission arising from the higher density central region. An example is displayed in Figure 3.9 which shows maps of the velocity integrated emission in the $J = 3 \rightarrow 2$ and $J = 4 \rightarrow 3$ lines toward the AGAL333.068 clump.

3.4.5 Sizes

To investigate a possible dependence of clump size with evolutionary stage we determined sizes from the moment zero maps of the HCO^+ and N_2H^+ $J = 3 \rightarrow 2$ emission. We selected these lines because they are the ones that exhibit the stronger emission. To compute sizes we used the *Astrodendro* package[3] (Robitaille et al. 2019). This algorithm allows us to extract the clump substructures when the clumps are embedded in filamentary structures or associated with complex/multiple structures. The *Astrodendro* requires three input parameters: the minimum value of the emission to be considered (I_{min}), the separation between the neighbouring peaks (δ) and the minimum number of pixels (A_{min}) in the substructure. We adopt

[3]https://dendrograms.readthedocs.io/en/stable/index.html

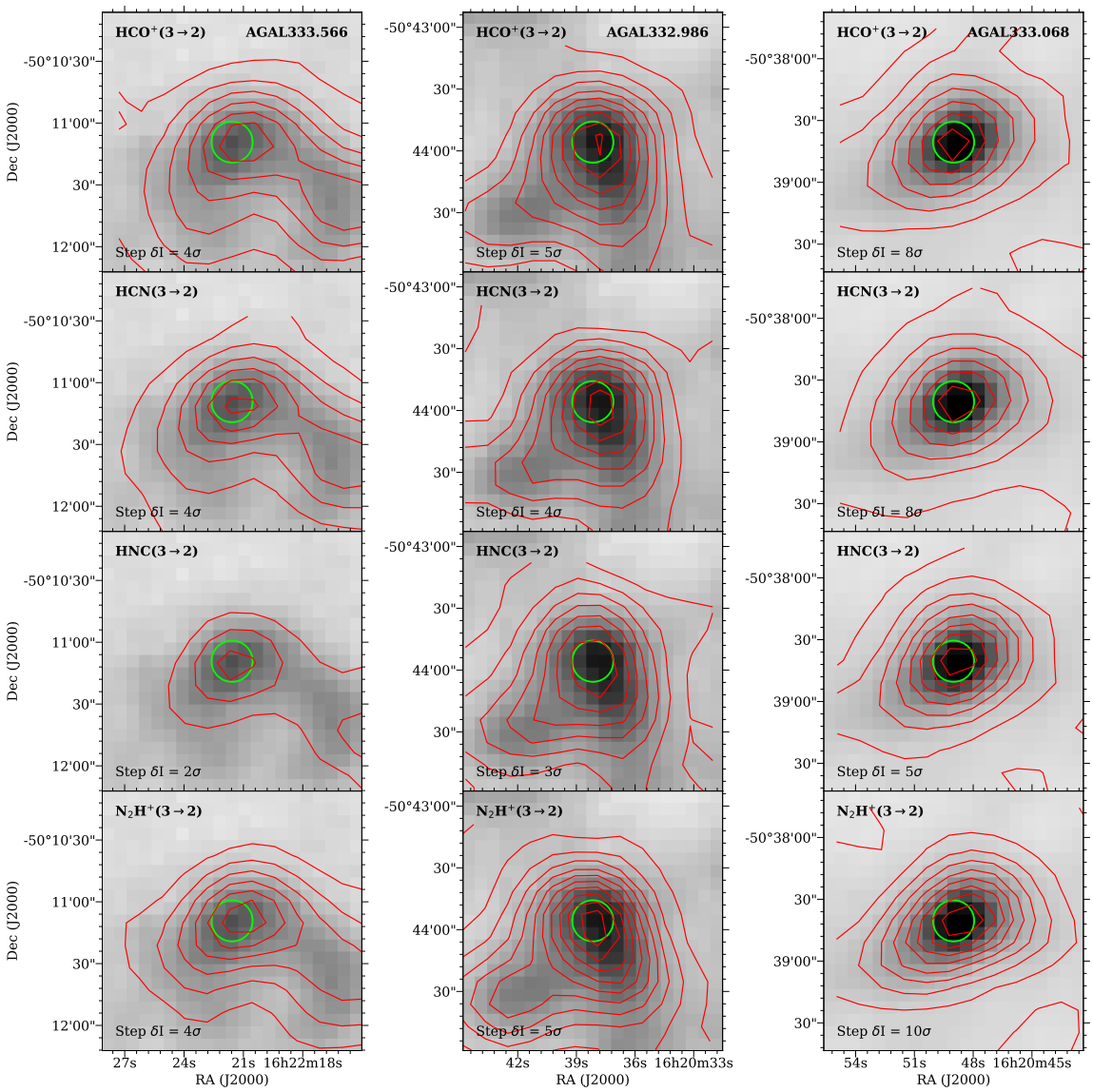

Figure 3.8: Contour maps of the $J = 3 \rightarrow 2$ velocity integrated line emission overlayed on a grey scale image of the 870μm continuum emission (from ATLASGAL) for three clumps in different evolutionary stages. Left: AGAL333.566-0.296 pre-stellar clump; Middle: AGAL332.986-0.489 proto-stellar clump; Right: AGAL333.068-0.447 H II clump. Top to bottom: HCO^+, HCN, HNC, N_2H^+. The green circle is centered at the peak position of the ATLASGAL dust emission and has a diameter of 20", roughly the beam size of the SuperMALT observations. The lowest contour is drawn at 4σ and the contour step is shown in the bottom left corner of each box.

I_{min}=5σ, δ=5σ and A_{min}= six pixels (similar to the area of one beam). From *Astrodendro* we extracted the major-sigma (a_{maj}) and minor-sigma (a_{min}) sizes of the clump structure which are derived from the intensity-weighted second moments perpendicular to the major-axis and minor-axis in the position-position plane. Then we computed the effective angular radius of the clumps as $R_{eff} = \eta\sqrt{a_{min} \times a_{maj}}$ (see Rosolowsky et al. 2010; Contreras et al. 2013). We adopted the value of $\eta = 2.4$.

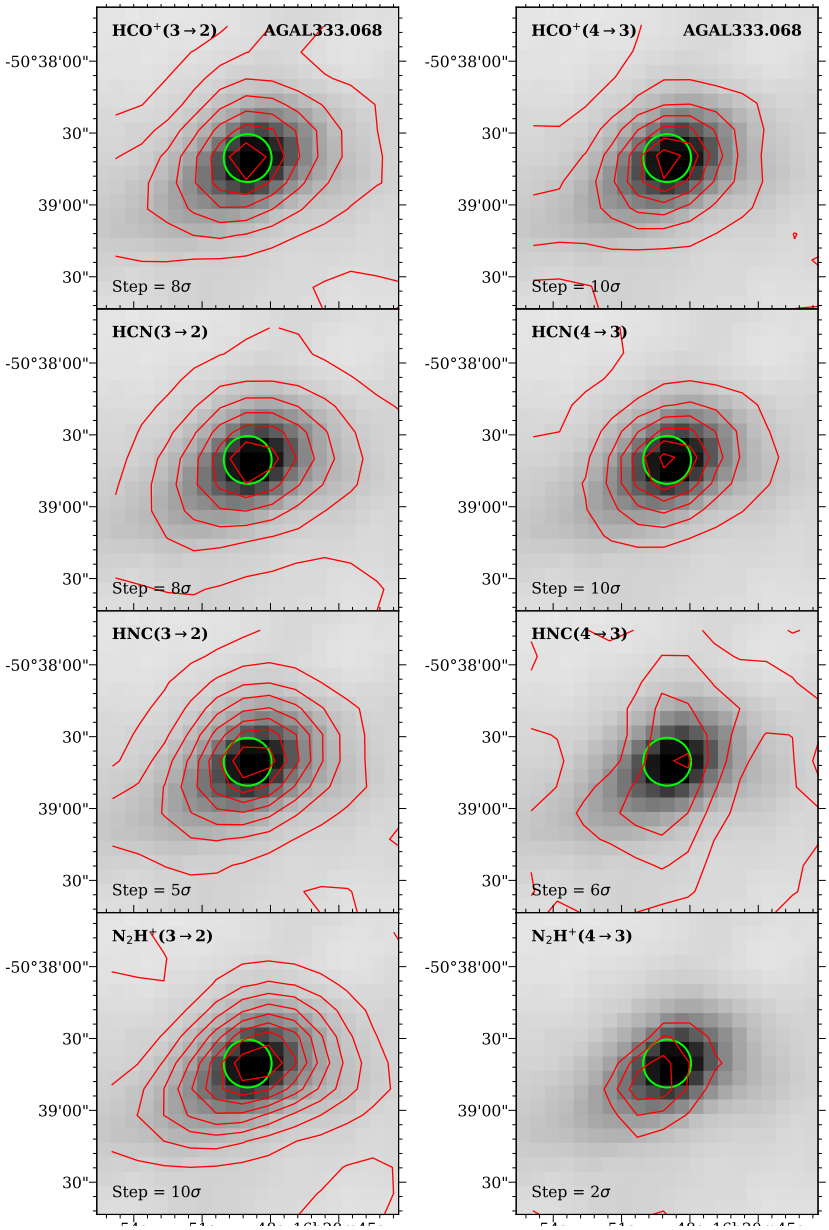

Figure 3.9: Contour maps of the $J = 3 \rightarrow 2$ and $J = 4 \rightarrow 3$ velocity integrated line emission overlayed on a grey scale image of the 870μm continuum emission (from ATLASGAL) toward the clump AGAL333.068-0.447. Left: $J = 3 \rightarrow 2$ maps; Right: $J = 4 \rightarrow 3$ maps. Top to bottom: HCO^+, HCN, HNC, N_2H^+. The lowest contour is drawn at 4σ and the contour step is shown in the bottom left corner of each box. Green circle: same as in Figure 3.8.

We note that Dendogram extracted a single component from fourty-nine HCO^+ maps and fifty N_2H^+ maps, and two components from sixteen HCO^+ maps and twelve N_2H^+ maps. The sizes of the molecular component associated with the ATLASGAL clump extracted from the HCO^+ and N_2H^+ maps are given in cols. 2 and 4 of Table 3.14 of Appendix 3.7.5, respectively. Table 3.5 lists the mean and median values of the molecular sizes for clumps in prestellar, protostellar and H II stages. Clearly the HCO^+ sizes are larger than the N_2H^+ sizes. This is illustrated in the left panel of Figure 3.10 which shows a plot of the HCO^+ versus N_2H^+ sizes. Typically HCO^+ sizes are 1.5 times larger than N_2H^+ sizes. Since the

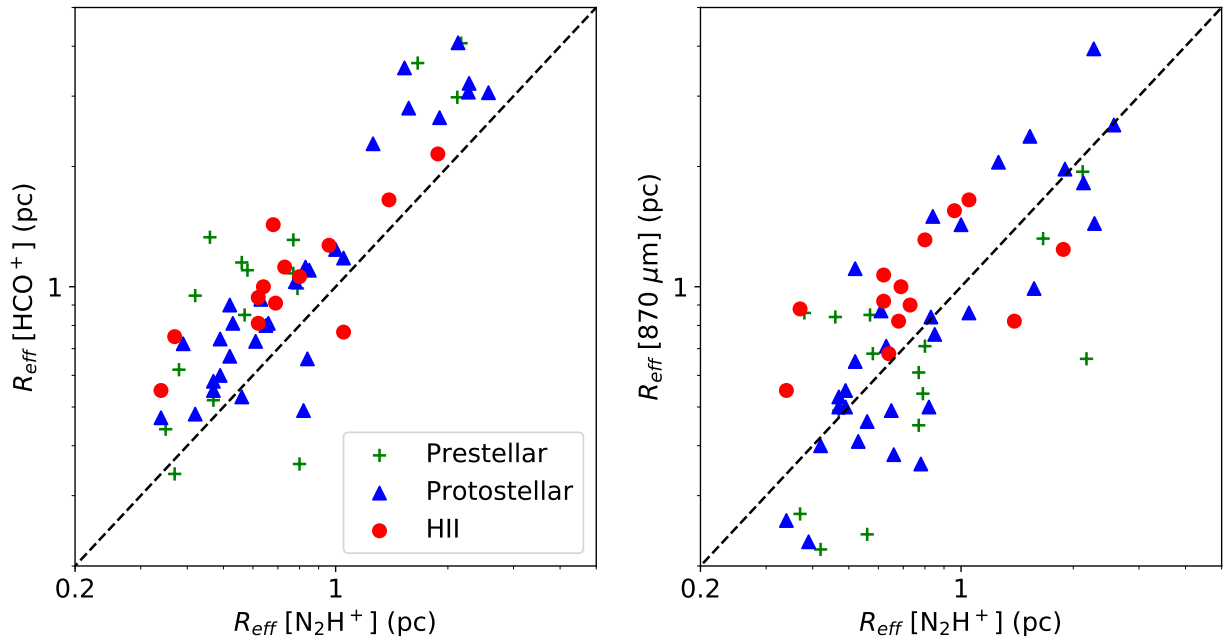

Figure 3.10: Comparison of the sizes from HCO^+ and N_2H^+ $J = 3 \rightarrow 2$ emission and the sizes from the ATLASGAL 870μm maps.

critical densities of the $J = 3 \rightarrow 2$ transitions of these two molecules are similar (see Table 3.5), this result can not be attributed to the presence of density gradients. The larger sizes of the HCO^+ emission are most likely due to the $[HCO^+/H_2]$ abundance ratio being larger than the $[N_2H^+/H_2]$ ratio. In this case, for a similar detection level, HCO^+ traces lower H_2 column densities than N_2H^+.

We find that among the four mapped species the line emission that shows the good agreement in morphology with that of the dust emission is that from N_2H^+. This is illustrated in the right panel of Figure 3.10 which shows a plot of the N_2H^+ size versus the 870 μm dust emission size reported in the ATLASGAL catalogue.

Table 3.5: Clump physical sizes.

Type	No. of clumps	R_{eff} (pc)			
		HCO^+ $(3 \rightarrow 2)$		N_2H^+ $(3 \rightarrow 2)$	
		Mean	Median	Mean	Median
Prestellar	16	1.36	1.04	0.83	0.58
Protostellar	32	1.39	0.86	0.92	0.66
H II	13	1.11	1.00	0.83	0.69

To investigate the degree of central condensation of clumps we use as a proxy the ratio of integrated intensities over two areas, enclosing, respectively, the 30% ($I_{30\%}$) and 90% ($I_{90\%}$) contour levels of the peak emission. For this, we consider the emission in the HCO^+ $J = 3 \rightarrow 2$ line, which is the brighter and most extended one among the four mapped species. In addition, to avoid difficulties with the presence of multiple components and/or filamentary structures, we only consider those clumps in which a single component was extracted by Dendrogram.

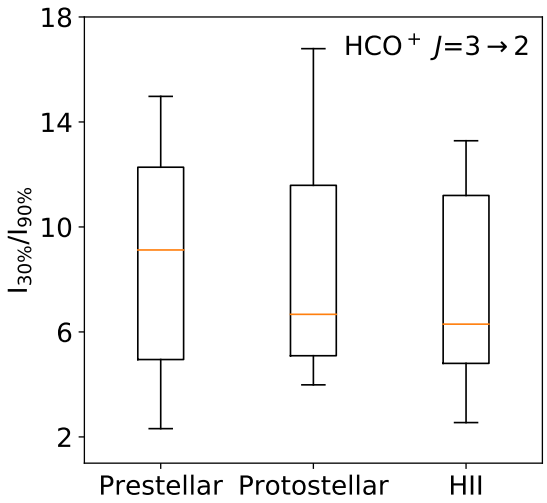

Figure 3.11: Distribution of the $I_{30\%}$ to $I_{90\%}$ integrated intensity ratios. $I_{30\%}$ and $I_{90\%}$ are computed within the regions enclosed by the 30% and 90% contour levels of the peak emission in HCO^+, respectively. The orange lines indicate the median values.

Figure 3.11 shows Whisker plots of the distribution of the $I_{30\%}/I_{90\%}$ ratios for clumps in different evolutionary stages. Clearly the median value of the ratio in quiescent/prestellar clumps is higher than for the proto-stellar and H II clumps suggesting that the prestellar clumps have shallower density profile than more evolved clumps.

3.5 Analysis and discussion

3.5.1 Integrated line intensities

Table 3.6 lists the velocity integrated $J = 3 \rightarrow 2$ line emission, measured from the central spectra (central 20"×20" region) of the clumps, in the four mapped molecular species. Recall that the velocity integrated $J = 3 \rightarrow 2$ line emission in $H^{13}CO^+$ is given in Table 5.6. The integrated line intensities of prestellar clumps, in all observed molecular species, are distinctively weaker than that of protostellar and H II clumps. This is illustrated in Figure 3.12 which presents Whisker plots of the velocity integrated line emission in the four molecular species. Figure 3.12 also shows that on average the HNC emission is the weakest among the four mapped species for clumps in all evolutionary stages.

Figure 3.13 presents a plot of the velocity integrated $J = 3 \rightarrow 2$ line emission versus the dust temperature for all clumps. Clumps with higher dust temperatures typically have higher values of $J = 3 \rightarrow 2$ line fluxes in all species. This is as expected since clumps with higher dust temperatures, likely due to embedded star formation, should have higher gas kinetic temperatures (e.g., Hacar et al. 2020) and larger molecular abundance due to a richer chemistry (e.g., Sanhueza et al. 2012).

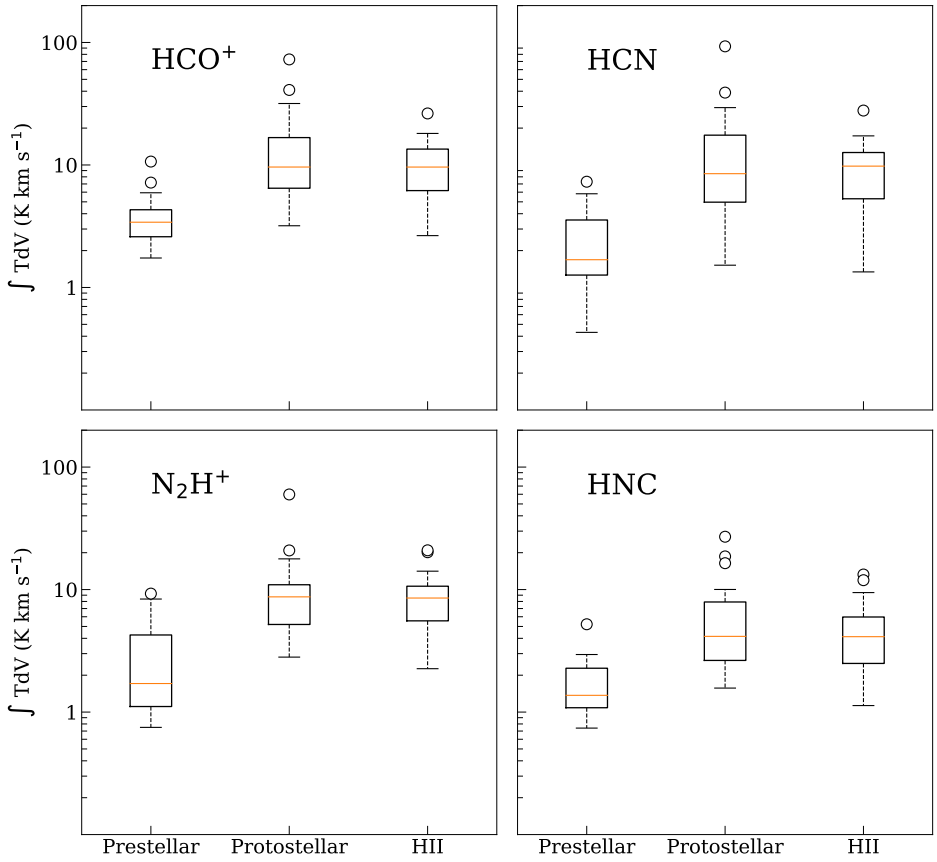

Figure 3.12: Distribution of the velocity integrated molecular emission for clumps in different evolutionary stages. Top left: HCO^+; Top right: HCN; Bottom left: N_2H^+; Bottom right: HNC. The boxes show interquartile range and the horizontal orange lines inside the boxes show median values and the green triangles show mean values. The open circles show outliers that are outside 1.5 times the interquartile range from the boxes' limit.

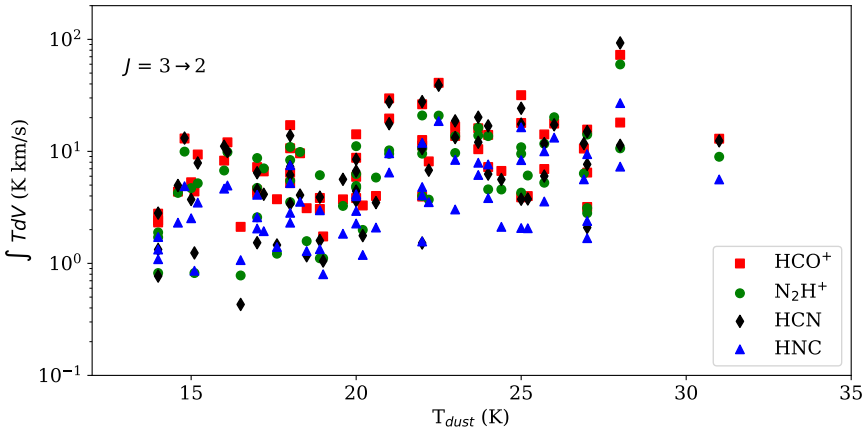

Figure 3.13: Velocity integrated $J = 3 \rightarrow 2$ emission of four molecular species versus dust temperature for all clumps.

Table 3.6: Velocity integrated $J = 3 \rightarrow 2$ line emissions from the central 20" $\times$ 20" region of the clumps.

Name	Vel. Range	$\int T\mathrm{d}V$ (K km s^{-1})			
	(km s^{-1})	HCO^+	N_2H^+	HCN	HNC
Quiescent/Prestellar clumps					
AGAL331.639+00.501_S	[-62.7,-42.7]	2.32 ± 0.23	1.89 ± 0.17	2.81 ± 0.26	1.72 ± 0.22
AGAL332.737-00.621_S	[-60.0,-40.0]	5.93 ± 0.20	4.75 ± 0.11	4.42 ± 0.18	2.94 ± 0.19
AGAL332.892-00.569_S	[-62.5,-49.5]	1.74 ± 0.17	1.11 ± 0.15	1.05 ± 0.16	0.80 ± 0.20
AGAL333.014-00.521_S	[-62.0,-44.0]	7.18 ± 0.21	9.61 ± 0.24	5.81 ± 0.19	4.19 ± 0.21
AGAL333.016-00.751_S	[-61.7,-47.7]	3.74 ± 0.16	1.22 ± 0.15	1.46 ± 0.15	1.40 ± 0.16
AGAL333.071-00.399_S	[-66.1,-41.4]	10.66 ± 0.23	8.37 ± 0.14	7.30 ± 0.18	5.21 ± 0.28
AGAL333.179-00.396_S	[-60.4,-40.4]	3.83 ± 0.16	4.91 ± 0.21	3.62 ± 0.15	2.27 ± 0.18
AGAL333.198-00.352_A	[-56.0,-43.0]	3.06 ± 0.17	1.11 ± 0.15	1.60 ± 0.16	1.34 ± 0.26
AGAL333.449-00.182_S	[-53.0,-35.0]	4.25 ± 0.22	2.58 ± 0.22	1.53 ± 0.18	2.05 ± 0.24
AGAL333.481-00.224_S	[-58.5,-45.5]	1.94 ± 0.16	NO	ND	0.74 ± 0.15
AGAL333.566-00.296_S	[-58.0,-36.0]	7.18 ± 0.22	9.27 ± 0.27	5.82 ± 0.18	2.95 ± 0.25
AGAL333.669-00.349_S	[-55.2,-41.2]	3.29 ± 0.17	1.99 ± 0.19	1.77 ± 0.16	1.19 ± 0.24
AGAL335.592+00.184_S	[-57.4,-41.4]	3.11 ± 0.19	1.58 ± 0.16	1.17 ± 0.18	1.29 ± 0.21
AGAL340.179-00.242_S	[-62.0,-44.0]	4.39 ± 0.19	0.82 ± 0.17	1.24 ± 0.17	0.86 ± 0.21
AGAL340.232-00.146_S	[-55.0,-45.0]	2.41 ± 0.16	0.82 ± 0.13	0.77 ± 0.16	1.09 ± 0.17
AGAL340.301-00.402_S	[-59.0,-42.0]	2.78 ± 0.19	1.71 ± 0.26	1.33 ± 0.17	1.33 ± 0.16
AGAL340.304-00.376_S	[-58.0,-43.0]	4.37 ± 0.14	4.26 ± 0.14	4.96 ± 0.14	2.31 ± 0.16
AGAL340.398-00.396_S	[-52.0,-42.0]	2.12 ± 0.16	0.78 ± 0.09	0.43 ± 0.15	1.07 ± 0.13
AGAL341.039-00.114_S	[-48.4,-38.4]	NO	0.75 ± 0.13	NO	0.80 ± 0.17
AGAL341.181-00.277_S	[-55.0,-35.0]	3.96 ± 0.18	NO	3.36 ± 0.22	2.62 ± 0.17
AGAL341.196-00.221_S	[-50.0,-36.0]	3.41 ± 0.20	NO	2.03 ± 0.19	2.22 ± 0.22
Protostellar clumps					
AGAL304.886+00.636_S	[-46.7,-27.6]	6.63 ± 0.20	7.05 ± 0.26	4.14 ± 0.20	1.94 ± 0.37
AGAL309.154-00.349_S	[-48.7,-33.7]	3.95 ± 0.18	3.99 ± 0.25	1.52 ± 0.15	1.57 ± 0.15
AGAL309.236-00.457_S	[-52.5,-30.5]	9.62 ± 0.20	9.88 ± 0.24	4.07 ± 0.21	3.55 ± 0.17
AGAL318.049+00.086_S	[-69.3,-32.3]	29.73 ± 0.26	9.52 ± 0.29	27.66 ± 0.27	9.62 ± 0.26
AGAL322.158+00.636_S	[-75.5,-37.5]	72.72 ± 0.44	59.76 ± 0.48	92.98 ± 0.42	27.00 ± 0.39
AGAL331.724-00.204_S	[-56.0,-38.0]	6.96 ± 0.24	5.25 ± 0.17	6.02 ± 0.24	3.57 ± 0.20
AGAL332.226-00.536_S	[-64.0,-41.0]	5.21 ± 0.49	3.52 ± 0.22	3.39 ± 0.31	2.31 ± 0.23
AGAL332.281-00.547_S	[-69.4,-37.4]	19.65 ± 0.28	10.21 ± 0.17	17.67 ± 0.24	6.48 ± 0.23
AGAL332.559-00.147_S	[-56.0,-38.0]	6.46 ± 0.23	5.46 ± 0.19	6.15 ± 0.20	2.83 ± 0.24
AGAL332.559-00.591_S	[-58.5,-41.5]	3.73 ± 0.24	3.26 ± 0.18	5.63 ± 0.16	1.84 ± 0.30
AGAL332.604-00.167_S	[-56.0,-34.0]	14.21 ± 0.24	11.13 ± 0.26	8.49 ± 0.20	4.15 ± 0.20
AGAL332.726-00.621_S	[-59.0,-40.0]	5.45 ± 0.20	3.55 ± 0.11	4.97 ± 0.18	2.64 ± 0.18
AGAL332.812-00.701_S	[-66.0,-40.0]	7.25 ± 0.25	4.58 ± 0.28	6.27 ± 0.24	3.83 ± 0.19
AGAL332.942-00.686_S	[-68.7,-28.7]	17.94 ± 0.30	9.52 ± 0.18	17.51 ± 0.25	8.36 ± 0.53
AGAL332.986-00.489_S	[-64.5,-40.5]	14.17 ± 0.26	11.70 ± 0.20	11.73 ± 0.28	10.02 ± 0.37
AGAL332.999-00.639_S	[-57.2,-38.2]	3.19 ± 0.24	2.81 ± 0.25	2.09 ± 0.21	1.68 ± 0.18
AGAL333.076-00.559_S	[-66.4,-45.4]	4.49 ± 0.31	4.72 ± 0.21	4.55 ± 0.33	2.58 ± 0.24
AGAL333.314+00.106_S	[-65.0,-28.0]	16.73 ± 0.25	13.64 ± 0.16	18.73 ± 0.23	8.40 ± 0.29
AGAL333.721-00.207_S	[-55.4,-37.4]	3.84 ± 0.20	6.13 ± 0.18	3.90 ± 0.18	2.98 ± 0.23
AGAL335.284-00.132_S	[-62.2,-28.2]	8.27 ± 0.24	6.75 ± 0.15	11.12 ± 0.24	4.65 ± 0.23
AGAL335.586-00.291_S	[-64.0,-24.0]	40.96 ± 0.27	20.87 ± 0.27	38.97 ± 0.32	18.65 ± 0.34
AGAL336.018-00.827_S	[-60.0,-30.0]	22.88 ± 0.22	17.81 ± 0.23	29.39 ± 0.19	9.48 ± 0.24
AGAL336.958-00.977_S	[-56.7,-30.7]	7.24 ± 0.22	8.72 ± 0.22	6.45 ± 0.21	4.10 ± 0.24
AGAL337.098-00.929_S	[-53.5,-30.5]	6.69 ± 0.21	4.57 ± 0.20	5.61 ± 0.20	2.12 ± 0.23
AGAL337.612-00.059_S	[-63.5,-38.5]	10.60 ± 0.23	6.35 ± 0.15	11.75 ± 0.22	5.63 ± 0.22
AGAL337.761-00.339_S	[-55.5,-25.5]	13.04 ± 0.25	9.95 ± 0.15	13.15 ± 0.21	4.89 ± 0.37
AGAL339.943-00.092_S	[-75.0,-40.0]	12.63 ± 0.29	9.54 ± 0.34	10.60 ± 0.27	4.81 ± 0.22
AGAL340.054-00.244_S	[-77.0,-35.0]	31.75 ± 0.45	10.89 ± 0.30	24.26 ± 0.41	16.42 ± 0.37

AGAL341.216-00.236_S	[-61.4,-28.4]	14.03 ± 0.21	13.69 ± 0.15	16.89 ± 0.20	7.65 ± 0.30
AGAL341.217-00.212_S	[-62.5,-26.5]	16.08 ± 0.28	16.26 ± 0.15	20.18 ± 0.29	7.92 ± 0.32
AGAL341.219-00.259_S	[-58.9,-29.9]	17.15 ± 0.25	10.95 ± 0.18	13.83 ± 0.24	7.53 ± 0.21
AGAL343.133-00.482_S	[-46.7,-24.7]	9.38 ± 0.15	5.19 ± 0.10	7.88 ± 0.16	3.49 ± 0.18
AGAL343.521-00.519_S	[-44.2,-23.2]	12.05 ± 0.25	9.84 ± 0.33	9.97 ± 0.20	4.96 ± 0.25
AGAL343.528-00.507_S	[-42.0,-27.0]	4.84 ± 0.21	5.29 ± 0.28	3.90 ± 0.17	1.94 ± 0.21
HII clumps					
AGAL310.014+00.387_S	[-57.0,-30.0]	18.09 ± 0.23	10.65 ± 0.34	11.32 ± 0.26	7.31 ± 0.22
AGAL312.108+00.309_S	[-57.0,-40.0]	12.98 ± 0.19	8.95 ± 0.26	12.42 ± 0.22	5.62 ± 0.17
AGAL314.264+00.091_S	[-62.0,-43.0]	8.77 ± 0.13	6.28 ± 0.14	6.67 ± 0.18	3.98 ± 0.17
AGAL320.676+00.244_S	[-68.9,-48.9]	8.14 ± 0.20	3.71 ± 0.11	6.79 ± 0.17	3.52 ± 0.16
AGAL331.418-00.356_S	[-71.3,-53.3]	13.74 ± 0.16	9.67 ± 0.16	13.29 ± 0.16	3.03 ± 0.21
AGAL332.094-00.421_S	[-66.5,-44.5]	15.65 ± 0.24	14.13 ± 0.12	15.03 ± 0.23	9.45 ± 0.19
AGAL332.584-00.559_S	[-58.5,-42.5]	3.89 ± 0.18	4.28 ± 0.17	3.74 ± 0.17	2.07 ± 0.20
AGAL333.053+00.029_S	[-53.5,-37.5]	6.47 ± 0.14	3.12 ± 0.19	7.66 ± 0.14	2.39 ± 0.18
AGAL333.068-00.447_S	[-66.3,-40.3]	17.72 ± 0.25	20.18 ± 0.20	17.28 ± 0.27	13.27 ± 0.27
AGAL335.687-00.812_S	[-58.5,-43.5]	4.00 ± 0.21	5.84 ± 0.09	3.49 ± 0.20	2.09 ± 0.23
AGAL336.020-00.816_S	[-65.5,-29.5]	10.46 ± 0.24	13.86 ± 0.25	12.06 ± 0.21	6.16 ± 0.26
AGAL337.284-00.159_S	[-60.0,-43.0]	3.99 ± 0.18	6.09 ± 0.24	3.76 ± 0.15	2.06 ± 0.16
AGAL340.248-00.374_S	[-69.0,-31.0]	26.34 ± 0.25	20.92 ± 0.15	27.81 ± 0.21	11.93 ± 0.32
AGAL340.401-00.381_S	[-54.0,-37.0]	5.30 ± 0.18	4.70 ± 0.21	3.72 ± 0.15	2.53 ± 0.23
AGAL343.689-00.017_S	[-52.0,-21.0]	11.28 ± 0.25	10.66 ± 0.35	11.32 ± 0.23	4.06 ± 0.23
PDR clump					
AGAL340.319-00.227_S	[-52.0,-40.0]	2.65 ± 0.15	2.26 ± 0.08	1.34 ± 0.13	1.13 ± 0.17
Unknown type clumps					
AGAL333.103-00.502_S	[-66.0,-47.0]	13.39 ± 0.21	7.84 ± 0.16	14.12 ± 0.24	5.91 ± 0.25
AGAL338.402+00.032_S	[-55.0,-28.0]	8.05 ± 0.21	8.11 ± 0.12	8.97 ± 0.24	4.68 ± 0.19

NO : not observed, ND : undetected

Table 3.7: Velocity integrated $J = 4 \rightarrow 3$ line emissions from the central 20" $\times$ 20" region of the clumps.

Name	Vel. Range	$\int T\mathrm{d}V$ (K.km s^{-1})			
	(km s^{-1})	HCO^+	N_2H^+	HCN	HNC
Quiescent/Prestellar clumps					
AGAL331.639+00.501_S	[-55.0,-48.0]	1.20±0.13	ND	1.28±0.17	0.46±0.11
AGAL333.071-00.399_S	[-60.0,-43.0]	3.39±0.22	1.00±0.24	2.13±0.22	3.31±0.31
AGAL333.566-00.296_S	[-53.0,-39.0]	3.85±0.17	0.67±0.23	2.12±0.17	1.20±0.15
Protostellar clumps					
AGAL318.049+00.086_S	[-62.2,-38.2]	20.62±0.24	0.72±0.37	16.63±0.24	6.89±0.50
AGAL322.158+00.636_S	[-72.7,-41.7]	51.22±0.19	3.95±0.22	54.81±0.27	16.78±0.27
AGAL332.942-00.686_S	[-64.0,-34.0]	10.54±0.27	1.94±0.35	11.85±0.37	2.63±0.32
AGAL332.986-00.489_S	[-59.0,-46.0]	6.08±0.16	0.53±0.30	4.79±0.17	NO
AGAL335.586-00.291_S	[-67.0,-27.0]	28.25±0.27	2.10±0.51	22.89±0.27	NO
AGAL337.761-00.339_S	[-52.0,-32.0]	7.59±0.20	0.95±0.24	6.38±0.20	1.65±0.28
HII clumps					
AGAL310.014+00.387_S	[-53.0,-29.0]	18.57±0.22	ND	7.97±0.22	4.25±0.24
AGAL331.418-00.356_S	[-69.0,-57.0]	6.48±0.22	1.63±0.25	5.87±0.17	3.10±0.17
AGAL333.068-00.447_S	[-63.0,-43.0]	16.08±0.22	2.61±0.62	15.97±0.22	5.94±1.12
AGAL340.248-00.374_S	[-59.0,-42.0]	10.96±0.24	2.60±0.27	BS	6.25±0.35
AGAL340.401-00.381_S	[-49.0,-41.0]	1.73±0.20	ND	ND	0.77±0.28
PDR clump					
AGAL340.319-00.227_S	[-49.0,-42.0]	0.85±0.20	0.44±0.26	0.85±0.20	0.35±0.14

NO : not observed, ND : undetected, BS: bad spectra.

3.5.2 Line ratios

Figure 3.14 shows whisker plots of ratios of velocity integrated $J = 3 \rightarrow 2$ line emission for clumps in different evolutionary stages. The orange line inside the box plot indicates the median value of the distribution. The values of the mean, median and standard deviation of the line ratios are given in Table 3.9. The ratio of integrated intensities in lines of different molecular species is considered as a proxy for the determination of the relative molecular abundances. This requires that lines are optically thin. In that case, the trends seen in Figure 3.14 may indicate changes in the relative molecular abundances with clump evolution, although the temperature of the clumps could play a role. To asses the latter, we plot in Figure 3.15 the individual $J = 3 \rightarrow 2$ line intensity ratios for all clumps in the sample as a function of dust temperature. This figure shows that all line intensity ratios, except for HCN/HCO^+ and HCN/HNC, show no significant correlation with clump temperature (see Table 3.8). The Pearson correlation coefficient r and associated $p - value$ of the linear relationship between HCN/HCO^+ and HCN/HNC versus dust temperature are 0.33, 0.01 and 0.29, 0.02, respectively.

Table 3.8: Correlation of line ratios and dust temperature.

Line ratio	Pearson correlation coefficient	
	r	$p - value$
N_2H^+/HCO^+	0.10	0.44
HCN/HCO^+	0.33	0.01
HNC/HCO^+	0.09	0.49
N_2H^+/HCN	-0.20	0.12
N_2H^+/HNC	0.06	0.65
HCN/HNC	0.29	0.02

In what follows we summarize our results regarding the ratios of velocity integrated intensities in the $J = 3 \rightarrow 2$ lines and compare them with those in the $J = 1 \rightarrow 0$ lines. The latter were computed using the values of the $J = 1 \rightarrow 0$ lines reported in the MALT90 catalogue (Rathborne et al. 2016).

N_2H^+/HCO^+: The mean of this ratio in the $J = 3 \rightarrow 2$ lines increases from early to late evolutionary stages, having values of 0.66±0.31, 0.80±0.25 and 0.91±0.31 for prestellar, protostellar and H II clumps, respectively. A similar trend is observed in the mean values of the $J = 1 \rightarrow 0$ ratios for the objects in our sample, with values of 0.89±0.35, 1.31±1.02 and 1.56±0.85 for, respectively, prestellar, protostellar and H II clumps. The $J = 1 \rightarrow 0$ ratios are, however, larger than the $J = 3 \rightarrow 2$ ratios in all evolutionary stages.

The mean of $J = 4 \rightarrow 3$ ratios are 0.24±0.06 for prestellar clumps, 0.10±0.05 for protostellar clumps and 0.22±0.04 for H II clumps. The values of this ratio in the higher J transitions are smaller than in the lower J transitions.

HCN/HCO^+: The mean of this ratio in $J = 3 \rightarrow 2$ lines increases from early to late evolutionary stages, having values of 0.61±0.26, 0.92±0.25 and 0.91±0.17 for prestellar, protostellar and H II clumps, respectively. A similar trend is observed in the $J = 1 \rightarrow 0$ ratios, with values of 0.86±0.24, 1.06±0.25 and 1.15±0.32 for, respectively, prestellar, protostellar

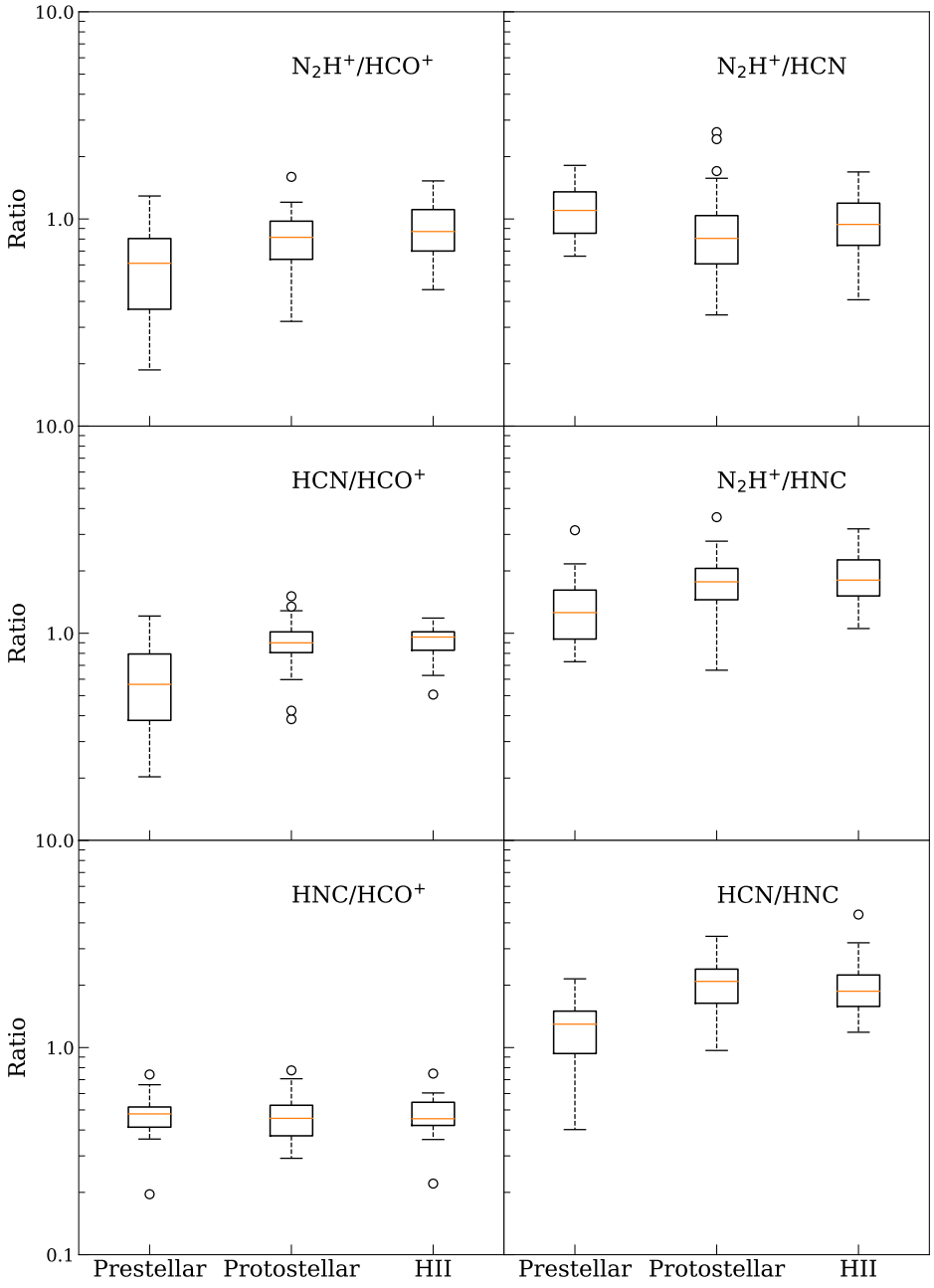

Figure 3.14: Whisker plots of the $J = 3 \rightarrow 2$ integrated intensity ratios for clumps in different evolutionary stages. The boxes show interquartile range and the horizontal orange lines inside the boxes show median values and the green triangles show mean values. The open circles show outliers that are outside 1.5 times the interquartile range from the boxes' limit.

and H II clumps. The $J = 1 \rightarrow 0$ ratios are larger than that of the $J = 3 \rightarrow 2$ ratios for clumps in all evolutionary stages.

The ratio in the $J = 4 \rightarrow 3$ lines increases significantly from prestellar clumps (mean value 0.39±0.27) to later stage clumps. In protostellar and H II clumps, the ratios are

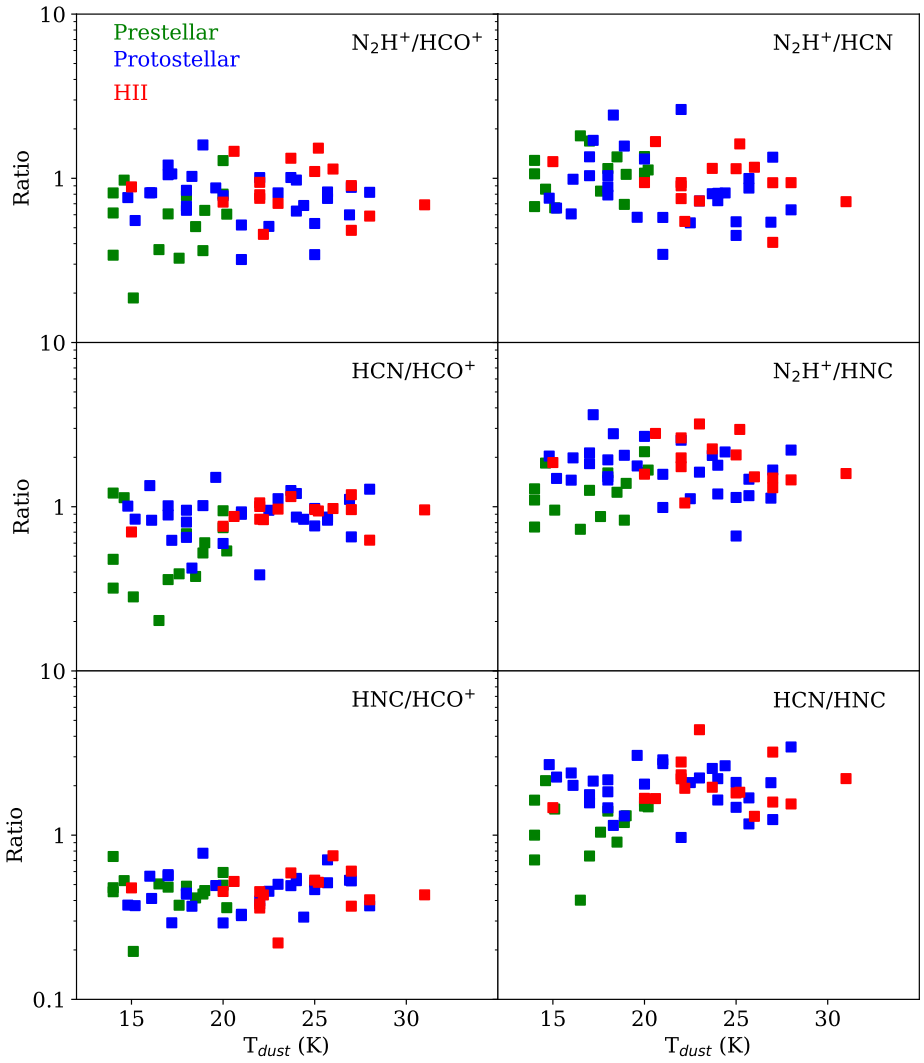

Figure 3.15: Line ratios of the $J = 3 \rightarrow 2$ velocity integrated emissions versus dust temperature for SuperMALT clumps. Different colors show clumps at different evolutionary stages.

similar with mean values of 0.90±0.14 and 0.78±0.25, respectively. The line ratio in the higher J transitions is smaller than in the lower J transitions.

Table 3.9: Summary of the $J = 3 \rightarrow 2$ line ratios from SuperMALT clumps.

Line ratio	Prestellar			Protostellar			H II		
	Mean	Median	Std.	Mean	Median	Std.	Mean	Median	Std.
N_2H^+/HCO^+	0.66	0.61	0.31	0.80	0.82	0.25	0.91	0.87	0.31
HCN/HCO^+	0.61	0.57	0.28	0.92	0.90	0.25	0.91	0.96	0.17
HNC/HCO^+	0.48	0.48	0.12	0.46	0.46	0.11	0.48	0.45	0.11
N_2H^+/HCN	1.14	1.10	0.35	0.96	0.81	0.51	1.03	0.94	0.38
N_2H^+/HNC	1.37	1.26	0.59	1.79	1.77	0.60	1.94	1.81	0.57
HCN/HNC	1.26	1.30	0.43	2.06	2.09	0.60	2.04	1.87	0.73

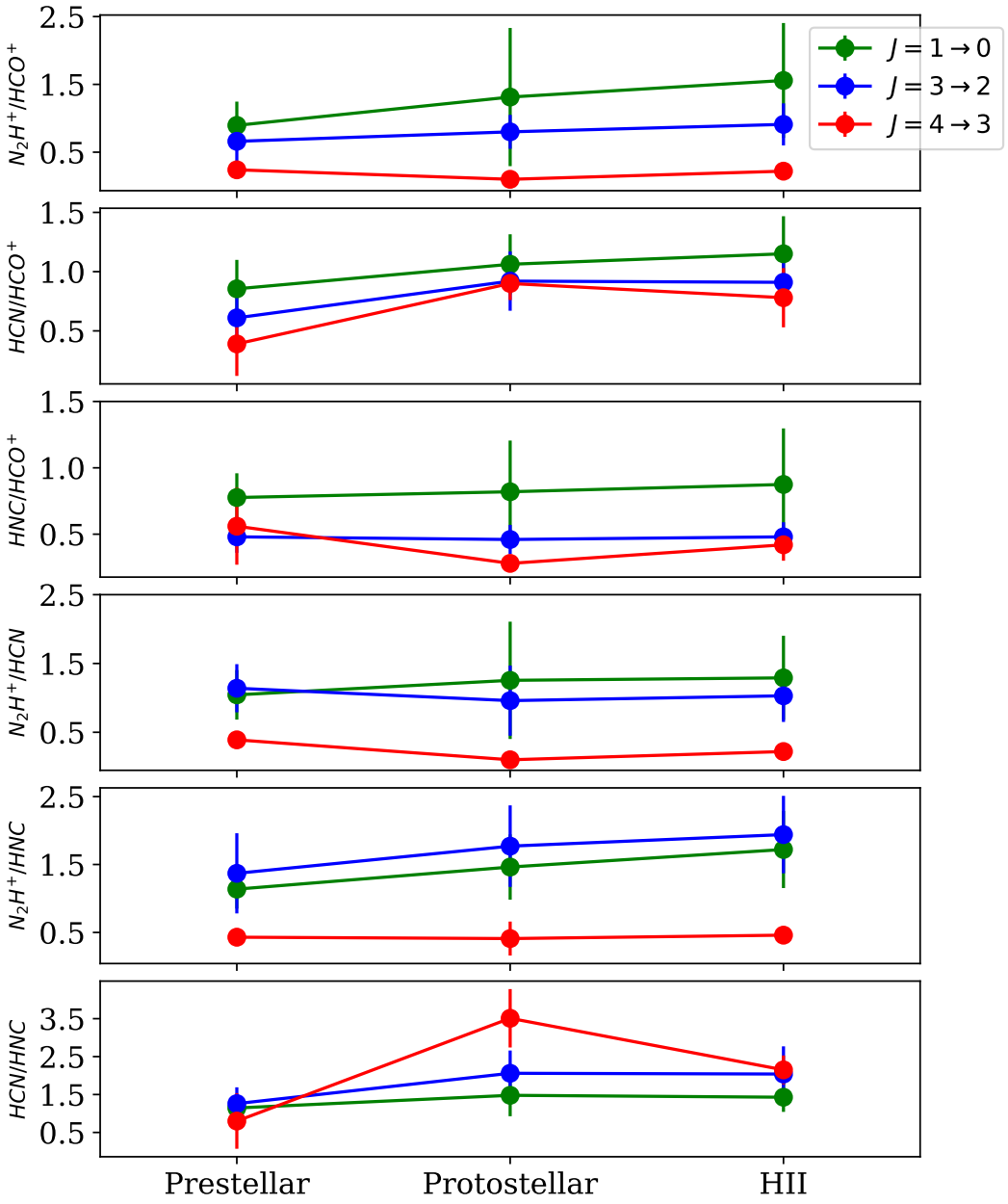

Figure 3.16: Left: Ratio of integrated intensities of different molecular species for clumps in different evolutionary stages. $J = 1 \rightarrow 0$ ratios are shown in green, $J = 3 \rightarrow 2$ ratios are shown by blue and $J = 4 \rightarrow 3$ ratios are shown in red . Error bars show the standard deviation.

HNC/HCO$^+$: The mean of this ratio in the $J = 3 \rightarrow 2$ lines is fairly constant for clumps in all evolutionary stages, with values of 0.48±0.12, 0.46±0.11 and 0.48±0.11 for prestellar, protostellar and H II clumps, respectively. The mean of this ratio in the $J = 1 \rightarrow 0$ lines are also fairly constant for clumps in different evolutionary stages, with values of 0.78±0.18, 0.82±0.38 and 0.88±0.42 toward prestellar, protostellar and H II clumps, respectively. The ratios in the $J = 1 \rightarrow 0$ lines are higher than in the $J = 3 \rightarrow 2$ lines by roughly a factor of 2.

In $J = 4 \rightarrow 3$, the mean values of this ratio are 0.56±0.29, 0.28±0.05 and 0.42±0.12 for prestellar, protostellar and H II clumps, respectively.

N_2H^+/HCN: The mean of this ratio in $J = 3 \rightarrow 2$ lines is the same, within the errors, for prestellar, protostellar and H II clumps, with values of 1.14±0.35, 0.96±0.51 and 1.03±0.38, respectively. The mean values of this ratio in the$J = 1 \rightarrow 0$ lines shows a slight increase from prestellar to protostellar and to H II clumps, with values of 1.04±0.36, 1.25±0.85 and 1.29±0.61, respectively.

The mean values of the $J = 4 \rightarrow 3$ line ratios is 0.39±0.08 for prestellar clumps, 0.10±0.05 for protostellar clumps and 0.22±0.06 for H II clumps.

N_2H^+/HNC: The mean value of this ratio in the $J = 3 \rightarrow 2$ lines increases from early to late evolutionary stages, with values of 1.37±0.59, 1.79±0.60 and 1.94±0.57 for prestellar, protostellar and H II clumps, respectively. A similar trend is seen in $J = 1 \rightarrow 0$ ratio with mean values of 1.14±0.29, 1.46±0.48 and 1.72±0.57 for prestellar, protostellar and H II clumps, respectively. The $J = 4 \rightarrow 3$ line ratios are 0.43±0.13, 0.41±0.25 and 0.46±0.05 toward prestellar, protostellar and H II clumps, respectively.

HCN/HNC: The mean value of this ratio in the $J = 3 \rightarrow 2$ and $J = 1 \rightarrow 0$ lines is significantly smaller for quiescent clumps than for protostellar and H II clumps, which have similar values. The $J = 3 \rightarrow 2$ ratios have mean values of 1.26±0.43, 2.06±0.60 and 2.04±0.73, while the $J = 1 \rightarrow 0$ ratios have mean values of 1.15±0.25, 1.48±0.55 and 1.43±0.38 for, respectively, prestellar, protostellar and H II clumps. A similar trend is seen in $J = 4 \rightarrow 3$ line ratios, with mean values 0.80±0.73, 3.51±0.77 and 2.15±0.38 for prestellar, protostellar and H II clumps, respectively. Molecular line studies toward high-mass star forming regions have reported similar trends of the HCN/HNC ratio with evolutionary phases (e.g., Hoq et al. 2013; Jin et al. 2015). The reason for the observed behaviour of the HCN/HNC ratio could be due to the decrease in HNC abundance with evolutionary stage (Hirota et al. 1998). The differences in the line ratio with evolutionary stages is further enhanced in the higher J transitions. Since, the high excitation emission lines suffer less from optical depth effects, the HCN/HNC ratios in higher J transition lines, such as $J = 3 \rightarrow 2$ and $4 \rightarrow 3$, can be a robust tracer of the evolutionary phases.

As shown Figure 3.15, the HCN/HNC ratios in the $J = 3 \rightarrow 2$ lines show an increasing trend with dust temperature of the clump (slope: 0.53 K^{-1}). This increase is most likely due to the the increase in the [HCN/HNC] abundance ratio with temperature as reported for clouds in the central ridge of the Orion Molecular Cloud (e.g., Goldsmith et al. 1986; Schilke et al. 1992; Hacar et al. 2020).

The ratio of the line emission from two species in the same rotational (e.g., $J \rightarrow J - 1$)

transition is given by,

$$\frac{T_{mb}(L1)}{T_{mb}(L2)} = \frac{f_{L1}}{f_{L2}} \frac{[J_\nu^{L1}(T_{ex}) - J_\nu^{L1}(T_b)]}{[J_\nu^{L1}(T_{ex}) - J_\nu^{L1}(T_b)]} \frac{1 - \mathrm{e}^{-\tau_{L1}}}{1 - \mathrm{e}^{-\tau_{L2}}} , \tag{3.1}$$

where J_ν is defined as,

$$J_\nu(T) = \frac{h\nu}{k} \frac{1}{\mathrm{e}^{h\nu/kT} - 1} , \tag{3.2}$$

τ is the optical depth of the line, f is the filling factor and the superscripts L1 and L2 refer to the lines considered. For optically thick lines the ratio is weakly dependent on excitation temperature, while for optically thin lines it is mainly dependent on the abundance ratio of the two molecules. Most of the derived ratios are close to 1, suggesting that the lines are optically thick. For most of the line ratios shown in Fig. 3.16, the values derived from higher J transitions are smaller than those derived from lower J transitions. Even though E_u/k values are similar for same transition line of the pair of species, the above result reflects varying excitation characteristics of the transition lines due to their critical densities ($n_{crit}^{L1}/n_{crit}^{L2}$) which could differ by a factor of ∼2-3 in lower and upper transitions (see Table 3.2).

3.5.3 HCO^+: Optical depths, excitation temperature and column densities

Table 3.10: Clump parameters derived from the HCO^+ and $H^{13}CO^+$ observations

Clump	$\tau_{32}(HCO^+)$	T_{ex} (K)	Δv (km s^{-1}) (km s^{-1})	N(HCO^+) (10^{14} cm^{-2})
Prestellar				
AGAL331.639+0.501_S	8.3	6.7	2.28	1.92±0.22
AGAL333.071–0.399_S	2.6	7.7	2.99	0.79±0.09
AGAL333.566–0.296_S	2.8	10.8	1.70	0.56±0.07
Average	4.6	8.4	2.3	1.09±0.08
Protostellar				
AGAL318.049+0.086_S	8.9	8.5	2.83	2.60±0.30
AGAL322.158+0.636_S	7.3	9.6	4.53	3.55 ±0.43
AGAL332.942–0.686_S	0.6	17.6	1.95	0.23±0.04
AGAL332.986–0.489_S	1.7	10.6	2.37	0.46±0.06
AGAL335.586–0.291_S	8.0	8.9	3.68	3.07±0.36
AGAL337.761–0.339_S	2.5	12.6	2.19	0.69±0.09
Average	4.9	11.3	2.9	1.77±0.11
HII clumps				
AGAL310.014+0.387_S	11.7	7.6	2.44	2.85±0.32
AGAL331.418–0.356_S	2.6	16.8	2.66	1.17±0.19
AGAL333.068–0.447_S	18.7	5.6	3.35	6.79±0.86
AGAL340.248–0.374_S	3.6	8.3	2.76	1.00±0.12
AGAL340.401–0.381_S	1.5	19.3	1.25	0.38±0.06
Average	7.6	11.5	2.5	2.44±0.19

Combining the observations of the $J = 3 \rightarrow 2$ and $J = 4 \rightarrow 3$ transitions of HCO^+ and $J = 3 \rightarrow 2$ transition of $H^{13}CO^+$ it is possible to derive the optical depths and excitation temperature of the lines using line ratios, making thus the estimates of these quantities independent of filling factors, as follows. The first ratio we use is that of the observed brightness temperatures of the $H^{13}CO^+$ and HCO^+ $J = 3 \rightarrow 2$ lines, given by

$$\frac{T_{mb}(H^{13}CO^+)_{32}}{T_{mb}(HCO^+)_{32}} = \frac{[J_{32}^{13}(T_{\rm ex}) - J_{32}^{13}(T_b)]}{[J_{32}(T_{\rm ex}) - J_{32}(T_b)]} \frac{1 - {\rm e}^{-\tau_{32}/r}}{1 - {\rm e}^{-\tau_{32}}} , \tag{3.3}$$

where, J_ν(T) is given by equation 3.2, τ is the optical depth, T_{ex} is the excitation temperature and T_{bg} is the background temperature. The subscripts '32' refer to quantities associated to the $J = 3 \rightarrow 2$ lines and superscript '13' refers to quantities associated to the $H^{13}CO^+$ line. The quantity r is the ratio of the optical depths in the $J = 3 \rightarrow 2$ lines of HCO^+ and $H^{13}CO^+$, given by,

$$r = \frac{\tau_{32}}{\tau_{32}^{13}} = [\frac{HCO^+}{H^{13}CO^+}] \frac{(kT_{ex}/hB_{32}^{13} + 1/3)}{(kT_{ex}/hB_{32} + 1/3)} \frac{exp(E_{32}^{13}/kT_{\rm ex})}{exp(E_{32}/kT_{ex})} \frac{1 - exp(-h\nu_{32}/kT_{\rm ex})}{1 - exp(-h\nu_{32}^{13}/kT_{\rm ex})} , \tag{3.4}$$

where E corresponds to the energy of the lower level of a transition and $[HCO^+/H^{13}CO^+]$ is the abundance ratio.

The second ratio we use is that of the observed brightness temperatures in the $J = 4 \rightarrow 3$ and $J = 3 \rightarrow 2$ lines of HCO^+, given by

$$\frac{T_{mb}(HCO^+)_{43}}{T_{mb}(HCO^+)_{32}} = \frac{[J_{43}(T_{\rm ex}) - J_{43}(T_b)]}{[J_{32}(T_{\rm ex}) - J_{32}(T_b)]} \frac{1 - {\rm e}^{-\tau_{32}/s}}{1 - {\rm e}^{-\tau_{32}}} , \tag{3.5}$$

where subscripts '43' and '32' refers to the $J = 4 \rightarrow 3$ and $J = 3 \rightarrow 2$ lines, respectively, and s is the ratio of the $J = 3 \rightarrow 2$ and $J = 4 \rightarrow 3$ optical depths, given by,

$$s = \frac{\tau_{32}}{\tau_{43}} = \frac{exp(E_{43}/kT_{\rm ex})}{exp(E_{32}/kT_{ex})} \frac{1 - exp(-h\nu_{32}/kT_{\rm ex})}{1 - exp(-h\nu_{43}/kT_{\rm ex})} . \tag{3.6}$$

Optical depths and excitation temperatures are then computed by an iterative process using expressions (3.3) and (3.5). First, we use equation (3.3), which is weakly dependent on T_{ex}, to estimate the value of τ_{32}. This value is then used in equation (3.5) to compute T_{ex}, which is in turn used in equation (3.3) to compute a new value of τ_{32} and so on, iterating until a convergence is achieved. For the calculations we assumed an $[HCO^+/H^{13}CO^+]$ abundance ratio of 50 (see Savage et al. 2002). Table 3.10 lists the optical depths and excitation temperatures of the clumps for which observations in the three lines are available.

The total column density of a molecule can be expressed in terms of the optical depth of a single line and the excitation temperature as (Garden et al. 1991),

$$N_{tot} = \frac{3k}{8\pi^3 B\mu^2} \frac{T_{\rm ex} + hB/3k}{J+1} \frac{exp(E_J/kT_{\rm ex})}{1 - exp(-h\nu/kT_{\rm ex})} \int \tau {\rm d}v, \tag{3.7}$$

where, $\int \tau_\nu {\rm d}v$ is the velocity integrated optical depth for a rotational transition from upper level $J + 1$ to lower level J, ν is the transition frequency, μ is the dipole moment of the

molecule, B is the rotational constant, h is the Plank constant and k is the Boltzmann constant. Col. 5 of Table 3.10 list the total column density of HCO^+, derived from eqn. 3.7, using the excitation temperature and optical depth of the $J = 3 \rightarrow 2$ line.

3.5.4 Clump physical parameters

To determine the temperature and density within the clumps, we use the 1D non-LTE radiative transfer code RADEX (van der Tak et al. 2007) and compute HCO^+ line intensities covering a broad range of values of temperatures and densities for the column density values given in the Table 3.10. The code uses collision parameters from LAMBDA database (Schöier et al. 2005). The inputs of the code are the molecular gas density (n_{H_2}), kinetic temperature (T_K) and column density (N_{HCO^+}). Since the model give intensities, to compare with the observations the later have to be corrected by a beam filling factor if the source size is smaller than the beam. The sizes derived from the $J = 3 \rightarrow 2$ observations are typically larger than the beams of the $J = 3 \rightarrow 2$ and $J = 4 \rightarrow 3$ observations but smaller than the beam of the $J = 1 \rightarrow 0$ observations (38"). Therefore we will apply a beam filling factor correction only to the $J = 1 \rightarrow 0$ data. The correction factor we apply is equal to $\Omega^2_{source}/(\Omega^2_{source} + \Omega^2_{beam})$ and adopt the source size determined from the $J = 3 \rightarrow 2$ observations.

Table 3.11: Clump parameters derived from the HCO^+ RADEX models

Clump	RADEX models	
	T_{kin} (K)	$n(H_2)$ (10^4 cm^{-3})
Prestellar		
AGAL331.639+0.501_S	–	–
AGAL333.071–0.399_S	51^{+3}_{-3}	$0.45^{+0.06}_{-0.06}$
AGAL333.566–0.296_S	20^{+5}_{-4}	$32.4^{+10.4}_{-6.7}$
Protostellar		
AGAL318.049+0.086_S	–	–
AGAL322.158+0.636_S	–	–
AGAL332.942–0.686_S	–	–
AGAL332.986–0.489_S	69^{+9}_{-6}	$0.38^{+0.06}_{-0.07}$
AGAL335.586–0.291_S	–	–
AGAL337.761–0.339_S	–	–
HII clumps		
AGAL310.014+0.387_S	–	–
AGAL331.418–0.356_S	32^{+12}_{-6}	$14.8^{+3.4}_{-4.8}$
AGAL333.068–0.447_S	–	–
AGAL340.248–0.374_S	20^{+7}_{-4}	$58.9^{+17.6}_{-17.6}$
AGAL340.401–0.381_S	77^{+10}_{-8}	$0.47^{+0.08}_{-0.09}$

We use a Bayesian approach to fit the three independent observed line ratios obtained from the J=1 $\rightarrow$ 0, 3 $\rightarrow$ 2 and 4 $\rightarrow$ 3 observations of HCO^+ with the model values obtained from the RADEX. The e*mc*ee (Foreman-Mackey et al. 2013) code is used to perform Markov Chain Monte Carlo (MCMC) calculations for exploring the parameter space (eg., Magalhães et al. 2018). A uniform probability is assumed within the boundaries of the input parameters

and zero outside the boundaries. The input parameter ranges are: n_{H_2} = 10^3 - 10^6 cm^{-3}, and T_{kin} = 3 - 100 K.

Figure 3.17 presents an example of the posterior probability distribution and marginal distribution of the parameters made using corner plot (Foreman-Mackey et al., 2017) toward the clump AGAL333.071.

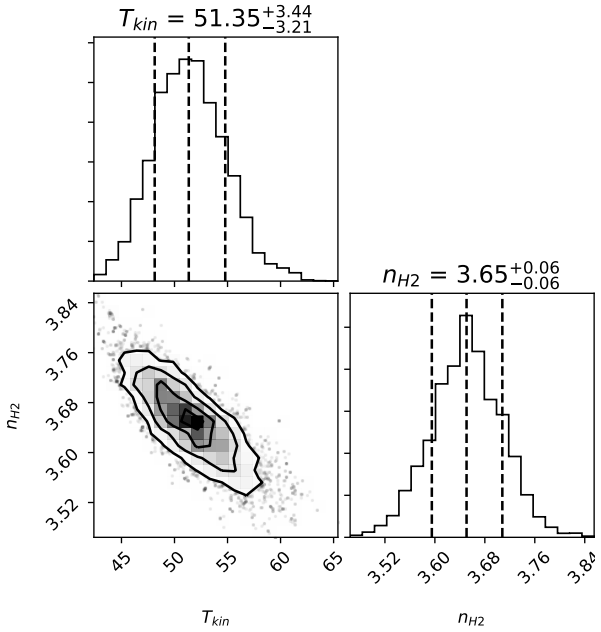

Figure 3.17: An example of a corner plot of the posterior distribution for prestellar clump AGAL333.071. The histograms show marginal probability distribution of kinetic temperature (top) and density in log value (right).

The kinetic temperature and density of the clumps obtained from the model are given in cols. 2 and 3 of Table 3.11. Toward six clumps we were able to obtain solutions to the kinetic temperature and the density of the clumps. They range from 20 to 69 K and 3.8×10^3 to 5.9×10^5 cm^{-3}, respectively. In all clumps the kinetic temperature is larger than the excitation temperature indicating that the HCO$^+$ emission is sub-thermal where $T_{ex} < T_{kin}$ (see Goldsmith & Langer 1999).

Figure 3.18 shows the contour map of the line ratios of HCO$^+$ for an average column density of 1.77×10^{14} cm^{-2} toward the clumps. Clearly, line ratios of HCO$^+$ alone are not sufficient to constrain physical parameters of the clumps. The complexity arises from the fact that each transition lines probe different excitation conditions toward the clumps which are known to have complex physical structures. Observations with angular resolutions higher than in the present work, eg., ALMA, have shown that clumps harbor complex substructures within them (eg., Neupane et al. 2020). Since the emission in different molecular lines originate from regions with different densities and excitation conditions, the physical parameters derived above corresponds to average values of the regions traced by HCO$^+$ specie.

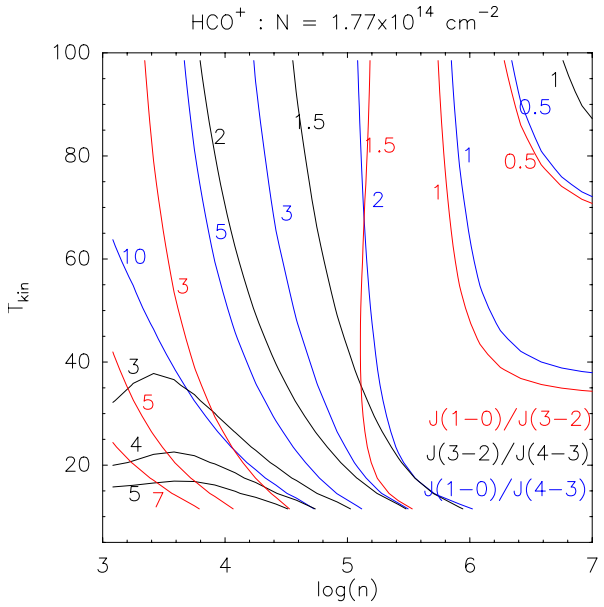

Figure 3.18: Contour map of model line ratios of $J = 1 \rightarrow 0$, $J = 3 \rightarrow 2$ and $J = 4 \rightarrow 3$ transition lines of HCO^+ for an average column density of 1.77×10^{14} cm^{-2}. Contour values are labeled in different color.

3.5.5 Line asymmetries

To investigate the presence of infalling or outflowing motions within the clumps, in this section we analyse the profiles of the two most optically thick lines: HCO^+ and HCN $J = 3 \rightarrow 2$. The spectral signature of such motions in an optically thick line is an asymmetric double peaked profile, with a stronger blueshifted peak for infalling motions and a stronger redshifted peak for expansion motions (e.g., Anglada et al. 1987; Mardones et al. 1997; De Vries & Myers 2005). Following Mardones et al. (1997), we compute a unit-less line shift parameter (δV) defined as the velocity difference between the peaks in optically thick (V_{thick}) and thin (V_{thin}) lines divided by the line width of the latter (Δv_{thin}),

$$\delta V = \frac{V_{thick} - V_{thin}}{\Delta v_{thin}}. \tag{3.8}$$

Cols. 6 and 7 of Table 3.12 lists the line shift parameters computed using the peak velocities of HCO^+ $J = 3 \rightarrow 2$ and HCN $J = 3 \rightarrow 2$ lines, respectively. As optically thin parameters (V_{thin} and Δv_{thin}) we use those determined from a Gaussian fit to the $H^{13}CO^+$ $J = 3 \rightarrow 2$ line. The error in the line shift parameter, which is dominated by the error in the determination of the peak velocity of the optically thick line, is typically 0.25 (c.f., Mardones et al. 1997, He et al. 2015, 2016). Hereafter, we consider that the gas in a clump is infalling if $\delta V \leq -0.25$ and expanding if $\delta V \geq 0.25$.

Table 3.12: Line shift parameter.

Clump	$H^{13}CO^+$		HCO^+	HCN	Shift parameter		Type[a]	Remark[b]
	V(km s^{-1})	ΔV(km s^{-1})	V_{peak}(km s^{-1})	V_{peak}(km s^{-1})	δV_{HCO^+}	δV_{HCN}		
Quiescent/Prestellar clumps								
AGAL331.639+00.501_S	-52.15	2.28	-53.5	-53.9	-0.59	-0.77	BB	
AGAL332.737-00.621_S	-50.14	1.93	-50.6	-50.9	-0.24	-0.44	- B	H
AGAL332.892-00.569_S	-56.91[c]	1.15[c]	-57.3	-57.3	-0.34	-0.35	BB	H, Y
AGAL333.014-00.521_S	-53.22	2.18	-54.1	-52.8	-0.40	0.19	B -	
AGAL333.016-00.751_S	-55.59	3.82	-55.8	-56.8	-0.06	-0.32	- B	
AGAL333.071-00.399_S	-54.49	2.99	-52.5	-52.6	0.67	0.63	RR	H
AGAL333.179-00.396_S	-50.31	2.24	-50.0	-50.2	0.14	0.06	- -	H
AGAL333.198-00.352_A	-49.49	1.53	-49.6	-50.0	-0.07	-0.33	- B	
AGAL333.449-00.182_S	-44.06	4.30	-45.7	-44.4	-0.38	-0.08	B -	H, Y
AGAL333.481-00.224_S	-48.77	1.50	-49.8	–	-0.69	–	B -	
AGAL333.566-00.296_S	-46.40	1.70	-46.2	-46.7	0.11	-0.20	- -	
AGAL333.669-00.349_S	-48.42	1.93	-48.2	-47.9	0.11	0.27	-R	
AGAL335.592+00.184_S	-49.71	1.23	-49.1	-48.8	0.49	0.75	RR	H
AGAL340.179-00.242_S	-53.10	1.46	-54.2	-53.4	-0.76	-0.21	B -	H, Y
AGAL340.232-00.146_S	-50.47	1.40	-49.8	-50.2	0.48	0.22	R -	H, Y
AGAL340.301-00.402_S	-50.54	1.38	-50.6	-49.9	-0.04	0.46	- R	H
AGAL340.304-00.376_S	-51.77	1.38	-50.5	-50.0	0.92	1.28	RR	H
AGAL340.398-00.396_S	-46.09	1.42	-46.6	–	-0.36	–	B -	
AGAL341.181-00.277_S	-44.10	1.32	-43.9	-45.0	0.15	-0.69	- B	H, Y
AGAL341.196-00.221_S	-41.38	2.66	-43.8	-44.9	-0.91	-1.32	BB	
Protostellar clumps								
AGAL304.886+00.636_S	-36.22	1.34	-36.5	-36.4	-0.21	-0.14	- -	H, Y
AGAL309.154-00.349_S	-40.97	2.51	-41.7	-42.0	-0.29	-0.41	BB	H, Y
AGAL309.236-00.457_S	-41.01	1.99	-40.7	-40.9	0.16	0.06	- -	
AGAL318.049+00.086_S	-49.89	2.83	-50.2	-51.9	-0.11	-0.71	- B	
AGAL322.158+00.636_S	-57.17	4.53	-58.6	-59.5	-0.32	-0.52	BB	
AGAL331.724-00.204_S	-47.54	3.13	-48.2	-45.3	-0.21	0.72	- R	

AGAL332.226-00.536_S	-52.34	1.56	-53.2	-52.1	-0.55	0.19	B -	H
AGAL332.281-00.547_S	-52.89	2.10	-51.8	-51.2	0.52	0.81	RR	H
AGAL332.559-00.147_S	-46.85	1.44	-46.9	-47.6	-0.01	-0.52	- B	H, Y
AGAL332.559-00.591_S	-50.35	1.96	-48.8	-47.6	0.79	1.40	RR	
AGAL332.604-00.167_S	-46.37	3.27	-45.7	-45.0	0.21	0.42	- R	H, Y
AGAL332.812-00.701_S	-53.45	1.95	-53.0	-52.7	0.23	0.38	- R	H
AGAL332.942-00.686_S	-49.46	3.66	-47.9	-46.3	0.43	0.86	RR	
AGAL332.986-00.489_S	-52.81	2.37	-52.9	-52.2	-0.04	0.26	- R	H
AGAL332.999-00.639_S	-48.12	2.28	-48.1	-49.6	0.01	-0.65	- B	H, Y
AGAL333.076-00.559_S	-56.34	2.62	-57.2	-57.9	-0.32	-0.60	BB	
AGAL333.314+00.106_S	-46.57	3.55	-45.3	-44.5	0.36	0.58	RR	H
AGAL333.721-00.207_S	-46.84	1.61	-47.2	-47.2	-0.22	-0.22	- -	
AGAL335.284-00.132_S	-45.11	2.36	-43.8	-43.1	0.55	0.86	RR	H
AGAL335.586-00.291_S	-46.71	3.68	-47.9	-49.5	-0.32	-0.76	BB	H, Y
AGAL336.958-00.977_S	-44.65	2.40	-43.8	-42.9	0.36	0.73	RR	
AGAL337.098-00.929_S	-41.91	2.09	-42.0	-41.9	-0.04	0.01	- -	H, Y
AGAL337.612-00.059_S	-50.14	4.40	-51.4	-52.4	-0.29	-0.51	BB	
AGAL337.761-00.339_S	-41.41	2.19	-42.9	-43.2	-0.68	-0.82	BB	H, Y
AGAL339.924-00.084_S	-53.02	2.86	-54.1	-55.5	-0.38	-0.87	BB	H, Y
AGAL340.054-00.244_S	-54.41	4.89	-56.4	-57.3	-0.41	-0.59	BB	H, Y
AGAL341.216-00.236_S	-44.02	3.12	-43.5	-42.4	0.18	0.52	- R	
AGAL341.217-00.212_S	-43.43	2.72	-44.1	-45.0	-0.25	-0.58	BB	H, Y
AGAL341.219-00.259_S	-44.72	2.60	-44.6	-46.7	0.04	-0.76	- B	H, Y
AGAL343.133-00.482_S	-35.91	2.26	-34.9	-33.3	0.44	1.15	RR	
AGAL343.528-00.507_S	-35.06	2.51	-33.7	-32.9	0.54	0.86	RR	H
HII clumps								
AGAL310.014+00.387_S	-40.90	2.44	-41.4	-41.6	-0.20	-0.29	- B	H, Y
AGAL312.108+00.309_S	-48.29	1.73	-48.4	-49.2	-0.06	-0.50	- B	H, Y
AGAL314.264+00.091_S	-51.76	3.10	-52.5	-54.2	-0.24	-0.78	- B	H, Y
AGAL320.676+00.244_S	-59.13	3.64	-59.2	-59.6	-0.02	-0.13	- -	
AGAL331.418-00.356_S	-63.36	2.66	-62.7	-61.6	0.25	0.66	RR	H
AGAL332.094-00.421_S	-57.06	3.26	-55.6	-54.5	0.45	0.79	RR	H

AGAL332.584-00.559_S	-51.29	1.69	-51.3	-49.6	-0.01	1.00	- R	
AGAL333.053+00.029_S	-45.31	1.75	-45.3	-45.8	0.01	-0.28	- B	H
AGAL333.068-00.447_S	-52.91	3.35	-52.6	-50.5	0.09	0.72	- R	H
AGAL335.687-00.812_S	-50.43	1.61	-51.4	-51.8	-0.60	-0.85	BB	
AGAL336.020-00.816_S	-48.06	2.72	-47.4	-46.7	0.24	0.50	- R	
AGAL337.284-00.159_S	-52.24	2.36	-52.5	-49.8	-0.11	1.03	- R	
AGAL340.248-00.374_S	-50.66	2.76	-48.9	-48.0	0.64	0.96	RR	H
AGAL340.401-00.381_S	-46.25	1.25	-44.2	-44.2	1.65	1.65	RR	
AGAL343.689-00.017_S	-34.90	1.92	-34.1	-33.7	0.42	0.65	RR	H
PDR clumps								
AGAL340.319-00.227_S	-46.06[c]	2.37[c]	-45.7	-45.10	0.15	0.41	- R	
Unknown clumps								
AGAL333.103-00.502_S	-57.06	3.48	-56.4	-56.4	0.19	0.20	- -	H
AGAL338.402+00.032_S	-41.40	5.14	-40.8	-41.8	0.12	-0.08	- -	H

[a] Characters B, R and − indicate blue, red and null shift parameters, respectively.
The first entry denotes the shift parameter in HCO^+ and the second denotes the shift parameter in HCN.
[b] H: source in the He et al. (2016) sample. Y: Infall candidate reported by He et al. (2016).
[c] Parameters from HNC $J = 3 \rightarrow 2$ gaussian fit.

Col. 8 of Table 3.12 gives a characterization of the spectra based on the computed shift parameters. The characters B, R and '–' denote, respectively, blue, red and null line shift parameters. The first and second characters refers, respectively, to shift parameters derived from the HCO^+ $J = 3 \rightarrow 2$ and HCN $J = 3 \rightarrow 2$ lines. As a check we visually inspected the spectra in these lines and found that the sign of the line shift is in agreement with that expected from the visually observed self-absorption or shoulder-like line profile. Only a few clumps (e.g., AGAL336.958-00.977_S) which were classified as blue or red shifted from line shift measurements do not show clear signature of self-absorption/shoulder in their HCO^+ and/or HCN profiles (see Figure 3.20). We do not find clumps for which contradictory results (i.e. BR or RB) are drawn from the analysis of the HCO^+ $J = 3 \rightarrow 2$ and HCN $J = 3 \rightarrow 2$ lines. A total of 29 clumps ($\sim 42\%$) show line shift in both lines, of which 13 are blueshifted and 16 are redshifted.

Figure 3.19 plots the line shift parameters determined from the HCO^+ line versus that determined from the HCN line for all clumps in Table 3.12. We find that most of the clumps (60 of 69) exhibit significant (i.e. $|\delta V| \geq 0.25$) line shifts in either the HCO^+ or HCN lines. Of these, 18 are prestellar, 27 are protostellar, 14 are H II clumps (see Table 3.13). Blue and red shifts are detected toward clumps in all evolutionary stages. A similar finding has been reported by Jackson et al. (2019) in a study of HCO^+ $J = 1 \rightarrow 0$ line asymmetry toward 1093 MALT90 clumps. The fraction of clumps in different evolutionary stages showing blue and red line shifts are, respectively, 60% and 30% for quiescent clumps, 48% and 39% for protostellar clumps and 33% and 60% for H II clumps. These results indicate that global collapse is common in quiescent clumps. Infalling gas motions are likely to be reversed in the later stages due to the feedback effects of newly formed massive stars.

The absolute values of the line shifts derived from HCN are typically larger than those derived from HCO^+. Whether this is an indication of HCN and HCO^+ probing different regions of the infalling gas or produced by a larger uncertainty in the determination of the HCN line shift parameter due to its HF structure cannot be discerned at the present stage.

Table 3.13: Summary of the line shift observed in HCO^+ $J = 3 \rightarrow 2$ and HCN $J = 3 \rightarrow 2$ lines toward different evolutionary stage clumps.

Clump type	Number of Clumps								
	Collapse				Expansion				
	[BB]	[BN]	[NB]	Total	[RR]	[RN]	[NR]	Total	[NN]
Pre-stellar	3	5	4	12 (60%)	3	1	2	6 (30%)	2
Proto-stellar	9	1	5	15 (48%)	8	0	4	12 (39%)	4
H II regions	1	0	4	5 (33%)	5	0	4	9 (60%)	1
PDR	0	0	0	0	0	0	1	1	0
Uncertain	0	0	0	0	0	0	0	0	2
Total Number	13	6	13	32 (46%)	16	1	11	28 (41%)	9 (13%)

He et al. (2016) analysed a sample of 732 MALT90 clumps in search of asymmetries in the HCO^+ and HNC $J = 1 \rightarrow 0$ lines. They found that 231 clumps ($\sim$32%) are infall candidates that show blue shift in at least one line. Forty-two of the 73 SuperMALT clumps are within the sample of He et al. (2016) of which twenty of them were reported as infall candidates (see Table 3.13). Toward all clumps common to our sample, eighteen clumps show consistent

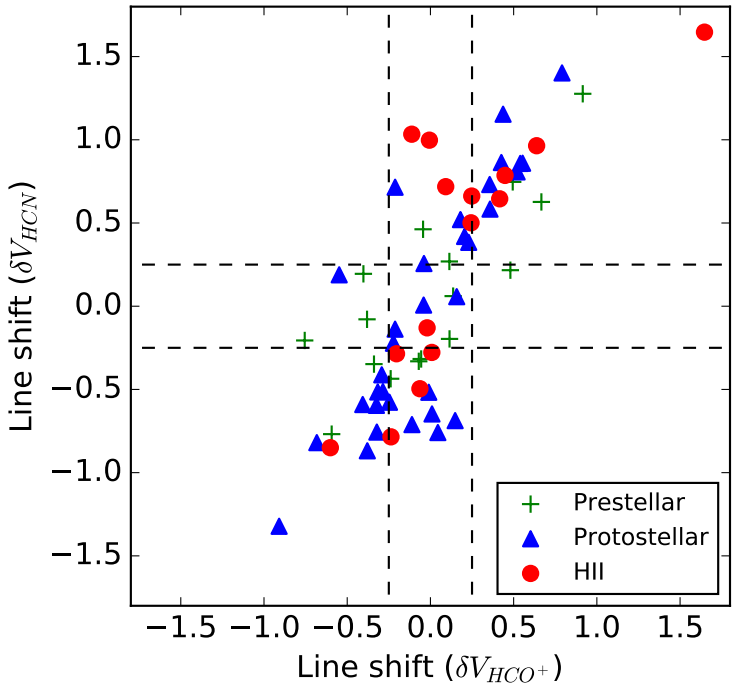

Figure 3.19: HCO^+ $J = 3 \rightarrow 2$ versus HCN $J = 3 \rightarrow 2$ line shift parameters for SuperMALT clumps. Dotted lines represent typical error in the line shift ($\delta V_{error} = 0.25$).

line shift (BB: 7 and RR: 11) in HCO^+ and HCN $J = 3 \rightarrow 2$ lines, twelve and six clumps show blue shift (B−: 3 and −B: 9) and red shift (R−: 1 and −R: 5) in at least one line, respectively, and six clumps show null shift (−−: 6) in both lines. When we only consider the infall candidates reported by He et al. (2016) in our sample, we find that most clumps (16 of 20) exhibit blue shift in at least one line (BB: 7, B−: 2 and −B: 7) indicating that infall motion traced by $J = 3 \rightarrow 2$ lines is consistent with that traced by $J = 1 \rightarrow 0$.

3.5.6 'Uncertain' clumps

Based on the infrared/far-infrared dust emission we were unable to classify two clumps AGAL333.103 and AGAL338.402. To constrain their evolutionary stages, we compare their line fluxes, line ratios and line widths (see Table 5.6 and 3.6) with those of the clumps in different evolutionary stages. The line fluxes and line widths of these 'Uncertain' type clumps are comparable to those of protostellar stages indicating that they are most likely protostellar clumps.

3.6 summary

We present a survey, made using the APEX 12m telescope, of the emission in the $J = 3 \rightarrow 2$ lines of HCO^+, HCN, HNC, N_2H^+ and $H^{13}CO^+$ toward 73 MALT90 clumps in different

evolutionary stages. Twenty-one clumps are in the prestellar or quiescent stage, thirty-four in the protostellar stage, fifteen in the H II stage , one is a PDR clump and two are unclassified (Uncertain). Fifteen clumps at different evolutionary stages are also observed in $J = 4 \rightarrow 3$ lines of HCO^+, HCN, HNC and N_2H^+. The results are summarized as follows:

1) Emission in the $J = 3 \rightarrow 2$ lines of HCO^+, $H^{13}CO^+$, HCN, HNC and N_2H^+ was detected, when observed, toward all clumps, except HCN emission in one clump. Emission in the $J = 4 \rightarrow 3$ lines of HCO^+, HCN and HNC was detected toward most observed clumps and only toward about two third of the clumps (10 of 15) in N_2H^+.

2) The brightness of the emission in all observed molecular lines ($H^{13}CO^+$, HCO^+, HCN, HNC, N_2H^+) increases from early stage clumps (prestellar) to later stage clumps (protostellar and H II). This can be explained by an increase of clump temperature with evolution.

3) The profiles of the emission in the $J = 3 \rightarrow 2$ lines of HCO^+ and HCN show a variety of shapes. While the profiles of prestellar clumps are typically nearly Gaussian, the more evolved (protostellar and H II) clumps show asymmetric features, self absorption, and line wings.

4) The profiles of the emission $J = 3 \rightarrow 2$ lines of $H^{13}CO^+$ and HNC from most clumps are Gaussian. The average value of the line widths in $H^{13}CO^+$ are 2.04±0.82, 2.67±0.87 and 2.42±0.71 km/s for, respectively, prestellar, protostellar and H II clumps and 2.65±1.08, 3.82±1.39 and 3.32±0.81 km/s in HNC. The increase in line widths with evolutionary stage may reflect an increase in turbulence due to star formation activities e.g., ouflows/jets and shocks, or an increase in the gas motions due to the gravitational collapse of the clumps.

5) The morphologies of the emission in the four mapped molecular lines (HCO^+, HCN, HNC, N_2H^+) are at first glance similar, but some differences can be appreciated. The HCO^+ emission is the brightest and most extended. On the other hand, the N_2H^+ emission more closely follows the 870 μm dust emission morphology. We determined sizes from maps of the velocity integrated $J = 3 \rightarrow 2$ emission, using Astrodendro. We find that the sizes in HCO^+ are typically 1.5 times larger than those in N_2H^+. In addition, we find that the N_2H^+ sizes are best correlated with the sizes derived from 870μm emission maps.

6) We find that the ratio of velocity integrated HCO^+ $J = 3 \rightarrow 2$ emission computed over areas enclosing the 30% and 90% levels of the peak emission, is higher for quiescent clumps than for proto-stellar and H II clumps, indicating that the prestellar clumps have shallower density profile than more evolved clumps. This is consistent with the prestellar clumps being in the initial process of building up a central density region and therefore show shallow density profiles while at more advanced stages the clumps have already gathered considerable amounts of gas towards its centers becoming centrally condensed and in the case of H II clumps entering in an active phase of star formation.

7) Ratios of velocity integrated emission. The mean values of the N_2H^+/HCO^+ and HCN/HCO^+ratios in the $J = 3 \rightarrow 2$ and $J = 1 \rightarrow 0$ lines increases from early to late evolutionary stages. The $J = 1 \rightarrow 0$ ratios are, however, larger than that of the $J = 3 \rightarrow 2$ ratios for clumps in all evolutionary stages. On the other hand, the mean values of the HNC/HCO^+ and N_2H^+/HCN ratios in the $J = 3 \rightarrow 2$ and $J = 1 \rightarrow 0$ lines are fairly

constant for clumps in all evolutionary stages. The ratios in the $J = 1 \rightarrow 0$ lines are higher than in the $J = 3 \rightarrow 2$ lines by roughly a factor of 2.

8) Combining the data obtained from the $H^{13}CO^+$ $J = 3 \rightarrow 2$, HCO^+ $J = 3 \rightarrow 2$ and $J = 4 \rightarrow 3$ observations, we estimated the optical depth, excitation temperature and column density of HCO^+ towards 14 clumps at different evolutionary stages. We find that the average values of optical depths, excitation temperatures and column densities increase with evolutionary stage.

9) We model the integrated line intensities of HCO^+ in $J = 3 \rightarrow 2$and $J = 4 \rightarrow 3$ combining the $J = 1 \rightarrow 0$ data from MALT90 survey toward clumps at different evolutionary stages using 1D radiative transfer model RADEX. We were able to estimate kinetic temperature and density of six (of fourteen) clumps. The derived kinetic temperature (T_{kin}) ranges from 20 to 69 K and the density ranges from 3.8×10^3 to 5.9×10^5 cm^{-3} for the clumps. The derived kinetic temperature are larger than excitation temperature ($T_{ex} < T_{kin}$) for all clumps suggesting HCO^+ emission is sub-thermal. Using 1D radiative transfer model, we also demonstrate that density tracer molecules like HCO^+ line ratios may not provide good results in constraining the physical parameters of the clumps that manifest complex substructures within them at higher resolution observations.

10) We used the line shift parameter, defined by $\delta V = (V_{thick} - V_{thin})/\Delta v_{thin}$, to estimate blue-red asymmetries in the HCO^+ and HCN line profiles. Blue and red line shifts are detected towards clumps in all evolutionary stages. The number of clumps showing blue and red line shift are 60% and 30% for prestellar clumps, 48% and 39% for protostellar clumps and 33% and 60% for H II clumps, respectively. This result, showing that global collapse is more common in early type clumps while expansion motions, signposted by the redshifted asymmetries, are more common in later evolutionary stages, may indicate a reversal of line asymmetries as clumps evolve.

Acknowledgements: GG and SN acknowledge support from ANID through Basal project AFB 170002. This publication is based on data acquired with the Atacama Pathfinder Experiment (APEX). APEX is a collaboration between the Max Planck Institut fur Radioastronomie, the European Southern Observatory, and the Onsala Space Observatory.

3.7 Appendix

3.7.1 Central spectra of $J = 3 \rightarrow 2$

The “Central spectra" refers those obtained toward the emission peak of the clumps in 870 μm ATLASGAL images and averaged over a circular region of 20” in diameter.

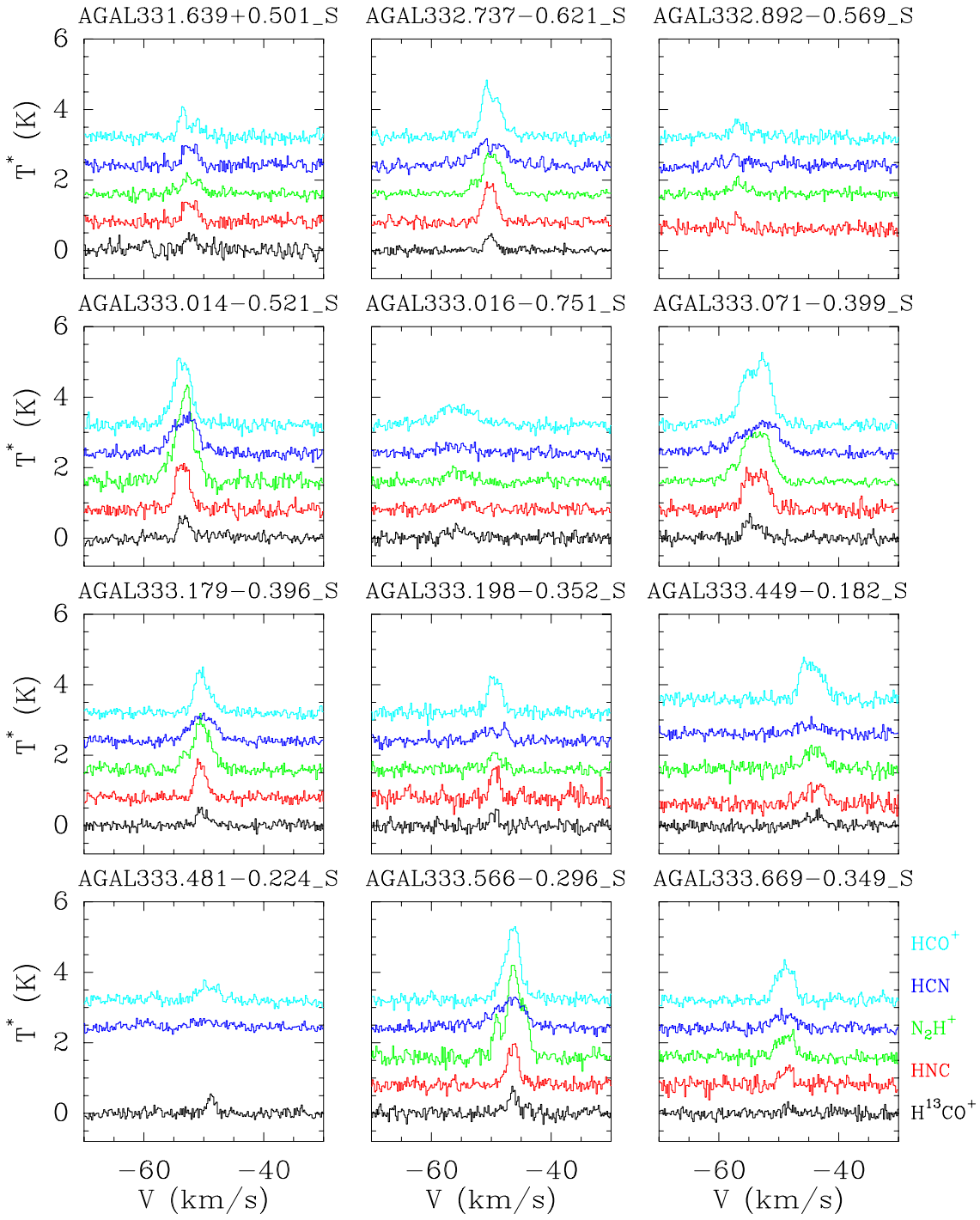

Figure 3.20: Central spectra of the $J = 3 \rightarrow 2$ emission from prestellar clumps. The clump name are given on top of each box. Different lines are plotted in distinct colors and labelled at the bottom right corner of the plot. The $H^{13}CO^+$ antenna temperature are multiplied by factor of three for all clumps.

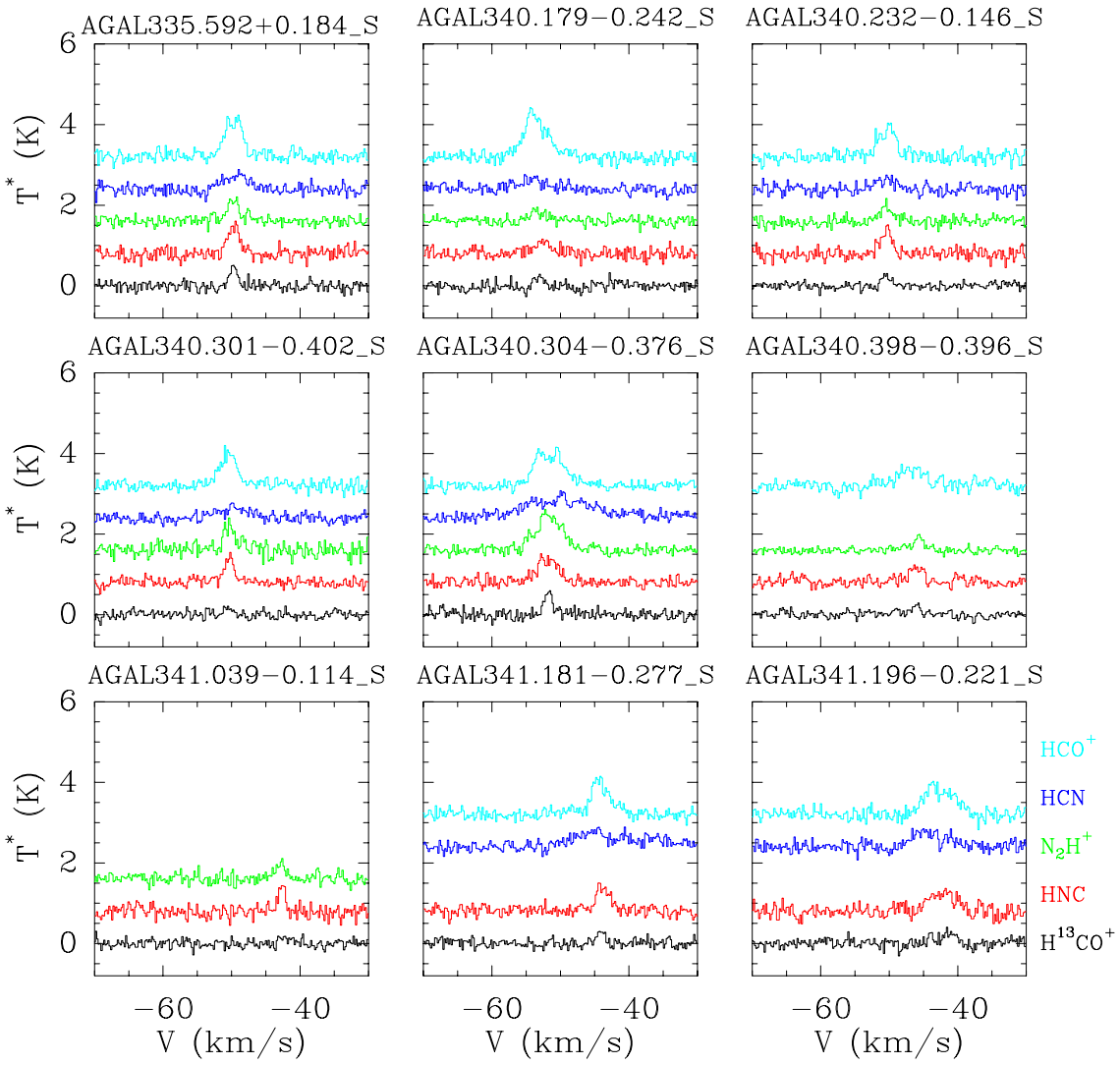

Figure 3.21: Same as Fig. 3.20

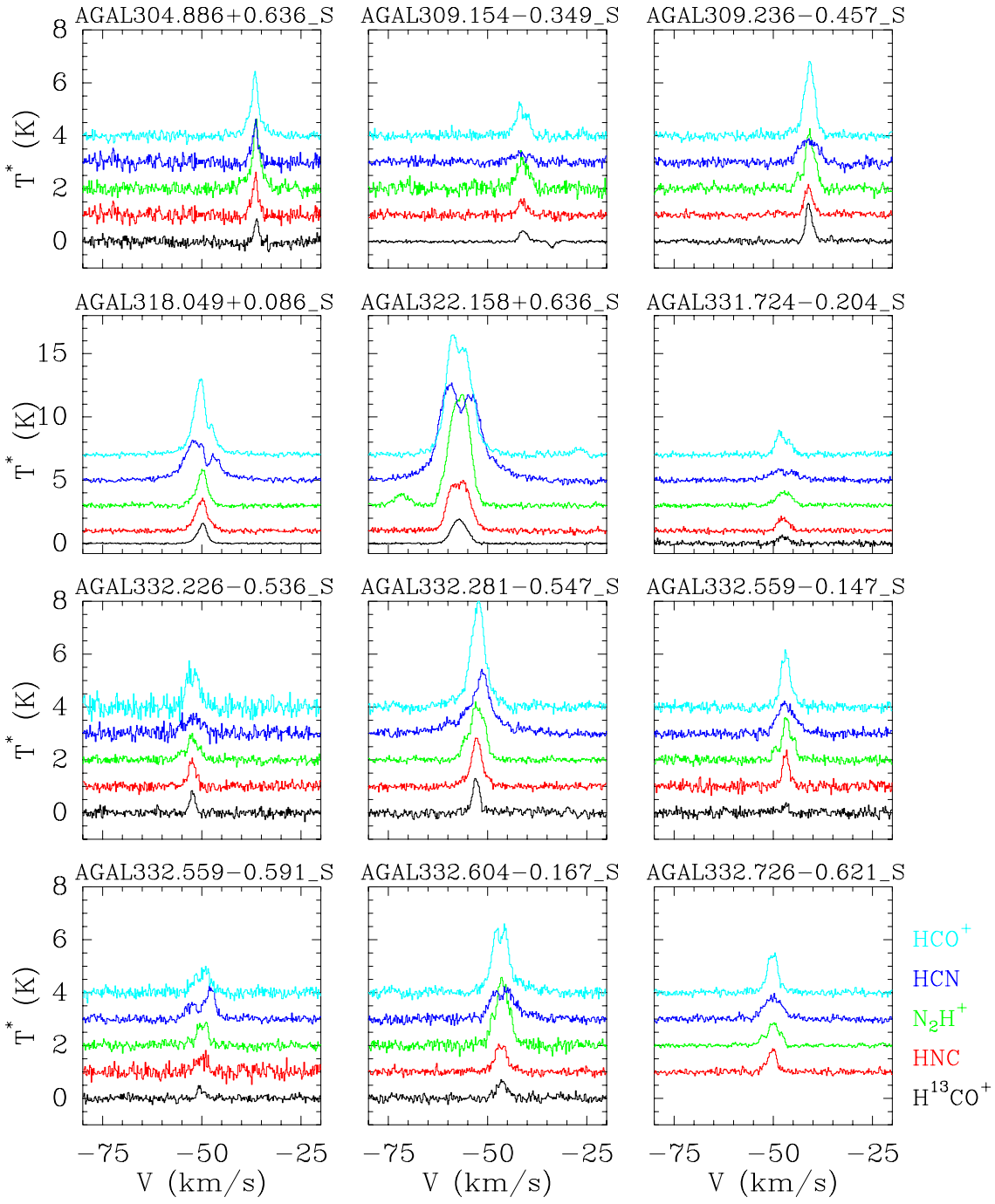

Figure 3.22: Central spectra of the $J = 3 \rightarrow 2$ emission from protostellar clumps. The clump name are given on top of each box. Different lines are plotted in distinct colors and labelled at the bottom right corner of the plot. The $H^{13}CO^+$ antenna temperature are multiplied by factor of three for all clumps.

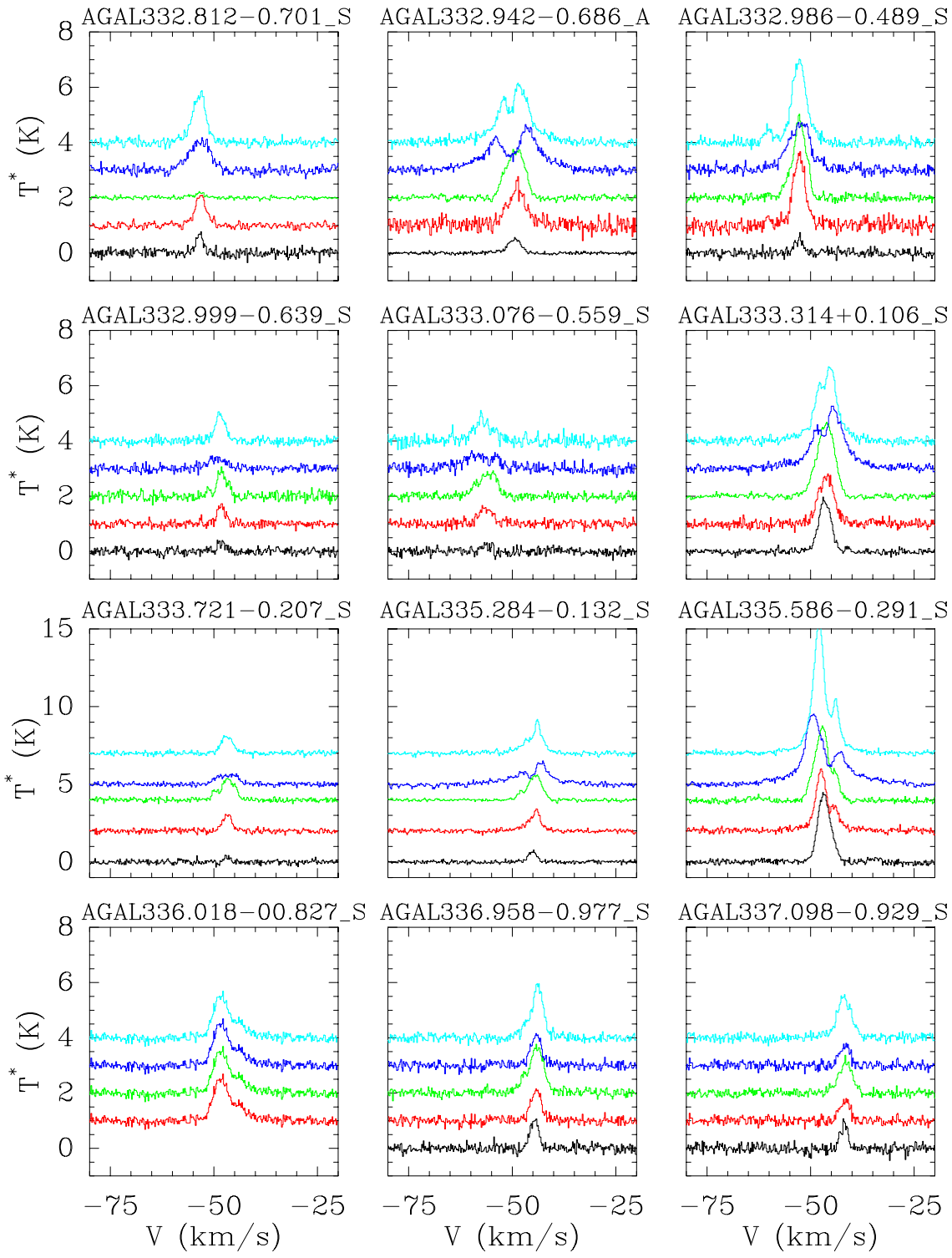

Figure 3.23: Same as Fig. 3.22

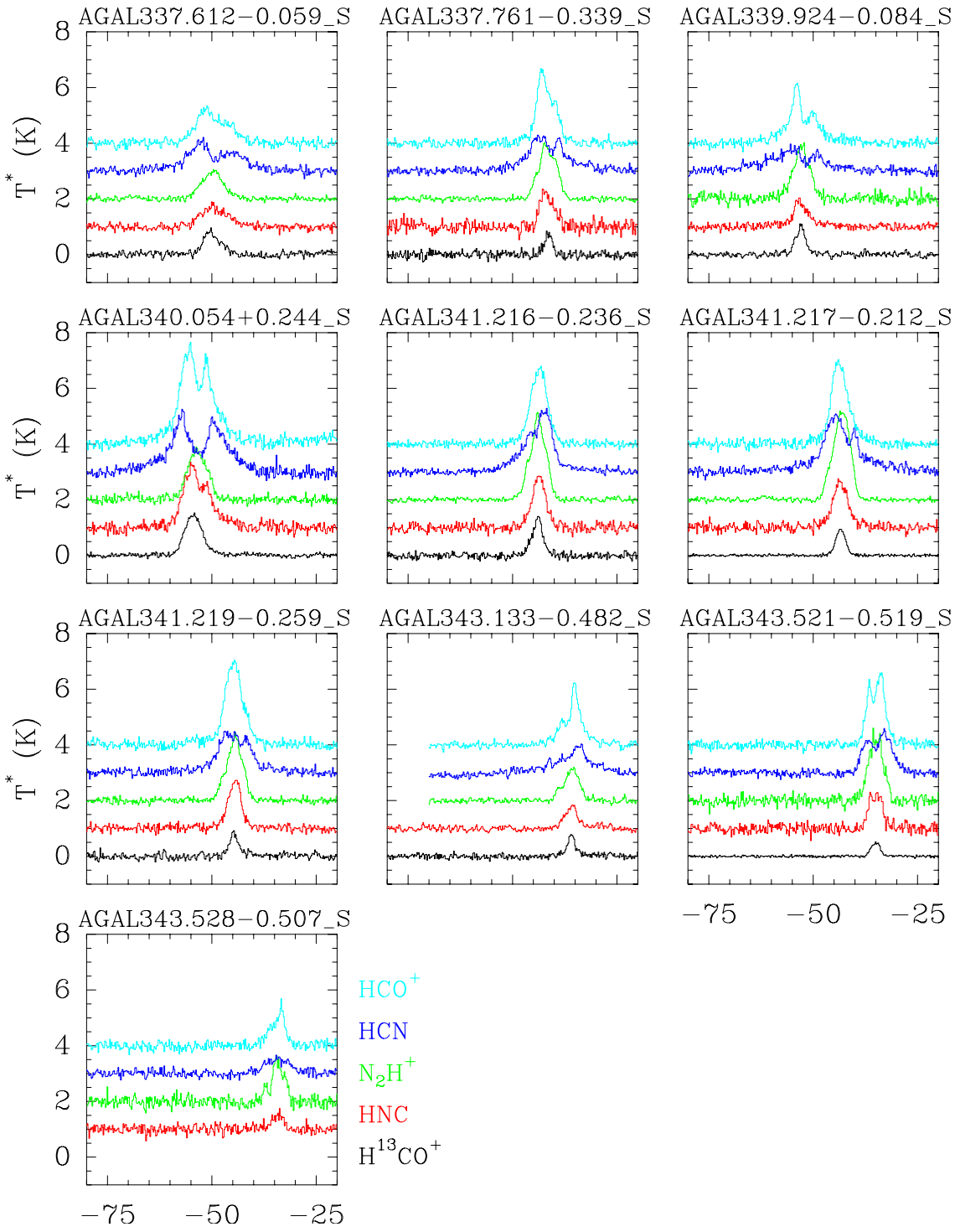

Figure 3.24: Same as Fig. 3.22

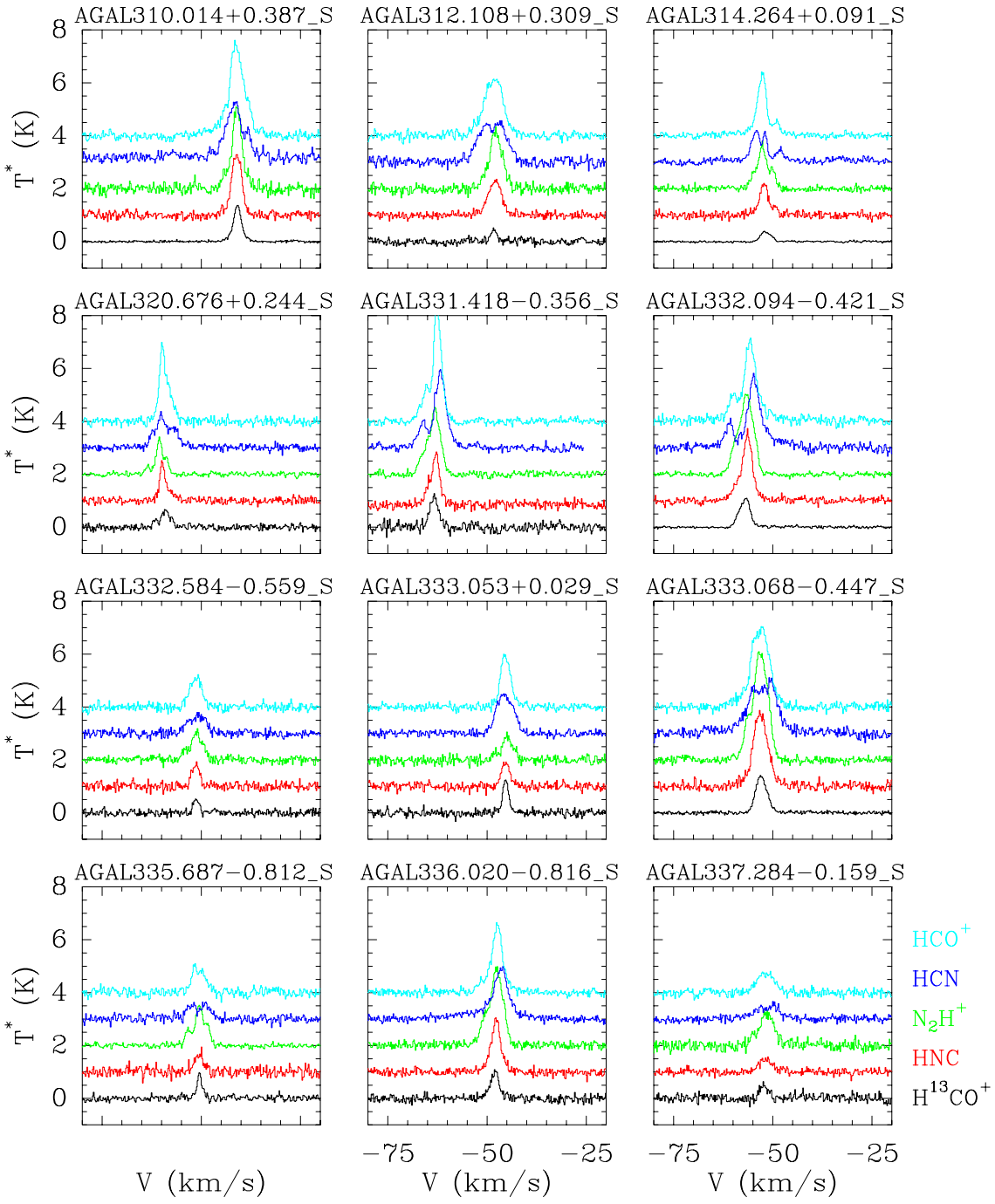

Figure 3.25: Central spectra of the $J = 3 \rightarrow 2$ emission from HII clumps. The clump name are given on top of each box. Different lines are plotted in distinct colors and labelled at the bottom right corner of the plot. The $H^{13}CO^+$ antenna temperature are multiplied by factor of three for all clumps.

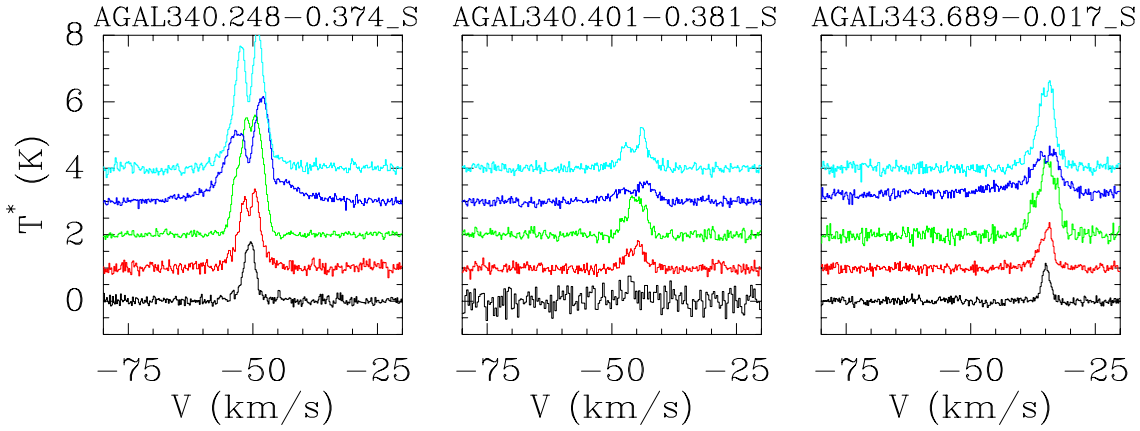

Figure 3.26: Same as Fig. 3.25

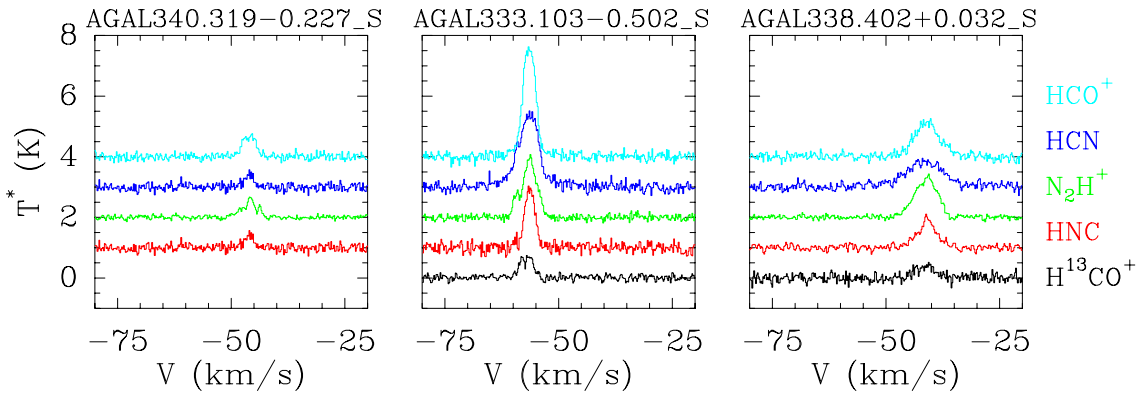

Figure 3.27: Central spectra of the $J = 3 \rightarrow 2$ emission from a PDR clump (left panel) and two unknown type clumps (middle and right panel). The clump name are given on top of each box. Each lines are plotted in different color and labelled at the bottom right corner of the plot. The $H^{13}CO^+$ antenna temperature are multiplied by factor of three for all clumps.

3.7.2 Central spectra of $J = 4 \rightarrow 3$

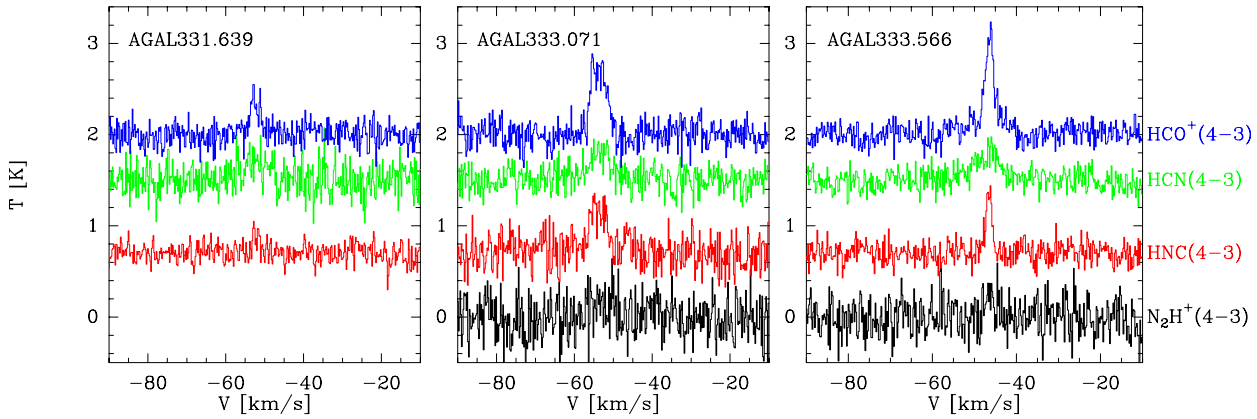

Figure 3.28: Central spectra of the $J = 4 \rightarrow 3$ emission from prestellar clumps. The clump name are given on top of each box. Each lines are plotted in different color and labelled at the bottom right corner of the plot.

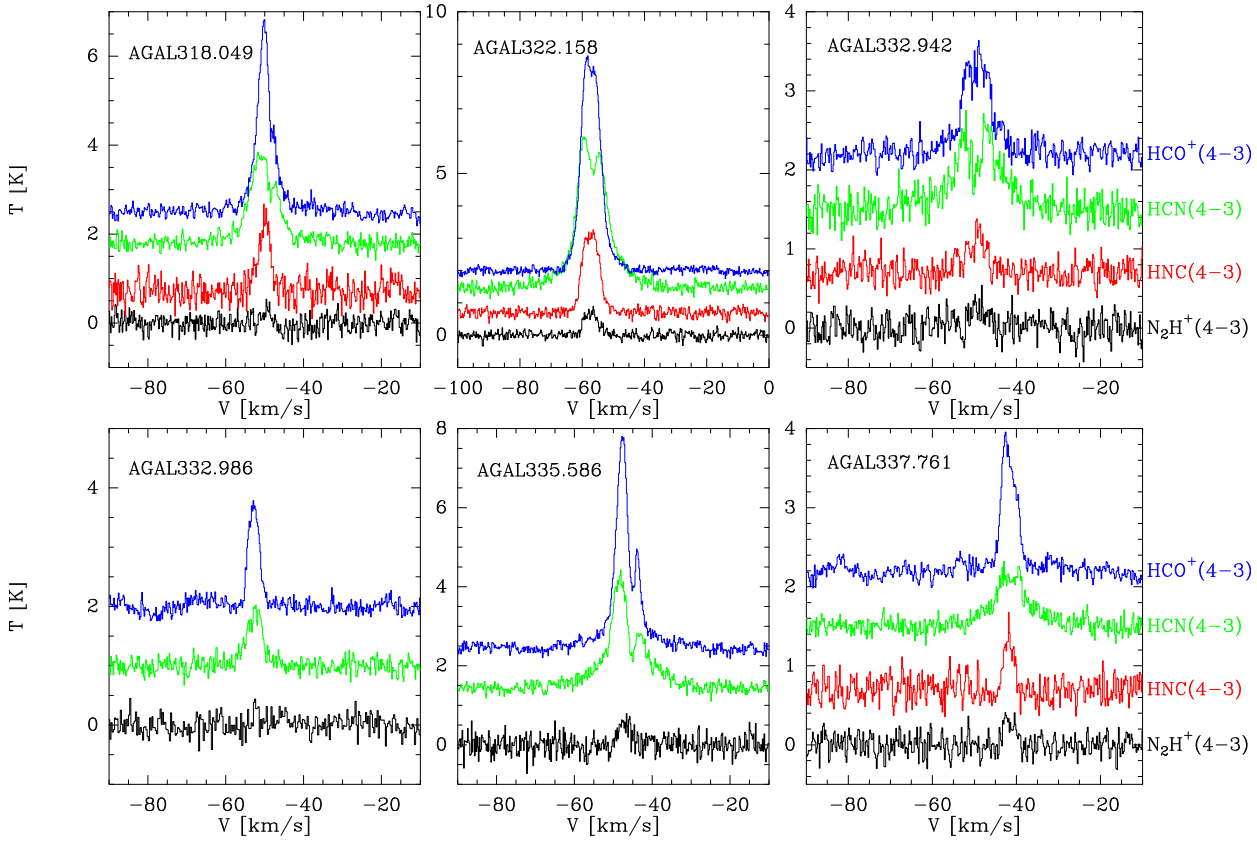

Figure 3.29: Central spectra of the $J = 4 \rightarrow 3$ emission from protostellar clumps. The clump name are given on top of each box. Each lines are plotted in different color and labelled at the bottom right corner of the plot.

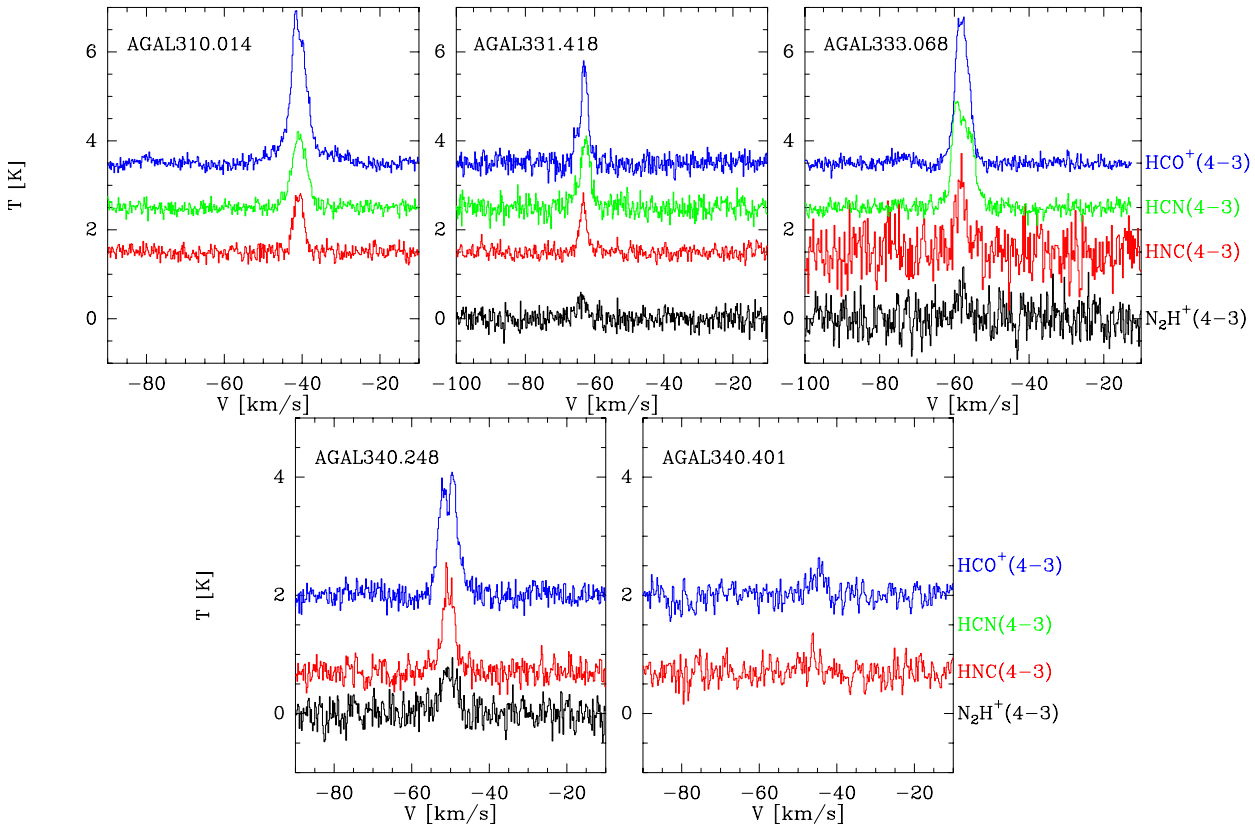

Figure 3.30: Central spectra of the $J = 4 \rightarrow 3$ emission from HII clumps. The clump name are given on top of each box. Each lines are plotted in different color and labelled at the bottom right corner of the plot.

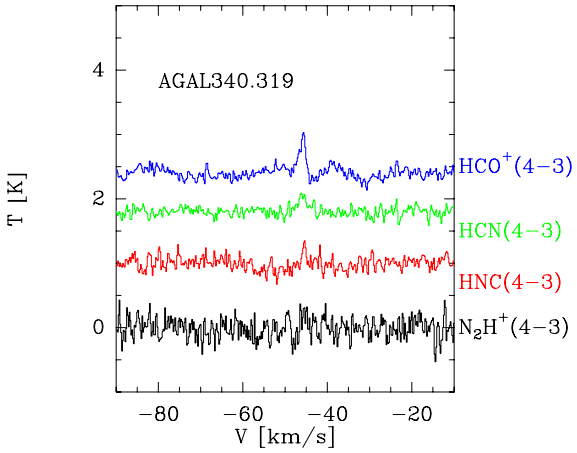

Figure 3.31: Central spectra of the $J = 4 \rightarrow 3$ emission from a PDR clump. The clump name is given on top of the box. Each lines are plotted in different color and labelled at the bottom right corner of the plot.

3.7.3 Contour maps of $J = 3 \rightarrow 2$

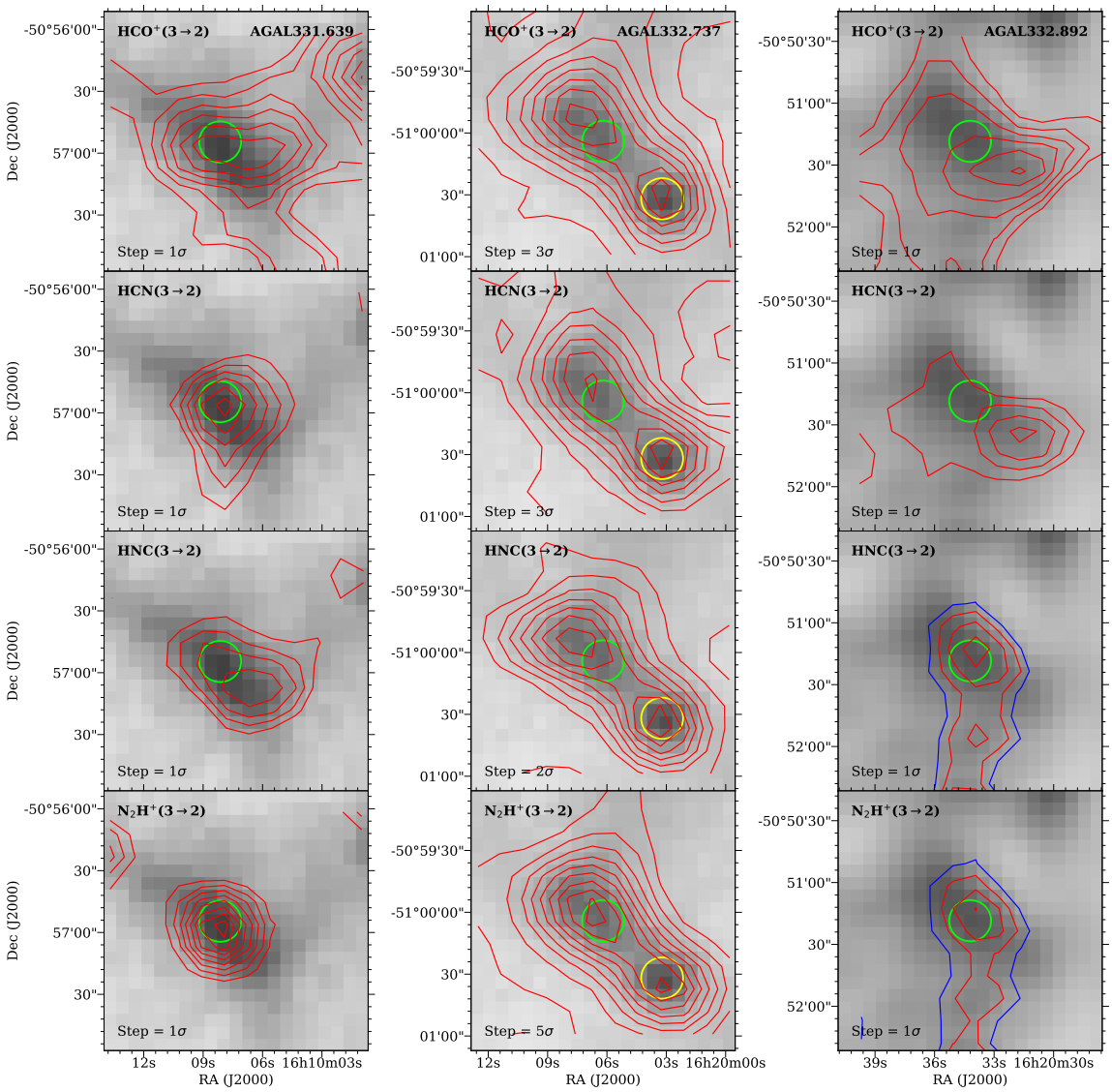

Figure 3.32: Contour maps of the velocity integrated $J = 3 \rightarrow 2$ line emission from prestellar clumps overlayed on grayscale images of the Atlasgal 870μm emission. Left: AGAL331.639. Middle: AGAL332.737 and AGAL332.726. Right: AGAL332.892. From top to bottom: HCO^+, HCN, HNC and N_2H^+ maps. The velocity range of integration for each clump is given in cols 2 of Table 3.6. The lowest contour level correspond to 4 times the rms noise (σ) in the map and the contour step, δI, is given inside each box. Emission line contours drawn at 3σ level are shown in blue. The green circle, with a diameter of $\sim$ 20", indicates the peak position of the clump. Emission line contours drawn at 3σ level are shown in blue.

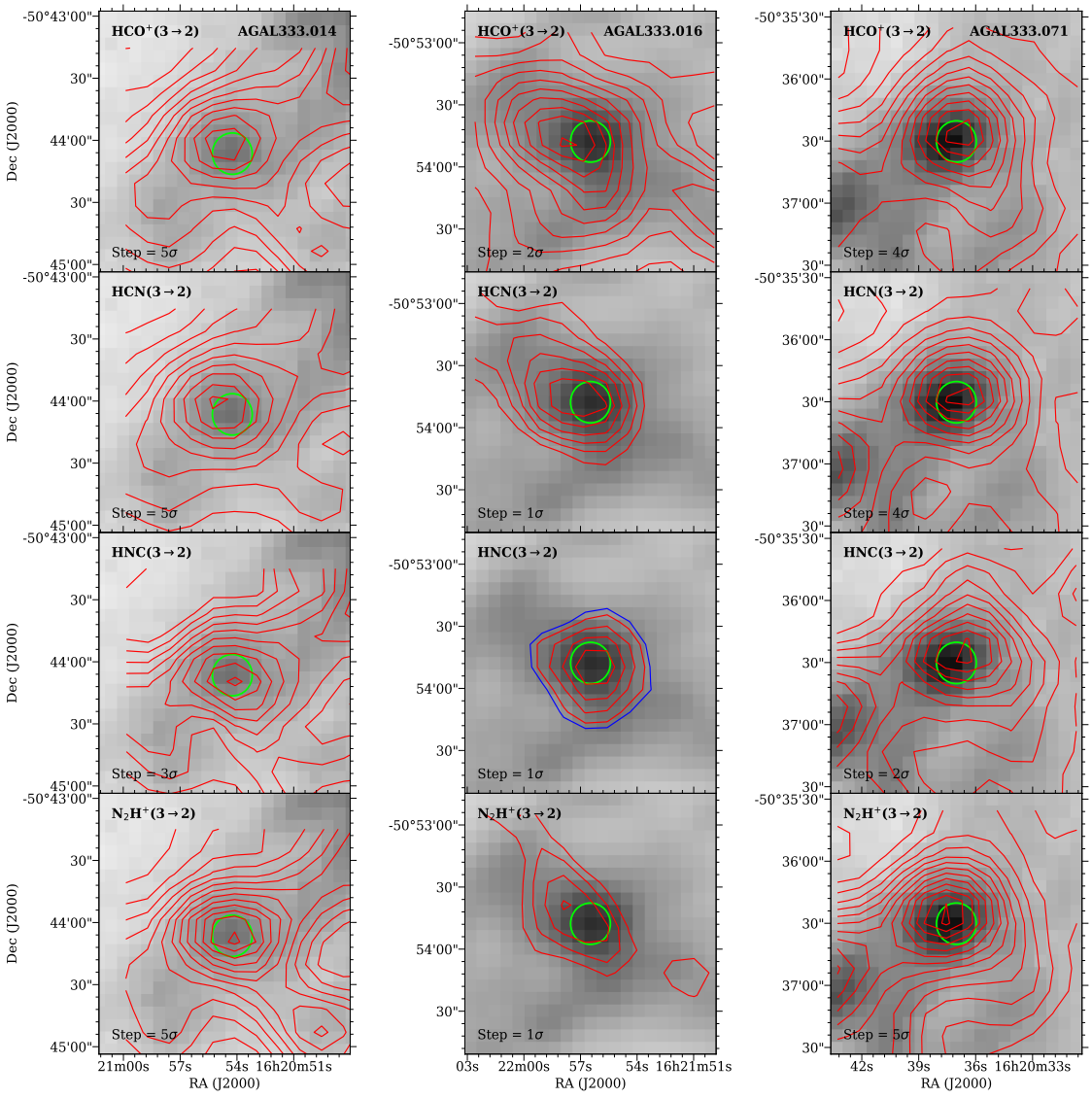

Figure 3.33: Same as Fig. 3.32. Left: AGAL333.014. Middle: AGAL333.016. Right: AGAL333.071.

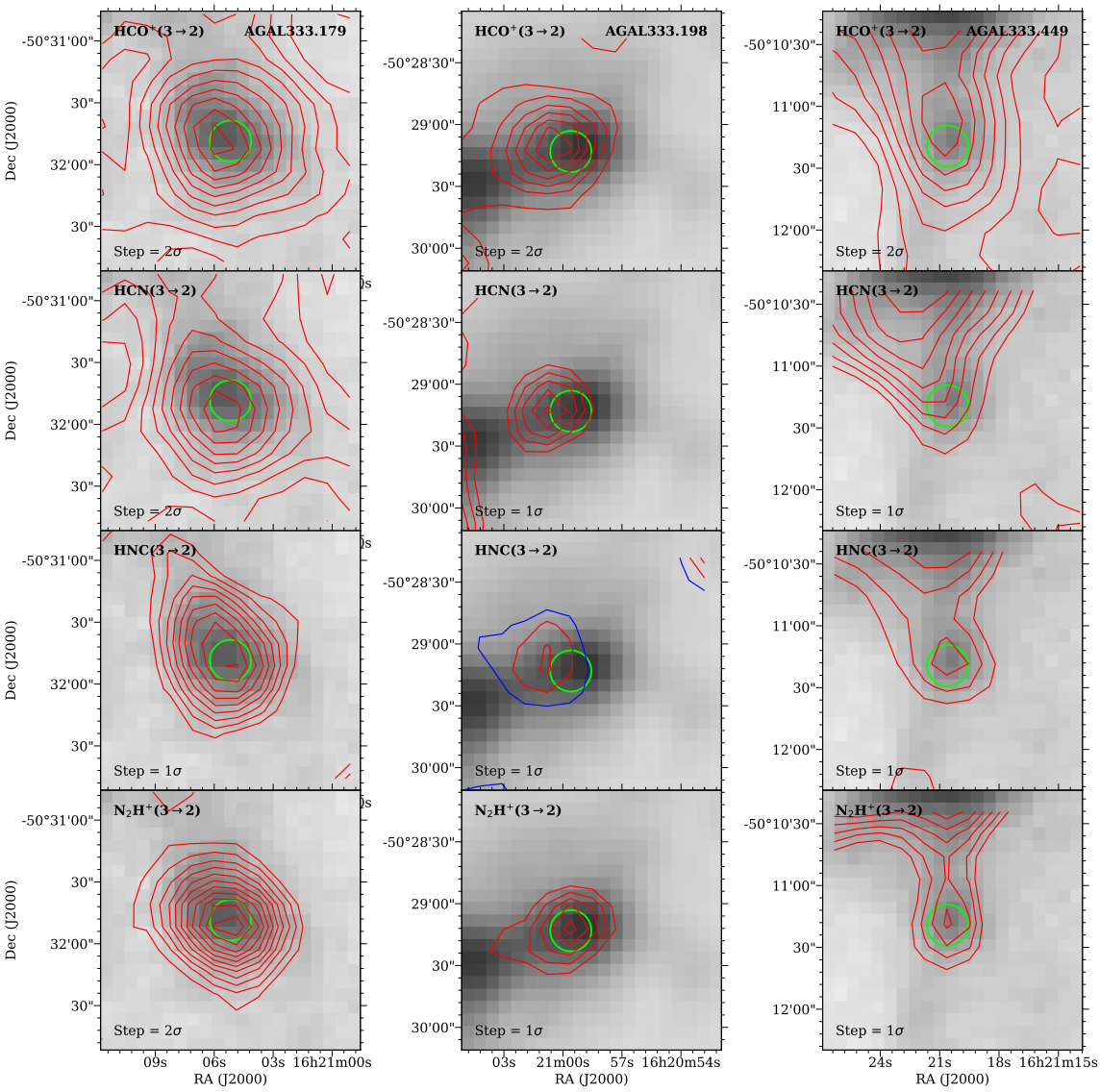

Figure 3.34: Same as Fig. 3.32. Left: AGAL333.179. Middle: AGAL333.198. Right: AGAL333.449

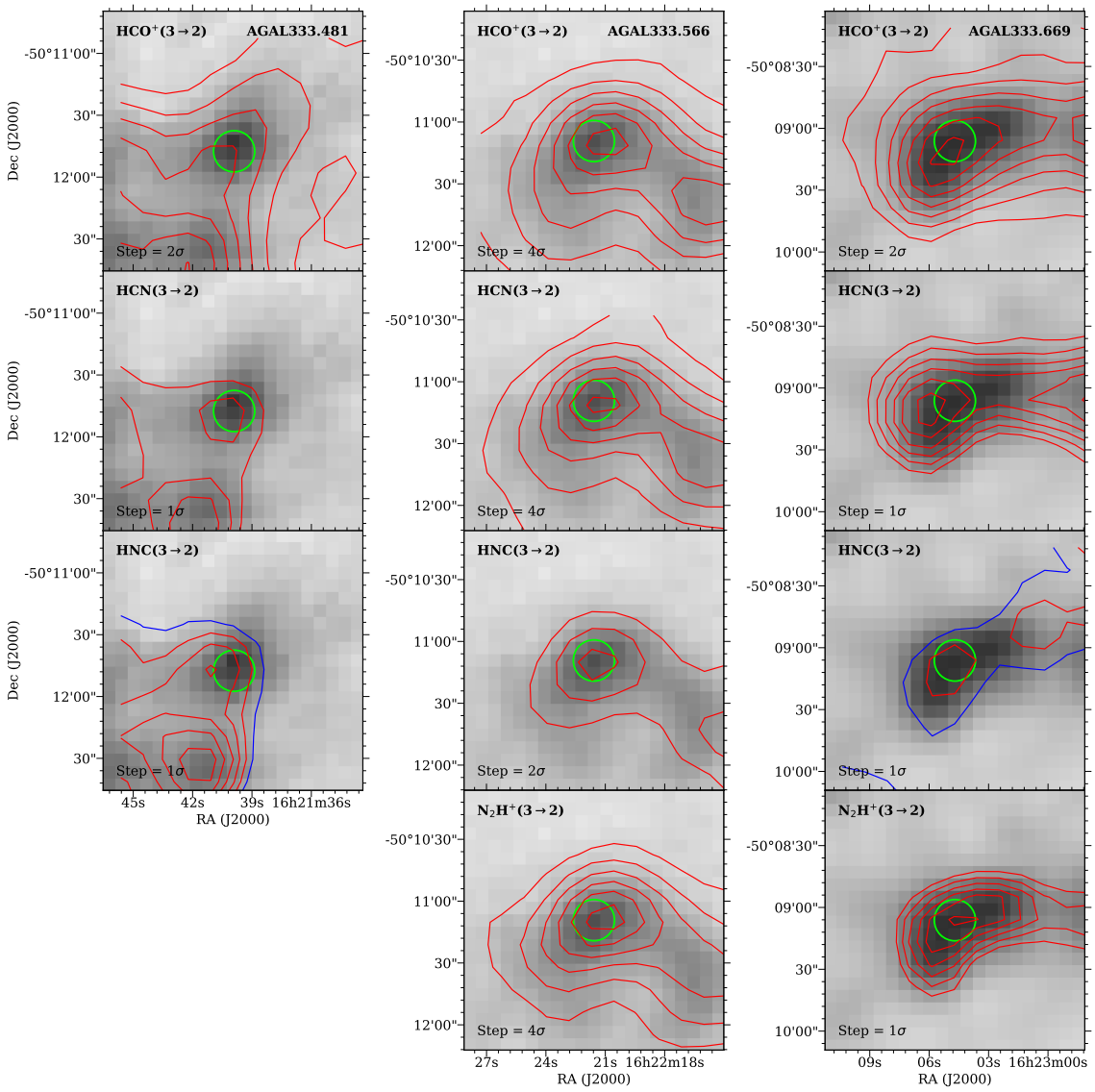

Figure 3.35: Same as Fig. 3.32. Left: AGAL333.481. Middle: AGAL333.566. Right: AGAL333.669.

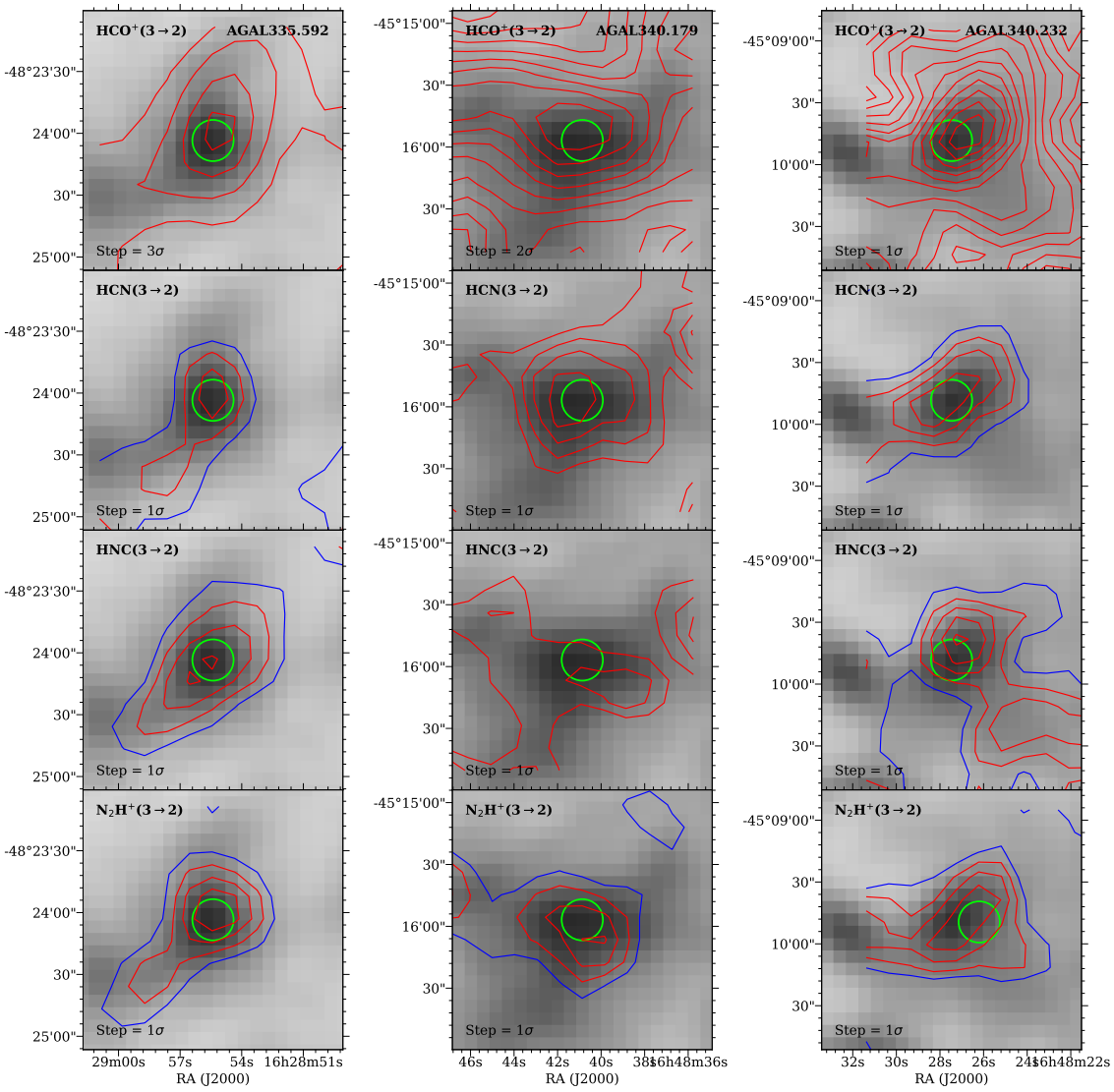

Figure 3.36: Same as Fig. 3.32. Left: AGAL335.592. Middle: AGAL340.179. Right: AGAL340.232.

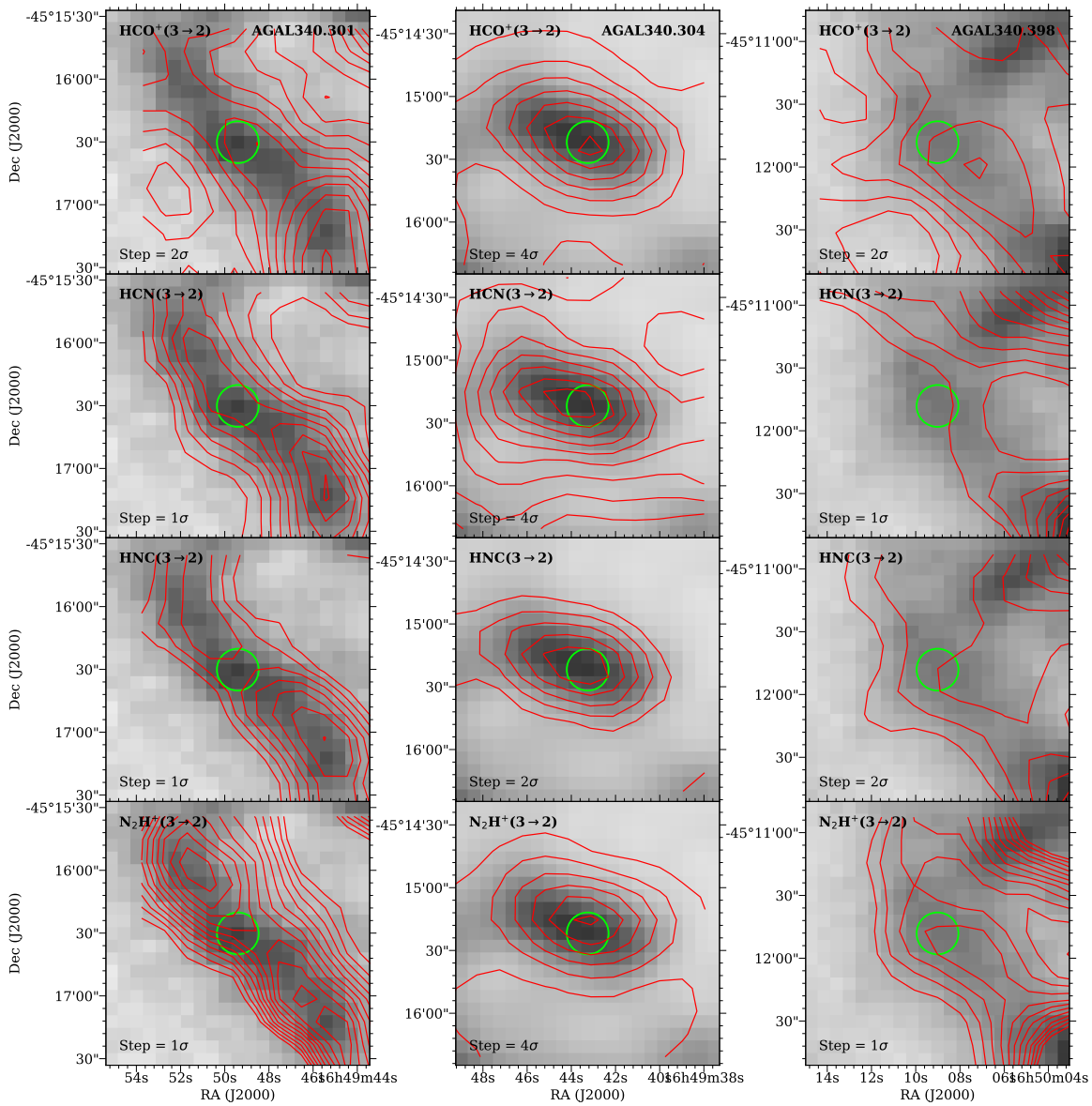

Figure 3.37: Same as Fig. 3.32. Left: AGAL340.301. Middle: AGAL340.304. Right: AGAL340.398.

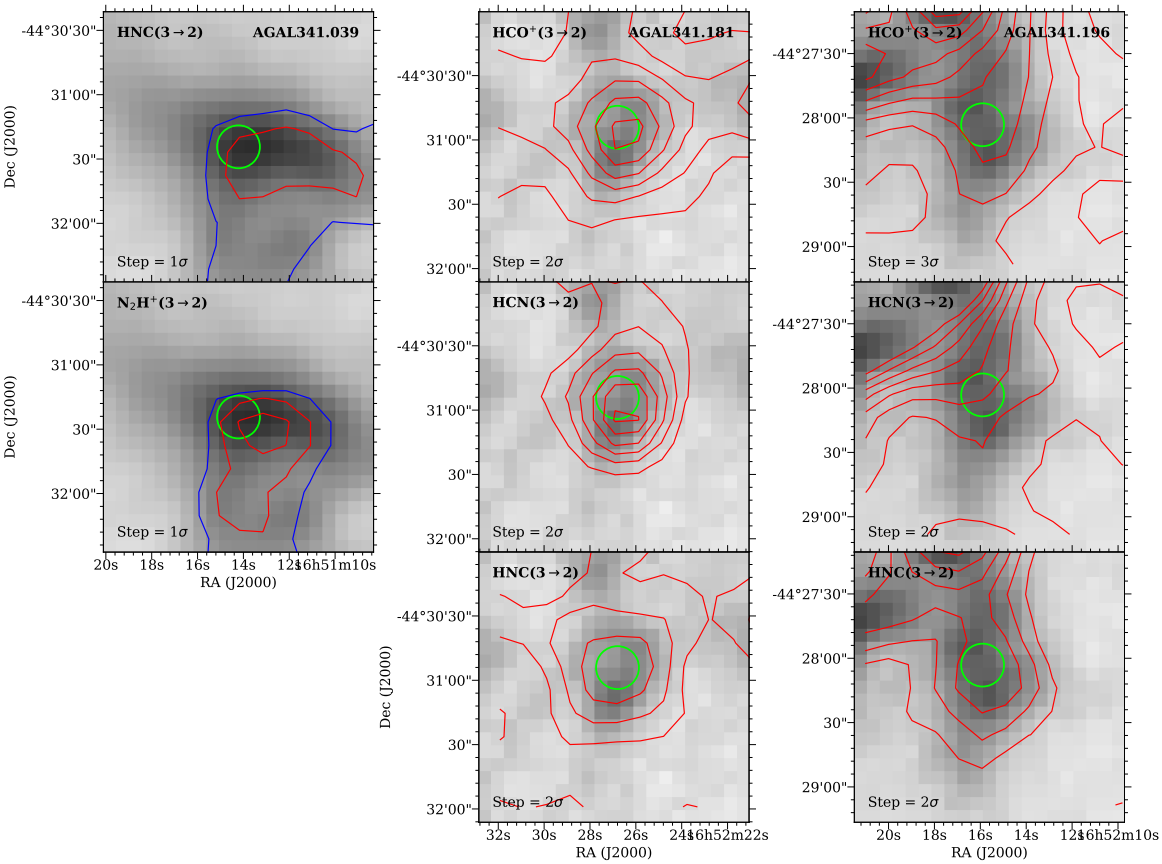

Figure 3.38: Same as Fig. 3.32. Left: AGAL341.039. Middle: AGAL341.181. Right: AGAL341.196.

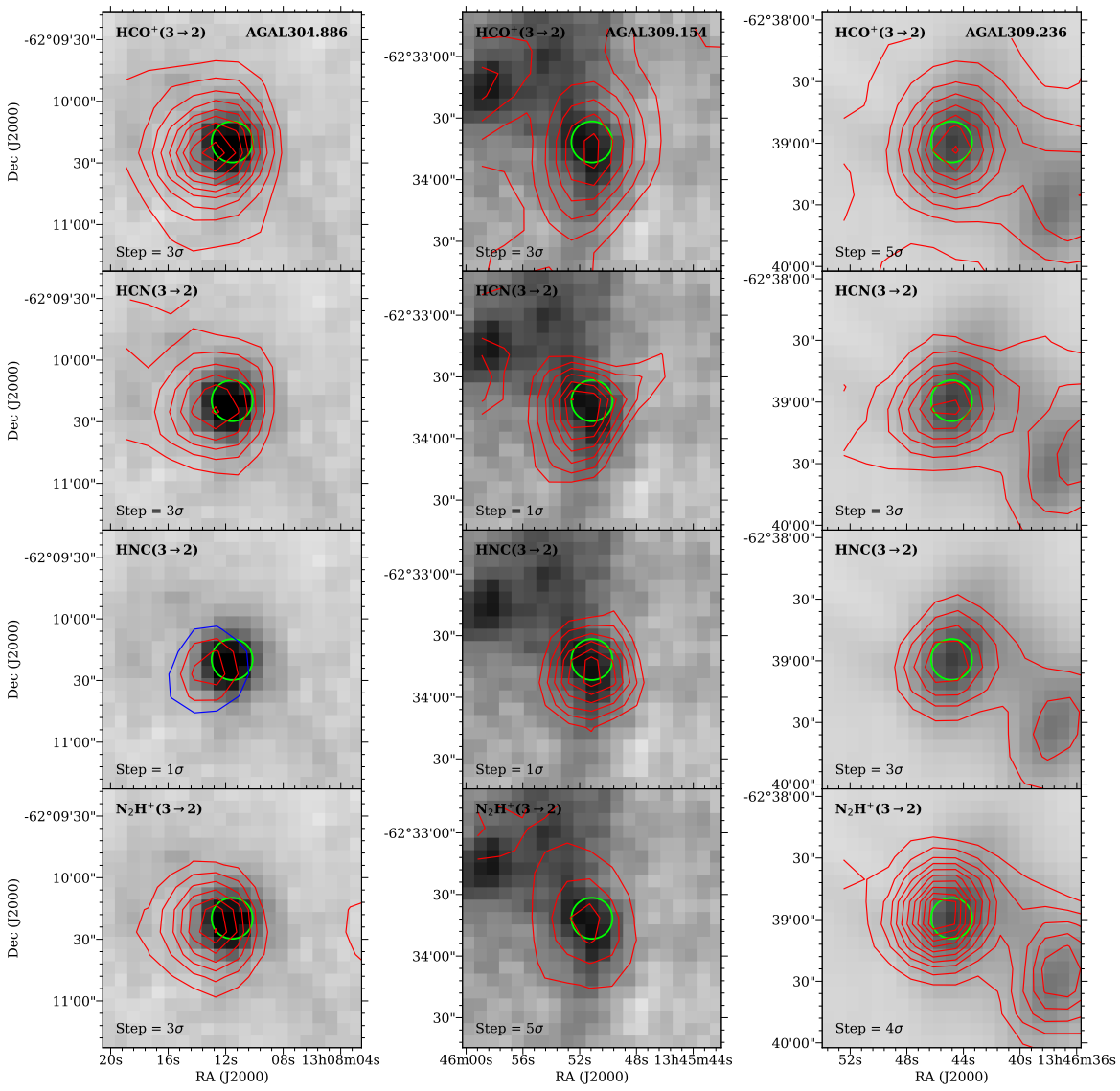

Figure 3.39: Contour maps of the velocity integrated $J = 3 \rightarrow 2$ emissions in four molecular lines overlayed on grayscale Atlasgal 870μm maps toward protostellar clumps. Left: AGAL304.886. Middle: AGAL309.154. Right: AGAL309.236. rom top to bottom: HCO^+, HCN, HNC and N_2H^+ maps. The velocity ranges of integration for each clumps are given in col. 2 of Table 3.6. Clump names and species are given inside each box. The lowest contour levels correspond to the 4σ level and the steps (δI) are given inside each box. Emission line contours drawn at 3σ level are shown in blue. The green/yellow circles in each maps, of size ~ 20", show peak position of the clumps.

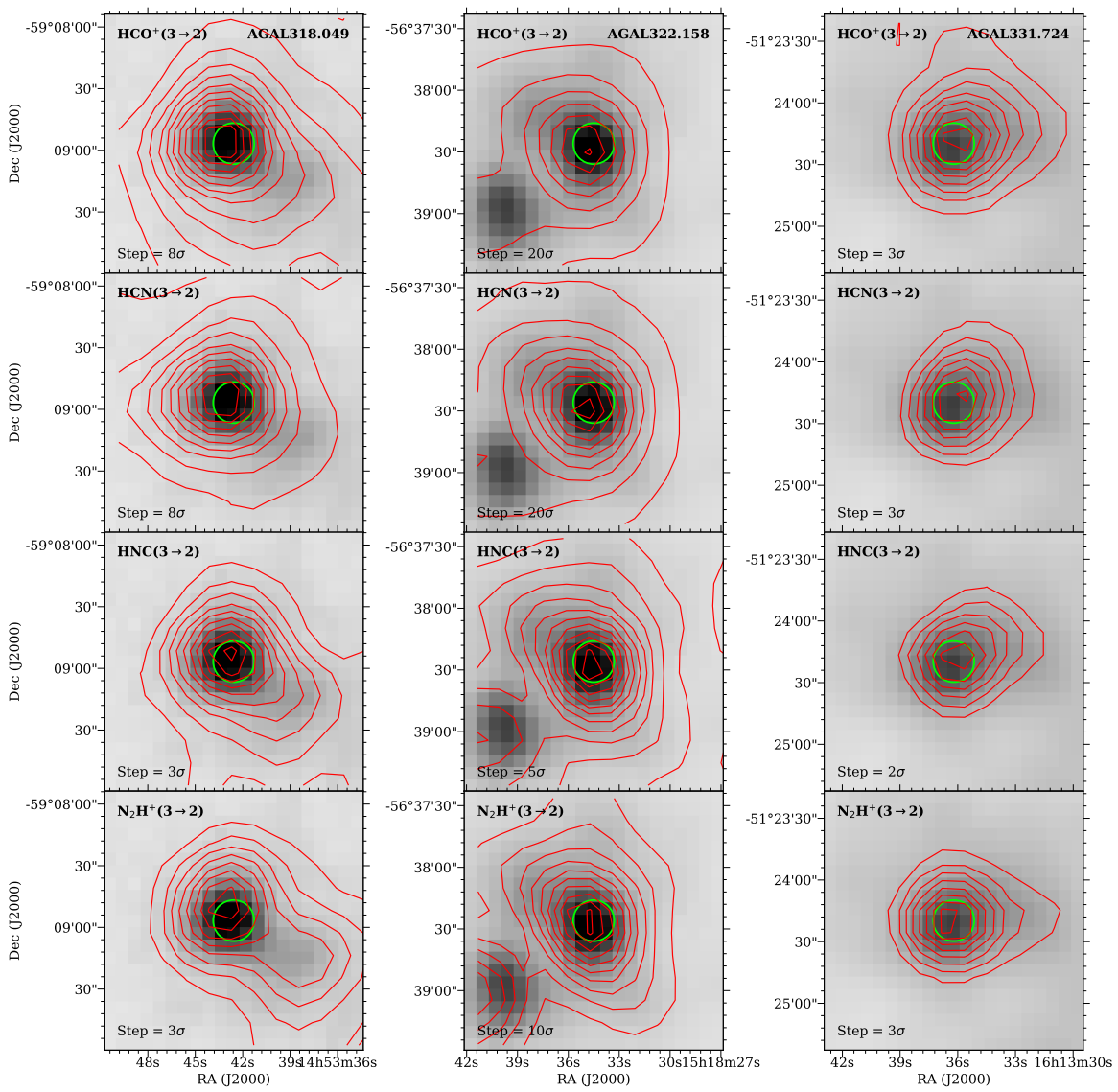

Figure 3.40: Same as Fig. 3.39. Left: AGAL318.049. Middle: AGAL322.158. Right: AGAL331.724.

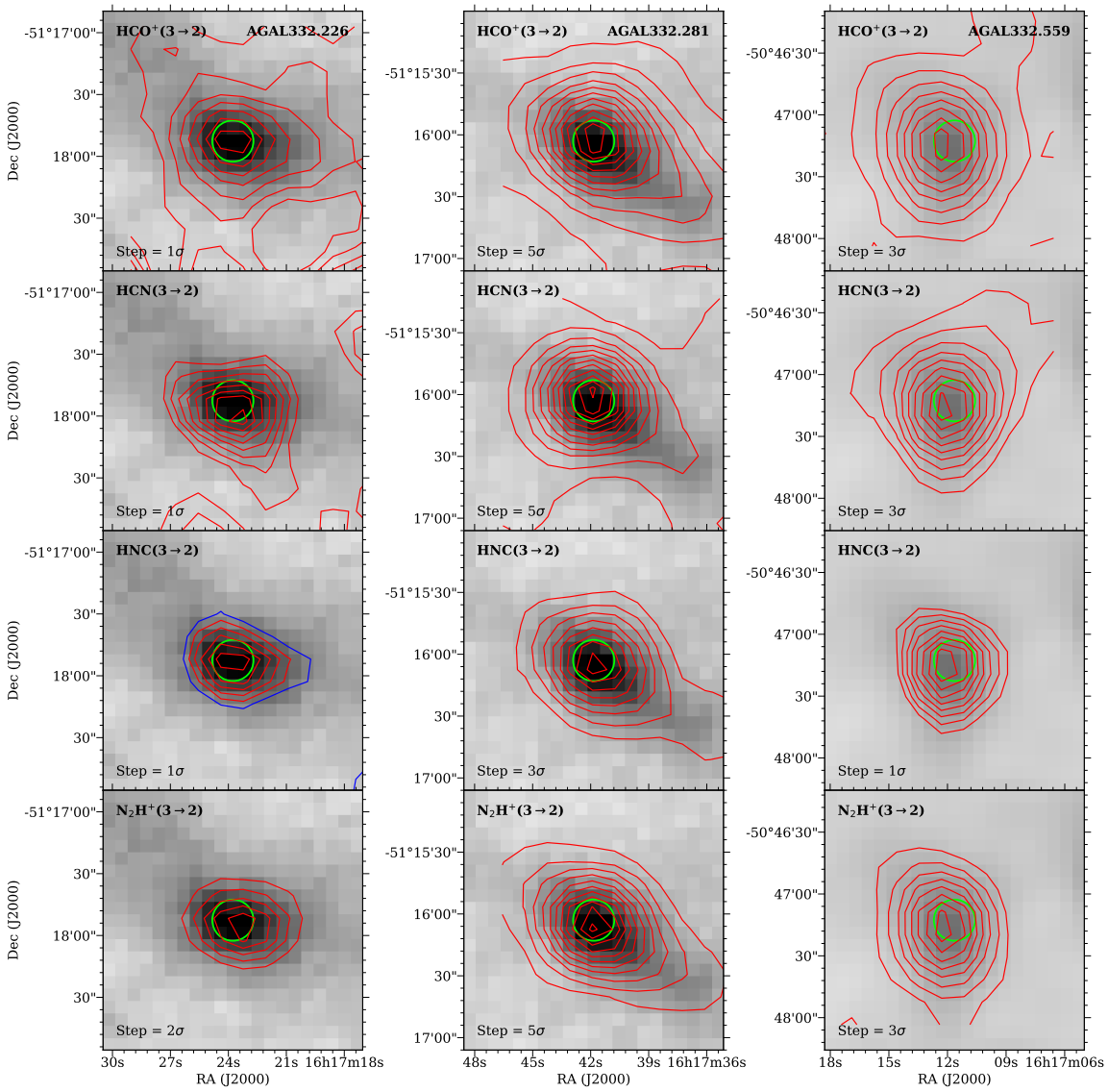

Figure 3.41: Same as Fig. 3.39. Left: AGAL332.226. Middle: AGAL332.281. Right: AGAL332.559-00.147.

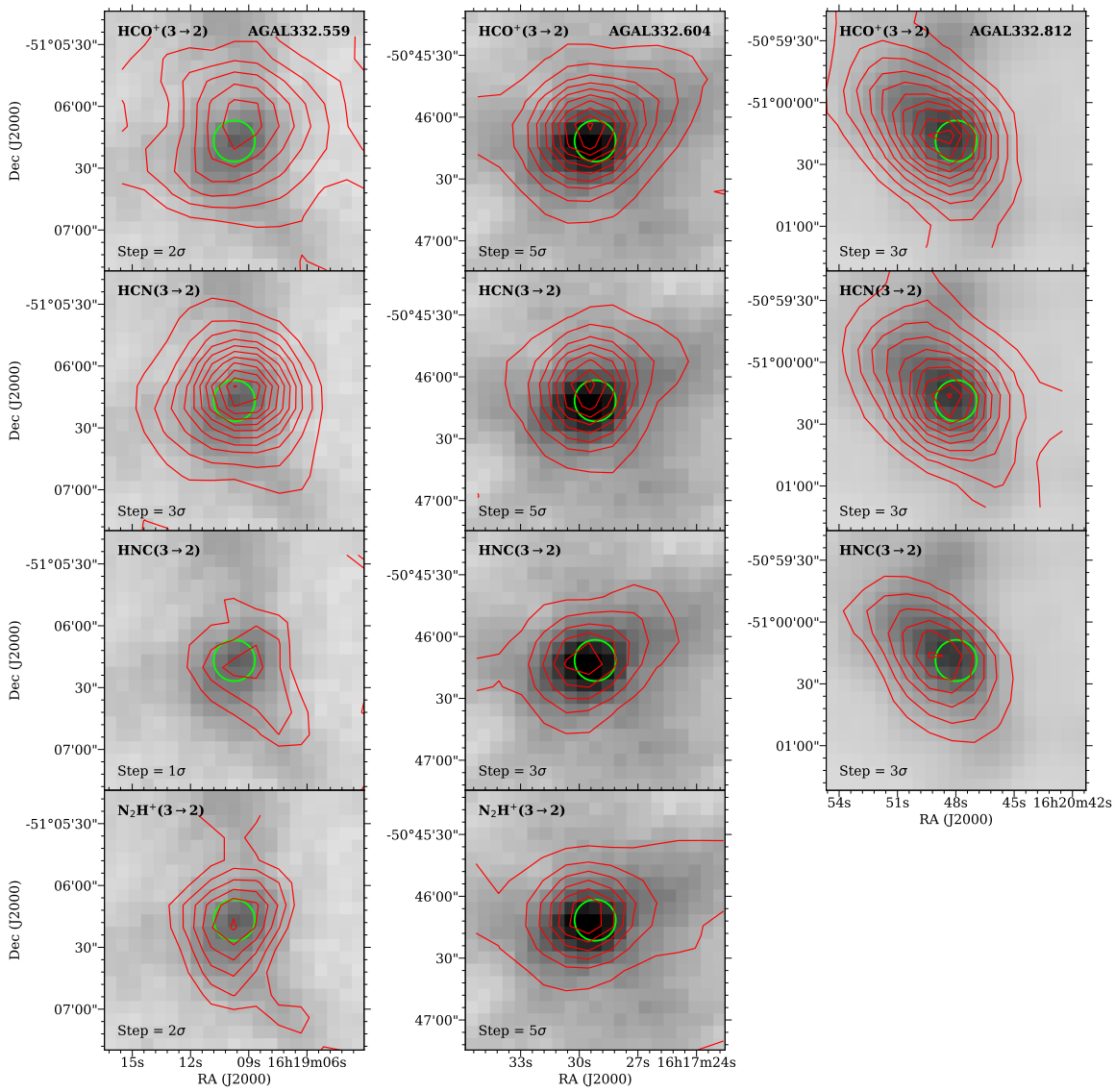

Figure 3.42: Same as Fig. 3.39. Left: AGAL332.559-00.591. Middle: AGAL332.604. Right: AGAL332.812.

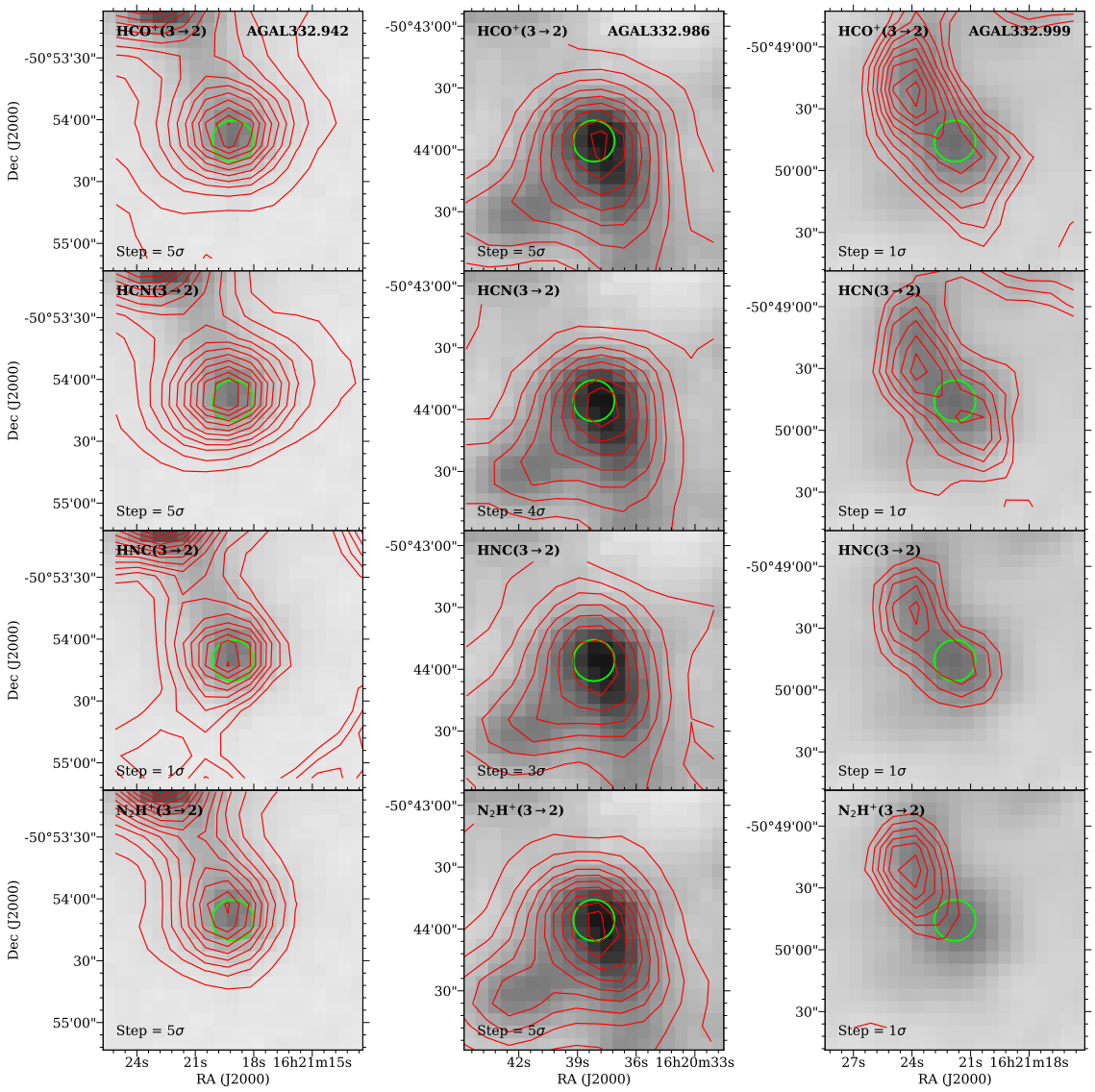

Figure 3.43: Same as Fig. 3.39. Left: AGAL332.942. Middle: AGAL332.986. Right: AGAL332.999.

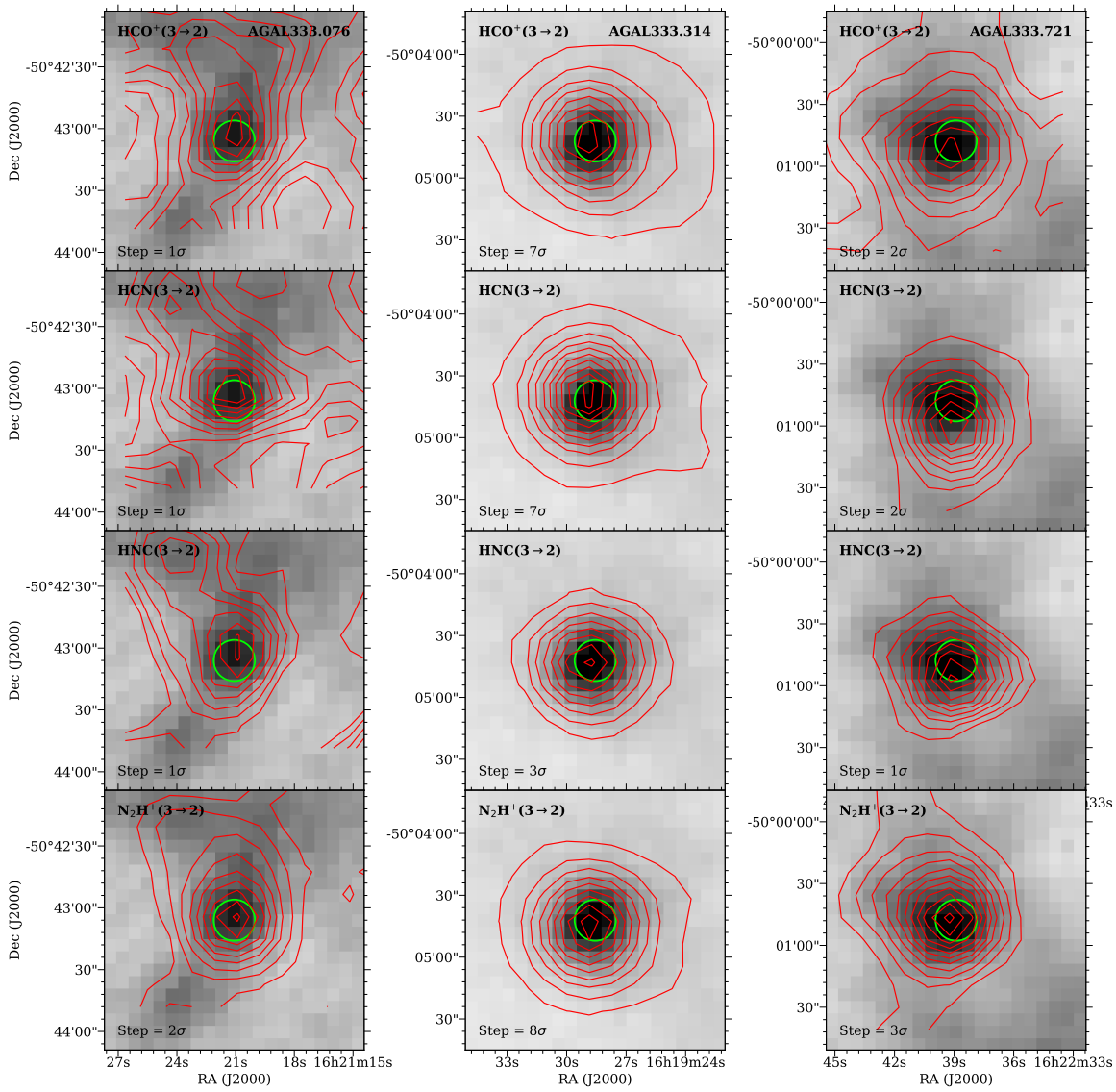

Figure 3.44: Same as Fig. 3.39. Left: AGAL333.076. Middle: AGAL333.314. Right: AGAL333.721.

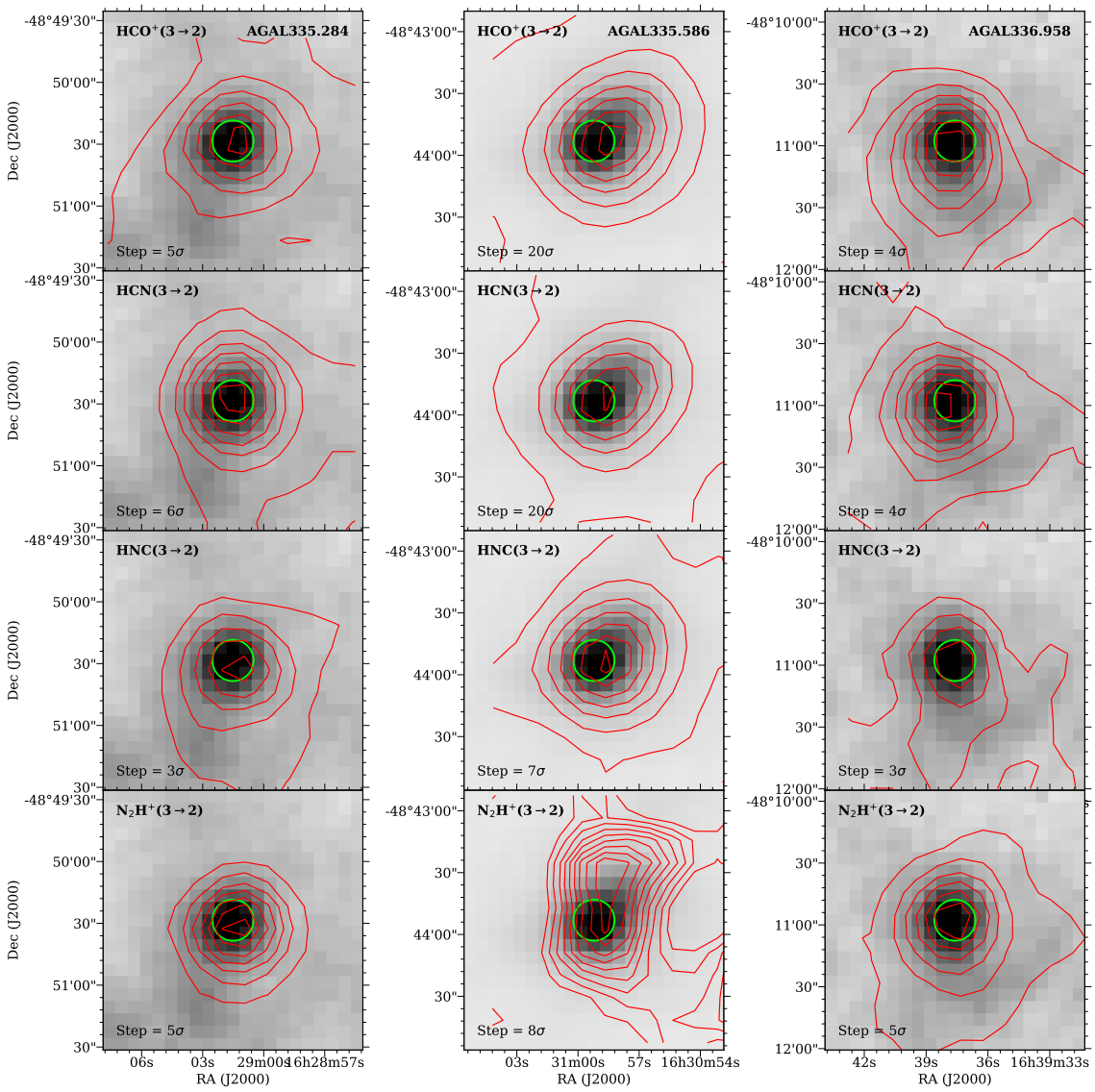

Figure 3.45: Same as Fig. 3.39. Left: AGAL335.284. Middle: AGAL335.586. Right: AGAL336.958.

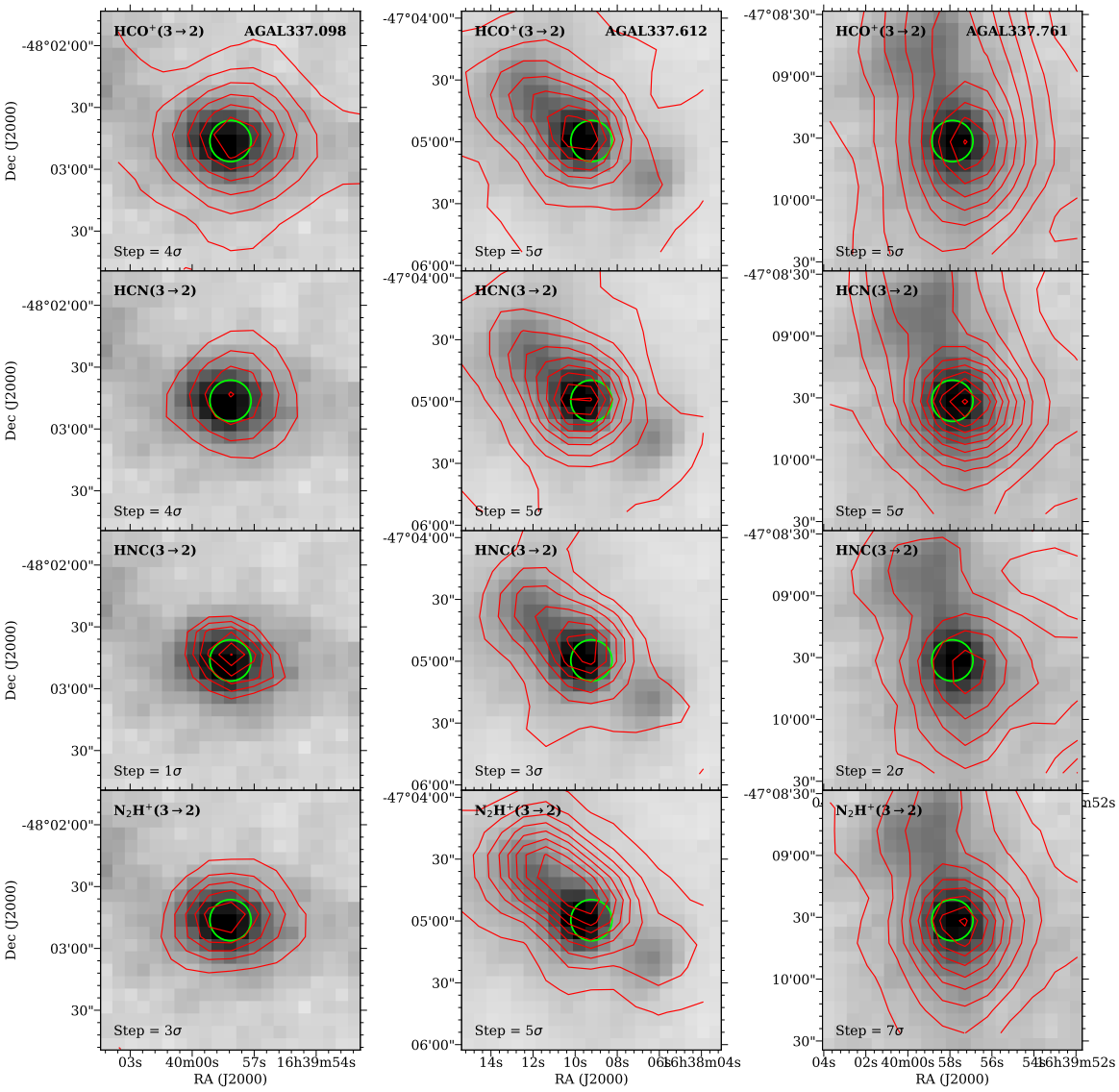

Figure 3.46: Same as Fig. 3.39. Left: AGAL337.098. Middle: AGAL337.612. Right: AGAL337.761.

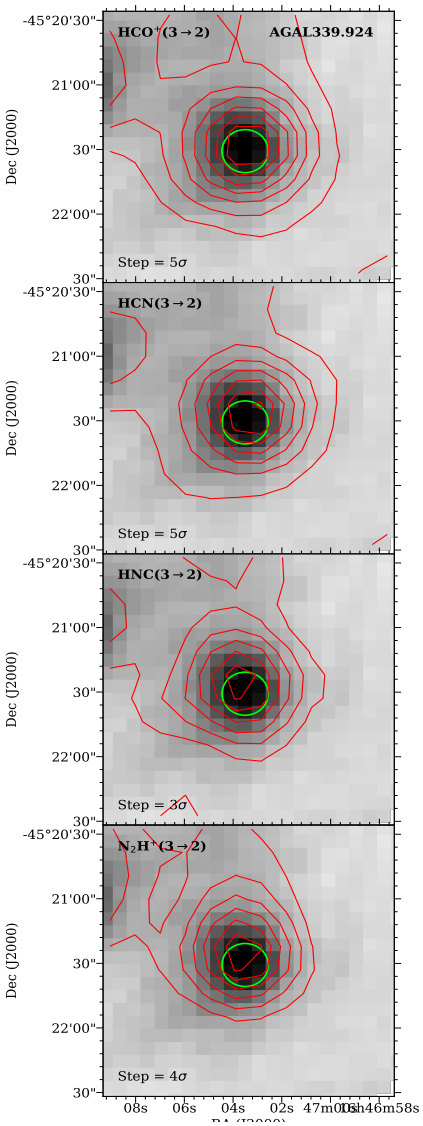

Figure 3.47: Same as Fig. 3.39. AGAL339.924-0.084.

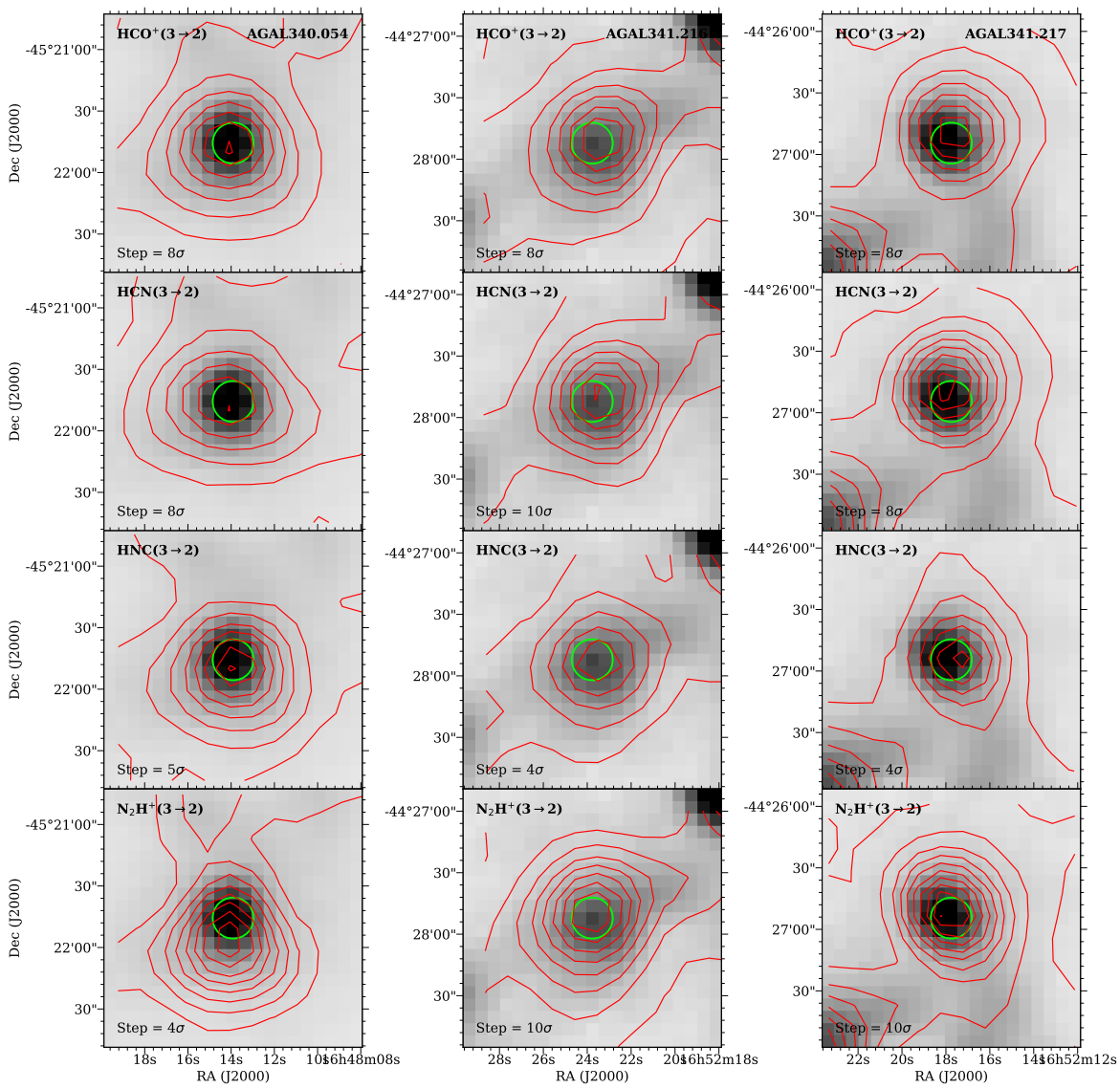

Figure 3.48: Same as Fig. 3.39. Left: AGAL340.054. Middle: AGAL341.216. Right: AGAL341.217.

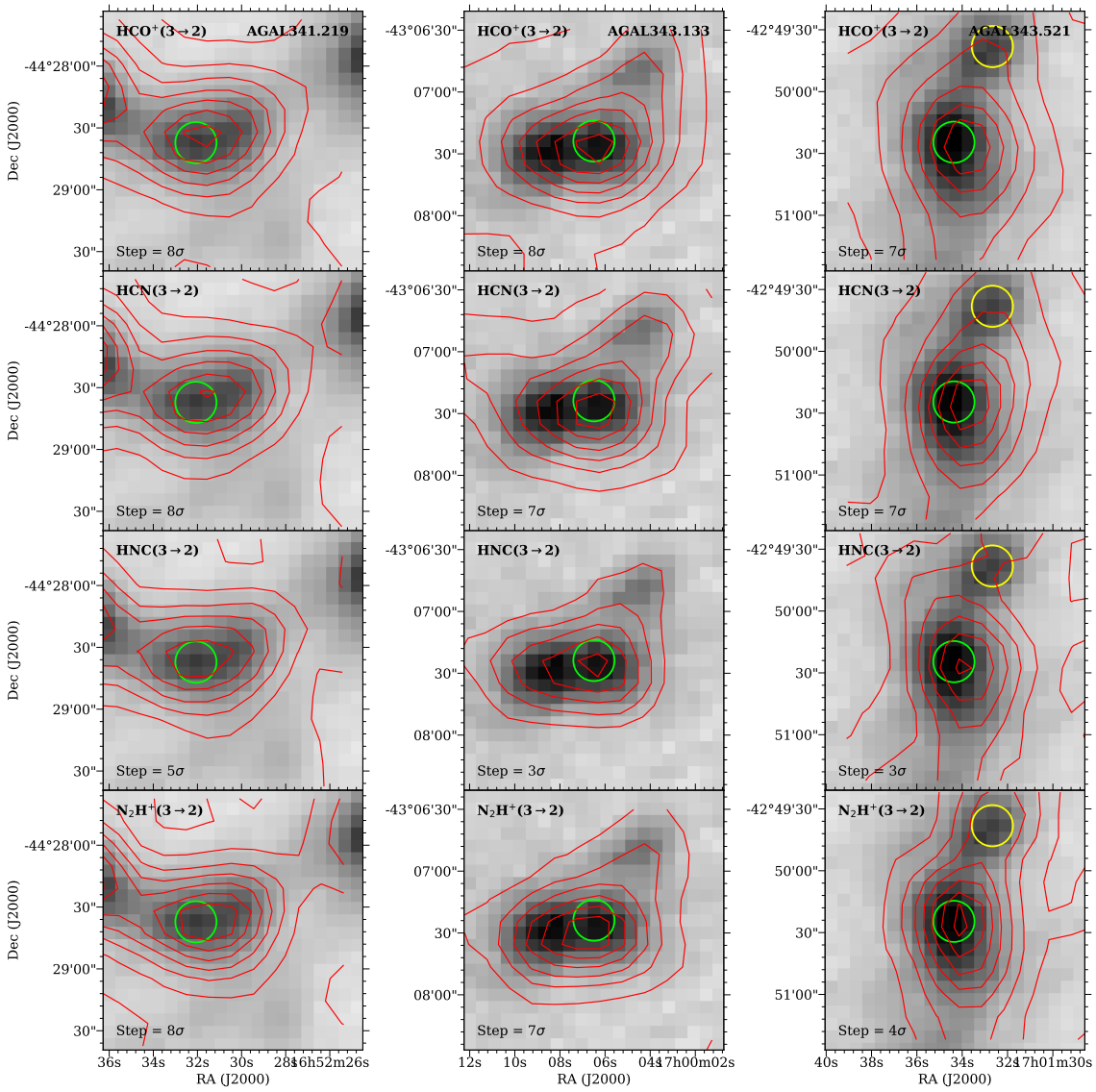

Figure 3.49: Same as Fig. 3.39. Left: AGAL341.219. Middle: AGAL343.133. Right: AGAL343.521 and AGAL342.528.

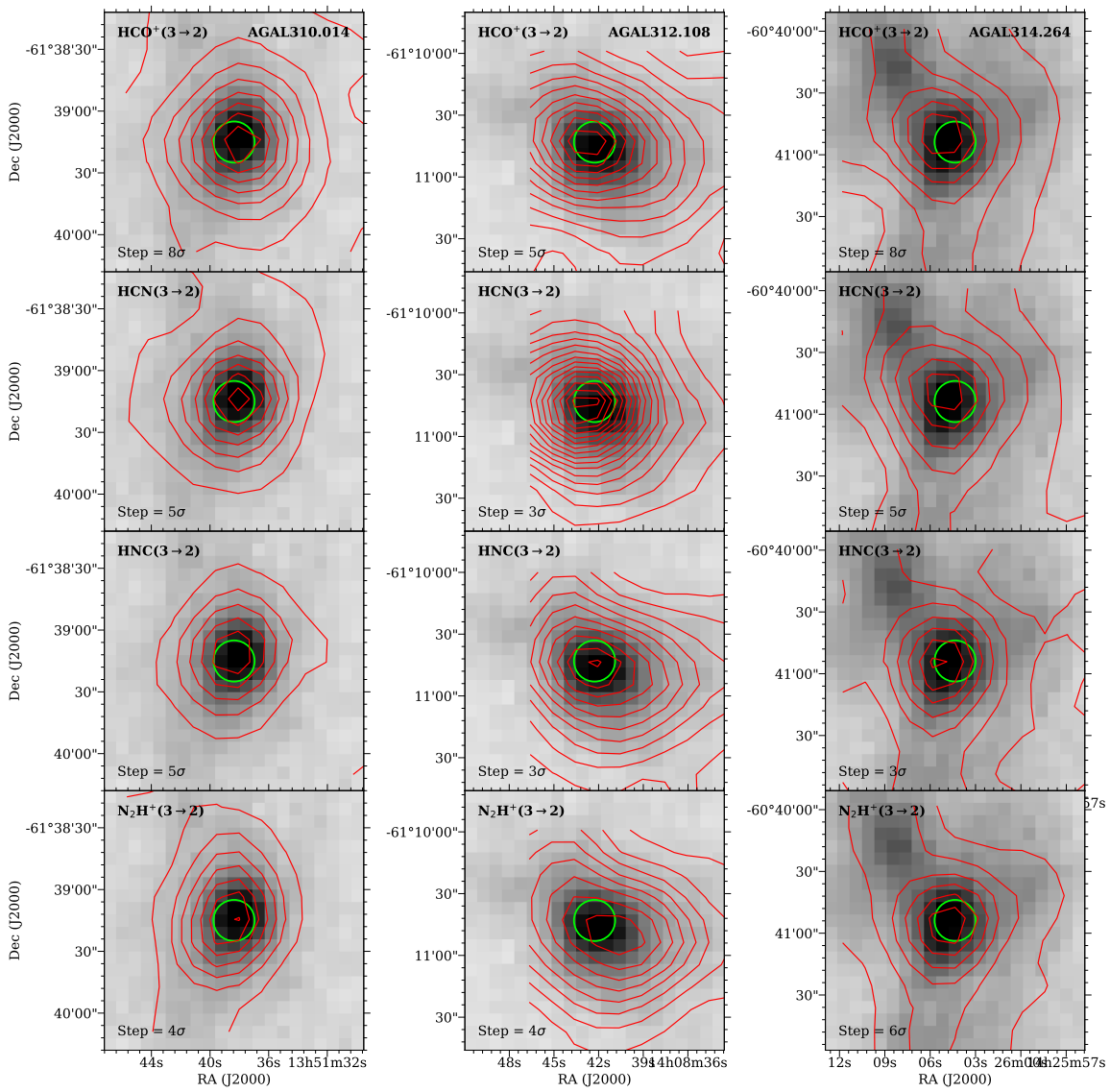

Figure 3.50: Contour maps of the velocity integrated $J = 3 \rightarrow 2$ emissions in four molecular lines overlayed on grayscale Atlasgal 870μm maps toward HII clumps. Left: AGAL310.014. Middle: AGAL312.108. Right: AGAL314.264. From top to bottom: HCO^+, HCN, HNC and N_2H^+ maps. The velocity ranges of integration for each clumps are given in col. 2 of Table 3.6. The lowest contour levels correspond to the 4σ level and the steps (δI) are given inside each box. Emission line contours drawn at 3σ level are shown in blue. The green/yellow circles in each maps, of size $\sim$ 20", show peak position of the clumps.

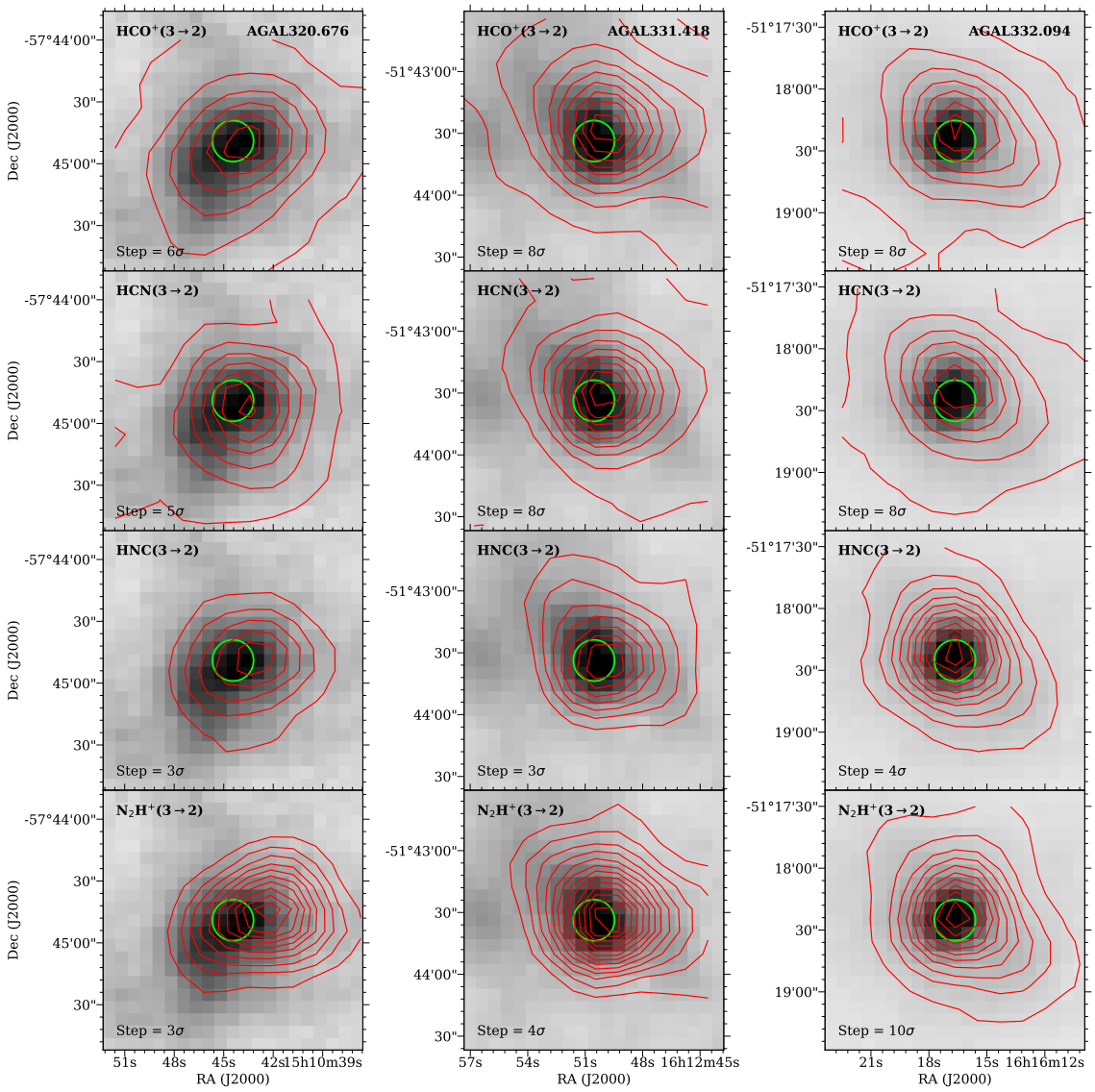

Figure 3.51: Same as Fig. 3.50. Left: AGAL320.676. Middle: AGAL331.418. Right: AGAL332.094.

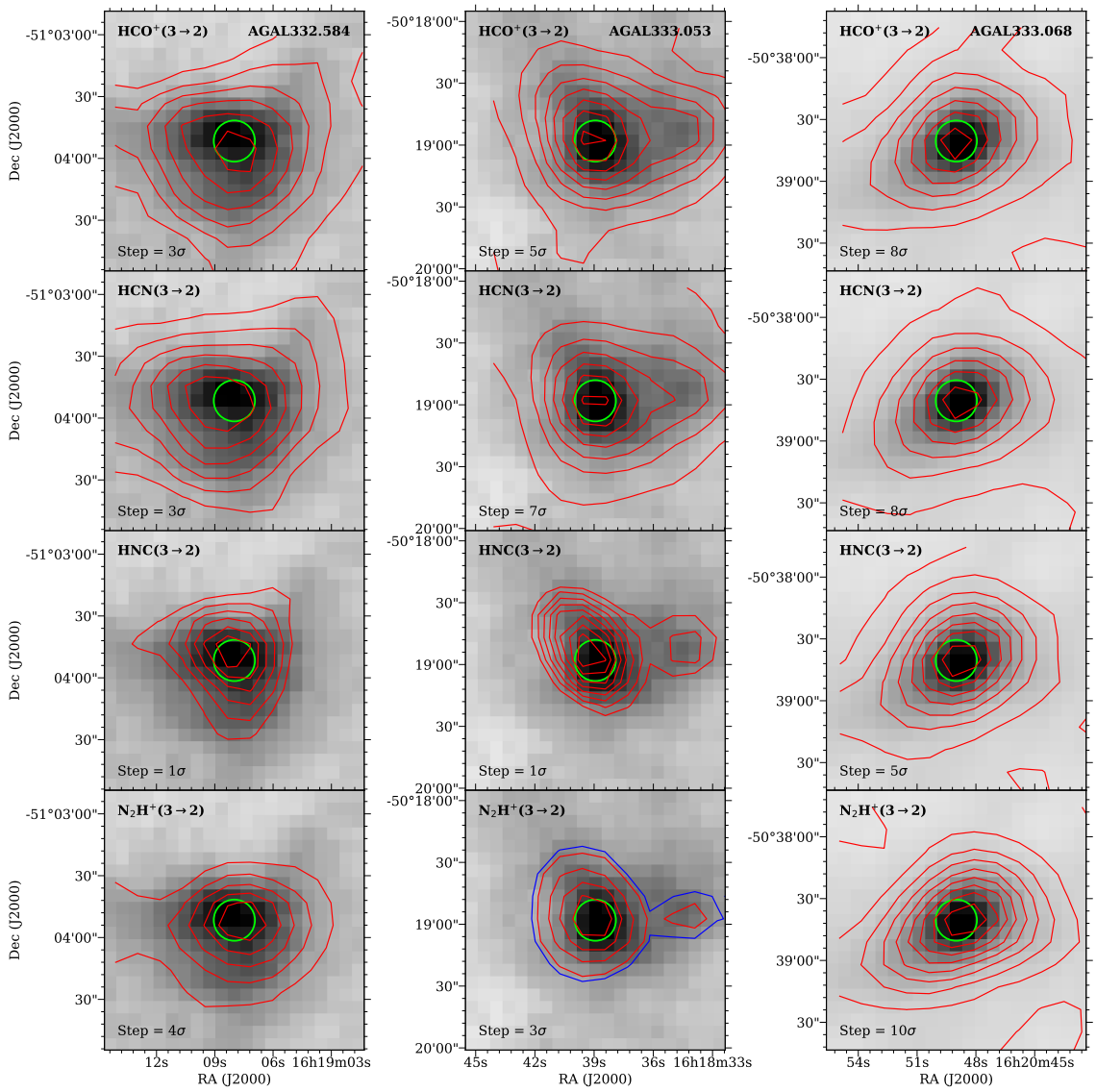

Figure 3.52: Same as Fig. 3.50. Left: AGAL332.584. Middle: AGAL333.053. Right: AGAL333.068.

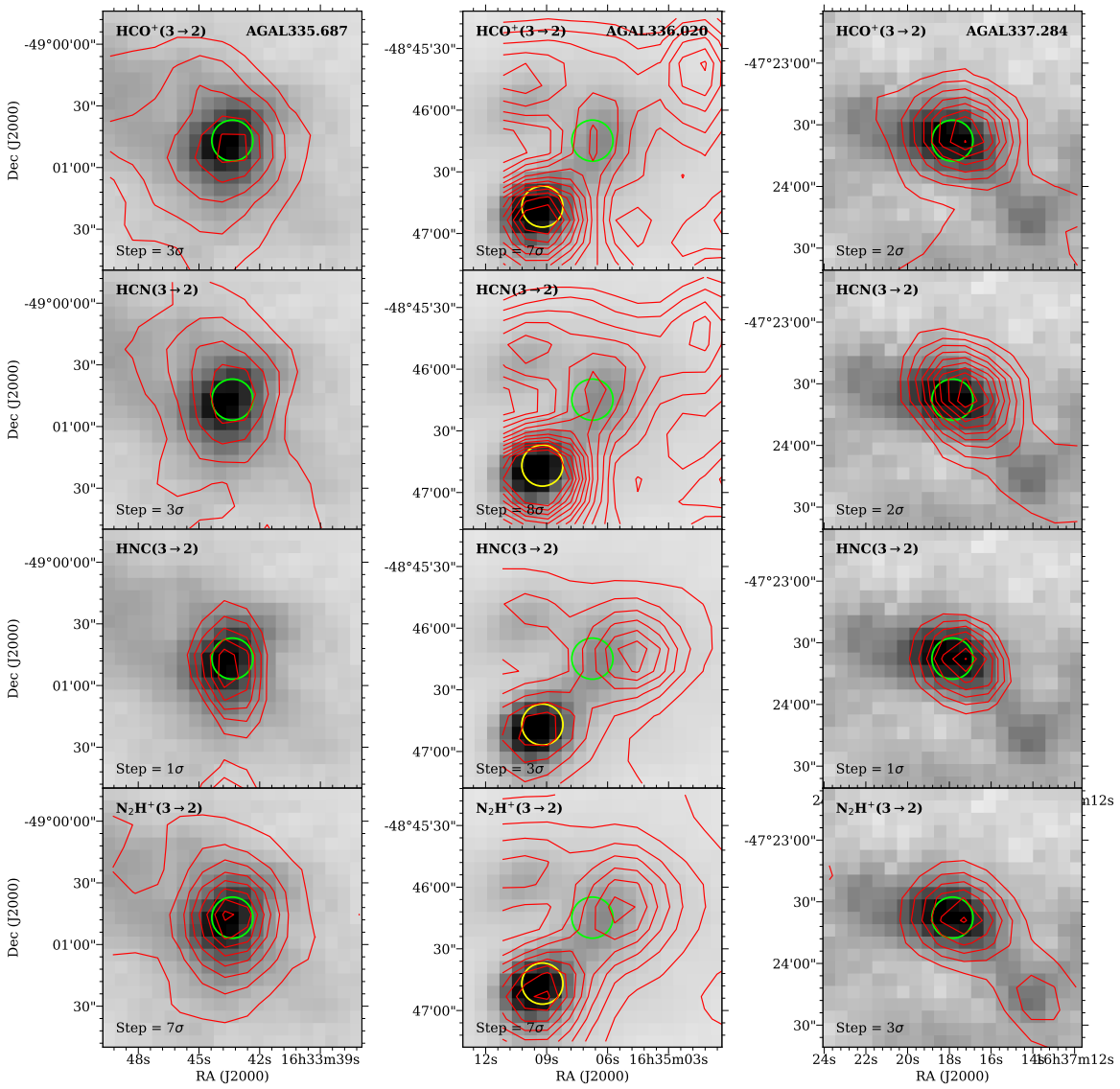

Figure 3.53: Same as Fig. 3.50. Left: AGAL335.687. Middle: AGAL336.018 and AGAL336.020. Right: AGAL337.284.

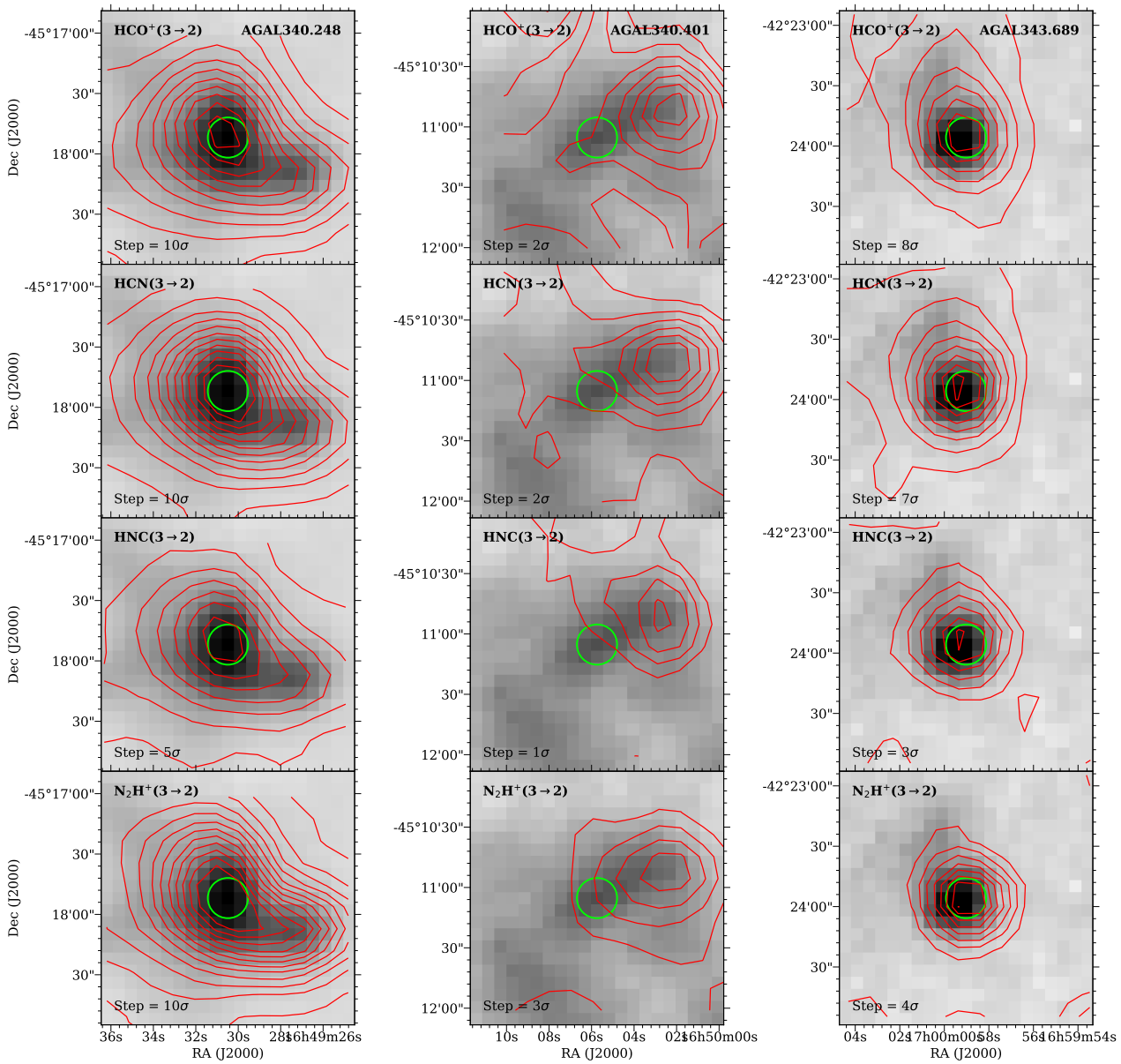

Figure 3.54: Same as Fig. 3.50. Left: AGAL340.248. Middle: AGAL340.401. Right: AGAL343.689.

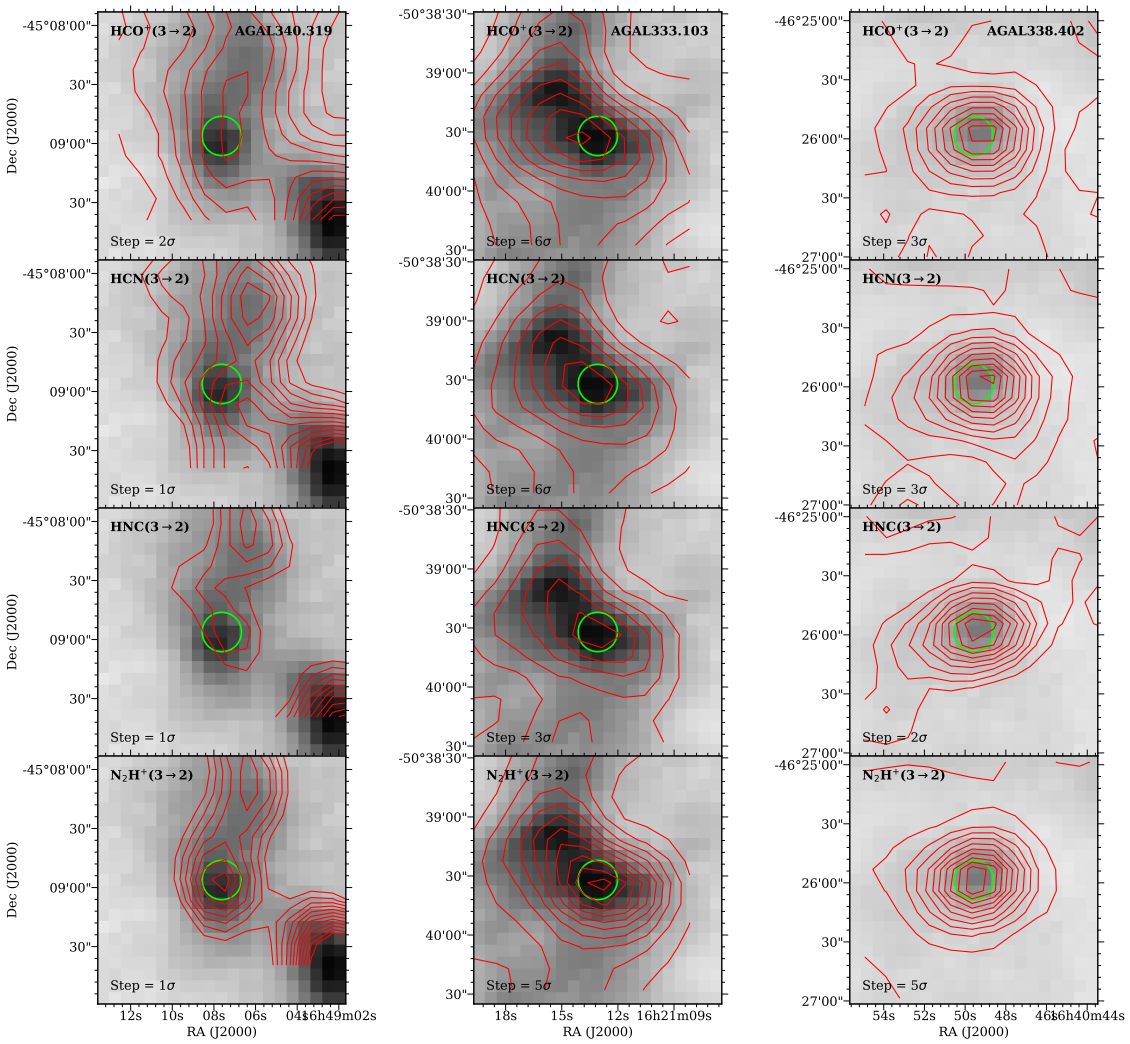

Figure 3.55: Contour maps of the velocity integrated $J = 3 \rightarrow 2$ emissions in four molecular lines overlayed on grayscale Atlasgal 870μm maps toward PDR clump (Left: AGAL340.319) and unknown clumps (Middle: AGAL333.103. Right: AGAL338.402). From top to bottom: HCO^+, HCN, HNC and N_2H^+ maps. The lowest contour levels correspond to the 4σ level and the steps (δI) are given inside each box. Emission line contours drawn at 3σ level are shown in blue. The green/yellow circles in each maps, of size $\sim$ 20", show peak position of the clumps.

3.7.4 Contour maps of $J = 4 \rightarrow 3$

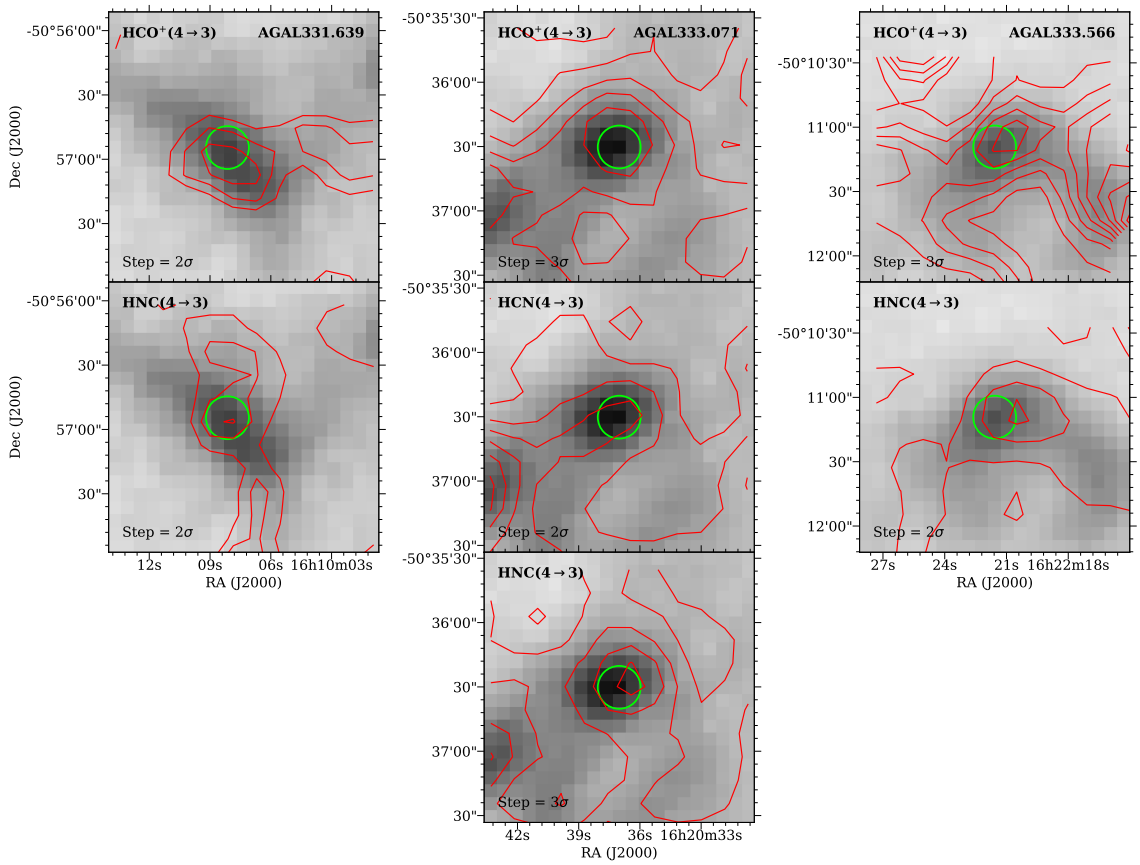

Figure 3.56: Contour maps of the velocity integrated $J = 3 \rightarrow 2$ emissions in four molecular lines overlayed on grayscale Atlasgal 870μm maps toward prestellar clumps. Left: AGAL331.639; Middle: AGAL333.071; Right: AGAL333.566. Name of the species are given inside each box. The velocity ranges of integration for each clumps are given in col. 2 of Table 3.7. The lowest contour levels correspond to the 4σ level and the steps (δI) are given inside each box. The green circles in each maps, of size $\sim$ 20", show peak position of the clumps.

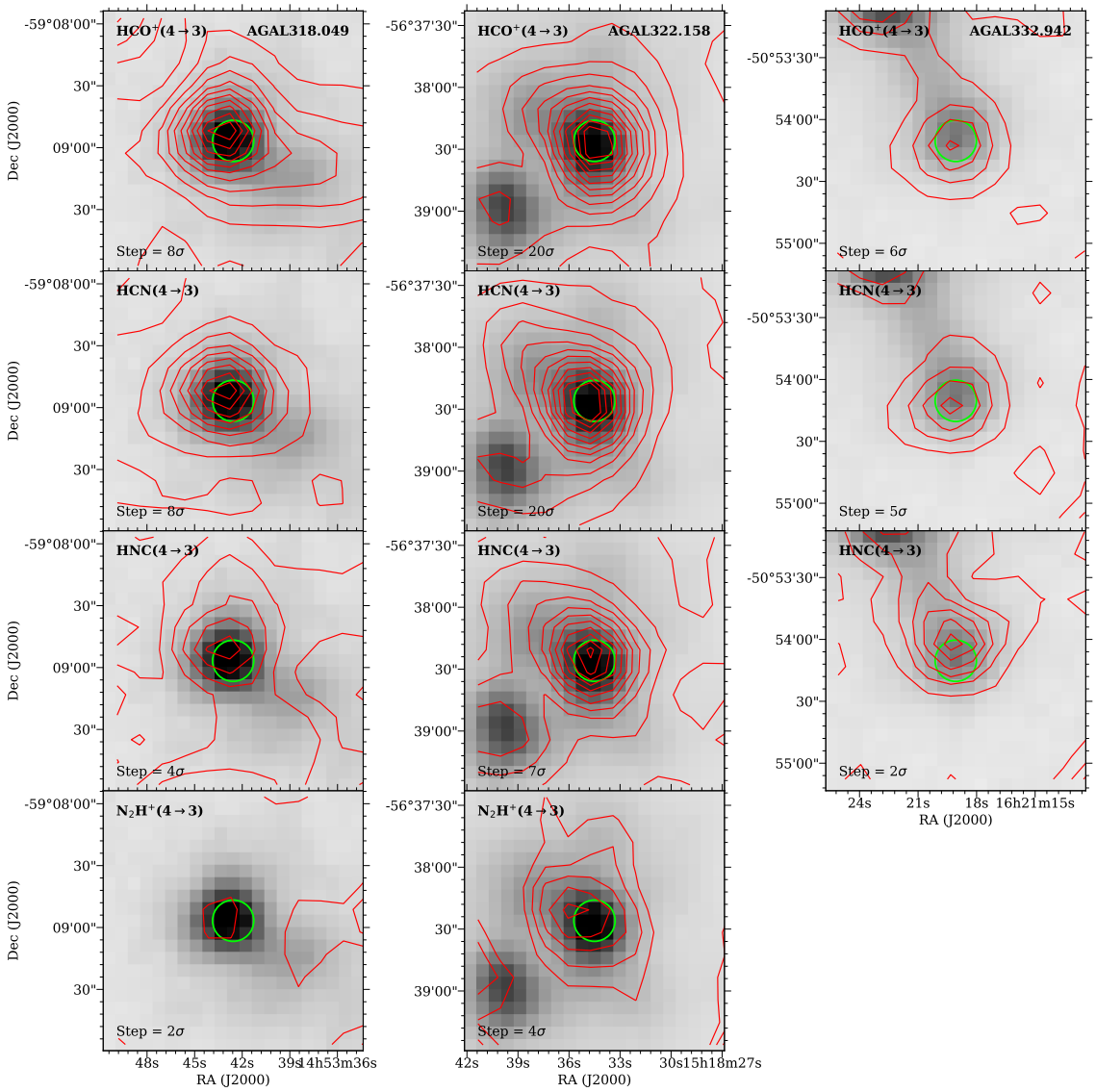

Figure 3.57: Contour maps of the velocity integrated $J = 3 \rightarrow 2$ emissions in four molecular lines overlayed on grayscale Atlasgal 870μm maps toward protostellar clumps. Left: AGAL318.049; Middle: AGAL332.158; Right: AGAL332.942. Name of the species are given inside each box. The velocity ranges of integration for each clumps are given in col. 2 of Table 3.7. The lowest contour levels correspond to the 4σ level and the steps (δI) are given inside each box. The green circles in each maps, of size $\sim$ 20", show peak position of the clumps.

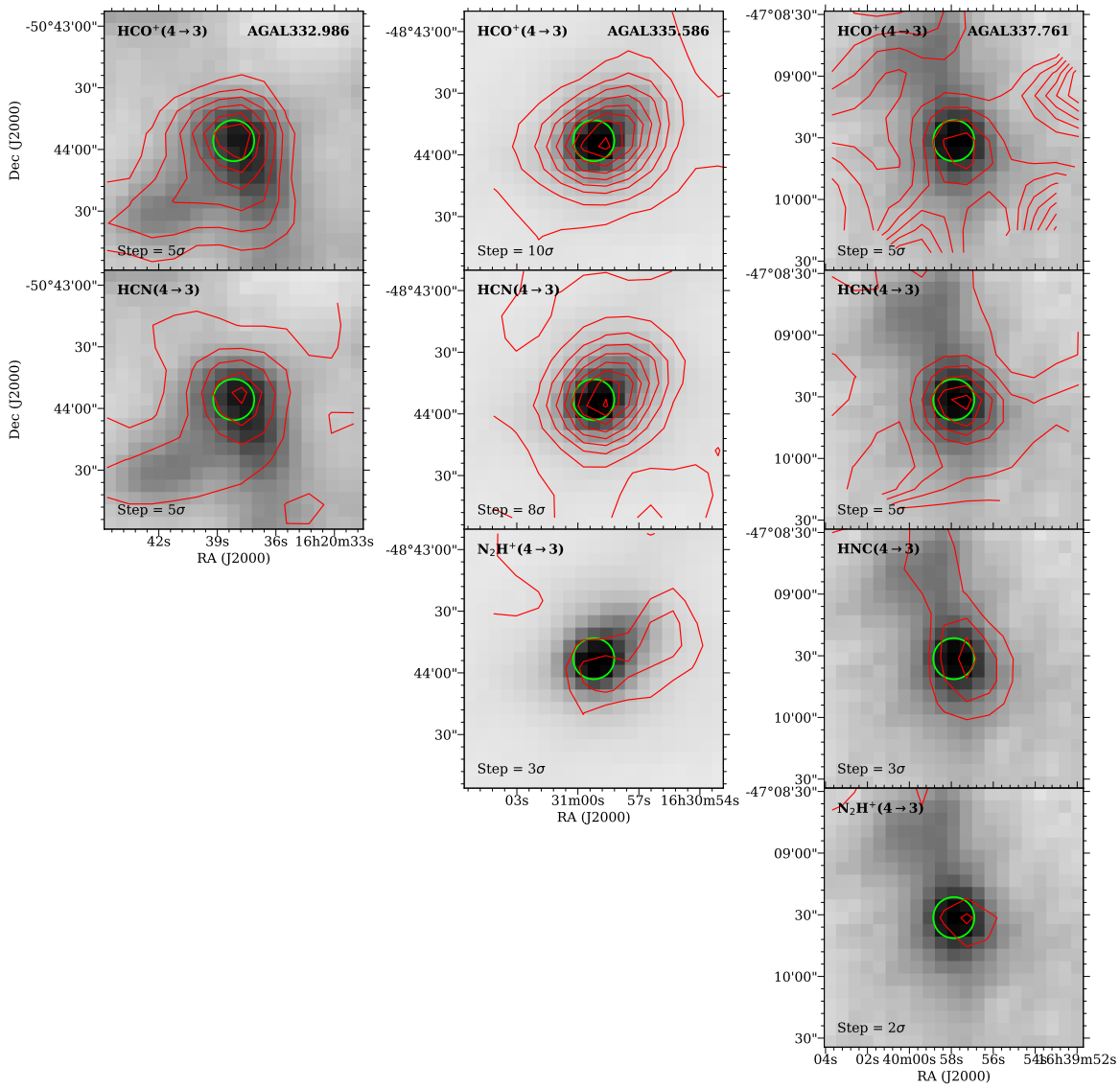

Figure 3.58: Same as Fig. 3.57. Left: AGAL332.986. Middle: AGAL335.586. Right: AGAL337.761.

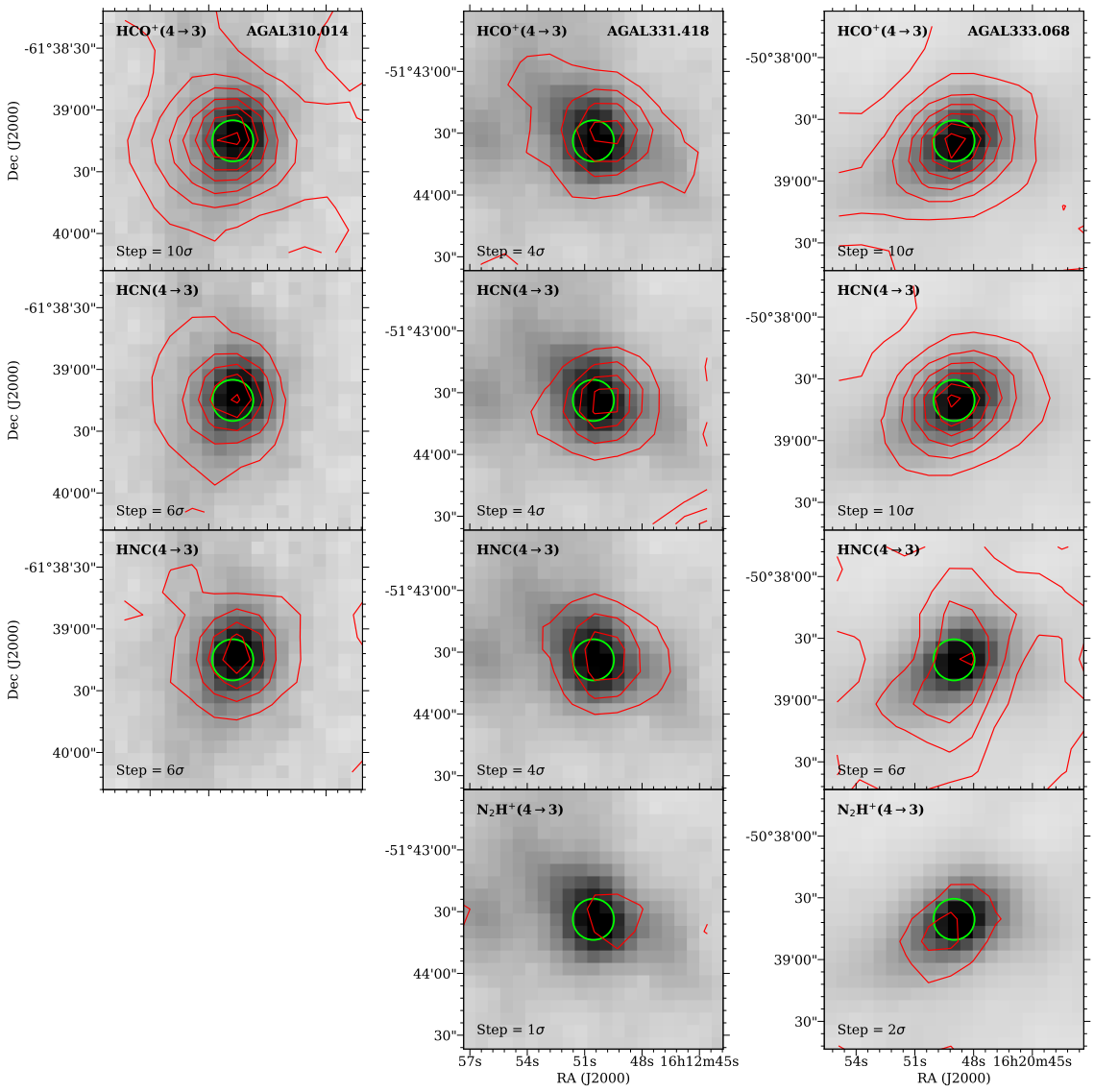

Figure 3.59: Contour maps of the velocity integrated $J = 4 \rightarrow 3$ emissions in four molecular lines overlayed on grayscale Atlasgal 870μm maps toward HII clumps. Left: AGAL310.014; Middle: AGAL331.418; Right: AGAL333.068. Name of the species are given inside each box. The velocity ranges of integration for each clumps are given in col. 2 of Table 3.7. The lowest contour levels correspond to the 4σ level and the steps (δI) are given inside each box. The green circles in each maps, of size $\sim$ 20", show peak position of the clumps.

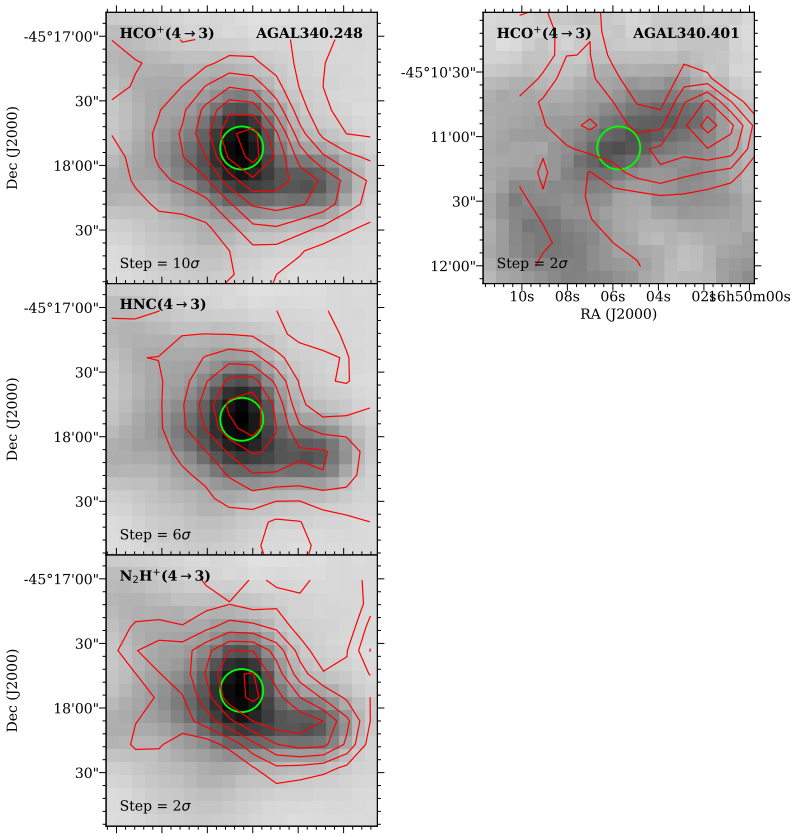

Figure 3.60: Same as Fig. 3.59. Left: AGAL340.248. Right: AGAL340.401.

3.7.5 HCO^+ and N_2H^+ $J = 3 \rightarrow 2$ sizes

Table 3.14: Clump size.

Clump	HCO^+		N_2H^+	
	R_{eff} (pc)	No. of comp.	R_{eff} (pc)	No. of comp.
Quiescent/Prestellar clumps				
AGAL331.639+00.501_S	0.62	3	0.38	
AGAL332.737-00.621_S	0.34	2	0.37	
AGAL332.892-00.569_S	1.15		0.56	2
AGAL333.014-00.521_S	0.52	2	0.47	4
AGAL333.016-00.751_S	1.10		0.58	
AGAL333.071-00.399_S	1.33		0.46	2
AGAL333.179-00.396_S	3.63		1.66	
AGAL333.198-00.352_A	0.44		0.35	
AGAL333.449-00.182_S	0.99		0.79	
AGAL333.481-00.224_S	1.06		–	
AGAL333.566-00.296_S	0.36	2	0.80	
AGAL333.669-00.349_S	2.98		2.12	
AGAL335.592+00.184_S	0.95		0.42	
AGAL340.179-00.242_S	0.85	2	0.57	
AGAL340.232-00.146_S	4.07		2.17	
AGAL340.301-00.402_S	–	3	–	2
AGAL340.304-00.376_S	1.08		0.77	
AGAL340.398-00.396_S	1.31		0.77	3
AGAL341.039-00.114_S	–		0.86	
AGAL341.181-00.277_S	1.07		–	
AGAL341.196-00.221_S	–		–	
Protostellar clumps				
AGAL304.886+00.636_S	0.74		0.49	
AGAL309.154-00.349_S	0.58	2	0.47	
AGAL309.236-00.457_S	0.48	2	0.42	2
AGAL318.049+00.086_S	1.10		0.85	
AGAL322.158+00.636_S	0.66	2	0.84	2
AGAL331.724-00.204_S	0.55		0.47	
AGAL332.226-00.536_S	2.28	2	1.26	
AGAL332.281-00.547_S	2.65		1.90	
AGAL332.559-00.147_S	0.60		0.49	
AGAL332.559-00.591_S	0.81		0.53	
AGAL332.604-00.167_S	0.90		0.52	
AGAL332.726-00.621_S	0.28		–	
AGAL332.812-00.701_S	2.23		–	
AGAL332.942-00.686_S	0.47	2	0.34	2
AGAL332.986-00.489_S	1.24		1.00	
AGAL332.999-00.639_S	0.72		0.39	
AGAL333.076-00.559_S	4.08		2.13	
AGAL333.314+00.106_S	0.67		0.52	

AGAL333.721-00.207_S	0.93		0.63	
AGAL335.284-00.132_S	3.53		1.53	
AGAL335.586-00.291_S	3.07		2.27	
AGAL336.018-00.827_S	–		–	
AGAL336.958-00.977_S	0.80		0.65	
AGAL337.098-00.929_S	2.80		1.57	
AGAL337.612-00.059_S	3.06		2.57	
AGAL337.761-00.339_S	1.12		0.83	
AGAL339.924-00.084_S	0.73	2	0.61	2
AGAL340.054-00.244_S	3.23	2	2.28	2
AGAL341.216-00.236_S	1.18		1.05	
AGAL341.217-00.212_S	0.53	2	0.56	2
AGAL341.219-00.259_S	0.49	2	0.82	2
AGAL343.133-00.482_S	0.81		0.66	
AGAL343.521-00.519_S	1.03		0.78	
AGAL343.528-00.507_S	–		–	
HII clumps				
AGAL310.014+00.387_S	1.00		0.64	
AGAL312.108+00.309_S	2.15		1.88	
AGAL314.264+00.091_S	1.43		0.68	2
AGAL320.676+00.244_S	1.12		0.73	
AGAL331.418-00.356_S	1.06		0.80	
AGAL332.094-00.421_S	0.91		0.69	
AGAL332.584-00.559_S	0.94		0.62	
AGAL333.053+00.029_S	0.75		0.37	
AGAL333.068-00.447_S	1.27		0.96	
AGAL335.687-00.812_S	0.81		0.62	
AGAL336.020-00.816_S	–		0.30	3
AGAL337.284-00.159_S	1.65		1.39	2
AGAL340.248-00.374_S	0.77		1.05	
AGAL340.401-00.381_S	–	3	2.12	
AGAL343.689-00.017_S	0.55		0.34	
PDR				
AGAL340.319-00.227_S	0.62	2	0.30	3
Unknown				
AGAL333.103-00.502_S	1.26		1.00	
AGAL338.402+00.032_S	3.11	2	1.63	

Chapter 4

Artemis survey: fragmentation of massive and dense clumps at the 0.1 pc scale

We observed 23 massive and dense clumps (MDCs), chosen from the MALT90 survey, at 350 μm with spatial resolution of ∼8″, using the Artemis+ receiver at the APEX telescope. The observed MDCs covers all evolutionary stages (Quiescent, Proto-stellar, H II and PDR regions) and are all located at ∼ 3.6 kpc, allowing to investigate their structure at scales of ∼ 0.1 pc and possible differences with evolutionary stage. While the MDCs are seen as single structures with at ATLASGAL and MALT90 survey, the 350 μm Artemis+ observations show that they are resolved into typically 2-3 substructures.

4.1 Introduction

Fragmentation of molecular clouds from large scale ($\geq$ 10pc) to clumps ($\sim$1pc) and to cores ($\sim$0.1 pc) has important consequences in understanding star formation process. Recent studies have shown that fragmentation of clouds to smaller scales is a hierarchical process (e.g., Pokhrel et al. 2018; Palau et al. 2018, and references therein). In each scale of fragmentation different mechanisms, for example, gravity, turbulence, magnetic field, feedback etc., may dominate the process acting alone or combined. A series of observational studies at different spatial scales have argued in favor and against the Jeans fragmentation. Palau et al. (2015) studied 19 massive dense clumps ($\sim$0.1pc scale) in OMC-1S ($\sim$1000 au) and argued in favor of thermal Jeans fragmentation in both scales. On the other hand, Pokhrel et al. (2018) in a multi-scale analysis of the Perseus molecular cloud suggested that Jeans fragmentation is inconsistent with observation based on either thermal or thermal plus non-thermal motions. Fontani et al. (2016) studied IRAS16061-5048c1 with ALMA at $\sim$278 GHz and reported a dominant role of magnetic support in fragmentation process. The inconsistency in the expected versus observed number of substructures (e.g., Pokhrel et al. 2018) with Jeans masses, fragments exceeding Jeans mass criteria (e.g., Csengeri et al. 2017), and in addition the likely role of magnetic fields (e.g., Fontani et al. 2016) in the process suggests that we need more

observational and theoretical studies to understand the fragmentation properties of molecular clouds. Pre-stellar stage cores that can form high-mass star has been illusive (e.g., Louvet et al. 2019). How clumps/cores fragments has obvious implications in discerning between the current star formation theories and in connecting low mass and high mass star formation processes.

We selected massive and dense clumps from the MALT90 survey, likely to give birth to massive stars, to study the fragmentation properties from the scale of ∼1 pc to ∼0.1 pc. The clumps are in different evolutionary stages as defined in the MALT90 survey (Rathborne et al. 2016, Guzmán et al. 2015). The goal is to determine the number of cores at the scale of 0.1 pc and their physical characteristics, and correlate these with the bulk properties of the 'parent' clump (i.e. Atlasgal clumps) such as turbulence, virial mass, density etc. In the following sections we describe the sample, the observations, method of analysis, the results and finally a discussion.

4.2 The sample

The sample consists of 23 massive dense clumps taken from the MALT90 survey, covering different evolutionary stages (five prestellar, ten protostellar, six H II, one PDR and one clump with 'unknown' classification). Fifteen of which are also observed in the SuperMALT survey. The clump identification, masses, sizes and evolutionary stages, taken from the MALT90 catalogue, are presented in Table 1. The MDCs are at similar distances of 3.3–3.9 kpc (Whitaker et al. 2017), have sizes of ∼0.5 - 1 pc, and masses of the order $\geq$200M$_\odot$, therefore the sample provide homogeneous physical scale and different evolutionary stage clumps to study the link between fragmentation, evolutionary stage and other physical properties. The clumps in the sample have dust temperatures ranging from 14.0 to 28.0 K, with an increase in temperature from prestellar to H II clumps consistent with increase in star formation activity with evolution (e.g., Guzmán et al. 2015).

4.3 Observations

Table 4.2 lists summary of our observations. The observations were made during June 2016, June 2017 and June 2018 using the Artemis camera on the Atacama Pathfinder Experiment (APEX) Telescope. Artemis, a larger format bolometer camera, provides 4608 pixels observing at 350 μm and 450 μm emission simultaneously. The mapping was undertaken in spiral on-the-fly mode covering a region of $\sim 5' \times 5'$ centered on the coordinates given in col. 3 of Table 4.2. We observed 14 fields, which contained 23 MDCs. The data were reduced using an standard Artemis data reduction pipeline (Roussel 2013).

In this work we only use the 350 μm maps for the derivation of dust properties of the cores and analisis of the morphologies. The rms sensitivity in the final mosaics ranges from $\sim$ 0.20–0.81 Jy/beam (see col. 4 of Table 4.2). The spatial resolution of the observations is $8''$ (∼0.1 pc at ∼3.6 kpc).

Table 4.1: Physical properties of the clumps.

Clump	Dist. (kpc)	Temp. (K)	Size (pc)	Mass (10^3 $M_\odot$)	M_{vir} (10^3 $M_\odot$)	Density (10^4 cm^{-3})	Comments
Prestellar clump							
AGAL331.639+00.501_S	3.6	14.0	0.86	1.44	0.63	0.92	(a)
AGAL333.481-00.224_S	3.5	18.9	0.50	0.59	0.53	1.91	(a)
AGAL333.483-00.246_S	3.5	21.0	0.61	1.03	0.85	1.56	
AGAL333.566-00.296_S	3.4	20.2	0.71	0.87	0.50	1.00	(a)
AGAL341.196-00.221_S	3.7	17.2	0.43	0.89	0.92	4.48	(a)
Protostellar clump							
AGAL318.049+00.086_S	3.6	28.0	0.76	1.50	0.95	1.43	(a)
AGAL322.158+00.636_S	3.9	25.7	1.59	5.52	6.97	0.56	(a)
AGAL329.184-0.314_S	3.5	28.0	0.32	0.94	0.77	1.00	
AGAL332.986-00.489_S	3.7	25.7	1.43	3.21	1.68	0.45	(a)
AGAL333.473-00.236_S	3.5	21.0	0.41	0.32	0.66	1.64	
AGAL337.761-00.339_S	3.3	14.8	0.84	2.12	1.52	1.49	(a)
AGAL341.216-00.236_S	3.7	16.0	1.15	2.69	1.58	0.62	(a)
AGAL341.217-00.212_S	3.7	24.0	0.54	0.84	1.21	1.88	(a)
AGAL341.219-00.259_S	3.7	18.0	0.50	1.48	0.70	4.87	(a)
AGAL341.236-00.271_S	3.7	18.0	0.84	1.47	1.99	0.85	
H II clump							
AGAL310.014+00.387_S	3.6	28.0	0.68	1.12	0.75	1.44	(a)
AGAL322.164+00.622_S	3.7	28.0	1.04	0.98	0.30	2.95	
AGAL331.626+00.526_S	3.6	21.0	0.75	0.87	0.72	1.38	
AGAL333.068-00.447_S	3.7	26.0	1.55	4.65	2.28	0.51	(a)
AGAL333.553-00.291_S	3.4	22.0	0.35	0.23	0.56	1.90	
AGAL340.248-00.374_S	3.9	22.0	1.65	6.27	3.13	0.58	(a)
PDR clump							
AGAL340.319-00.227_S	3.7	22.5	0.75	0.87	0.84	0.86	(a)
Unknown type clump							
AGAL340.299-00.222_S	3.7	17.0	0.84	1.59	1.35	0.93	

(a) Clumps observed in the SuperMALT survey.

Table 4.2: Summary of observations.

Observing group				σ_{rms}
No.	Date	(l^o, b^o)	Clumps	(Jy/beam)
1	2017-06-23	331.639, 0.501	AGAL331.639, AGAL331.626	0.20
2	2017-06-23	333.481, -0.224	AGAL333.481, AGAL333.483, AGAL333.473	0.33
3	2017-06-22	333.566, -0.296	AGAL333.566, AGAL333.553	0.20
4	2016-06-19	341.196, -0.221	AGAL341.196, AGAL341.216, AGAL341.217	0.32
5	2017-06-22	318.049, 0.086	AGAL318.049	0.30
6	2016-06-19	322.158, 0.636	AGAL322.158, AGAL322.164	0.81
7	2018-08-27	329.184, -0.314	AGAL329.184	0.64
8	2017-06-22	332.986, -0.489	AGAL332.986	0.33
9	2017-06-22	337.761, -0.339	AGAL337.761	0.20
10	2017-06-22	341.219, -0.259	AGAL341.219, AGAL341.236	0.20
11	2017-06-22	310.014, 0.387	AGAL310.014	0.15
12	2016-06-19	333.086, -0.447	AGAL333.068	0.35
13	2017-06-22	340.248, -0.374	AGAL340.248	0.20
14	2017-06-22	340.319, -0.227	AGAL340.319, AGAL340.299	0.23

Ancillary data

The MALT90 clumps were selected from the Atlasgal project, a survey of the dust continuum emision at the wavelength of 870 μm (Schuller et al. 2009; Contreras et al. 2013) conducted using the LABOCA receiver at the Apex telescope with an angular resolution of 19.5″ . We downloaded archival ATLASGAL continuum maps as calibrated and reduced fits images of size 4.9′X4.9′. We also made use of the MALT90 molecular line catalogue (Rathborne et al. 2016), specifically the N_2H^+ $J = 1 \rightarrow 0$, and, in addition, HCO^+ and $H^{13}CO^+$ (3-2) spectra from the SuperMALT survey (Neupane et al. 2018, Neupane et al. *in submission*) toward a few clumps to infer the gas kinematics.

4.4 Results

4.4.1 Artemis 350μm emission

Figure 4.1 to 4.7 present the 14 full images of the 350μm emission which included 23 MDC clumps in different evolutionary stages. Also shown are the ATLASGAL 870 μm images toward the clumps. The spatial resolution is ∼8″ in the Artemis maps which is about three times higher than provided by the ATLASGAL survey. Contour levels (grey) on both images start from 3σ level and drawn increasingly at levels of 5σ, 10σ and 50σ. The morphologies of emission varies from simple to complex shapes. The detected 350μm emission is always within the lowest contour of the 870 μm emission maps.

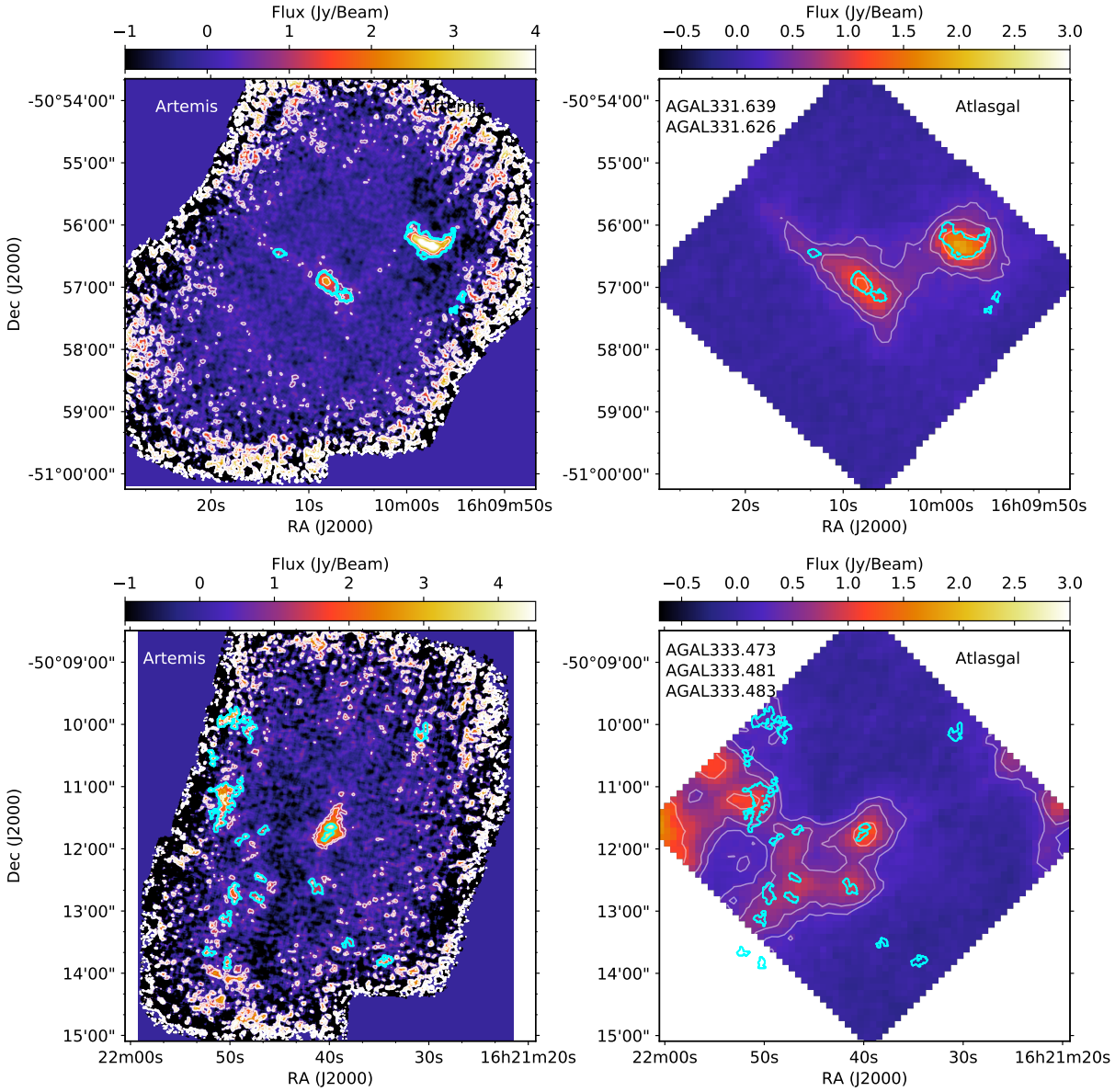

Figure 4.1: Artemis 350μm maps (left panel) and Atlasgal 870μm maps (right panel). Top: AGAL331.626 and AGAL331.639. Bottom: AGAL333.473, AGAL333.481, AGAL333.483. Contour levels (white) on both maps start from 3σ level and drawn increasingly at levels of 5σ, 10σ and 50σ. The cyan contours in both maps show substructures determined from Artemis maps using Astrodendro.

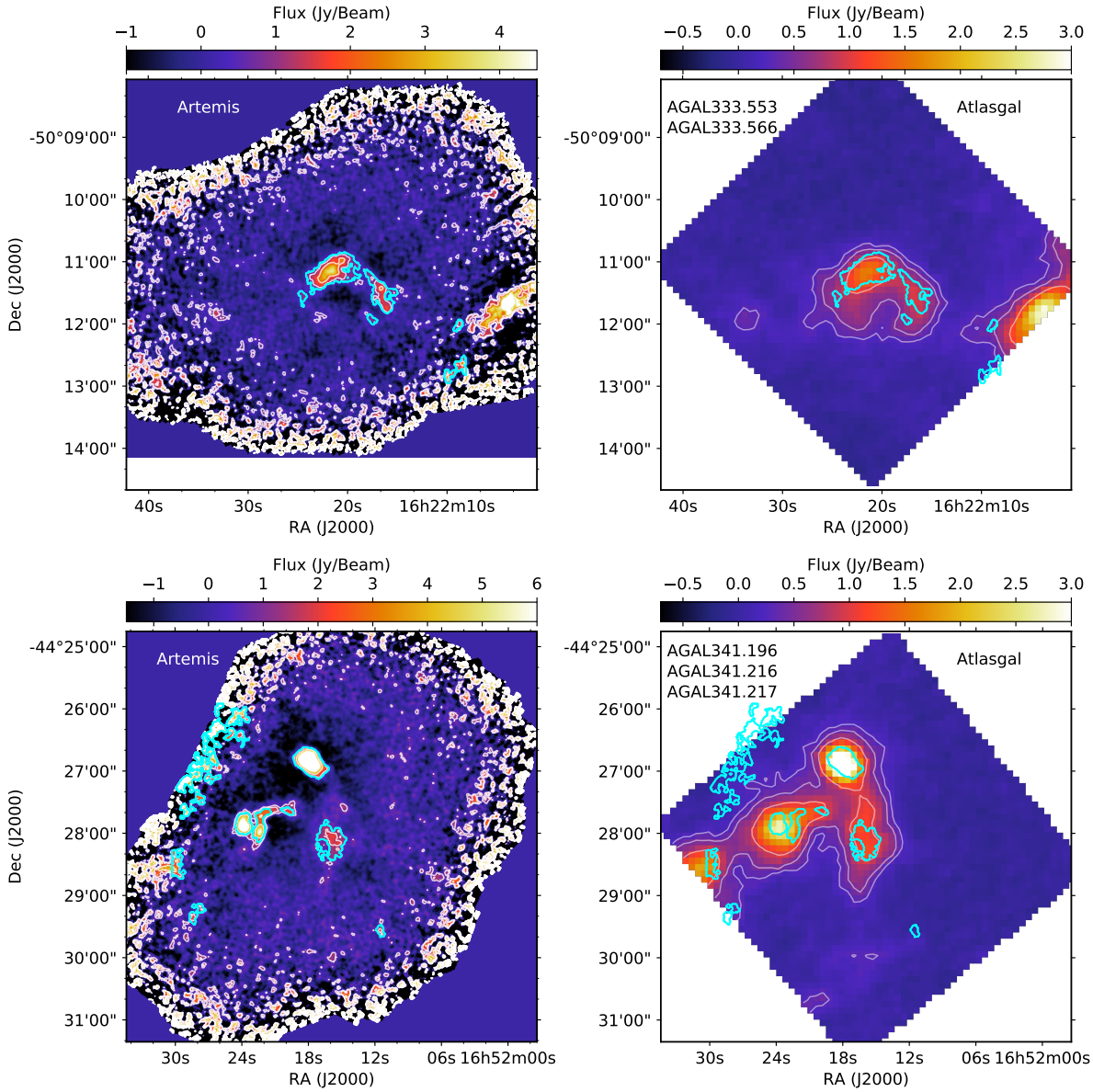

Figure 4.2: Same as Fig. 4.1. Top: AGAL333.553 and AGAL333.566. Bottom: AGAL341.196, AGAL341.216 and AGAL341.217.

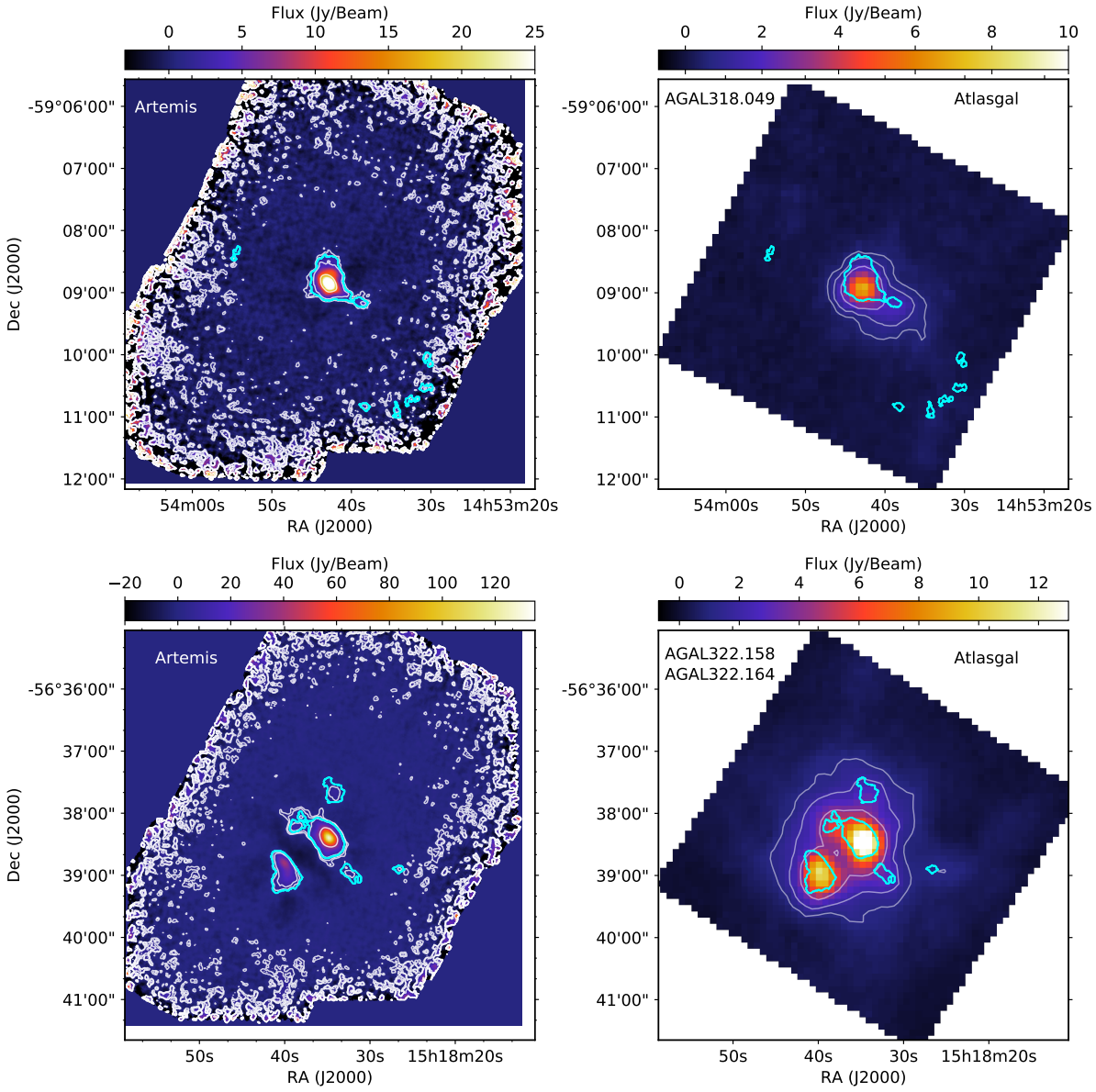

Figure 4.3: Same as Fig. 4.1. Top: AGAL318.049. Bottom: AGAL322.158 and AGAL322.164.

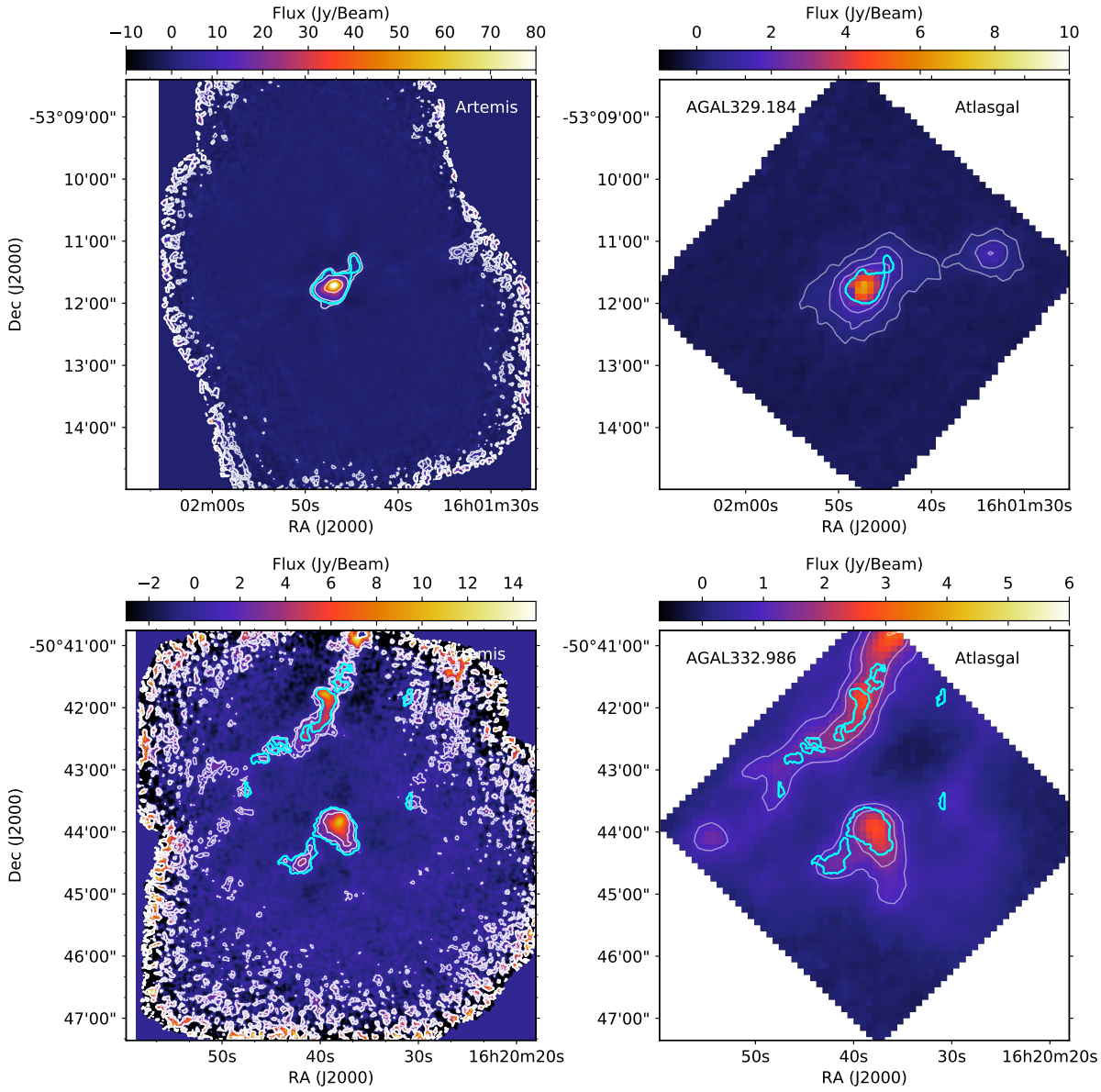

Figure 4.4: Same as Fig. 4.1. Top: AGAL329.184, Bottom: AGAL332.986.

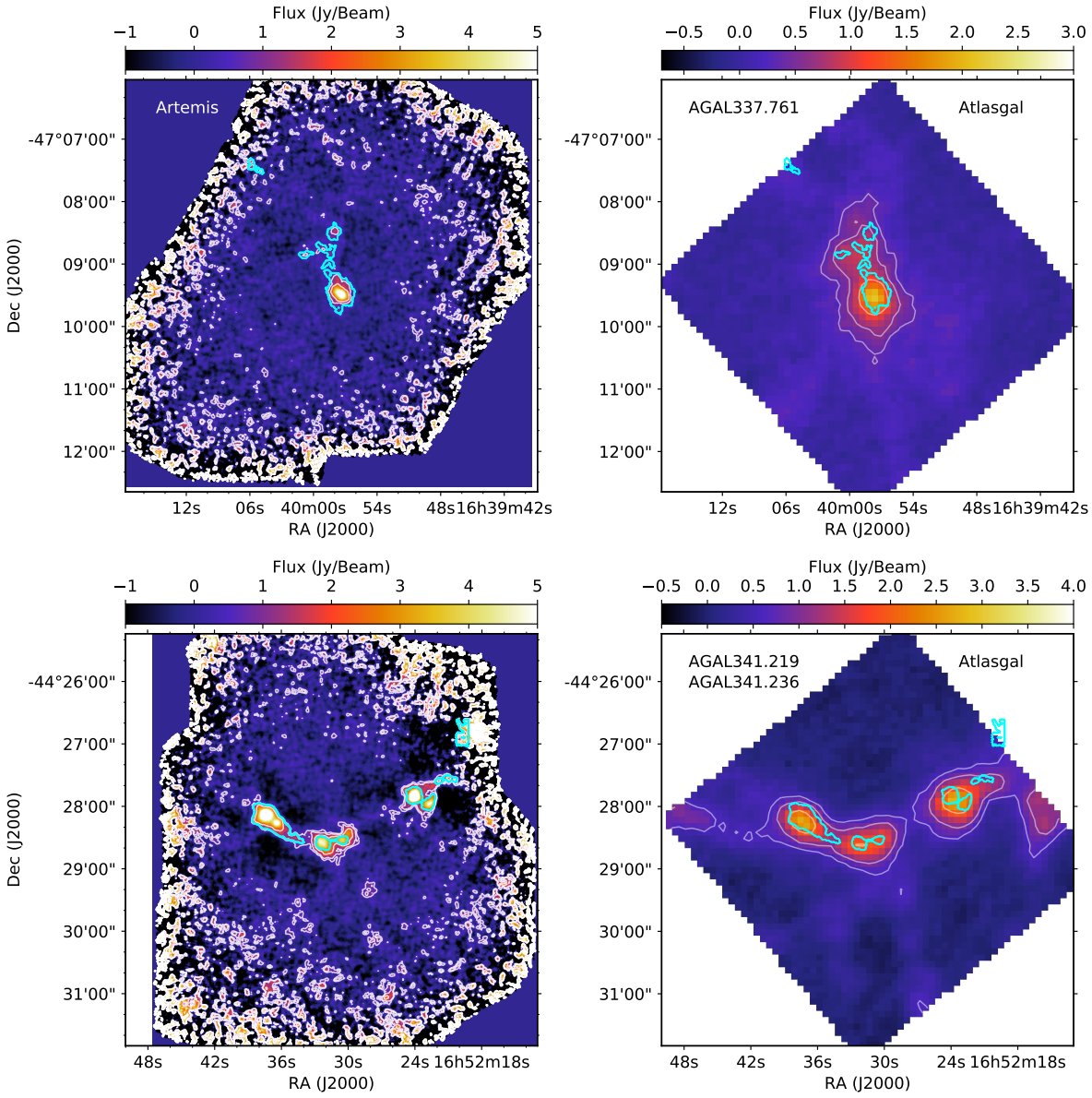

Figure 4.5: Same as Fig. 4.1. Top: AGAL337.761, Bottom: AGAL341.219 and AGAL341.236. Clump AGAL341.217 is same source as in map 4.2 (bottom panel)

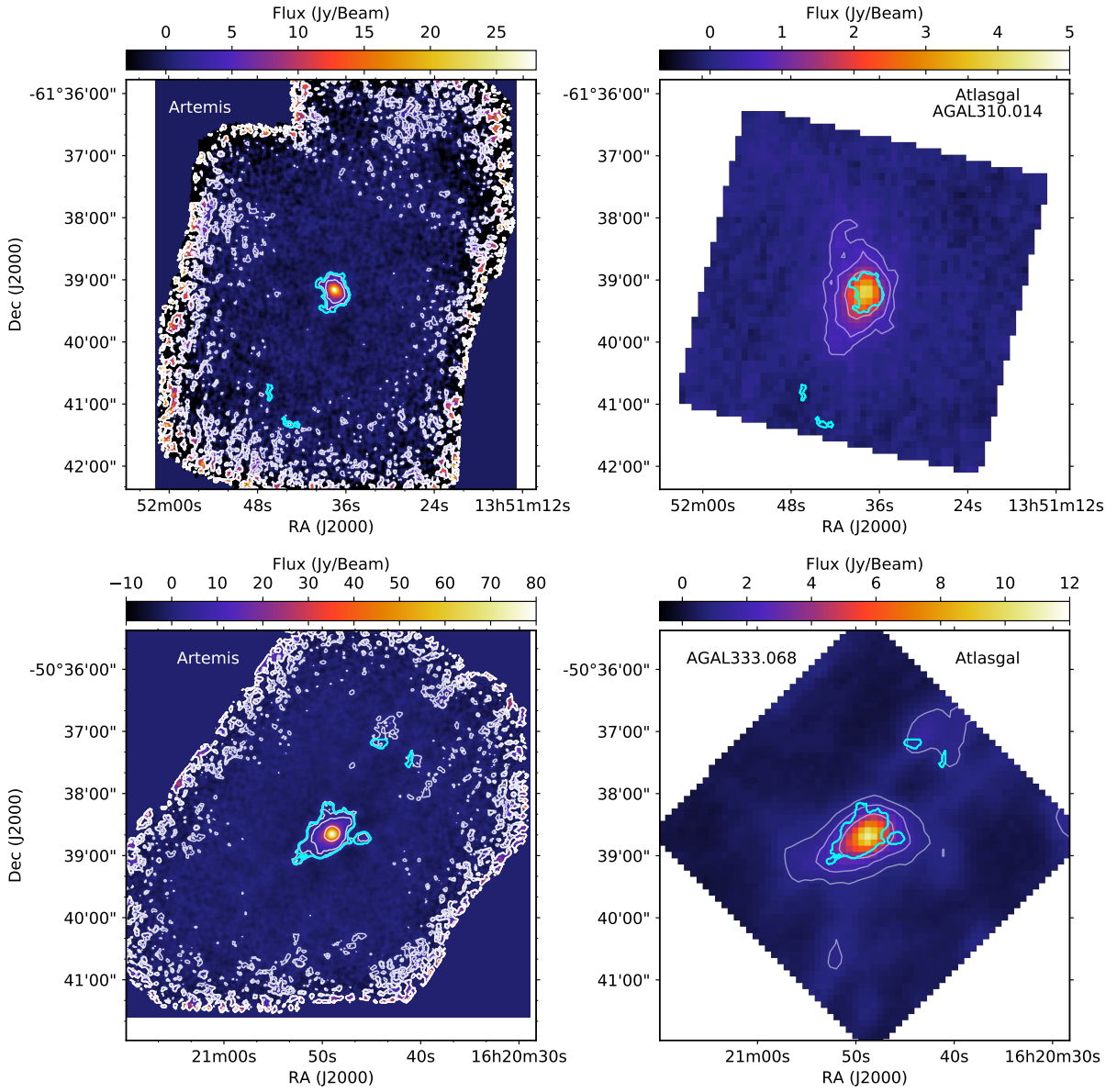

Figure 4.6: Same as Fig. 4.1. Top: AGAL310.014. Bottom: AGAL333.068.

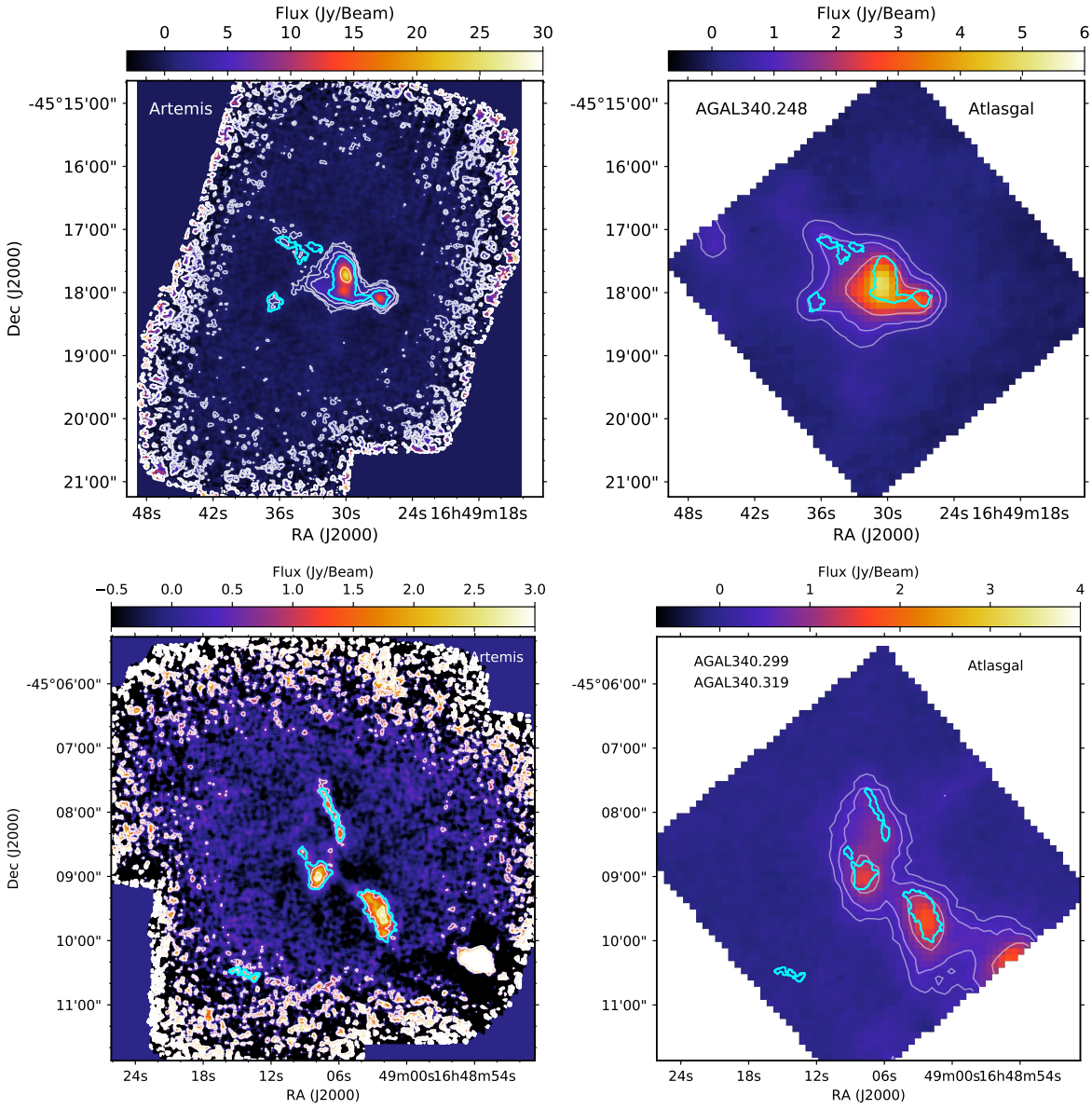

Figure 4.7: Same as Fig. 4.1. Top: AGAL340.248. Bottom: AGAL340.299 and AGAL340.319.

4.4.2 Astrodendro: core identification

To identify structures (also referred as cores) within the Artemis maps we used the Astrodendro[1] algorithm based on the dendogram method (Rosolowsky et al. 2008). The algorithm has three variables as an input for the identification of substructures; minimum flux to be considered (F_{min}), step (δ) that defines separation of neighboring peaks and minimum pixels (A_{min}) to be included in a defined structure. For a robust extraction of cores we adopted F_{min}=3σ, δ=1σ and A_{min} equal to half the beam area. These parameters allows the selection of cores with a minimum peak value of 4σ and minimum size equal to half the beam size. Although the algorithm is able to detect cores at the edges of the maps we did not considered them for further analysis.

The substructure identified using the Astrodendro algorithm in the Artemis images are shown in cyan contours and are also overlayed in the ATLASGAL images to visualize the position of the substructures within the clumps. Cols. 2 to 8 of Table 4.4.2 present, respectively, number of substructures, flux density, radius, and position angle of the cores.

Most clumps, defined by the 3σ contours in ATLASGAL images, exhibit a central core surrounded by smaller cores within the clump region. The central core observed in the 350μm image coincide with the peak position of the clump in ATLASGAL. Exception are a few clumps in which two cores are detected around the peak position of the clump (e.g., AGAL333.481) or clumps with few cores but no central substructure (e.g., AGAL333.483).

We identified 55 substructures within the 23 observed clumps. Eight clumps show no fragmentation (meaning single structure in Artemis map), seven clumps exhibit 2 cores and three clumps exhibit 3 cores. We also found clumps with either 4, 5 and 6 cores. With respect to the number of substructures in the different evolutionary stages, we found 1 to 4 cores in prestellar clumps, 1 to 5 in protostellar clumps, and 1 to 6 in H II clumps. The PDR and unknown clumps exhibit four and one core, respectively.

[1]http://www.dendrograms.org/

Table 4.3: Core parameters.

Clump	No. of comp.	Coordinates		Flux	Radius		PA	Mass	Density	f^a
		RA	DEC	(Jy/beam)	(arcsec)	(pc)	(deg)	(10^3 $M_\odot$)	(10^5 cm^{-3})	
Prestellar										
AGAL331.639+00.501_S	3	16:10:06.35	-50:57:08.59	1.23	2.7	0.05	162	21 ± 3	6.8 ± 1	7%
		16:10:08.15	-50:56:55.41	4.57	3.9	0.07	135	77 ± 12	8.1 ± 1.2	
		16:10:13.00	-50:56:27.14	0.55	1.9	0.03	168	9.2 ± 1.4	7.9 ± 1.2	
AGAL333.481-00.224_S	2	16:21:40.19	-50:11:47.42	2.12	1.9	0.03	-139	15 ± 2	16 ± 2	5%
		16:21:39.87	-50:11:39.21	2.06	1.8	0.03	-174	14 ± 2	19 ± 3	
AGAL333.483-00.246_S	4	16:21:50.34	-50:13:06.99	1.09	2.8	0.05	-143	5.9 ± 0.9	1.9 ± 0.3	3%
		16:21:49.58	-50:12:43.06	2.48	3.2	0.05	96	14 ± 2	3.1 ± 0.5	
		16:21:47.27	-50:12:46.88	1.09	2.2	0.04	148	6 ± 0.9	4.3 ± 0.6	
		16:21:46.96	-50:12:27.54	0.84	1.8	0.03	150	4.6 ± 0.7	5.6 ± 0.8	
AGAL333.566-00.296_S	2	16:22:24.52	-50:11:34.04	0.49	2.2	0.04	98	2.8 ± 0.4	1.9 ± 0.3	13%
		16:22:21.61	-50:11:09.09	19.47	7.8	0.13	-152	109 ± 16	1.8 ± 0.3	
AGAL341.196-00.221_S	1	16:52:15.91	-44:28:07.19	9.53	6.8	0.12	104	96 ± 14	1.8 ± 0.3	11%
Protostellar										
AGAL318.049+00.086_S	2	14:53:38.83	-59:09:09.51	2.50	2.3	0.04	161	7.9 ± 1.2	4.1 ± 0.6	27%
		14:53:42.84	-59:08:49.73	124.11	6.6	0.12	113	393 ± 59	9 ± 1.4	
AGAL322.158+00.636_S	5	15:18:32.29	-56:38:58.19	7.64	3.5	0.07	138	33 ± 5	3.9 ± 0.6	31%
		15:18:34.98	-56:38:23.76	351.59	6	0.11	127	1544 ± 232	36 ± 5	
		15:18:38.60	-56:38:12.50	12.01	2.9	0.05	-164	53 ± 8	12 ± 2	
		15:18:37.97	-56:38:03.84	4.36	2	0.04	130	19 ± 3	13 ± 2	
		15:18:34.23	-56:37:39.45	13.90	4.3	0.08	117	61 ± 9	4.1 ± 0.6	
AGAL329.184-0.314_S	2	16:01:47.02	-53:11:44.29	197.55	5.6	0.1	-158	590 ± 89	24 ± 4	65%
		16:01:44.68	-53:11:22.57	5.47	2.8	0.05	98	17 ± 3	5.9 ± 0.9	
AGAL332.986-00.489_S	2	16:20:41.88	-50:44:27.49	11.25	6.5	0.12	-139	45 ± 7	1 ± 0.2	8%
		16:20:38.18	-50:43:56.12	53.61	8.1	0.14	127	212 ± 32	2.4 ± 0.4	
AGAL333.473-00.236_S	1	16:21:41.37	-50:12:36.78	1.46	2.9	0.05	129	7.9 ± 1.2	2.3 ± 0.3	2%

AGAL337.761-00.339_S	5	16:39:57.52	-47:09:27.08	15.00	5.7	0.09	111	180 ± 27	8.3 ± 1.2	10%
		16:39:58.57	-47:08:59.80	0.45	2.4	0.04	-168	5.3 ± 0.8	3.5 ± 0.5	
		16:40:00.76	-47:08:50.89	0.55	2	0.03	-168	6.6 ± 1	7.2 ± 1.1	
		16:39:58.77	-47:08:46.49	1.05	3.4	0.05	150	13 ± 2	2.8 ± 0.4	
		16:39:58.06	-47:08:29.54	1.42	2.9	0.05	67	17 ± 3	5.7 ± 0.9	
AGAL341.216-00.236_S	3	16:52:22.31	-44:27:53.02	10.05	4.5	0.08	77	121 ± 18	7.9 ± 1.2	12%
		16:52:23.81	-44:27:51.76	16.02	3.7	0.07	93	193 ± 29	23 ± 4	
		16:52:19.81	-44:27:38.69	1.15	1.9	0.03	158	14 ± 2	12 ± 2	
AGAL341.217-00.212_S	1	16:52:17.92	-44:26:51.23	62.89	4.7	0.09	140	290 ± 40	16 ± 2	35%
AGAL341.219-00.259_S	2	16:52:32.24	-44:28:35.31	6.32	3.1	0.05	157	56 ± 8	12 ± 2	5%
		16:52:30.54	-44:28:32.38	2.52	2.1	0.04	-175	22 ± 3	14 ± 2	
AGAL341.236-00.271_S	1	16:52:36.98	-44:28:12.52	26.70	6.4	0.12	142	231 ± 35	5.2 ± 0.8	16%
HII clump										
AGAL310.014+00.387_S	1	13:51:37.55	-61:39:10.87	57.89	5.8	0.1	99	183 ± 27	6 ± 0.9	16%
AGAL322.164+00.622_S	1	15:18:39.96	-56:38:54.97	122.29	6.3	0.08	104	410 ± 60	9.7 ± 1.5	42%
AGAL331.626+00.526_S	1	16:09:57.78	-50:56:17.67	19.43	7.1	0.12	165	112 ± 17	2.1 ± 0.3	13%
AGAL333.068-00.447_S	3	16:20:52.42	-50:39:04.34	1.56	1.9	0.03	-151	6 ± 0.9	5.6 ± 0.8	22%
		16:20:49.20	-50:38:38.93	256.16	7.8	0.14	-139	989 ± 148	12 ± 2	
		16:20:45.93	-50:38:43.19	5.27	2.9	0.05	-166	20 ± 3	5 ± 0.8	
AGAL333.553-00.291_S	2	16:22:17.57	-50:11:55.67	0.43	1.9	0.03	136	2 ± 0.3	2.2 ± 0.3	14%
		16:22:16.62	-50:11:30.94	6.49	6.4	0.11	118	30 ± 5	0.9 ± 0.1	
AGAL340.248-00.374_S	6	16:49:36.48	-45:18:09.11	2.57	3.3	0.06	80	15.7 ± 2.4	2.2 ± 0.3	12%
		16:49:26.93	-45:18:05.09	18.03	3.3	0.06	154	110 ± 17	16 ± 3	
		16:49:30.09	-45:17:48.68	102.82	7.3	0.14	100	626 ± 94	8.1 ± 1.2	
		16:49:34.07	-45:17:23.93	1.58	3	0.06	102	9.6 ± 1.4	1.9 ± 0.3	
		16:49:32.84	-45:17:16.96	0.94	2.2	0.04	159	5.7 ± 0.9	2.6 ± 0.4	
		16:49:35.42	-45:17:12.45	1.87	2.8	0.05	156	11 ± 2	2.8 ± 0.4	
PDR										
AGAL340.319-00.227_S	4	16:49:07.84	-45:08:58.92	6.59	4.8	0.09	75	34 ± 5	1.8 ± 0.3	6%
		16:49:09.18	-45:08:37.85	0.53	1.9	0.03	118	2.8 ± 0.4	2.6 ± 0.4	

		16:49:05.92	-45:08:18.95	1.14	2.3	0.04	97	5.9 ± 0.9	2.8 ± 0.4	
		16:49:06.88	-45:07:53.05	2.08	3.4	0.06	116	11 ± 2	1.7 ± 0.3	
Unknown										
AGAL340.299-00.222_S	1	16:49:02.48	-45:09:34.42	15.09	7.2	0.13	116	154 ± 23	2.5 ± 0.4	10%

[a] $f = \sum M_{core}/M_{clump}$

4.5 Analysis and discussion

4.5.1 Core parameters

The physical parameters of the cores are listed in Table 4.4.2. In the following we describe the derivation of the physical parameters.

Sizes

Cols. 6 and 7 of Table 4.4.2 present size of the cores in arcsec and pc. The latter is derived using the clump distance given in col. 2 of Table 4.1. In prestellar clumps the core radii range from 0.03 to 0.13 pc with an average value of 0.06 pc, for in protostellar clumps the core radii range from 0.03 to 0.14 pc with an average value of 0.07 pc, and in H II clumps the core radii range from 0.03 to 0.14 pc with an average value of 0.12 pc.

Masses

The mass of the cores were calculated from the continuum flux density, S_ν, using the expression,

$$M = \frac{S_\nu D^2 R_{gd}}{k_\nu B_\nu(T)}, \tag{4.1}$$

where k_ν is the dust mass absorption coefficient at frequency ν, B(T) is the Planck function at temperature T, D is the distance and R_{gd} is the gas-to-dust ratio. We use $k_{350\mu m} = 0.07\ cm^2$ gm^{-1} (e.g., André et al. 2016) assuming a gas to dust ratio of R_{gd}=100.

Col. 9 of Table 4.4.2 lists the mass of the cores. We assume temperature of the parent clump given in col. 3 of Table 4.1 and distance given in col. 2 of Table 4.1 for the mass determination of the cores. The masses range from 4.6 to 109 $M_\odot$ in prestellar clumps, 6.6 to 1544 $M_\odot$ in protostellar clumps and 2 to 989 $M_\odot$ in H II clumps. The PDR clump has cores with masses ranging from 2 to 34 $M_\odot$ and the unknown clump has one substructure with mass of 154 $M_\odot$. The average mass of the combined sample is 131 $M_\odot$.

Densities

The molecular hydrogen density of the cores is obtained from the expression,

$$n = \frac{M}{\frac{4}{3}\pi\mu m_H r^3} \tag{4.2}$$

where radius r is the core radius, μ is the molecular weight per hydrogen molecule and m_H is the mass of hydrogen. Col. 10 of Table 4.4.2 lists the densities of the cores, which

range from 1.0×10^5 to 3.6×10^6 cm^{-3}.

4.5.2 Mass distribution

Figure 4.8 presents the mass distribution of the whole sample of cores detected towards the 23 clumps. The minimum mass is 2 $M_\odot$ and the most massive core has a mass of 1.5×10^3 $M_\odot$. The average core mass is 131 $M_\odot$ (indicated by the dotted black line in the plot). Also shown in the plot (indicated by the dotted red line) is the Jeans mass (13.3 $M_\odot$) estimated using an average density (1.53×10^4 cm^{-3}) and average temperature (21.6 K) of the sample clumps.

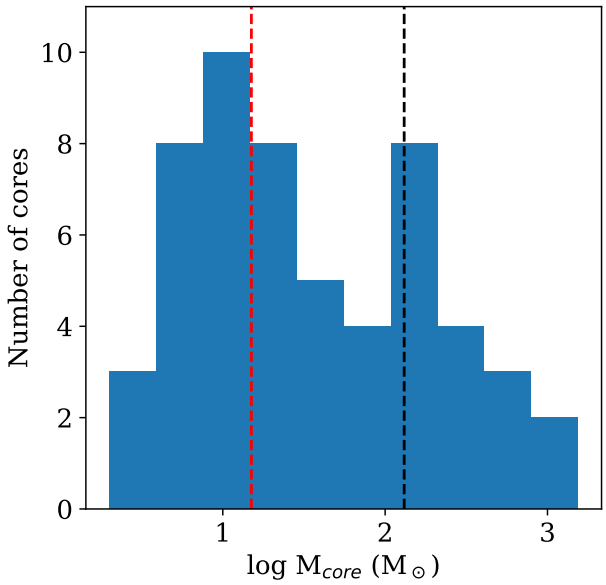

Figure 4.8: Mass distribution of the combined sample of cores in all 23 clumps. The dotted red line indicates Jeans mass for clumps with average density and temperature. The dotted black line shows the mean mass of the cores.

The fragmentation properties of clumps in the prestellar, protostellar and H II stages are summarized in Table 4.4. In addition to the average number of observed substructures, average clump temperature and average line widths, Table lists the core mass fraction defined as total mass in the form of cores divided by the clump mass as well as the fraction of the mass of the central core relative to the clump mass.

The core mass fraction range from 3% to 13% for prestellar clumps, 2% to 65% for protostellar and 12% to 42% for H II clumps. The average value of the core mass fraction increases from prestellar (8%) to protostellar (21%) and H II clumps (20%). This result suggests that at early stages the fragmented cores are smaller in mass while at later stages they have gathered a significant fraction of the clump mass. In addition, we find that most of the mass is contained in the central or most massive substructure as indicated by the central core mass fraction with respect to the clump mass given in line 6 of Table 4.4.

4.5.3 Fragmentation properties

In the following we explore possible correlations between the fragmentation level of a clump with its physical properties, such as line width (proxy for the non thermal motion or turbulence), dust temperature, molecular hydrogen density and virial parameter. No correlations are found between the number of cores in a clump and its bulk properties. On the other hand, correlations are found between the fraction of the mass of the central core relative to the clump mass and clump parameters.

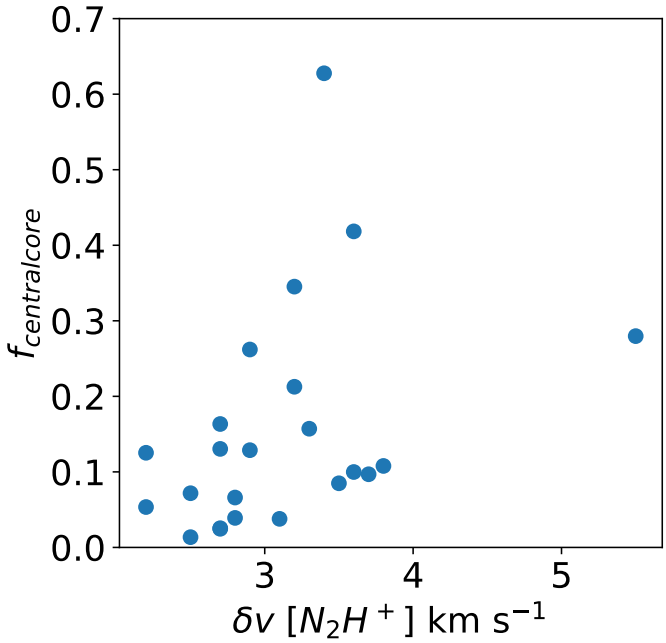

Figure 4.9: Line widths from N_2H^+ (1→0) toward the clumps versus mass fraction of the central core.

Figure 4.9 presents a plot of the mass fraction of the central core versus clump line width. Clumps containing central cores with large mass fraction tend to have larger line widths ($\geq$ 3 km s^{-1}). This suggests that the central cores may be supported against fragmentation by high levels of turbulence. We note that given our small sample we can not draw general conclusions. The larger line widths could also be due to increased star formation activity

Table 4.4: Fragmentation properties.

Properties	Clump type		
	Prestellar	Protostellar	H II
No. of substructures	1 to 4	1 to 5	1 to 6
Average no. of substructures	2.4	2.4	2.3
Average T_{dust} (K)	18.3	21.9	24.5
Average line widths (δv km s^{-1})	2.7	3.3	3.1
Core mass fraction (f = $\sum M_{core}/M_{clump}$)	8%	21%	20%
Central core mass fraction ($M_{centralcore}/M_{clump}$)	7%	20%	19%

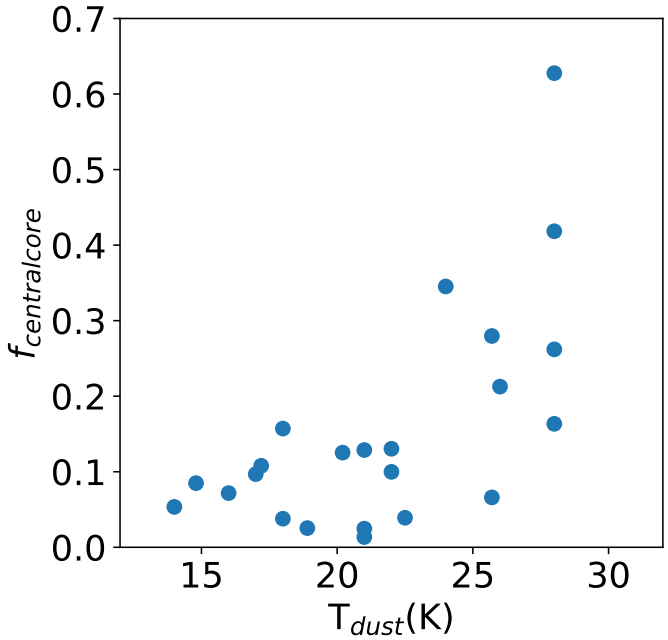

Figure 4.10: Line widths from N_2H^+ (1→0) toward the clump versus mass fraction of the central core.

and global gravitational collapse.

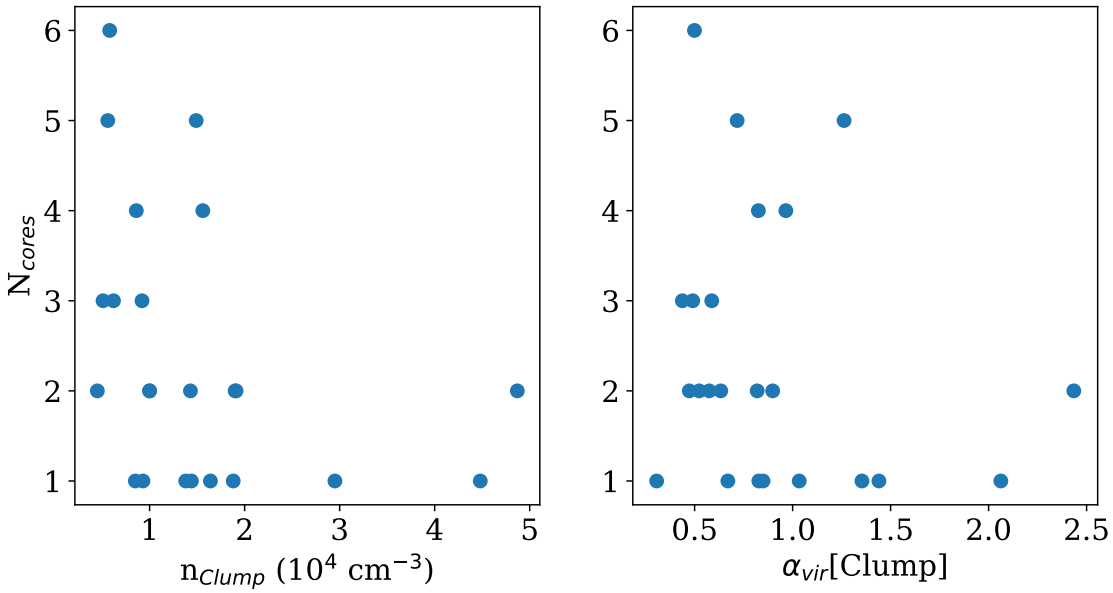

Figure 4.11: Left: Molecular hydrogen density of clumps versus number of cores. Right: virial parameter of the clump versus number of cores.

Fig 4.10 shows that the mass fraction of the central core seems to be correlated with clump temperature. This result may reflect that the more massive central core in the clump is likely in an active accretion phase heating up the surrounding dust and gas that results in an increase in temperature. Although Jeans mass is higher for clumps with higher temperature

and predicts less number of fragmentation, the high mass fraction of central core can not be explained solely by Jeans fragmentation analysis.

Fig 4.11 plots the number of cores in a clump as a function of its density (left panel) and virial parameter (right panel). It shows that clumps containing higher number of cores are at sub-virial and virial state (left) and that clumps with higher densities contain less number of fragments.

To investigate a possible relationship between the clump fragmentation characteristics, evolutionary stage and global kinematics, we list in Table 3.12 the 15 Artemis clump for which their overall kinematics was reported in the SuperMALT survey (see 3.5.5 of Chapter 3). Col. 1 lists the large scale motion of the clump, as determined from the shape of the HCO^+(3-2) and/or HCN (3-2) line profiles, col. 2 gives the fragmentation characteristics, cols. 3 and 4 give, respectively the fraction of the total mass of the cores relative to the clump mass and the fraction of the mass of the central core relative to the clump mass. Of the 15 Artemis clumps, 9 exhibit infalling motions and 5 exhibit expansion motions. Considering only the collapsing clumps, protostellar clumps show considerable larger total core to clump mass fraction and central core to clump mass fraction than prestellar clumps. The average value of the total core to clump mass ratio is 8% for prestellar clumps and 22% for protostellar clumps. These results strongly support the global collapse scenario for the evolution of the clumps with the cores in the protostellar phase accreting mass from the clump environment.

Table 4.5: Global gas motion and fragmentation characteristics of the clumps.

Clump	Gas motion[a]	Fragmentation characteristics	f^b_{core}	$f^c_{centralcore}$
		Prestellar stage		
AGAL331.639+00.501_S	Infall	1 central core and 2 less massive cores	7%	5%
AGAL333.481-00.224_S	Infall	2 central cores, similar mass	5%	3%
AGAL333.566-00.296_S	Steady	1 central core and 1 less massive core	13%	12%
AGAL341.196-00.221_S	Infall	Single core	11%	11%
		Protostellar stage		
AGAL318.049+00.086_S	Infall	1 central core and 1 less massive core	27%	26%
AGAL322.158+00.636_S	Infall	1 central core and 4 less massive cores	31%	28%
AGAL332.986-00.489_S	Expansion	1 central core and 1 less massive core	8%	7%
AGAL337.761-00.339_S	Infall	1 central core and 4 less massive cores	10%	9%
AGAL341.216-00.236_S	Expansion	2 central core and 1 less massive core	12%	7%
AGAL341.217-00.212_S	Infall	Single core	35%	35%
AGAL341.219-00.259_S	Infall	2 cores centrally located, one less massive	5%	4%
		H II stage		
AGAL310.014+00.387_S	Infall	Single core	16%	16%
AGAL333.068-00.447_S	Expansion	1 central core and 2 less massive cores	22%	21%
AGAL340.248-00.374_S	Expansion	1 central core and 5 less massive cores	12%	10%
		PDR		
AGAL340.319-00.227_S	Expansion	1 central core and 3 less massive cores	6%	4%

[a] Large scale motion of the clump observed in SuperMALT survey (See Table 3.12).
[b] $f_{core} = \sum M_{core}/M_{clump}$
[c] $f_{centralcore} = M_{centralcore}/M_{clump}$

Limited number of fragmentation

The Jeans mass in a clump with an average density of 10^4 cm^{-3} and temperature of 20 K is M_J = 15 M$_\odot$. Therefore a clump with a mass of 1000 M$_\odot$ is expected to fragment, under the Jeans criteria, into ∼70 cores with Jeans masses. In our observations we achieved an average *rms* noise level of 0.32 Jy/beam allowing to detect cores with masses of ∼2 M$_\odot$, assuming an average distance of 3.6 kpc and dust temperature of 20 K. However, the number of detected fragments range from 1 to 6 per clump with an average number of 3 fragments per clump. 35 % of the clumps show no fragmentation (that is to say one single structure is detected), 30% of clumps exhibit 2 substructures, 13% show 3 substructures, and 22% show more than four substructures. In summary, we only observe 2-3 fragments per clump at the scale of our observations (0.1pc at 3.5 kpc). Csengeri et al. (2017) made ALMA 7m array observations towards a sample of clumps with similar physical properties than those in our sample reporting a fragmentation level of 2-3 cores per clump consistent with our findings. The low level of fragmentation can be attributed to large levels of turbulence, the presence of magnetic fields or to the presence of large scale kinematics of the clump, such as global gravitational collapse.

Core mass function

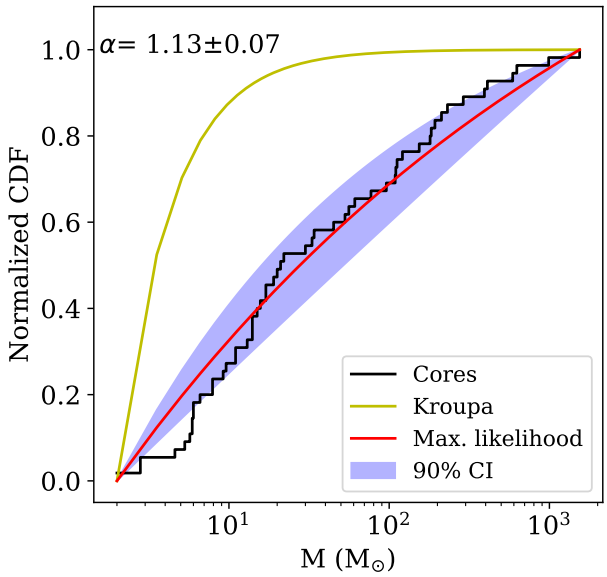

Figure 4.12: The normalized cumulative distribution function (CDF) for the combined sample of cores within 23 clumps observed in Artemis survey. The red line and purple shaded area show the maximum likelihood estimation of the power law index fit and its 90% confidence interval, respectively. The yellow line shows the initial mass function distribution from Kroupa (2001)

Fig. 4.12 shows the normalized cumulative mass distribution of the full sample of cores. Assuming that the core mass function is such that dN/dM ∝ M$^\alpha$, the best fit to the empirical cummulative distribution function (eCDF), using a maximum likelihood method (e.g.,

Servajean et al. 2019; Neupane et al. 2020) gives a power law index α = -1.13±0.07. The 90% confidence interval is from -1.01 to -1.25. Also shown in the plot is the Kroupa (2001) initial stellar mass function (IMF) slope for stars with masses greater than 1 $M_\odot$ of α = - 2.3 (Kroupa 2001). The slope of the core mass function is much shallower than the Kroupa IMF slope. This reflects that the fragmentation process of massive and dense clumps is a complex process. They typically exhibit high-mass core forming efficiency higher at the early stages of their evolution.

4.6 Summary

We observed the 350μ continuum emission from 23 MALT90 MDCs in different evolutionary stages (5 prestellar, 10 protostellar, 6 H II, 1 PDR and 1 Unknown clump) using the Artemis camera mounted at the APEX telescope located in the Chajnantor plateau in the Atacama desert, Chile. The spatial resolution is 8″ (∼0.1 pc at the average distance of the sample of 3.6 kpc) and the sensitivity is 0.32 Jy/beam. The results of the Artemis observations are summarized as follows.

1) While the clumps exhibit singular structure in the Atlasgal 870 μm maps (19.5 ″), the emission at 350μ is typically resolved in a few (2-3) subtructures. The substructures (or cores) are found within the minimum (3σ) contour level in Atlasgal emission maps, but are not necessarily located near the peak position of the clump.

2) The number of cores, extracted using the Dendogram algorithm, range from 1 to 4 in prestellar clumps, 1 to 5 in protostellar clumps and 1 to 6 in H II clumps. A PDR clump harbour 3 substructures and an unknown type clump harbour one core. On average, we observed 2 to 3 substructures per clump, similar to the findings of Csengeri et al. (2017).

3) The sizes of the cores range from 0.03 to 0.14 pc, the masses from 2 to 1544 $M_\odot$ and the densities from 1.0×10^5 to 3.6×10^6 cm^{-3}. The average values of the size, mass and density are 0.08 pc, 131 $M_\odot$ and 7.3×10^5 cm^{-3}, respectively.

4) We investigated possible correlations between number of cores within a clump and its physical properties such as line width (turbulence), dust temperature, density and virial parameter. We do not find significant correlation between the clump physical properties and number of substructures. On the other hand, we find that clumps with large line widths and high temperatures exhibit more massive core at their centers. The clumps with more fragments are the less dense ones and are at virial or sub-virial state.

5) The average core mass fraction, defined as the total mass in the form of cores divided by the clump mass, is 8% for prestellar clumps, 21% for protostellar clump and 20% for H II clump. This result can be explained as an evolutionary effect, in which the core mass fraction increases with the clump evolution.

We conclude that clump fragmentation takes place during the early stages of evolution, giving rise to cores with masses close to the Jean mass. Thereafter the cores accrete more mass from the clump environment. The centrally located cores become more massive because

they gather mass at a higher rate due to their preferential location in the gravitational potential well. The profiles of the molecular line emission from the central core show blueshifted asymmetries, indicating infall signatures, as well as strong wing emission indicating outflowing motions. It is in these cores that a single or a cluster of high-mass stars will form.

Acknowledgements: This work is based on data acquired with the Atacama Pathfinder Experiment (APEX). APEX is a collaboration between the Max Planck Institut fur Radioastronomie, the European Southern Observatory, and the Onsala Space Observatory.

Chapter 5

ALMA observations of two massive and dense MALT90 clumps

This work has been published in Neupane et al 2020, ApJ, 890, 76.

We report Atacama Large Millimeter Array observations of 3 mm dust continuum emission and line emission, in HCO^+, $H^{13}CO^+$, N_2H^+ and CH_3CN, towards two massive and dense clumps (MDCs) in early but distinct evolutionary phases (prestellar and protostellar), made with the goal of investigating their fragmentation characteristics at angular scales of $\sim 1''$. Towards the prestellar clump we detected ten compact structures (cores), with radius from 1200 to 4500 AU and masses from 1.6 to 20 $M_\odot$. Half of these cores exhibit inverse P Cygni profiles in HCO^+ and are subvirialized indicating that they are undergoing collapse. Towards the protostellar clump we detected a massive (119 $M_\odot$) central core, with a strong mass infall rate, and nine less massive cores, with masses from 1.7 to 27 $M_\odot$ and radius from 1000 to 4300 AU. CH_3CN rotational temperatures were derived for 8 cores in the protostellar clump and 3 cores in the prestellar clump. Cores within the prestellar clump have smaller linewidths and lower temperatures than cores within the protostellar clump. The fraction of total mass in cores to clump mass is smaller in the prestellar clump ($\sim$6%) than in the protostellar clump ($\sim$23%). We conclude that we are witnessing the evolution of the dense gas in globally collapsing MDCs; the prestellar clump illustrating the initial stage of fragmentation, harboring cores that are individually collapsing, and the protostellar clump reflecting a later stage in which a considerable fraction of the gas has been gravitationally focused into the central region.

5.1 Introduction

A wealth of observations have shown that filamentary structures are ubiquitous within molecular clouds (e.g., Schneider & Elmegreen 1979; Myers 2009; Molinari et al. 2010; André et al. 2010). These long molecular structures are inhomogeneous and present over-densities, most likely a result of fragmentation (e.g., Takahashi et al. 2013; Teixeira et al. 2016; Contreras et al. 2016). It is in the most massive ($\sim 10^3$ $M_\odot$) and dense ($\sim 10^4$ cm^{-3}) overdensities, which we refer as massive and dense clumps (or MDCs), where high-mass stars form (Faúndez et al.

2004; Contreras et al. 2017). However, the early evolution of MDCs and the ensuing fragmentation leading to the formation of cores is not well understood. The relative importance of primordial clump fragmentation versus large-scale accretion in determining the distribution of core masses still remains to be assessed. Recent ALMA observations with moderate angular resolution ($\sim$3.5″) towards a sample of MDCs in early evolutionary stages (infrared quiet) with masses in the range from 200 to 2000 $M_\odot$ revealed limited fragmentation at the scale of $\sim$0.1 pc, showing typically $\sim$3 cores, and a high efficiency in the formation of high-mass cores (Csengeri et al. 2017). Observations with higher resolution ($\sim$0.03-0.05 pc) of clumps with similar characteristics show a range of substructures – from a few fragments (e.g., Peretto et al. 2013; Sanhueza et al. 2017) to ten or more fragments (e.g., Lu et al. 2018, Contreras et al. 2018). Some works concluded that the fragmentation properties of clumps are described by gravo-turbulence (e.g., Zhang et al. 2015) while others find them consistent with pure thermal Jeans fragmentation (e.g., Palau et al. 2015, 2018). Teixeira et al. (2016) found that the separation of clumps within a filamentary cloud is consistent with the Jeans length of the filament while the separation between the individual cores within the clumps is smaller than the Jeans length of the clump, which they suggest indicates that the local collapse of the clumps ocurrs at a much faster pace than the global collapse of the filament.

Determining the physical and kinematical properties of the molecular gas in MDCs at both, the large clump scale ($\sim$ 1 pc) and small core scale (5000 AU), will permit to investigate the presence of global or localized collapse and the characteristics of the primordial fragmentation. These properties together constitute a key discriminator between current models of the fragmentation and evolution of MDCs, such as Competitive accretion (Bonnell & Bate 2006), Turbulent fragmentation (Padoan & Nordlund, 2002), Hierarchical gravitational fragmentation (Vázquez-Semadeni et al. 2009, 2017).

In this work we present a study of two MDCs, one in the prestellar stage and the other in the protostellar stage of evolution, using high resolution ALMA Band 3 continuum and molecular line observations with the goal of identifying and determining the physical characteristics of the dense and compact structures within the MDCs and to test models of the fragmentation and evolution of MDCs, and possibly to guide future theories. In section 5.2 we briefly review the characteristics of the observed MDCs. In section 5.3 and section 5.4 we describe the observations and present the results, respectively. In section 5.5 we discuss the analysis of the continuum and molecular observations. In section 5.6 we compare our results with the predictions of different models.

5.2 The targets

The two MDCs studied in this work were selected from the MALT90[1] catalog (Rathborne et al. 2016), one AGAL333.014-0.521 (hereafter AGAL333) classified as been in the prestellar stage and the other AGAL329.184-0.314 (hereafter AGAL329) classified in the protostellar stage of evolution (see Figure 5.1). The MALT90 project (Foster et al. 2011; Jackson et al. 2013) surveyed, with the Mopra telescope, the emission in 15 different molecular lines (mostly

[1]The Millimetre Astronomy Legacy Team 90 GHz Survey: http://malt90.bu.edu

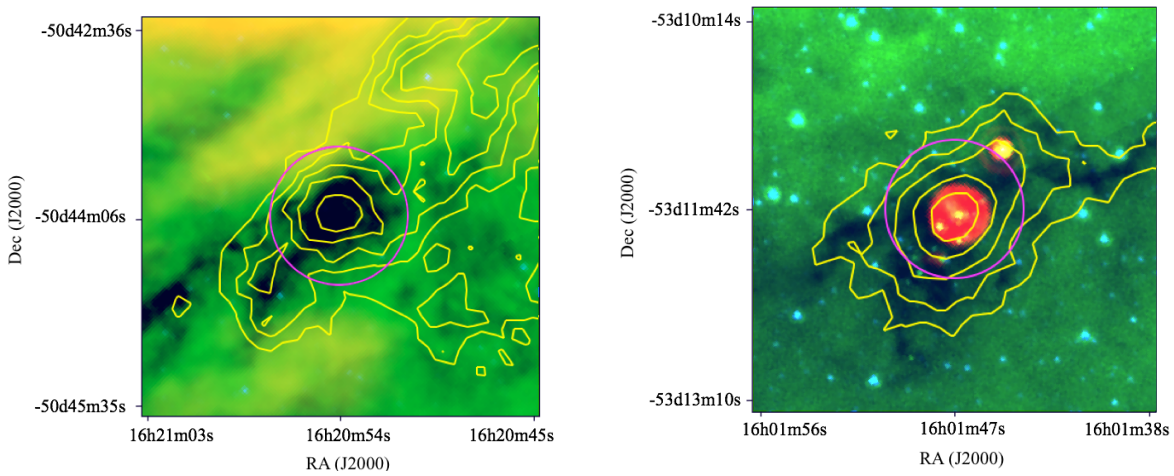

Figure 5.1: Three colour Spitzer images (blue: 3.6 μm, green: 8 μm and red: 24 μm)(IRAC: Fazio et al. 2004, MIPS: Rieke et al. 2004) of the MALT90 targets overlaid with contours of the 870 μm emission from the Atlasgal survey (FWHM$\sim$20$''$). The magenta circle indicate the ALMA primary beam (FWHM) of $\sim$62$''$ in Band 3. Left panel: Prestellar clump AGAL333. Contour levels are drawn at 3σ, 5σ, 7σ, 9σ and 11σ (σ = 93.3 mJy beam^{-1}). Right panel: Protostellar clump AGAL329. Contour levels are drawn at 3σ, 6σ, 12σ, 24σ and 48σ (σ = 89.3 mJy beam^{-1}).

J=1$\rightarrow$0 transitions) and one recombination line towards $\sim$3200 MDCs. Towards AGAL329 and AGAL333 emission was detected in, respectively, 9 and 8 lines, including the high density tracers HCO^+, HNC, HCN and N_2H^+. The J=1$\rightarrow$0 transitions of these four species have critical densities[2] of the order of 10^5-10^6 cm^{-3} for a temperature of 20 K, indicating that the clumps indeed have high densities, a requisite for the formation of high-mass stars. The spectra of the optically thick HCO^+ emission from the protostellar clump shows a double peak profile, with the blueshifted peak being stronger than the redshifted peak, while the spectra of the optically thin $H^{13}CO^+$ emission shows a single line with a peak velocity in between the velocities of the blue and red peaks of the HCO^+ line. These profile characteristics are signposts of infall motions (e.g, Anglada et al. 1987; Mardones et al. 1997; De Vries & Myers 2005) suggesting that AGAL329 is undergoing a large scale collapse. On the other hand, the profiles of the HCO^+ and $H^{13}CO^+$ emission from the prestellar clump are nearly Gaussian, indicating a more static, quiescent region. As expected, SiO emission, which traces outflow/shocked gas (e.g., Martin-Pintado et al. 1992), is only detected towards AGAL329.

Table 5.1 lists observed and derived parameters of the clumps. The velocities and line widths correspond to those determined from the hyperfine (HF) fitting of the N_2H^+ emission as observed with the Mopra telescope in the MALT90 survey. The dust temperatures were determined by us from a fit to the spectral energy distributions (SEDs), shown in Figure 5.2, using a single temperature modified blackbody model (c.f., Guzmán et al. 2015; König et al. 2017) ,

$$S_\nu = \Omega_s B_\nu(T_\mathrm{d})(1 - \mathrm{e}^{-\tau_\nu}) \quad , \tag{5.1}$$

where S_ν, B_ν, T_d and Ω_s are, respectively, the flux density, Planck function, dust temperature and effective solid angle subtended by the clump. We assume that the dependence of the

[2]Defined as, $n_{crit} = A_{ul}/\gamma_{ul}$, where A_{ul} is Einstein coefficient and γ_{ul} is the collisional rate.

Table 5.1: Observed and derived parameters of the clumps.

Parameter	AGAL333.014-0.521	AGAL329.184-0.314	Reference
Clump type	Prestellar	Protostellar	(1)
Distance (kpc)	3.72	3.46	(2)
V_{lsr} (km s^{-1})	-53.8	-50.5	(1)
Line width (km s^{-1})	3.1	3.4	(1)
$F_{870\mu m}$ (Jy)	16.42	23.02	(3),(4)
θ ($'' \times ''$)	43×17	24×15	(3),(4)
Size (pc)	0.49	0.32	(5)
T_{dust} (K)	22	28	(5)
$M_{dust}(M_\odot)$	1080	940	(5)
n(H_2) (10^5cm^{-3})	0.32	1.00	(5)
$M_{vir}(M_\odot)$	980	770	
α_{vir}	0.91	0.82	
Jeans mass ($M_\odot$)	6.8	5.5	
Jeans radius (pc)	0.09	0.06	

(1) Rathborne et al. 2016; (2) Whitaker et al. 2017; (3) Contreras et al. 2013;
(4) Urquhart et al. 2014; (5) this work.

optical depth, τ_ν, with frequency ν can be expressed as

$$\tau = (\nu/\nu_o)^\beta \quad , \tag{5.2}$$

where ν_o is the frequency at which the dust opacity is unity and β is the spectral index of the dust absorption coefficient.

The data points at infrared wavelengths (70 to 500 μm; red circles) were obtained from the Hi-Gal images (Molinari et al. 2010) available in the Herschel Science Archive and the data point at 850 μm (black square) was obtained from ATLASGAL images (Schuller et al. 2009). The fluxes were extracted using simple aperture photometry of a circular region with radii of 27$''$ and 20$''$ for the prestellar and protostellar clumps, respectively. Errors in the flux densities, mostly due to calibration uncertainties, are less than 30%. Error bars are then smaller than the size of the symbols. Also incorporated in the SED are the flux densities measured at 100 GHz using the ACA array alone (present work; blue stars) and for the protostellar clump the 1.2 mm flux density reported by Beltrán et al. 2006 (open square). A least squares fit to the SED, using the SciPy optimize module in Python (Virtanen et al. 2019), gave values of T_d and β of 22 K and 2.1 for the prestellar clump and 28 K and 1.6 for the protostellar clump. Shown in the SED of the protostellar clump (Figure 5.2 - left panel) are the flux densities at 18 GHz and 22 GHz observed with ATCA (Sánchez-Monge et al. 2013; triangles). These flux densities are well above those expected from the dust emission model, and most likely correspond to free-free emission from either an ultra-compact H II region or a region of shocked gas.

The clump size, mass, and density, given in lines 7, 9 and 10 in Table 5.1, were derived from the 870 μm continuum emission. The last two parameters were computed using the dust temperatures derived from the SED, a dust absorption coefficient of 1.85 cm^2 gr^{-1} (Ossenkopf & Henning 1994), and a gas to dust ratio of 100. The virial masses, $M_{vir} = 5\sigma^2 R/\mathrm{G}$, where

$\sigma = \Delta V/(8\ln 2)^{1/2}$, are 980 $M_\odot$ for the prestellar clump and 770 $M_\odot$ for the protostellar clump. The virial parameter, defined as $\alpha_{vir} = M_{vir}/M_{dust}$, is 0.91 for the prestellar clump and 0.82 for the protostellar clump, suggesting that both of them are gravitationally bound. Also given in Table 5.1 are the Jeans mass and Jeans radius at the average temperature and density for both clumps.

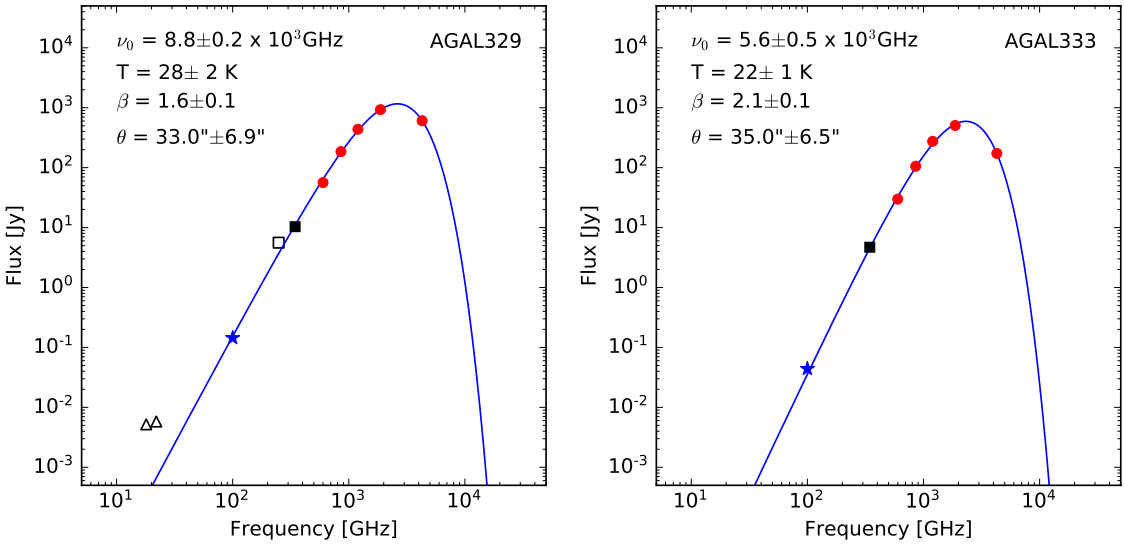

Figure 5.2: Spectral energy distribution of clumps AGAL329 (left) and AGAL333 (right). Symbols are described in the text. The continuous lines (blue) correspond to the SEDs fit obtained from a least squares method. The fitted parameters are given inside each box.

In summary, the clumps selected for this study, which are at similar distances fom the Sun, have masses, sizes and densities characteristics of high-mass star forming regions and their virial parameters indicate that they are gravitationally bound. The IR and molecular line observations suggest, however, that they are in different evolutionary stages. AGAL329 harbors a strong 24 μm point source and show line profiles characteristics of infalling motions, indicating it is in a more advanced stage of evolution than AGAL333, which exhibits Gaussian profiles and no energy sources at IR wavelengths.

5.3 Observations

We made ALMA Band 3 (86-116 GHz) dust continuum and molecular line observations towards the MDCs AGAL333 and AGAL329. Since the sizes of these MDCs are smaller than the ALMA field of view at 3 mm ($\sim$62″), single pointing observations were carried out, as part of Cycle 4, during Dec 2016 and Jan 2017 using both the 12 m array and 7m Atacama Compact Array (ACA). We used two different spectral set ups (see Table 5.2). In the first one, five separate spectral windows (SPW) were used, three for continuum observations and two for observations of the N_2H^+J=1$\rightarrow$0 and CH_3CN J=5$\rightarrow$4 lines. In the second set up, the bandwidth was separated into four SPWs, two for continuum observations and two for observations of the HCO^+J=1$\rightarrow$0 and $H^{13}CO^+$ J=1$\rightarrow$0 lines. The observed molecular species were chosen for the following reasons. N_2H^+ suffers little depletion and is one of the best

Table 5.2: Observational parameters.

SPW	Center Freq. (MHz)	Bandwidth (MHz)	Vel. res. (km s^{-1})	On source integration time (12m Array)	(ACA)
		Observing setup I			
N_2H^+	93173.402	117.19	0.393	23 min	32 min
CH_3CN	91985.284	117.19	0.398		
Cont. 1	92500.000	1875.00	101.262		
Cont. 2	103500.000	1875.00	90.500		
Cont. 3	105400.000	1875.00	88.869		
		Observing setup II			
HCO^+	89188.526	117.19	0.205	23 min	32 min
$H^{13}CO^+$	86754.288	117.19	0.211		
Cont. 4	99000.000	1875.00	94.614		
Cont. 5	100900.000	1875.00	92.832		

tracers of the dense and cold gas (Bergin & Langer 1997; Caselli et al. 2002). The emission in the HCO^+ and $H^{13}CO^+$ lines are, respectively, usually optically thick and thin towards dense clumps and therefore their simultaneous observations are useful to probe the presence of infall or expansion motions. The CH_3CN molecule is a good temperature probe, of both the large scale diffuse gas and small scale dense gas (e.g., Güsten et al. 1985; Blake et al. 1987; Araya et al. 2005; Jones et al. 2008).

Table 5.3: Synthesized beam and rms noise from 7m+12m combined maps.

Maps	AGAL329			AGAL333		
	rms noise (mJy/beam)	Beam ($'' \times ''$)	PA ($^\circ$)	rms noise (mJy/beam)	Beam ($'' \times ''$)	PA ($^\circ$)
Continuum	8.5×10^{-2}	1.5 x 1.3	155	4.7×10^{-2}	1.5 x 1.3	138
HCO^+	4.0	1.6 x 1.3	155	4.0	1.6 x 1.3	147
$H^{13}CO^+$	3.7	1.7 x 1.3	155	3.7	1.7 x 1.3	146
N_2H^+	4.0	2.1 x 1.7	66	4.0	2.1 x 1.7	67
CH_3CN	3.9	2.1 x 1.8	68	3.7	2.1 x 1.8	68

The integration time on source in each of the setups was 23 and 32 minutes for the 7m and 12m array observations, respectively. The bandpass and flux calibrations were carried out using multiple quasars (J1603−4904, J1617−5848, J1427−4206, J1603−4904, J1312−0424, J1617−5848, J1650−5044, J1924−2914, J2131−1207), Mars and Callisto. Data calibration and reduction were made using the Common Astronomy Software Application (CASA: McMullin et al. 2007) version 4.7 package. Independently calibrated 12m and 7m dataset were concatenated and cleaned together using the CASA *tclean* task with a Briggs weighting of 0.5. We used a *multi-scale* clean deconvolver (Cornwell 2008), with scale values of 0, 6, 10 and 30 times the image pixel size (0.3″). For the continuum imaging we concatenated all 5 continuum spectral windows. We used interactive mode for continuum imaging while spectral cubes were made using continuum subtracted spectra with automated masking procedure *auto-multithresh* using noise threshold parameter *noisethreshold* of 2 sigma. This parameter corresponds to the minimum signal-to-noise value that is masked. This technique mimics

what we would do in manual masking in interactive cleaning procedure. From the final spectral line cubes, integrated intensity and velocity maps were made using casa task *immoments*. The angular resolution achieved in the continuum observations are $1.46'' \times 1.34''$ (P.A. 155°) and 1.46″x1.33″ (P.A. 138°) for AGAL329 and AGAL333, respectively. The rms values achieved in the continuum and line maps are listed in the Table 5.3. For the molecular lines the root mean square values of the noise reported is that determined from line-free channels.

5.4 Results

5.4.1 Continuum emission

Figure 5.3 shows our ALMA images of the 3 mm continuum emission towards AGAL329 and AGAL333. The emission from AGAL329 arises from an extended, bright central source and a handful of compact, weaker structures. The emission from AGAL333 arises from several compact structures spread out across the region, most of them being aligned in a NE-SW direction.

Table 5.4: Observed parameters of the cores.

Core	Peak position		Clumpfind		Astrodendro		Remarks
	RA	DEC	Flux	Ang. size	Flux	Ang. size	
	hh:mm:ss	dd:mm:ss	(mJy)	(HWHM ″)	(mJy)	(HWHM ″)	
AGAL329							
mm-1	16:01:48.62	-53:11:45.47	4.69	0.65	3.78	0.65	
mm-2	16:01:48.59	-53:12:02.87	0.49	0.29	0.50	0.41	
mm-3	16:01:47.99	-53:11:54.17	5.12	0.75	5.17	1.09	
mm-4	16:01:47.99	-53:11:46.07	9.84	1.14	5.60	0.84	
mm-5	16:01:47.95	-53:12:04.07	1.04	0.50	1.05	0.61	
mm-6	16:01:46.95	-53:11:43.67	102.15	1.77	93.55	1.66	
mm-7	16:01:46.22	-53:11:37.67	1.00	0.51	0.61	0.45	
mm-8	16:01:44.88	-53:11:15.17	2.48	0.77	2.50	1.06	
mm-9	16:01:44.72	-53:11:24.77	2.74	1.24	–	–	(a)
mm-10	16:01:44.62	-53:11:27.17	8.88	0.67	11.74	1.42	
AGAL333							
mm-1	16:20:56.83	-50:44:01.98	0.32	0.31	0.33	0.43	
mm-2	16:20:56.01	-50:43:59.88	1.77	0.61	1.81	0.74	
mm-3	16:20:55.31	-50:44:01.69	0.46	0.53	0.31	0.50	
mm-4	16:20:54.99	-50:44:07.39	3.12	1.22	2.44	1.23	
mm-5	16:20:54.43	-50:44:03.49	4.25	0.91	3.76	0.97	
mm-6	16:20:53.83	-50:44:17.29	1.38	0.50	1.41	0.60	
mm-7	16:20:53.48	-50:44:09.19	0.58	0.78	0.60	0.77	
mm-8	16:20:52.28	-50:44:18.78	0.57	0.39	0.59	0.50	
mm-9	16:20:52.02	-50:44:20.28	0.42	0.34	0.43	0.45	
mm-10	16:20:51.52	-50:43:45.18	0.68	0.87	0.22	0.45	
mm-11	16:20:51.71	-50:43:46.62	–	–	0.25	0.43	(b)

(a) Core not detected by Astrodendro. (b) Core not detected by Clumpfind.

In order to be quantitative in the identification of structures in the images we used two

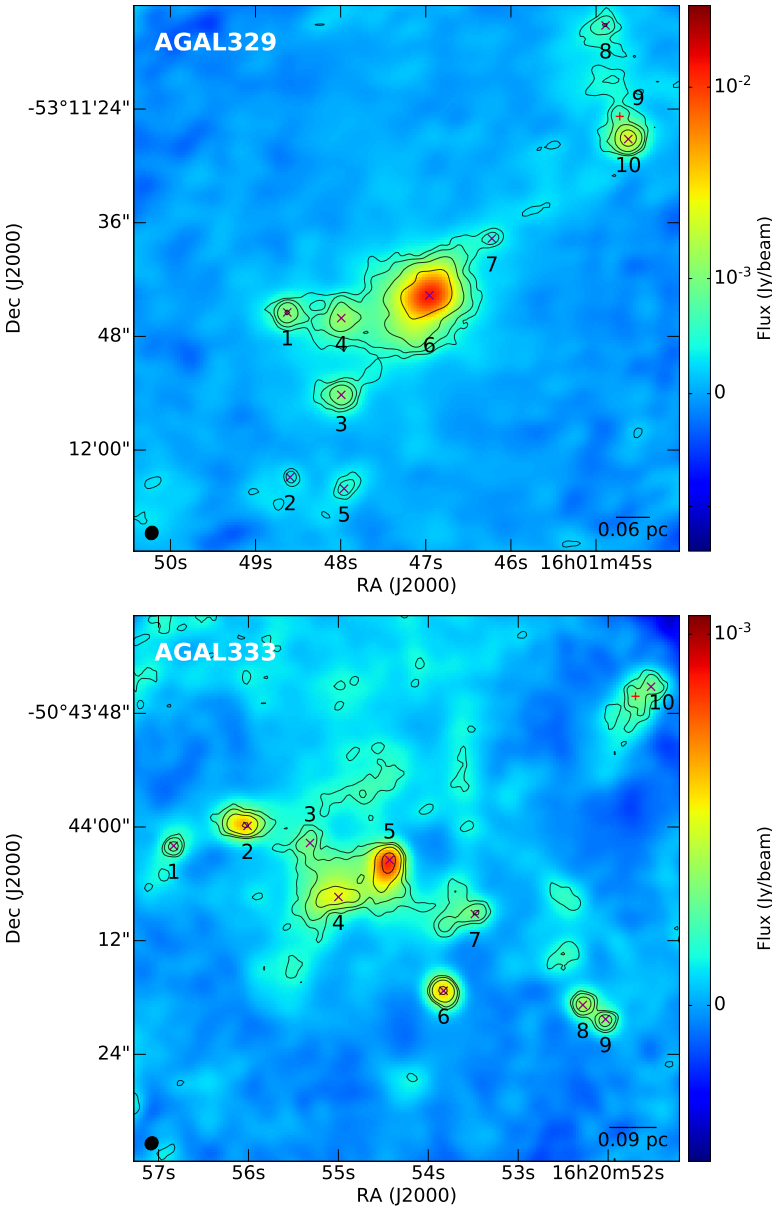

Figure 5.3: Images of the 3 mm continuum emission observed with ALMA towards the protostellar clump AGAL329 (upper panel) and prestellar clump AGAL333 (lower panel). The magenta crosses indicate the cores extracted in common by Astrodendro and Clumpfind. The '+' symbols in red indicate cores identified only by Clumpfind or Astrodendro. The scale bar in the bottom right corner indicates the Jeans radius of the clumps. Also shown are contour levels of the 3mm emission, drawn at 3, 5, 10 and 30 σ, where σ are 4.7×10^{-2} and 8.5×10^{-2} mJy/beam for AGAL333 and AGAL329, respectively. The black ellipse shown at the bottom left corner indicates the beam size.

commonly employed methods: *Astrodendro*[3] and *Clumpfind* (Williams et al. 1994). We note that, in general, the number of extracted features and their parameters depend on the applied method (e.g., Pineda et al. 2009). To identify structures in the *Astrodendro* algorithm, based on a dendrogram analysis (Rosolowsky et al. 2008), requires three inputs parameters: the

[3]http://www.dendrograms.org/

minimum flux to be considered (F_{min}), the separation between neighboring peaks (δ) and the minimum number of pixels (A_{min}) an structure should have. For a robust extraction of structures we adopted F_{min}=3σ, δ=1σ and A_{min} = 1 beam. The key characteristic of this algorithm is its ability to track hierarchical structures over a range of scales. The *Clumpfind* algorithm (Williams et al. 1994) is based on contouring the data array at different levels. The three input parameters are: the minimum flux level to be considered (T_{low}), the contour step (ΔT) and the minimum number of pixels (S_{min}) required to be defined as a unique substructure. For core extraction we adopted T_{low}=3σ, ΔT=2σ and S_{min} = 1 beam.

Towards AGAL329, Astrodendro identified 9 cores while Clumpfind recovered 10. Towards AGAL333, Astrodendro identified 11 cores while Clumpfind identified 10 cores. The list of cores and their observed parameters are presented in Table 5.4. Cols. 2 and 3 give the peak position, cols. 4 and 5 give, respectively, the flux densities and deconvolved angular sizes (HWHM) determined from Clumpfind and cols. 6 and 7 those determined using Dendrogram. We find that the flux densities and angular sizes of the structures (cores) obtained from both methods are similar. Given the similarities, in the remaining of this paper we will use the parameters of the cores determined from the Clumpfind method (labeled in Figure 5.3).

5.4.2 Molecular line emission

Molecular line emission was detected in all four observed species towards both MDCs. We note that the spectrum of the J=1→0 transition of N_2H^+ consists of 7 hyperfine (HF) components (Caselli et al. 1995), however, due to the overlap of closely spaced HF components, only 3 distinct lines are observed. This is illustrated in Figure 5.4 which shows the N_2H^+ spectrum observed toward core mm-4 in AGAL333. The lower velocity component of these three lines, centered at the frequency of 93176.265 MHz, corresponds to a single HF component whereas the other two lines are blends of HF components. Also shown in Figure 5.4 is the spectrum of the rotational J=5→4 transition of CH_3CN observed toward core mm-6 in AGAL329. This rotational transition consists of 5 K components (marked in red), with K being the projection of the total angular momentum of the molecule about the principal rotation axis of the molecule. Their line frequencies, upper state energy levels and line strengths are given in Table 5.5.

Table 5.5: CH_3CN $J = 5 \rightarrow 4$ rotational lines.

Transition	Frequency (MHz)	Velocity shift a (km s^{-1})	Eu/k (K)	Strength $(J^2 - K^2)/J$	S(I,K) $g_k g_I$
$5_0 \rightarrow 4_0$	91987.09	.....	13.2	5.0	1/2
$5_1 \rightarrow 4_1$	91985.31	5.79	20.4	4.8	1/2
$5_2 \rightarrow 4_2$	91979.99	23.14	41.8	4.2	1/2
$5_3 \rightarrow 4_3$	91971.13	52.04	77.5	3.2	1
$5_4 \rightarrow 4_4$	91958.73	92.50	127.6	1.8	1/2

(a) Shift with respect to the $5_0 \rightarrow 4_0$ line

To describe the emission at each position within the MDCs we performed moment analysis of the data (Sault et al., 1995), computing the zeroth (integrated intensity), first (intensity

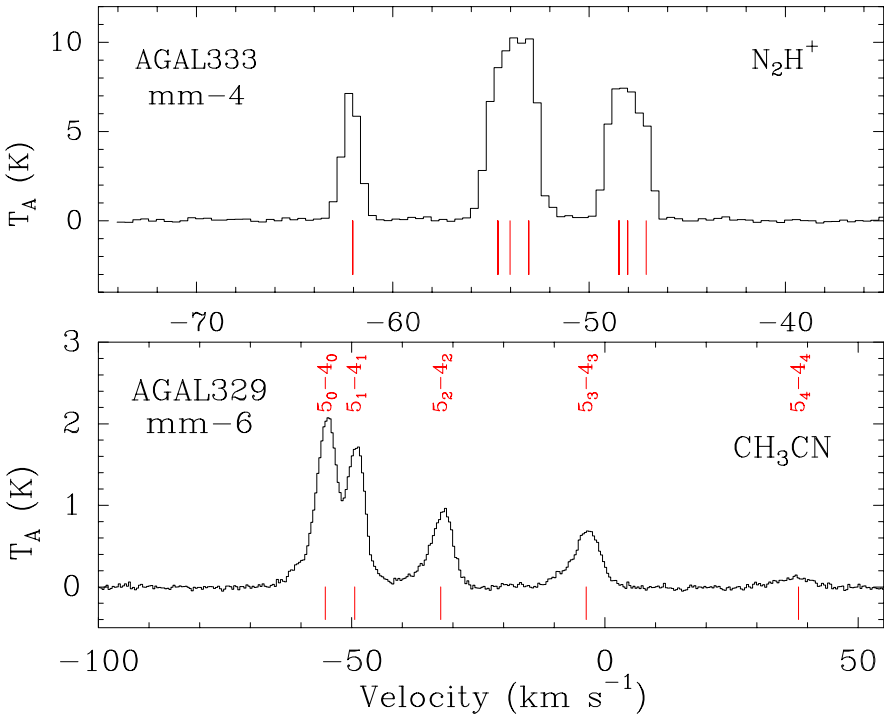

Figure 5.4: Top panel: $N_2H^+(J = 1 \rightarrow 0)$ spectrum from core mm-4 in AGAL333. The red vertical lines at the bottom mark the velocities of the seven hyperfine components. Bottom panel: $CH_3CN(J = 5 \rightarrow 4)$ spectrum from core mm-6 in AGAL329. The red vertical lines at the bottom mark the velocities of the five K components, labeled at the top.

weighted velocity field) and second (intensity weighted velocity dispersion) moments. This approach allows an easy comparison of the characteristics of the emission in the different molecular transitions. The moments of the N_2H^+ emission were computed using the lower velocity component of the three observed lines because it corresponds to a single HF component. To make moment maps of the CH_3CN J=5→4 emission towards AGAL329 we used the emission observed in the $K = 2$ component which is the stronger unblended component. Emission in this line was not detected towards AGAL333 and therefore we used the emission in the $5_0 \rightarrow 4_0$ component for the moment analysis.

Morphology

AGAL329: Figure 5.5 show images of the velocity integrated line emission (moment 0) in all four observed species towards AGAL329. The peak position of the continumm cores are marked with crosses. The velocity range of integration is from -84.0 to -32.0 km s^{-1} for HCO^+, -64.0 to -40.0 km s^{-1} for $H^{13}CO^+$, from -64.0 to -54.0 km s^{-1} for N_2H^+ (corresponding to the lower velocity component of the hyperfine structure) and from -41.0 to -23.0 km s^{-1} for the CH_3CN corresponding to the $J_K = 5_2 \rightarrow 4_2$ component. The morphology of the line emission is noticeably different in the four transitions, most likely due to differences in optical depths, excitation conditions and chemistry.

The emission in the N_2H^+ line (upper left panel) is the brightest and most extended

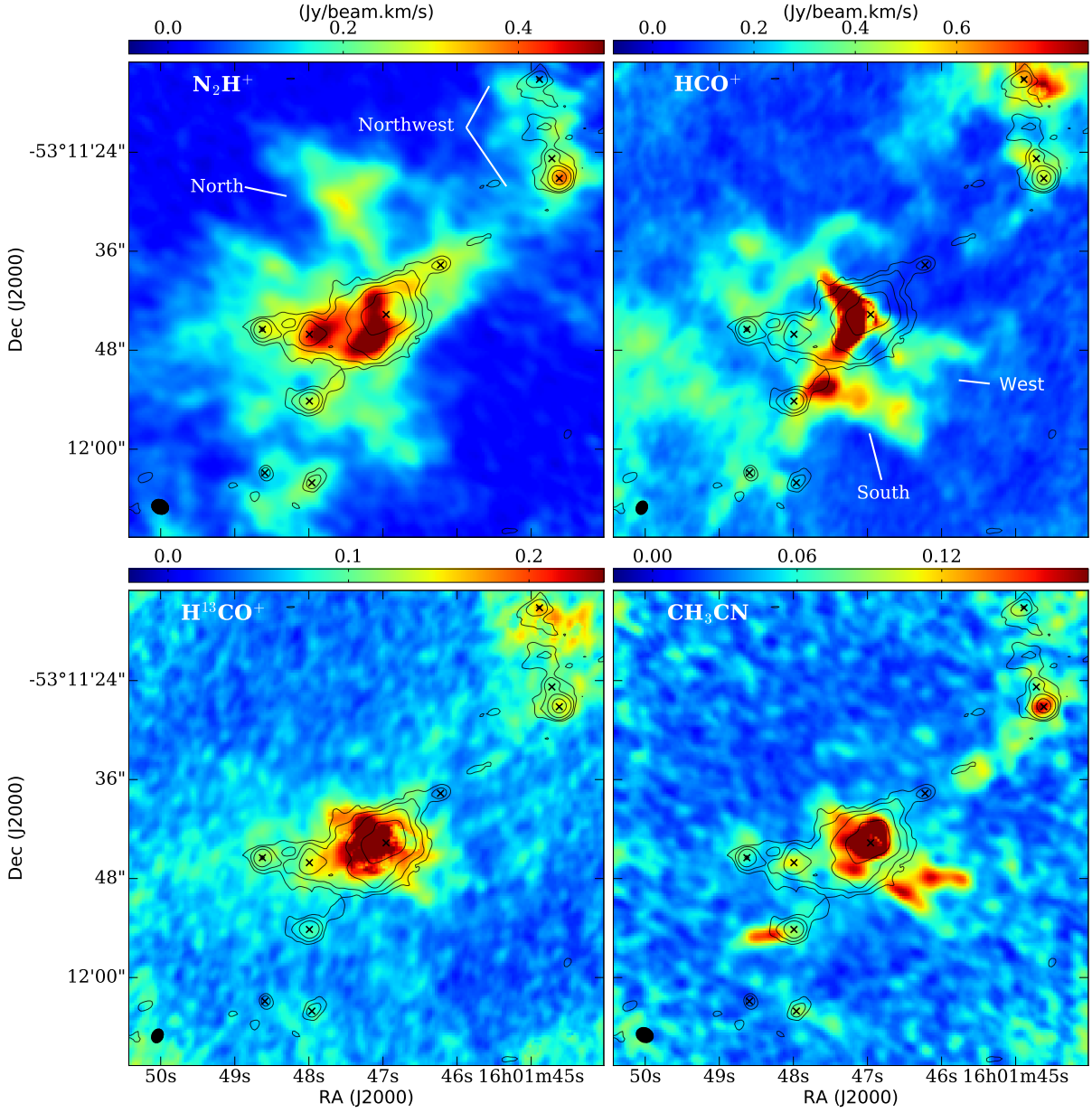

Figure 5.5: Images of the velocity integrated line emission towards AGAL329. Superimposed are contours of the continuum emission. Black crosses mark the peak position of the continuum cores. The black ellipse shown at the bottom left corner indicates the beam size. Top left: N_2H^+; top right: HCO^+, bottom left: $H^{13}CO^+$, bottom right: CH_3CN. Labeled in the different panels are conspicuous features discussed in the text.

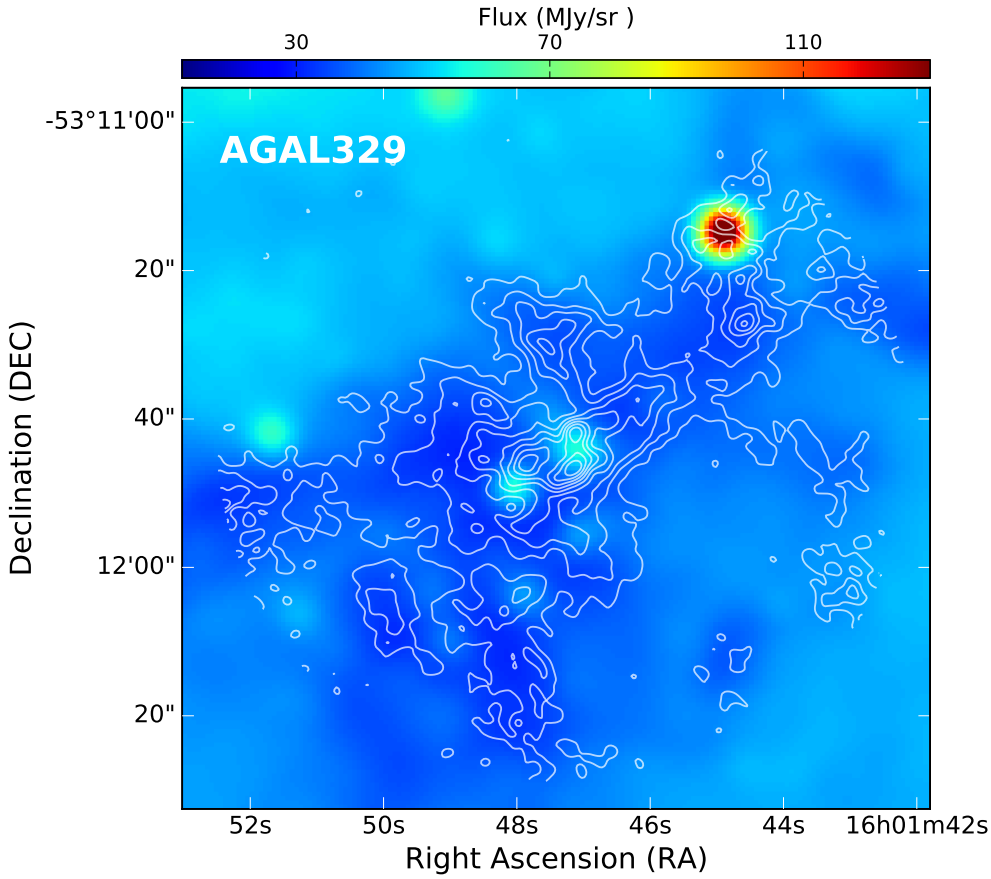

Figure 5.6: Spitzer 8μm image towards AGAL329 overlaid with contours of the velocity integrated N_2H^+ emission observed with ALMA. Contour levels are drawn from 10% to 90% of the peak emission of 0.70 Jy beam^{-1} km s^{-1}, with a step of 10%.

one of the four observed species. It exhibits a bright central region, with a radius of $\sim 6''$, surrounded by weaker emission from a region of $\sim 20''$ in radius, and an extended region of emission seen toward the northwest of the image (labeled Northwest) which is associated with the GLIMPSE source G329.1845-00.3045 (Robitaille et al. 2008). The bright central region exhibits a clumpy ring-like structure with three distinct condensations. The two westernmost condensations are associated with the mm-6 core, but their peak positions do not agree with the peak position of the continuum source, and the easternmost condensation is associated with the mm-4 core. All continuum cores are associated with N_2H^+ emission. A conspicuous feature of the N_2H^+ image, is a region $\sim 15''$ north of the central cores (labeled North), with a size of $\sim 11''$ in diameter, which is not present in the other images and does not harbor continuum sources. Figure 5.6 presents an Spitzer image of the 8μm emission towards AGAL329, which clearly shows that this MDC is associated with an infrared dark cloud, superimposed with contours of the N_2H^+ emission. The morphology of the later closely follows the 8μm dark features, indicating that N_2H^+ is tracing gas with high column densities. Interestingly the North N_2H^+ region is well correlated with an 8μm dark feature. This, together with lack of emission in the HCO^+, $H^{13}CO^+$ and CH_3CN lines suggests that this region is composed of dense and cold gas, which has undergone high levels of depletion.

The morphology of the HCO^+ emission exhibits noticeable differences with respect to that of the N_2H^+ emission. Towards the central N_2H^+ region, the HCO^+ emission shows a banana-like morphology which is roughly coincident with the 2 westernmost N_2H^+ condensations, but no HCO^+ emission is seen from the eastern N_2H^+ condensation. The peak position of the mm-6 core is located at the western edge of the banana. Towards the extended Northwest region, the brighter HCO^+ emission is seen at its northern end (core mm-8) while the brighter N_2H^+ emission is seen at its southern end (core mm-10). In addition, the HCO^+ image shows two conspicuous features: a bright clumpy structure, located $\sim 18''$ south of the central region, elongated in the NE-SW direction (labeled South), barely seen in N_2H^+, and a weak V shaped feature located $\sim 10''$ west from the central region (labeled West), not seen in the N_2H^+ image.

The $H^{13}CO^+$ emission exhibits a bright central component, with a size of $5.5''$, which encompasses mm-6, diffuse emission seen towards the east, similar in extent to that seen in N_2H^+, and emission from the Northwest region.

The most prominent features in the CH_3CN image are a bright central region, with a size of $6''$, whose peak position coincides with the peak position of core mm-6, a bright V shaped region coincident with the West region seen in HCO^+ and an elongated, clumpy structure of weak emission running from northwest to southeast which is closely associated with dark lanes seen in the 8 μm Spitzer images. We note here that the moment zero map of the CH_3CN emission was made using the emission in the K = 2 component in AGAL329 in order to avoid blending effects. The emission in the lower K components is much brighter and extended than in the higher K components.

Figure 5.5 also shows clear differences in the strength of emission from the cores in the different lines, likely caused by differences in optical depths, excitation conditions and/or chemistry. The differences are illustrated by considering the three cores located in the north-west region of the clump: core mm-8 shows bright emisssion in HCO^+ and $H^{13}CO^+$, core

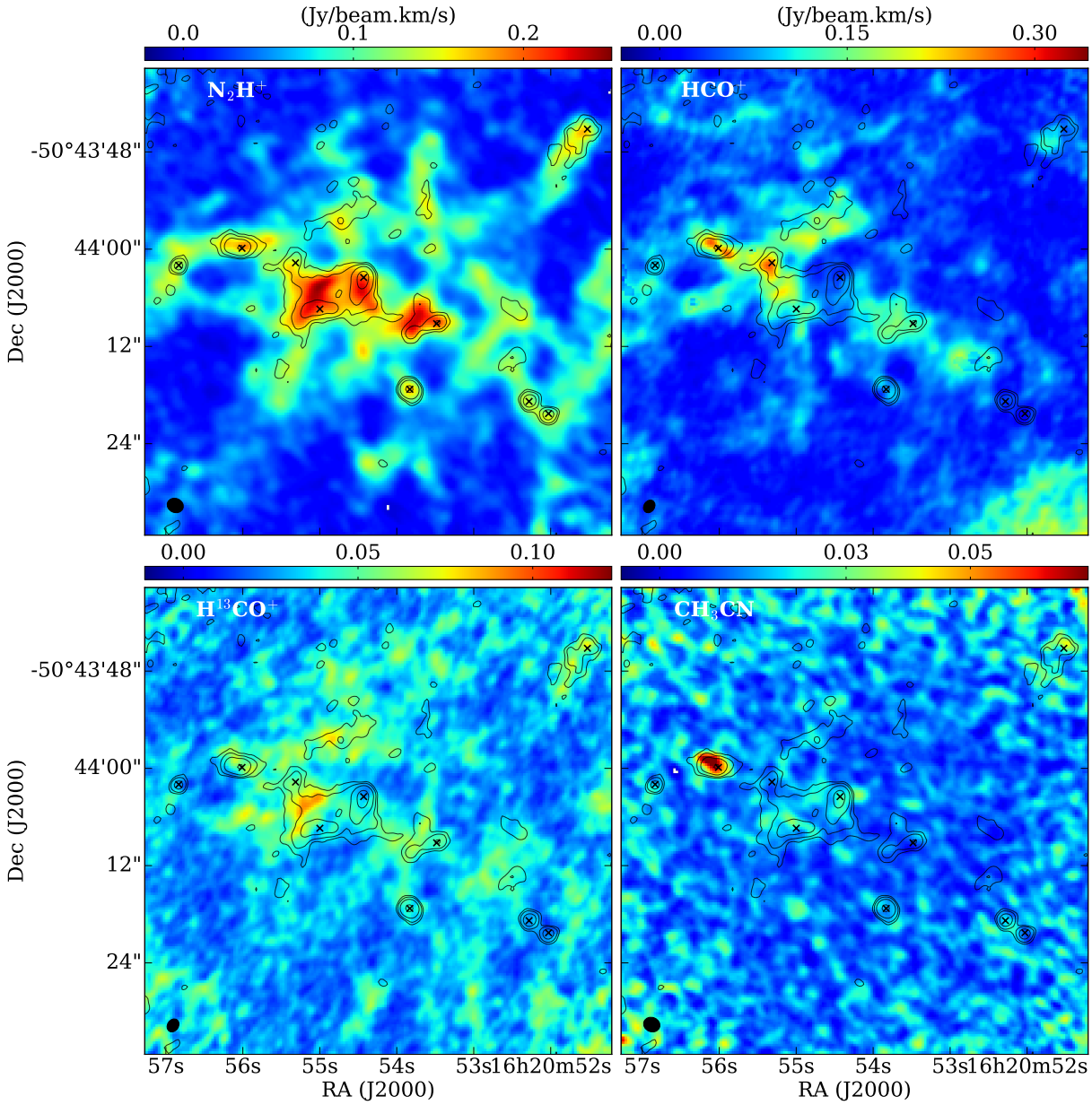

Figure 5.7: Images of the velocity integrated line emission towards AGAL333. Superimposed are contours of the continuum emission. Black crosses mark the peak position of the continuum cores. The black ellipse shown at the bottom left corner indicates the beam size. Top left: N_2H^+; top right: HCO^+, bottom left: $H^{13}CO^+$, bottom right: CH_3CN.

mm-10 is brighter in N_2H^+ and CH_3CN, while core mm-9 is brighter in HCO^+.

AGAL333: Figure 5.7 presents images of the velocity integrated emission (moment 0) in all four observed species toward AGAL333, showing that the morphology of the line emission is different in the four molecules. The peak position of the continumm cores are marked with crosses. The velocity range of integration is -60.0 to -48.0 km s^{-1} for HCO^+ and $H^{13}CO^+$, -67.0 to -60.0 km s^{-1} for N_2H^+ and from -64.0 to -57.0 km s^{-1} for the CH_3CN corresponding to the $J_K = 5_0 \rightarrow 4_0$ component. The emission in N_2H^+ line is the brightest and most extended one, delineating a complex network of filamentary structures across the whole region. The main structure is a clumpy filament running from northeast to southwest, P.A. of 60 degrees. All of the continuum cores are associated with N_2H^+ emission and most of them lie within the main filament. There is a high degree of correlation between the N_2H^+ and the continuum emissions.

The HCO^+ emission (upper right panel) clearly delineates the main filament running from northeast to southwest. The brighter peaks of the HCO^+ emission are associated with cores mm-2 and mm-3. The morphology of the $H^{13}CO^+$ emission shows some similarities to that of N_2H^+, exhibiting a network of filamentary structures. However, the peak position of the brighter $H^{13}CO^+$ structures do not coincide with those of the continuum cores. In fact there is an anticorrelation between the $H^{13}CO^+$ and continuum emissions. The brighter feature in both the $H^{13}CO^+$ and N_2H^+ images corresponds to a region in between cores mm-3 and mm-4. Finally, emission in the CH_3CN line (lower right panel) was clearly detected only towards core mm-2 core and weakly detected towards cores mm-1, 3, 4 and 5.

Velocity field

In order to investigate the velocity field across the MDCs we consider the emission in the N_2H^+ line which is bright and optically thin and therefore less affected by self-absorption effects. Figure 5.8 shows images of the velocity field (moment 1) of the N_2H^+ emission towards AGAL329 and AGAL333.

Figure 5.8 (right panel) shows that there is a significant velocity gradient from northeast to southwest across AGAL333. There is a velocity shift of 4.2 km s^{-1} over a region of about 50″, which at the distance of 3.72 kpc corresponds to a velocity gradient of 4.7 km s^{-1} pc^{-1}. Assuming that the velocity gradient is due to gravitationally bound rotation of an structure with radius R and mass M, then $M = (dV/dR)^2 R^3/G$ (c.f., Armstrong et al. 1985). The observed velocity gradient implies a mass within a radius of 0.45 pc of 460 $M_\odot$. This mass is within a factor of two from the mass derived from the dust observations, giving support to the bound rotation hypothesis.

The velocity field towards the protostellar clump (Figure 5.8, left panel) appears complex, with no organized motions nor clear velocity gradients seen across the clump. The redder velocities seen towards the north and the bluer velocities seen towards the south are probably caused by the presence of outflows, as discussed next. In several positions across this clump the profiles of the HCO^+ line emission exhibit the presence of wing emission. To investigate the spatial distribution of the wing emission, we made contour maps of the velocity integrated

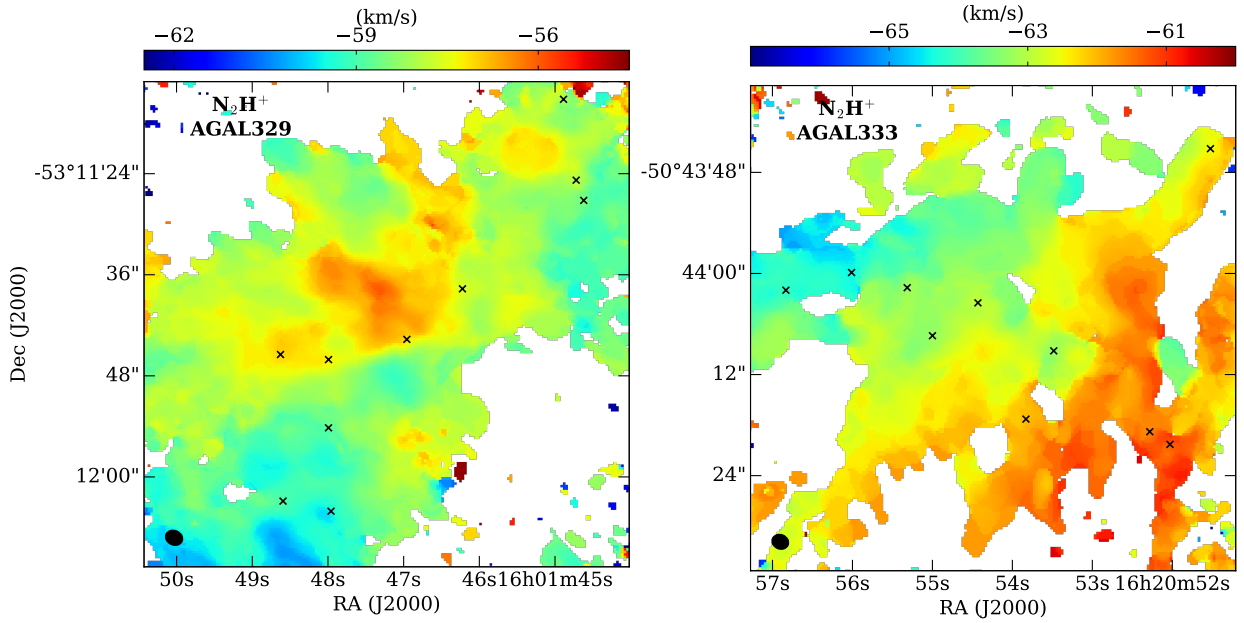

Figure 5.8: Moment one images of the N_2H^+ emission from AGAL329 (left) and AGAL333 (right). Crosses mark the peak position of the continuum cores.

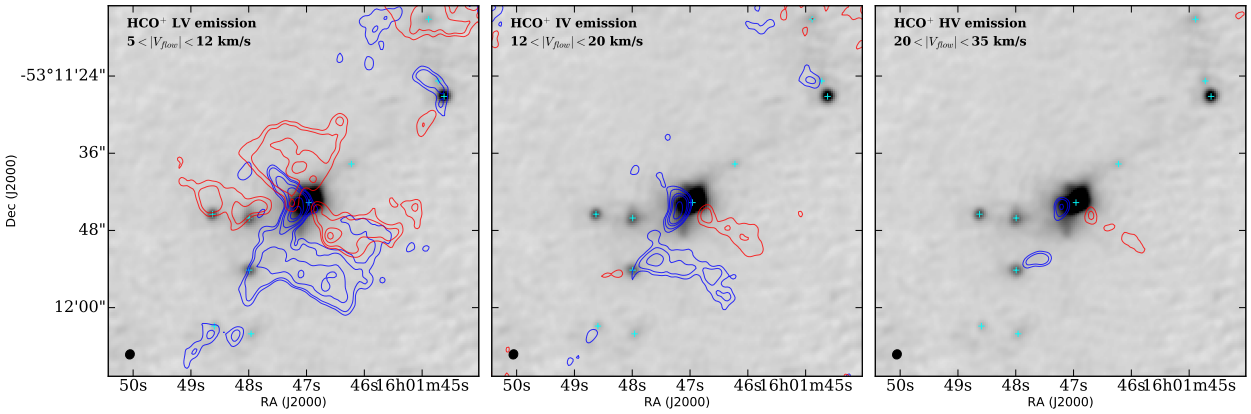

Figure 5.9: Contour maps of low velocity (LV), intermediate velocity (IV) and high velocity (HV) HCO^+ emission towards AGAL329 overlaid in the 3 mm ALMA continuum map (gray scale). The blue and red color contours mark blue-shifted and red-shifted emission, respectively. The flow velocity range is shown in the top left corner of each map.

emission in three ranges of radial flow velocities. The radial flow velocity, v_{flow}, is defined as $v_{LSR} - v_0$, where v_0 is the systemic velocity of the clump, assumed to be -50.5 km s^{-1}. Figure 5.9 shows maps of the wing emission, overlaid on the ALMA dust continuum image, in three ranges of flow velocities: $20 < |v_{flow}| < 35$ km s^{-1}, referred as the high velocity (HV) wing, $12 < |v_{flow}| < 20$ km s^{-1}, referred as the intermediate velocity (IV) wing, and $5 < |v_{flow}| < 12$ km s^{-1}, referred as the low velocity (LV) wing. The morphology of the HCO^+ wing emission is complex. Clearly distinguished in the LV map is an extended bipolar-like structure with a wide opening angle (half opening angle of $\sim$43°), consisting of a lobe of redshifted emission seen towards the north and a lobe of blueshifted emission seen towards the south, located on opposite directions from core mm-6. The position angle of the symmetry axis of the outflow

is P.A. ∼5 degrees. The linear extensions of the redshifted and blueshifted lobes along the symmetry axis are ∼0.23 pc (∼14″) and ∼0.27 pc (∼16″), respectively. Also distinguished in the LV map is a second, more collimated, bipolar-like structure, with a position angle of 45 degrees, consisting of a redshifted lobe extending toward the southwest and a blueshifted lobe extending toward the northeast from core mm-6. The blueshifted lobe extends ∼0.12 pc (∼7″) northeast while the redshifted lobe extends ∼0.25 pc (∼15″) southwest. In addition, seen in the LV map is a weak blueshifted feature extending towards the northeast and a weak redshifted feature extending towards the southeast from core mm-10. These features may correspond to streams of gas infalling towards core mm-10.

In the IV map, emission from the wide angle bipolar structure is only seen from the blueshifted lobe. In this velocity range emission from the more collimated bipolar structure is clearly seen at redshifted velocities. In the HV map, the blueshifted emission associated with the mm-core 6 is compact (∼3″) while the redshifted emission extending west shows three separate 'knot' like features, at distances of ∼3″, ∼6.5″ and ∼10″ from peak position of mm-6. It is notable that this emission region is also detected in CH_3CN emission (see Figure 5.5, labeled West). Also seen in HV map is a narrow blueshifted emission, of size ∼4″, associated with mm-3.

5.4.3 Line emission from cores

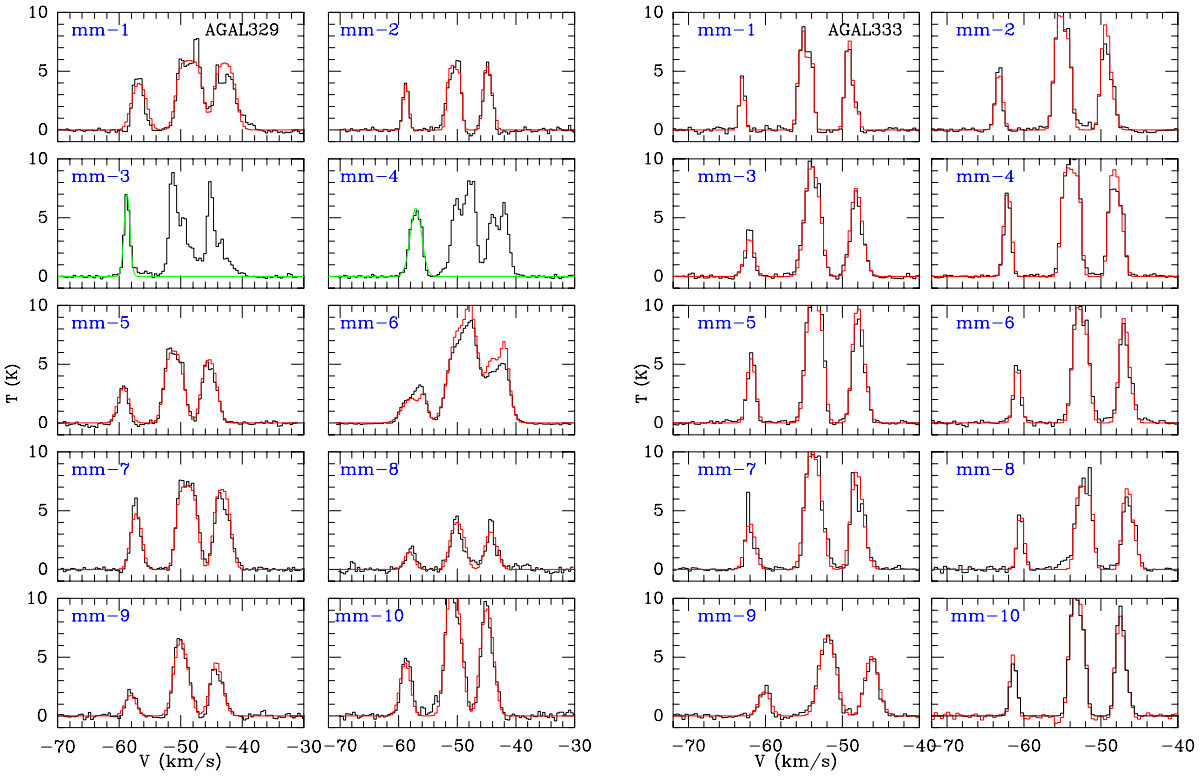

Figure 5.10: Average spectra of the N_2H^+ emission from cores. Left panel: AGAL329 cores. Right panel: AGAL333 cores. The red line indicates the result of a simultaneous fit to the whole hyperfine structure and the green line indicates the result of a Gaussian fit to the lower velocity component.

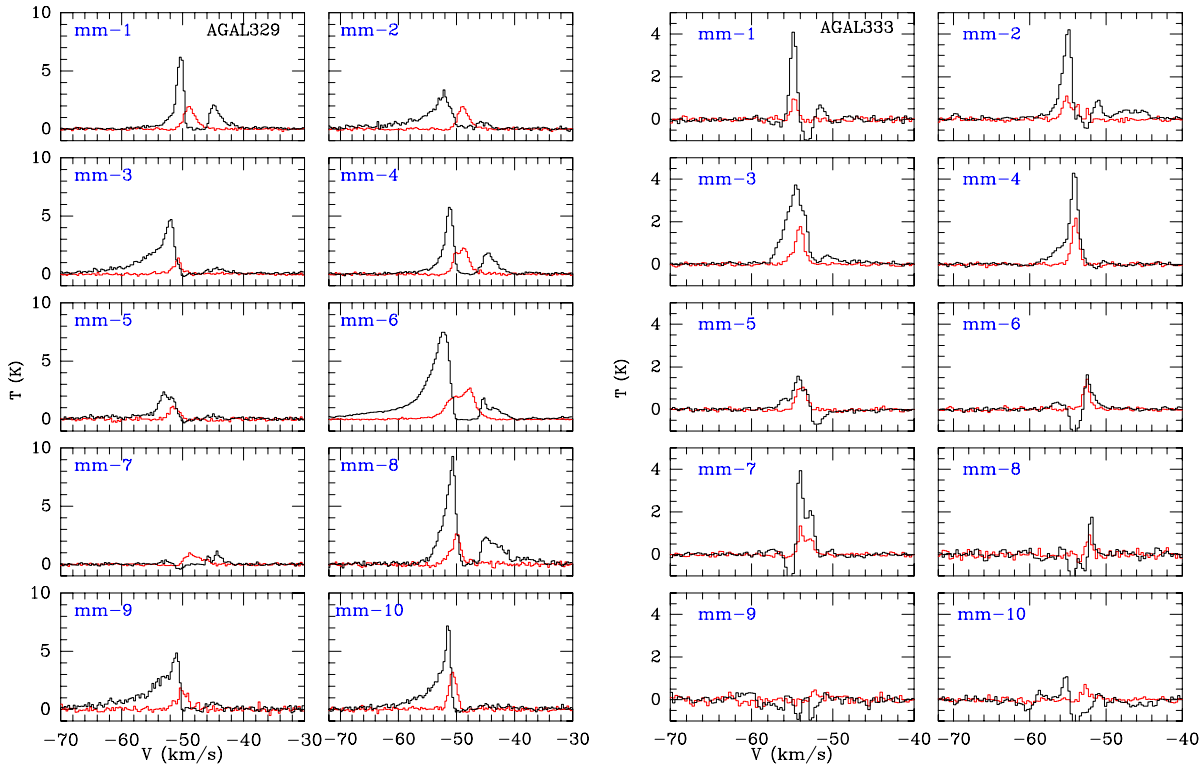

Figure 5.11: Average spectra of the HCO^+ (black line) and $H^{13}CO^+$ (red line) emission from cores. Left: AGAL329 cores. Right: AGAL333 cores.

In this section we present the characteristics of the spectra of the molecular line emision from the continuum cores. The spectra correspond to the average spectra of the spatially integrated emission over the solid angle subtended by each core (hereafter refereed as the core spectra).

Figure 5.10 shows the spectra of the N_2H^+ J=1→0 line. Emission is clearly detected towards all cores in both MDCs. The red line shows the result of a simultaneous fit to the emission from the whole hyperfine structure for a single velocity component, made using the task *pyspeckit.models* in *PySpecKit* (Ginsburg & Mirocha, 2011). This approach gave good results for all cores in AGAL333 and for most cores in AGAL329, except cores mm-3, mm-4 and mm-6 which exhibits either self-absorption profiles or strong wing emission. Thus, for cores mm-3 and mm-4 in AGAL329 we fitted a single gaussian profile to the lower velocity (single HF) component (green line), while for core mm-6, two velocity components were used to fit the spectra.

Figure 5.11 shows, in the same panel, the spectra of the HCO^+ (black line) and $H^{13}CO^+$ (red line) emission. Emission in these lines was detected from all cores in both MDCs, except toward core mm-9 in AGAL333 in which the $H^{13}CO^+$ line was not detected ($<3\sigma$). The HCO^+ profiles from several cores in AGAL329 display line asymmetries and self absorption features. Typically the HCO^+ profile shows two peaks with a strong blueshifted peak and weak redshifted peak relative to the velocity of the optically thin $H^{13}CO^+$ line. This is a characteristic signature of infalling gas, probably due to the global collapse of the clump (see section 5.5.4).

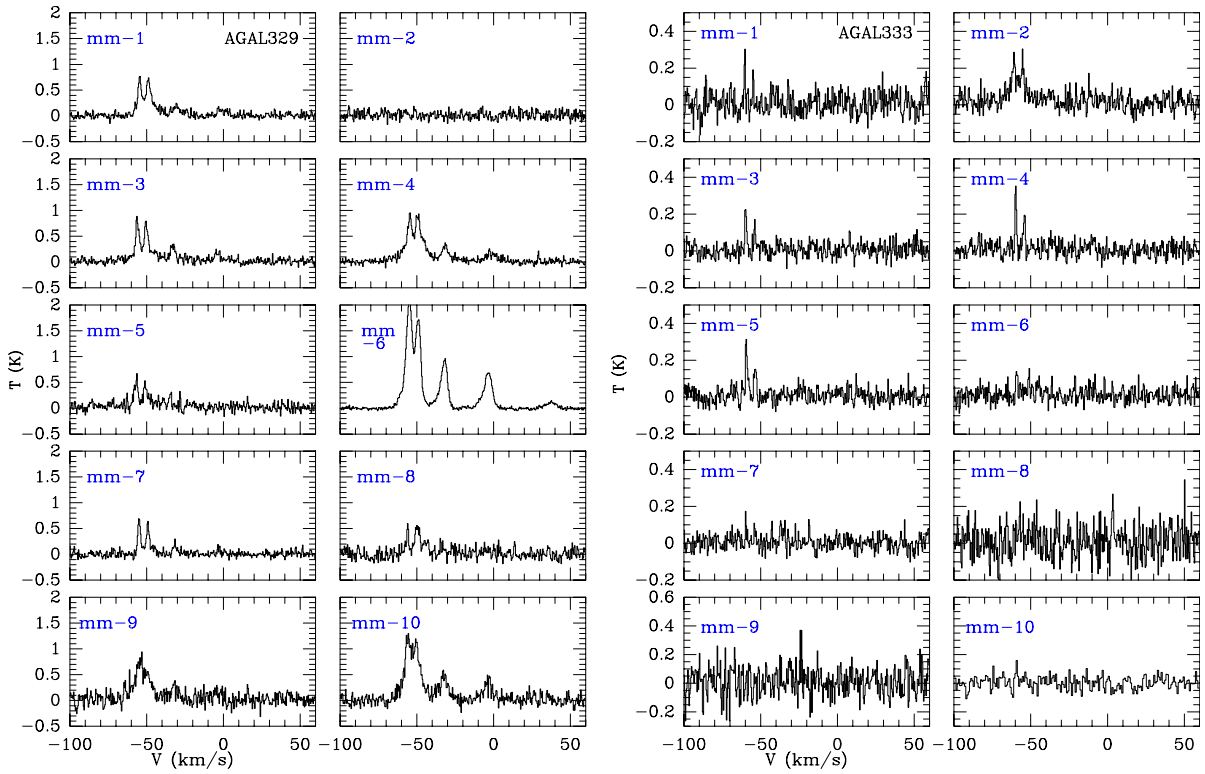

Figure 5.12: Average spectra of the CH_3CN emission from cores. Left: AGAL329 cores. Right: AGAL333 cores.

Most cores within the AGAL333 prestellar clump show absorption features and/or shoulders in the HCO^+ line. Cores mm-1, mm-2, mm-4, mm-5 and mm-10 show inverse P-Cygni profiles, suggesting that they are undergoing contraction motions. On the other hand cores mm-6, mm-7 and mm-8 show P-Cygni like profiles, usually taken as a signpost of outflowing or expanding gas motions. It is possible that some of the cores formed in MDCs be transient objects and therefore be expanding. In fact the mm-7 core has a virial parameter of 2.5, further suggesting it is not bounded.

Figure 5.12 presents the observed spectra in the $J_K = 5_K \rightarrow 4_K$ CH_3CN K-ladder. Emission was detected from all cores within AGAL329, except mm-2. Emission was detected in all five K components towards one core (mm-6), in four K components towards five cores (mm-1, 3, 4, 7 and 10), in three K components towards two cores (mm-5 and mm-9), and in two K components towards one core (mm- 8). Towards AGAL333, only weak CH_3CN emission was detected from cores mm-1, mm-2, mm-3, mm-4 and mm-5.

Line parameters of optically thin transitions

The determination of the kinematics (velocities), turbulence (line widths) and dynamical state of the cores (virial parameter) requires observations of the emission in optically thin molecular lines, since they are free of self-absorption features. Table 5.6 lists the parameters of the core emission in the optically thin J=1→0 lines of $H^{13}CO^+$ and N_2H^+. The former were determined from a Gaussian fit to the core spectra while the latter were derived in

Table 5.6: Line parameters of the core emission in optically thin lines.

Core		N_2H^+ J=1→ 0			$H^{13}CO^+$ J=1→ 0		
	HFS Comp.	V_{lsr} km s^{-1}	ΔV km s^{-1}	τ_{tot}	V_{lsr} km s^{-1}	ΔV km s^{-1}	T_A K
				AGAL329			
mm-1		-48.71 ± 0.04	2.35 ± 0.09	10.0 ± 1.4	-48.87 ± 0.04	2.11 ± 0.09	2.55 ± 0.09
mm-2		-50.72 ± 0.02	1.01 ± 0.05	10.1 ± 1.3	-50.85 ± 0.11	1.27 ± 0.27	0.95 ± 0.17
mm-3[a]	[a]	-50.76 ± 0.09	1.09 ± 0.24	–	-50.92 ± 0.03	1.00 ± 0.07	2.25 ± 0.13
mm-4[a]	[a]	-49.05 ± 0.10	2.29 ± 0.02	–	-49.09 ± 0.02	2.84 ± 0.04	2.23 ± 0.10
mm-5		-51.24 ± 0.02	2.00 ± 0.05	5.2 ± 0.5	-51.70 ± 0.09	2.22 ± 0.22	1.27 ± 0.11
mm-6		-49.82 ± 0.20	3.48 ± 0.35	1.1 ± 0.4	-50.59 ± 0.05	4.86 ± 0.12	3.36 ± 0.04
		-47.61 ± 0.05	1.36 ± 0.21	0.5 ± 0.1	-47.57 ± 0.02	1.49 ± 0.07	2.53 ± 0.11
mm-7		-49.15 ± 0.02	1.81 ± 0.05	9.6 ± 0.9	-48.39 ± 0.13	2.12 ± 0.30	0.81 ± 0.10
mm-8		-50.13 ± 0.05	1.86 ± 0.14	2.7 ± 1.0	-50.30 ± 0.07	2.48 ± 0.17	2.56 ± 0.15
mm-9		-49.71 ± 0.03	2.72 ± 0.07	2.2 ± 0.4	-50.03 ± 0.16	2.82 ± 0.38	1.29 ± 0.15
mm-10		-50.83 ± 0.02	1.97 ± 0.07	3.6 ± 0.5	-50.84 ± 0.04	1.63 ± 0.09	3.97 ± 0.19
				AGAL333			
mm-1		-54.97 ± 0.01	0.75 ± 0.02	4.0 ± 0.5	-54.94 ± 0.06	0.81 ± 0.14	1.14 ± 0.17
mm-2		-55.18 ± 0.01	1.03 ± 0.05	4.0 ± 0.6	-55.16 ± 0.09	1.86 ± 0.21	1.23 ± 0.12
mm-3		-54.03 ± 0.02	1.46 ± 0.05	1.4 ± 0.4	-54.13 ± 0.05	1.51 ± 0.11	1.61 ± 0.10
mm-4		-54.07 ± 0.01	0.96 ± 0.02	12.5 ± 1.3	-54.24 ± 0.02	0.91 ± 0.06	2.13 ± 0.12
mm-5		-53.80 ± 0.01	1.22 ± 0.02	4.7 ± 0.5	-53.80 ± 0.05	1.11 ± 0.11	1.31 ± 0.11
mm-6		-52.81 ± 0.01	1.10 ± 0.02	3.4 ± 0.5	-52.78 ± 0.04	0.93 ± 0.09	1.70 ± 0.14
mm-7		-53.95 ± 0.03	1.46 ± 0.07	2.6 ± 0.8	-54.01 ± 0.03	1.02 ± 0.07	1.70 ± 0.10
mm-8		-52.37 ± 0.02	0.96 ± 0.05	8.0 ± 1.3	-52.32 ± 0.10	0.86 ± 0.24	0.91 ± 0.22
mm-9		-52.10 ± 0.01	1.50 ± 0.05	2.8 ± 0.4	–	–	–
mm-10		-53.28 ± 0.01	1.06 ± 0.02	2.3 ± 0.4	-53.07 ± 0.04	0.95 ± 0.10	1.91 ± 0.17

(a) N_2H^+ line velocity and widths is obtained from the Gaussian fit to the lower velocity component.

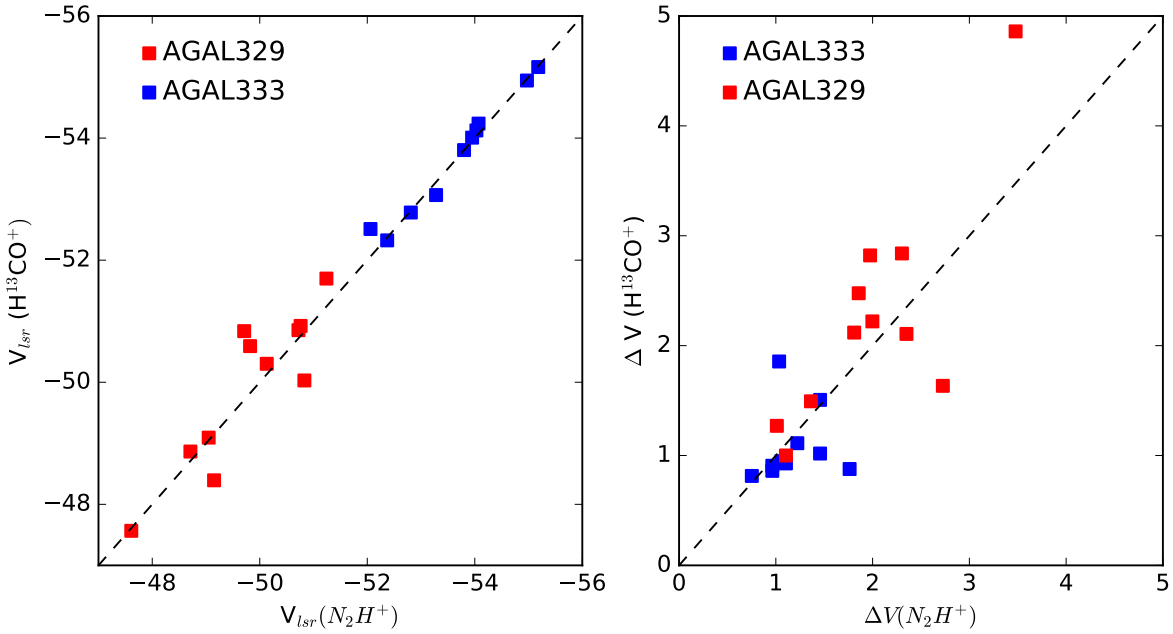

Figure 5.13: Comparison between the line velocities (left panel) and line widths (right panel) derived from the N_2H^+ hyperfine fit and the $H^{13}CO^+$ gaussian fit. Blue and red squares indicate values for cores in AGAL333 and in AGAL329, respectively.

most cases from a simultaneous fit to all hyperfine lines. For core mm-6 in AGAL329 two velocity components were used to fit the N_2H^+ and $H^{13}CO^+$ profiles. In addition to the central velocity and linewidth, the simultaneous hyperfine fit provides the total optical depth in the N_2H^+ J=1→0 transition. The derived total optical depths range from ∼1.4 to 12.5 for the cores in prestellar source and from ∼0.5 to 10.1 for the cores in protostellar source. Even though the total optical depths are ≥1, the individual hyperfine components are mostly optically thin. As shown in Figure 5.13, the velocities and line widths of the cores derived from both lines are in good agreement.

In general the line widths of the cores in the prestellar clump are smaller than those of the cores in the protostellar clump (see Figure 5.13). The average line width of the cores within AGAL333 and AGAL329 are 1.2 km s^{-1} and 2.0 km s^{-1}, respectively. The explanation of the large linewidths in cores within the protostellar clump is not straightforward, it may reflect either an increase in the level of turbulence due to the beginning of star formation activity or an increase in the gas velocities due to collapse motions. In particular, Vázquez-Semadeni et al. (2009) concluded that in a cloud undergoing global gravitational collapse, the velocity dispersion at all scales are caused by infall motions rather than by turbulence.

5.5 Analysis and discussion

In this section we discuss the physical parameters of the cores, their spatial distribution, virial state and the fraction of the total mass in cores relative to the parent clump mass, all of which are key properties to discern among the different models of fragmentation of MDCs.

5.5.1 Core parameters

Table 5.7: Derived core parameters.

Derived parameters								
Core	Temp.	Mass	Radius		n(H_2)	σ_{vir} †	M_{vir}	α_{vir}
	(K)	($M_\odot$)	(pc)	(10^3AU)	(10^7 cm^{-3})	(km s^{-1})	($M_\odot$)	
AGAL329								
mm-1	30	14.8	0.011	2.3	3.9	1.05	14.0	0.95
mm-2	28	1.7	0.005	1.0	4.6	0.53	1.6	0.96
mm-3	41	11.6	0.012	2.5	2.3	0.59	4.9	0.42
mm-4	34	27.2	0.019	3.9	1.4	1.03	23.4	0.86
mm-5	33	3.0	0.008	1.7	2.0	0.91	7.7	2.60
mm-6	68	118.8‡	0.030	6.2	1.5	1.55	84.2	0.71
mm-7	31	3.1	0.009	1.9	1.5	0.83	7.3	2.38
mm-8	28	8.5	0.013	2.7	1.3	0.85	10.9	1.28
mm-9	28	9.3	0.021	4.3	0.4	1.20	34.9	3.74
mm-10	41	20.1	0.011	2.3	5.3	0.91	10.7	0.53
AGAL333								
mm-1	22	1.6	0.006	1.2	2.6	0.42	1.2	0.74
mm-2	31	6.3	0.011	2.3	1.6	0.54	3.8	0.60
mm-3	22	2.4	0.010	2.1	0.8	0.68	5.3	2.25
mm-4	30	11.4	0.022	4.5	0.4	0.51	6.8	0.59
mm-5	24	19.8	0.016	3.3	1.7	0.59	6.5	0.33
mm-6	22	7.1	0.009	1.9	3.4	0.54	3.0	0.43
mm-7	22	3.0	0.014	2.9	0.4	0.68	7.5	2.50
mm-8	22	2.9	0.007	1.4	3.0	0.49	1.9	0.66
mm-9	22	2.2	0.006	1.2	3.5	0.80	4.4	2.04
mm-10	22	3.5	0.016	3.3	0.3	0.52	5.1	1.46

† $\sigma_{vir} = \sqrt{(\sigma_{th}^2 + \sigma_{tur}^2)}$, where σ_{th} is the thermal width and σ_{tur} is the turbulent width. ‡ Computed from the observed flux density at 3mm corrected by the contribution from the free-free emission.

The physical parameters of the cores are listed in Table 5.7 and their derivation is discussed in what follows.

Sizes

The radius of the cores were computed from the geometric mean of the semi-major and minor axis determined from Clumpfind and the distances given in Table 5.1. For cores in AGAL329 the radii range from 0.005 to 0.030 pc (1000 to 6200 AU) with an average value of 0.014 pc (2900 AU), while for cores in AGAL333 the radii range from 0.006 to 0.022 pc (1200 to 4500 AU) with an average value of 0.012 pc (2500 AU).

Temperatures

The detection of emission in at least two J=$5_K \rightarrow 4_K$ transitions of CH_3CN allows to determine the rotational temperature of methyl cyanide, which is known to provide a good estimate of the kinetic temperature of the gas (e.g., Güsten et al. 1985; Remijan et al.

Table 5.8: Observed and derived parameters from CH_3CN observations.

Core	Velocity integrated flux density (Jy km s^{-1})					θ	T_{rot}	$N_t(CH_3CN)$
	$K=0$	$K=1$	$K=2$	$K=3$	$K=4$	($''$)	(K)	(10^{14} cm^{-2})
AGAL329								
mm-1	0.22	0.24	0.08	0.04	–	2.0	30±3	4.4±1.0
mm-2	–	–	–	–	–	–	–	–
mm-3	0.22	0.23	0.11	0.07	–	2.0	41±5	6.3±1.3
mm-4	0.33	0.34	0.13	0.07	–	2.0	34±3	7.3±1.4
mm-5	0.15	0.13	0.05	–	–	2.0	33±4	3.0±0.7
mm-6	5.90	4.89	2.62	2.09	0.34	5.0	68±7	32.1±6.5
mm-7	0.12	0.12	0.05	0.02	–	2.0	31±2	2.4±0.3
mm-8	–	–	–	–	–	–	–	–
mm-9	0.17	0.13	0.05	–	–	2.0	28±1	4.8±0.2
mm-10	0.43	0.39	0.17	0.12	–	2.0	41±3	11.0±1.7
AGAL333								
mm-2	0.08	0.09	0.03	–	–	2.5	31±12	1.1±0.7
mm-4	0.07	0.05	0.02	–	–	2.0	30±1	0.51±0.03
mm-5	0.04	0.02	0.01	–	–	3.0	24±1	0.50±0.06

2004; Hernández-Hernández et al. 2014). We use the standard rotational diagram analysis (Turner 1991; Sutton et al. 1995) which assumes that the lines are optically thin and that the population levels are characterized by a single excitation temperature (LTE assumption). Integration of the transfer equation of the emission in a line with an upper energy level, E_u, leads to the expression (e.g., Blake et al. 1987; Araya et al. 2005),

$$ln\Big[\frac{3c^2}{16\pi^3\Omega_s\nu^3}\frac{J}{\mu^2 S(I,K)(J^2-K^2)}\int S_\nu \mathrm{d}v\Big] = ln\Big[\frac{N_t}{Q(T_{rot})}\Big] - \Big[\frac{E_u}{kT_{rot}}\Big] \quad ,$$

where $\int S_\nu \mathrm{d}v$ is the velocity integrated flux density of the line, Ω_s the solid angle subtended by the source, $S(I,K)$ the degeneracy due to spin, ν and μ the transition frequency and dipole moment of the molecule, respectively, T_{rot} the rotational temperature, $Q(T_{rot})$ the rotational partition function, and N_t is the total column density. The dipole moment of CH_3CN molecule is 3.91 debye and the spin degeneracies for the $J = 5 \rightarrow 4$ transitions are given in Table 5.5.

Rotational diagrams for AGAL329 and AGAL333 cores, for which at least three lines in the 5_K - 4_K K-ladder were detected above the 3σ level, are shown in Figures 5.14 and 5.15, respectively. The velocity integrated flux density, obtained by integrating the flux per beam over a circular region with angular radius given in col. 7 of Table 5.8, are given in cols. 2 to 6 for K = 0, 1, 2, 3 and 4 lines, respectively. From a least squares fit to the data we derived the rotational temperatures given in column 8 of Table 5.8. Clearly, the cores within the protostellar clump are warmer than in the prestellar clump. The temperature of cores within the protostellar clump range from 28 to 68 K, with an average value of ∼38 K. Within the prestellar clump only three cores (mm-2, mm-4 and mm-5) were detected in at least three 5_K - 4_K lines, for which we derived temperatures of 31, 30 and 24 K, respectively. Whether the

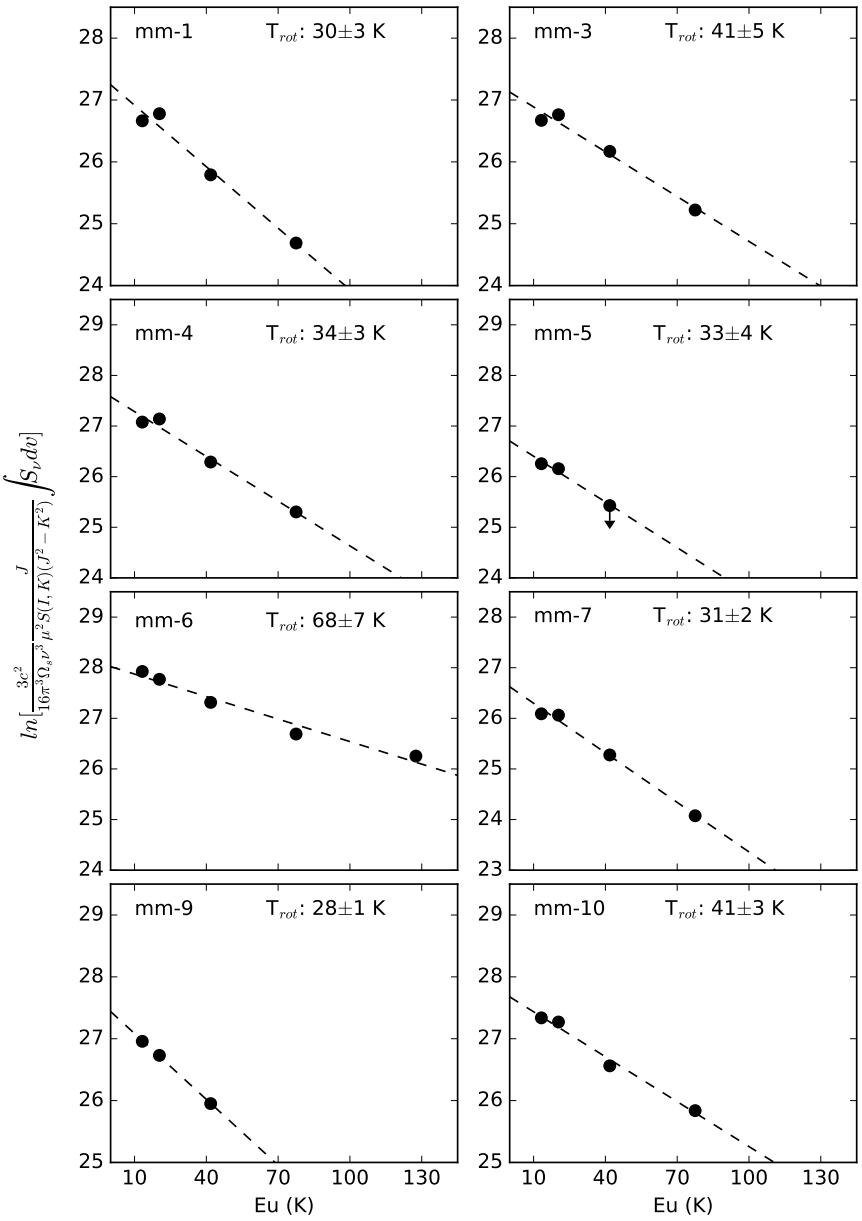

Figure 5.14: CH_3CN rotational diagram for cores in the protostellar clump. The derived rotational temperature is given in the upper right corner.

source of heating of the cores in the protostellar clump is due to the presence of embedded protostellar activity or from their gravitational collapse remains to be investigated.

The fit also gives the value of $\frac{N_t}{Q(T_{rot})}$ which allows to derive the CH_3CN column density. Using the following expression for the partition function of CH_3CN (Araya et al. 2005),

$$Q(T_{rot}) = 3.89 \ \frac{T_{rot}^{1.5}}{(1-\mathrm{e}^{-524.8/T_{rot}})^2} \quad ,$$

and the rotational temperatures of the cores, the derived the CH_3CN column densities are given in column 9 of Table 5.8. The cores in the protostellar clump have column densities ranging from 2.4x10^{14} cm^{-2} to 3.2x10^{15} cm^{-2}, while the mm-2, mm-4 and mm-5 cores in the

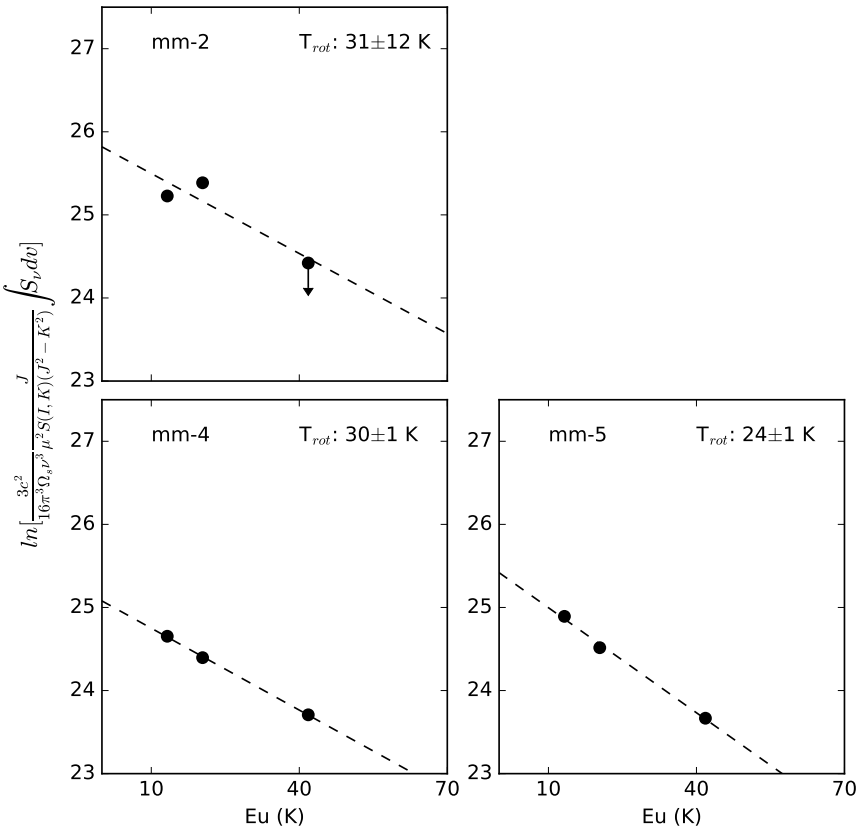

Figure 5.15: CH_3CN rotational diagram for cores in the prestellar clump. The derived rotational temperature is given in the upper right corner.

prestellar clump have column densities of 1.1x10^{14}, 5.1x10^{13} and 5.0x10^{13} cm^{-2}, respectively.

It is worth to mention that one of the assumptions of the rotational diagram method applied above, namely that lines should be optically thin, it is well fulfilled by the emission in the J=5$_K$ $\rightarrow$ 4$_K$ lines from all cores. For instance, for core mm-6 in AGAL329, the most extreme case since it exhibits the largest column density, the optical depths in the CH_3CN $J = 5_K \rightarrow 4_K$, K = 0, 1, 2, 3, 4 lines are 0.23, 0.19, 0.11, 0.04 and 0.02, respectively. If we use the more general rotational diagram method which takes into account optical depth effects (c.f., Goldsmith & Langer 1999), the differences in the derived temperatures and column densities are well within the errors determined from the "traditional" approach.

Due to the large spatial extent of the CH_3CN emission from the central region of AGAL329, whose peak position coincides with the peak position of core mm-6, it was possible to determine the dependence of the rotational temperature with radius. Figure 5.16 (left panel) shows rotational diagrams of the CH_3CN emission integrated over six different regions: from top to bottom, an inner disk with a radius of 1″ and 5 circular annuli with inner radius from 1″ to 5″ and width of 1″. The derived rotational temperature and column densities are given in cols. 8 and 9 of Table 5.9, respectively. The rotational temperature decreases from 131±24 K at the peak position to 30±3 K at a radial distance of 6″ from the center. Also shown in the middle and right panels of Figure 5.16 are, respectively, the rotational temperature and CH_3CN column density dependence with radius. Power law fits to the rotational temperature

Table 5.9: Observed and derived parameters from CH_3CN observations toward core mm-6 in AGAL329.

Region	Velocity integrated flux density (Jy km s^{-1})					Ω_{eff} [a]	T_{rot}	$N_t(CH_3CN)$
	$K=0$	$K=1$	$K=2$	$K=3$	$K=4$	($''^2$)	(K)	(10^{15} cm^{-2})
1	0.65	0.46	0.36	0.39	0.09	3.1	131±24	25.4±8.1
2	1.03	0.77	0.52	0.50	0.10	9.1	94±12	8.4±1.9
3	0.94	0.81	0.41	0.31	0.06	15.2	63±8	2.8±0.7
4	1.14	1.00	0.46	0.31	0.05	21.2	53±6	2.0±0.5
5	1.10	0.95	0.45	0.30	0.03	28.3	42±1	1.2±0.1
6	1.04	0.90	0.41	0.28	0.01	31.2	30±3	0.8 ±0.2

[a] Effective solid angle of the region.

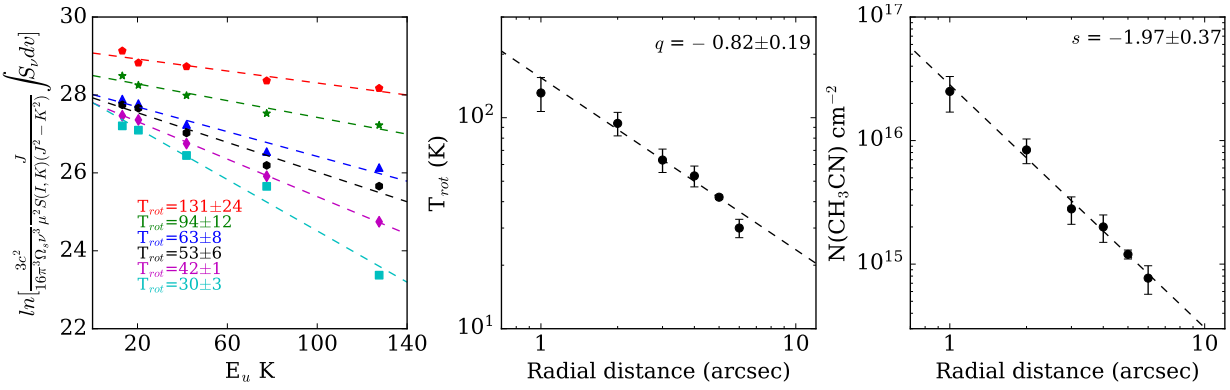

Figure 5.16: Left: Rotational diagram of the CH_3CN emission from six different regions within core mm-6 in AGAL329 (see text for the description of the regions). The derived rotational temperatures are shown in the lower left corner. Middle: Rotational temperature dependence with radius. Right: CH_3CN column density dependence with radius.

profile ($T_{rot} \propto r^q$) and column density profile ($N \propto r^s$) give power law indices of -0.8 ± 0.2 and -2.0 ± 0.4, respectively.

Masses

The mass of the cores were calculated from the continuum flux density, S_ν, using the expression,

$$M = \frac{S_\nu D^2 R_{g\rm d}}{k_\nu B(T,\nu)} \quad , \tag{5.3}$$

where k_ν is the dust mass absorption coefficient at frequency ν, B(T,ν) is the Planck function at temperature T, D is the distance and $R_{g\rm d}$ is the gas-to-dust ratio. We assume $R_{g\rm d}$=100 and $k_{100GHz} = 0.21$ cm^2 g^{-1} corresponding to the dust grains with ice mantles at gas densities of 10^6 cm^{-3} (Ossenkopf & Henning 1994). For the temperatures we used the values of the rotational temperatures derived from the CH_3CN observations (see section 5.5.1). For cores in which no rotational temperature is available we adopted the temperature of the clump. The masses, listed in col. 3 of Table 5.7, range from 1.6 to 20 $M_\odot$ for cores in the prestellar clump and from 1.7 to 119 $M_\odot$ for cores in the protostellar clump. The uncertainties in the mass are estimated to be ∼40%, considering errors in the flux density, temperature, distance and dust mass absorption coefficient (c.f., Sanhueza et al. 2017). It is worth to note that to compute the mass of the central core in AGAL 329, we subtracted from the observed flux density at 100 GHz the expected contribution from free-free emission. The latter was determined from an extrapolation of the observed flux densities at 18 GHz and 22 GHz (Sánchez-Monge et al. 2013). The total mass in the form of cores is ∼6% of the clump mass in the prestellar clump and ∼23% in the protostellar clump (see Table 5.11).

Column densities

The source averaged H_2 column densities of the cores can be computed from the continuum flux density, S_ν, using the expression,

$$N_{H_2} = \frac{S_\nu R_{g\rm d}}{\Omega_c \mu_{H_2} m_H k_\nu B(T,\nu)} \quad , \tag{5.4}$$

where $\mu_{H_2} = 2.8$ is the molecular weight per hydrogen molecule, m_H is the H-atom mass, Ω_c is the solid angle subtended by the core. Col. 4 of Table 5.10 lists the source averaged column densities, computed using the flux density measured in circular regions with the angular radius given in col. 3 and as dust temperature the CH_3CN rotational temperature of the cores (or clump temperature for cores in which rotational temperature is not available). They range from 6.0×10^{22} – 2.6×10^{23} cm^{-2} for cores in the prestellar clump and from 1.0×10^{23} – 7.5×10^{23} cm^{-2} for cores in the protostellar clump. The highest values of the H_2 column densities are found towards the centrally located cores, mm-6 in AGAL329 and mm-5 in AGAL333. The uncertainties in the column densities are estimated to be ∼35%.

From the observations of the N_2H^+ line emission it is possible to compute the source averaged column densities using the expression (e.g., Garden et al. 1991; Mangum & Shirley 2015),

Table 5.10: Source averaged H_2 and N_2H^+ column densities.

Core	S_ν (mJy)	θ ($''$)	N(H_2) (10^{23} cm^{-2})	N(N_2H^+) (10^{14} cm^{-2})	X(N_2H^+) (10^{-9})
			AGAL329		
mm-1	5.1	2.5	3.9	16.1	4.2
mm-2	0.9	2.0	1.1	6.2	5.4
mm-3	5.8	3.0	2.2	–	–
mm-4	10.7	3.0	4.9	–	–
mm-5	2.1	3.0	1.0	8.6	8.5
mm-6	93.8	5.0	7.5	12.4	1.7
mm-7	1.5	2.0	1.8	2.1	1.2
mm-8	3.3	3.0	1.9	3.0	1.6
mm-9	1.7	1.5	3.9	3.6	0.9
mm-10	8.4	2.0	7.1	8.9	1.3
Average			3.5	7.6	3.1
			AGAL333		
mm-1	0.7	2.5	0.7	1.1	1.6
mm-2	2.4	3.0	1.2	3.0	2.5
mm-3	1.4	3.0	1.0	0.8	0.8
mm-4	2.8	3.0	1.5	8.3	5.5
mm-5	3.8	3.0	2.6	2.6	1.0
mm-6	1.7	2.5	1.8	1.4	0.8
mm-7	1.3	3.5	0.7	1.4	2.1
mm-8	0.9	2.0	1.4	3.0	2.1
mm-9	0.7	2.0	1.1	0.8	0.7
mm-10	1.1	3.5	0.6	0.9	1.6
Average			1.3	2.3	1.9

$$N_{tot}(N_2H^+) = \frac{3k}{8\pi^3\mu^2 B}\frac{(T_{\rm ex}+hB/3k)}{J_u}\frac{exp(\frac{E_u}{kT_{ex}})}{exp(h\nu/kT_{\rm ex})-1}\int \tau_\nu {\rm d}v \quad , \tag{5.5}$$

where, E_u is the upper level energy, B is the rotational constant of the molecule, T_{ex} is the excitation temperature, ν is the frequency, μ is the dipole moment, Q_{rot} is the partition function, k is the Boltzmann constant, h is the Planck constant and τ is the total optical depth. For observations of the J=1→0 line,

$$N_{tot}(N_2H^+) = 3.10\times10^{11}(T_{\rm ex}+0.74)\frac{exp(\frac{4.47}{T_{ex}})}{exp(\frac{4.47}{T_{ex}})-1}\int \tau_\nu {\rm d}v \quad cm^{-2} \quad , \tag{5.6}$$

where dv is in km s^{-1}.

Col. 5 of Table 5.10 lists the N_2H^+ column densities of the cores computed from the above relation using the line widths and total optical depths determined from the HF fit. For the temperature, we adopted the CH_3CN rotational temperature of the cores. For cores for which no rotational temperature is available the temperature of the clump was used. As shown in Figure 5.17, which plots the H_2 versus N_2H^+ column densities, cores in the protostellar clump

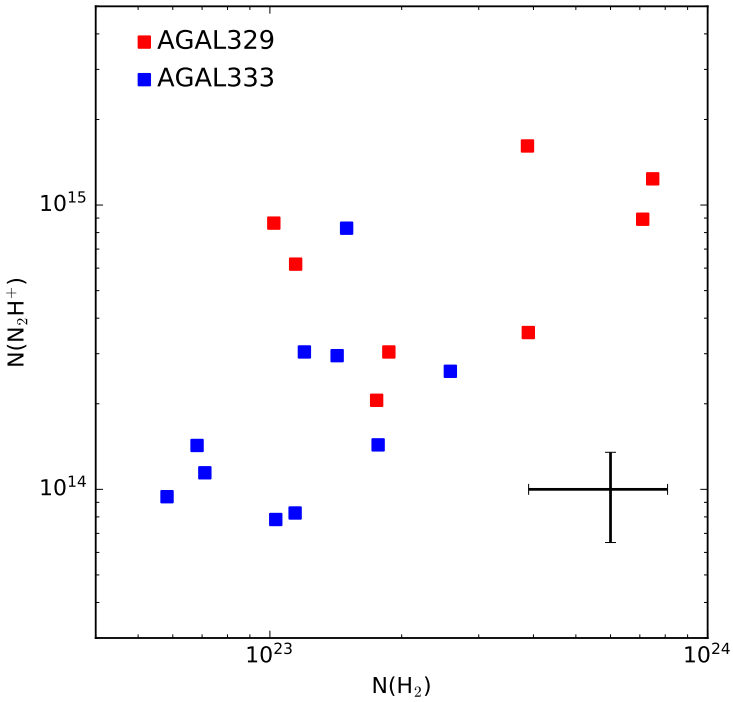

Figure 5.17: H_2 column densities versus N_2H^+ column densities for prestellar cores (blue squares) and protostellar cores (red squares). Typical errors in column densities are shown in the lower right corner.

have typically larger H_2 and N_2H^+ column densities than cores in the prestellar clump. The average N_2H^+ column density of the cores in the prestellar and prostellar clumps are, respectively, 2.3×10^{14} cm^{-2} and 7.6×10^{14} cm^{-2} and the average H_2 column density are 1.3×10^{23} cm^{-2} and 3.5×10^{23} cm^{-2}. The average abundance of N_2H^+ relative to H_2, computed as the ratio of the respective column densities, are 1.9×10^{-9} and 3.1×10^{-9} for cores in the prestellar and protostellar clumps, respectively, indicating that in protostellar cores the abundance of N_2H^+ is typically larger than in prestellar cores. An increase in the N_2H^+ abundance with evolutionary stage has also been reported for clumps (e.g., Sanhueza et al. 2012; Hoq et al. 2013).

5.5.2 Mass distribution

Figure 5.18 shows the distribution of the core masses in each clump. The dotted line indicates the value of the Jeans mass at the average clump conditions (see Table 5.1). The masses of the cores are of the order or slightly higher than the clump Jeans mass, except for the central core in AGAL329 which highly exceeds the Jeans mass. The number of cores detected in each clump ($\sim$10) is much smaller than the number of thermal Jeans masses contained in the clumps, of $\sim$ 160, showing that fragmentation is not efficient during the early stages of evolution. This conclusion was previously reported by Csengeri et al. (2017), who found that the fragmentation of infrared quiet MDCs at scales of 0.06 to 0.3 pc is limited, with most clumps hosting typically 3 cores with masses of $\geq$ 40 $M_\odot$.

Our observations with spatial resolution of ∼0.03 pc, ten times smaller than that of Csengeri et al. (2017), show that the number of cores per clump increases to 10, suggesting that we are resolving further fragmentation within MDCs. Recent studies of clumps with similar characteristics to those observed by Csengeri et al. (2017) have reported levels of fragmentation ranging from 5 to 20 cores when observed at scales of 0.03-0.05 pc (e.g., Lu et al. 2018; Contreras et al. 2018).

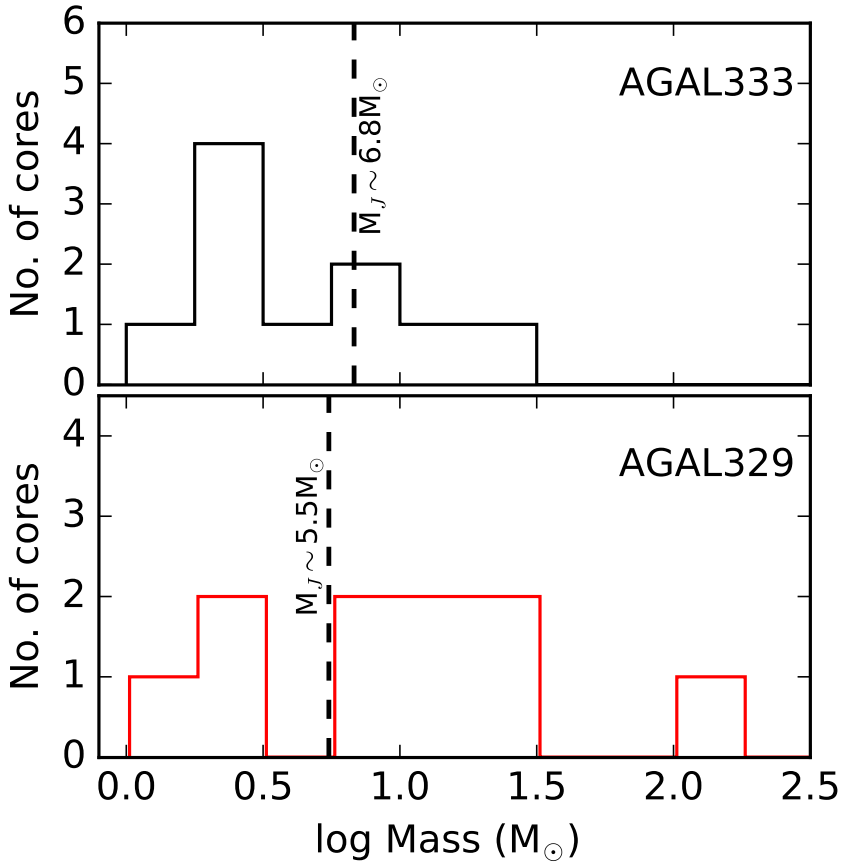

Figure 5.18: Core mass distribution. Upper panel: AGAL333. Bottom panel: AGAL329. The dotted line indicates the Jeans mass at the average conditions of the clump.

Figure 5.19 shows the normalized cumulative distribution function (CDF), also known as empirical cumulative distribution function (eCDF). We prefer to use the eCDF over the differential form of the core mass function because the later approach contains the numerical bias introduced by binning. Given the relatively small number of cores detected in each clump, we considered the combined sample of cores in the prestellar and protostellar clumps including, in addition, the cores detected by Servajean et al. (2019) towards the prestellar clump (AGAL305), which have similar characteristics to the clumps considered here. We adopt here as mass sensitivity limit the mass computed using a flux density equal to the 3σ noise level and the temperature of the clump. The mass sensitivity limits are 0.9, 0.7 and 1.4 $M_\odot$ for AGAL329, AGAL333 and AGAL305, respectively.

Assuming that the core mass function (CMF) can be described by a power-law $dN/dM \propto M^\alpha$, the value of the α index that best reproduces the eCDF, using the maximum likelihood

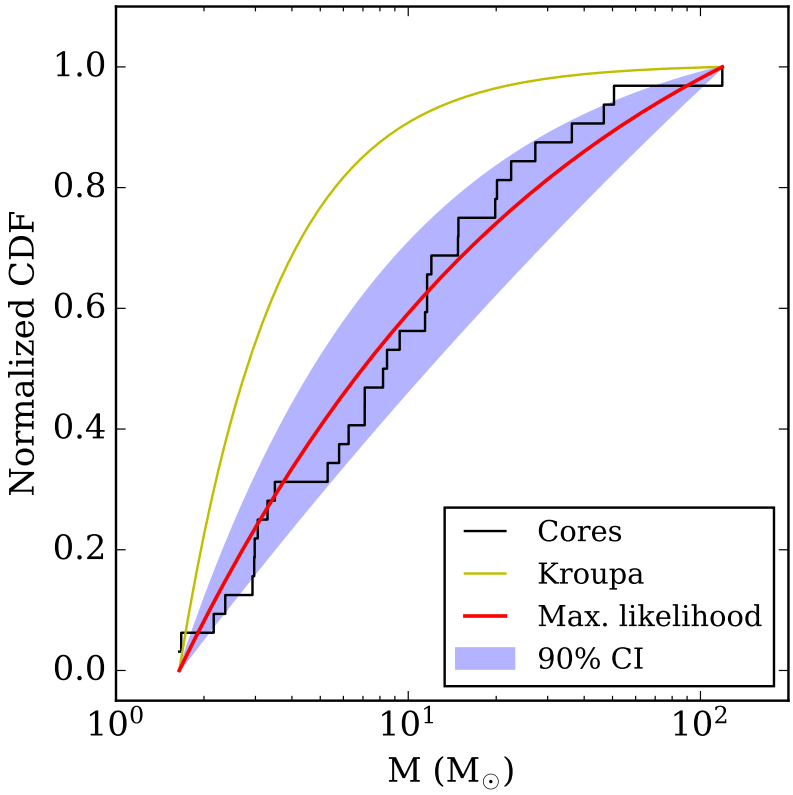

Figure 5.19: The normalized cumulative distribution function (CDF) for the combined sample of cores within clumps AGAL333, AGAL329 and AGAL305. The red line and purple shaded area show the maximum likelihood estimation of the power law index fit and its 90% confidence interval, respectively. The yellow line shows the initial mass function distribution from Kroupa 2001.

method (see Servajean et al. 2019), is -1.33 ± 0.15, and the 90% confidence interval is -1.58 to -1.08. This power-law index is much shallower than that of the initial stellar mass function (IMF) for stars with masses greater than $1M_\odot$, of -2.35 (Kroupa 2001), suggesting that in the early stage of fragmentation of clumps, high mass cores are more efficiently formed than low mass cores. Our result is alike to that of the recently reported ALMA study of CMF towards the high-mass star forming region W43-MM1 (Motte et al. 2018b) and towards infrared dark clouds (IRDCs) (Liu et al. 2018) indicating the top-heavy nature of CMF in high-mass star forming regions.

5.5.3 Dynamical state

To assess the dynamical state of the cores we compute the virial parameter, $\alpha_{\rm vir}$, defined as $\alpha_{\rm vir} = M_{\rm vir}/M_{\rm dust}$, where $M_{\rm vir}$ is the virial mass defined as

$$M_{vir} = \frac{5\sigma^2 R}{G} \tag{5.7}$$

Table 5.11: Summary of core characteristics.

	Prestellar clump AGAL333	Protostellar clump AGAL329
Number of cores	10	10
Mean core size	0.012 pc	0.014 pc
Mean velocity dispersion	0.50 km s^{-1}	0.85 km s^{-1}
ΣM_{cores}	60 $M_\odot$	218 $M_\odot$
$f(\Sigma M_{cores}/M_{clump})$	0.06	0.23
$M_{centralcore}$	20 $M_\odot$	119 $M_\odot$
$f(M_{centralcore}/\Sigma M_{cores})$	0.33	0.55
$f(M_{centralcore}/M_{clump})$	0.02	0.13

where $\sigma = \sqrt{(\sigma_{th}^2 + \sigma_{tur}^2)}$, σ_{th} and σ_{tur} are the thermal and turbulent velocity dispersions, respectively, R is the radius and G the gravitational constant. The turbulent velocity dispersion was computed from the observed N_2H^+ or $H^{13}CO^+$ line widths and the thermal velocity dispersion was computed using the temperature given in col. 2 of Table 5.7 for a particle with a molecular weight of 2.33 (e.g., Bertoldi & McKee 1992). The virial mass and virial parameter of the cores are given in columns 8 and 9 of Table 5.7, respectively. Given the uncertainties in the values of the quantities that enter in the calculation of α_{vir} we consider that cores which have $0.71 < \alpha_{vir} < 1.4$ are in virial equilibrium (i.e. we are considering an error of up to 40%).

In the prestellar clump, five cores are sub-virial (i.e. $\alpha_{vir} \leq 0.7$) indicating that their gravitational energy dominates their kinetic energy and, in absence of other means of support (e.g. magnetic energy), they are likely to be undergoing gravitational collapse. Two cores are in virial equilibrium and the three others have $\alpha_{vir} \geq 1.5$ suggesting that they may correspond to transient features. In the protostellar clump, five cores are in virial equilibrium, two are sub-virial and three have $\alpha_{vir} \geq 1.5$.

5.5.4 The massive core at the center of the protostellar clump

The massive (119 $M_\odot$) core located at the center of the protostellar clump has a virial parameter of 0.71, suggesting it is gravitationally bound and could be undergoing gravitational collapse. This hypothesis is strongly supported by the observed profiles in the optically thick HCO^+ line, which exhibits a double-peaked profile with the blue-shifted peak being brighter than the red-shifted peak, and in the optically thin $H^{13}CO^+$ line, which shows a single peak profile with a peak velocity near the dip in HCO^+ (see Figure 5.20). These characteristics of the line profiles are a classical signature of infalling motions (c.f. Mardones et al. 1997).

To estimate the infall velocity we fitted the observed HCO^+ core spectrum with analytical infall models presented by De Vries & Myers (2005). The best fit is attained with the "Hill5" model (see Figure 5.20), which assumes that the excitation temperature increases inwards as a linear function of the optical depth, indicating an infall velocity, v_{in}, of 1.6 km s^{-1}. We note that none of the simple models is able to reproduce the observed deep absorption feature

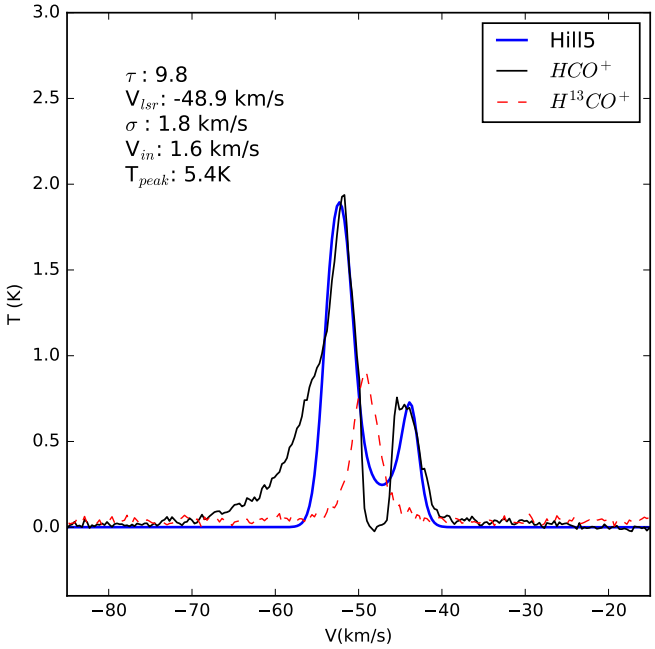

Figure 5.20: Average spectra of the HCO^+ (black line) and $H^{13}CO^+$ (red line) emission from the central massive core in AGAL329. The blue line shows the best fit using the analytical infall models of De Vries & Myers 2005. Fitted parameters are given in the upper left corner.

(reaching zero intensity). To reproduce it requires a more sophisticated modeling, which is beyond the scope of this work. From the derived values of the infall speed (1.6 km s^{-1}), core radius (0.03 pc), molecular weight μ_{H_2} (2.8), and molecular hydrogen density (1.5×10^{7}cm^{-3}) we estimate a mass infall rate $\dot{M}$ ($= 4\pi\ R^2\ n(H_2)\mu_{H_2}m_H v_{in}$) of 1.9×10^{-2} $M_\odot$/yr, value similar to those reported in other high-mass star forming regions (e.g., Garay et al. 2002; Beuther et al. 2002; Contreras et al. 2018).

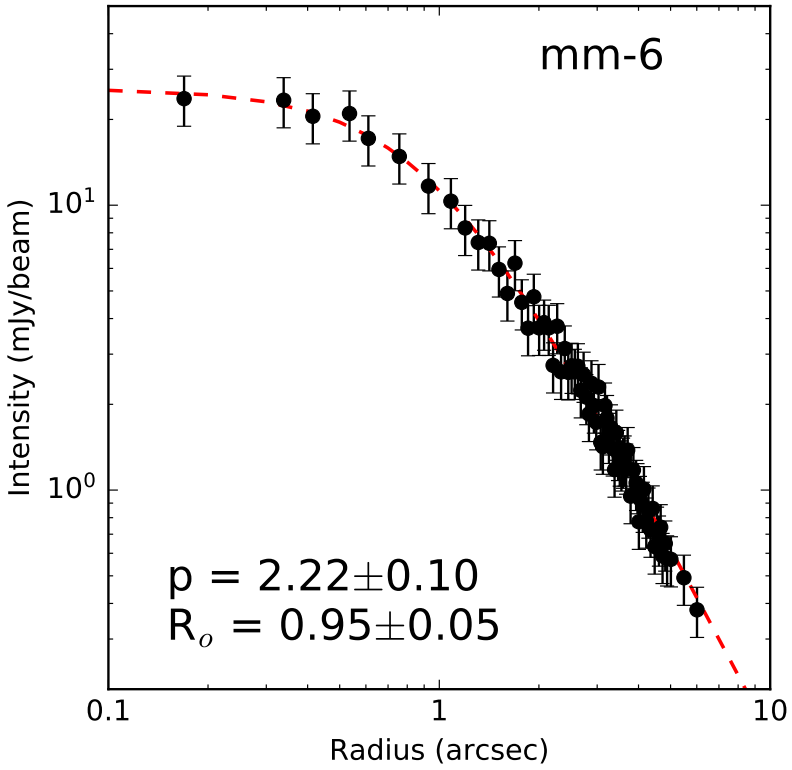

Figure 5.21: Radial intensity profile of the massive core (mm-6) at the center of AGAL329. The dotted red line correspond to a fit with a Plummer-like profile. Error bars correspond to 10% errors in the observed intensities.

The observed radial intensity profile of the massive core, shown in Figure 5.21, deviates significantly from a Gaussian profile but is well approximated with a Plummer-like radial intensity profile of the form,

$$I(I_0, R_0, p) = \frac{I_0}{(1 + (\frac{R}{R_0})^2)^{\frac{p}{2}}} \tag{5.8}$$

where p is the power law index, I_0 is the peak intensity and R_0 is the Plummer radius. The best fit (shown as a red line) indicates a power law index p of 2.2±0.1 and R_0 of 0.95±0.05". Whitworth & Ward-Thompson (2001) have already shown that the density profile of cores undergoing collapse can be successfully fit with Plummer-like profiles.

In summary, the observed and derived properties of this massive core, e.g., collapse and outflow signatures, high mass infall rate, and Plummer-like density profile, are consistent with a picture in which large-scale collapse is feeding gas into this core which is forming a massive protostar at its center.

5.5.5 Comparison with models of the fragmentation of clumps and the formation of high-mass stars

The formation of a cluster of stars is thought to proceed through a sequence of fragmentation, merging and collapse process within massive and dense clumps (e.g., Vázquez-Semadeni et al. 2009; Motte et al. 2018a). Given the complexity of this process most of the recents advances in this field have been made through numerical simulations. To better constrain the models, and hence to understand the formation of stars, it is crucial to know the initial conditions of the sequence. In particular, the properties of the cores at the early stages of evolution of MDCs are poorly known.

Our ALMA observations of the two MDC in early stages of evolution, with spatial resolutions of ∼0.02 pc, allowed us to determine the characteristics of the fragmentation at early stages of evolution, such as the number of cores, their physical and kinematical characteristics and the initial core mass function (CMF). Both clumps have masses of $\sim 10^3$ $M_\odot$ and therefore can potentially form a cluster of stars, and in particular, from the empirical mass-size relationship (Kauffmann et al. 2010) will probably give rise to high-mass stars. Thus we can compare our findings with models of massive star and cluster formation, although we note that few of them have made predictions concerning the fragmentation at early stages of clump evolution. We recall that one clump is in the prestellar stage and the other in the protostellar stage, thus we can investigate differences in the cores due to evolution.

The Competitive accretion model (Bonnell 2002; Bonnell & Bate 2006) proposes that a clump initially fragments into cores of thermal Jeans masses. These cores then accrete mass from the reservoir material in the clump via Bondi-Hoyle accretion. Cores located near the center of the gravitational potential accretes at a higher rate leading to the formation of a high mass protostar. In the competitive accretion scenario cores in an early stage after the fragmentation are expected to be subvirial.

The turbulent core accretion model (McKee & Tan 2003) proposes that stars form via a monolithic collapse of cores in virial equilibrium supported by the internal pressure due to turbulence and/or magnetic fields and hence should have masses much larger than the thermal Jeans mass. In this model the core mass distribution is then set at early evolutionary times, and therefore shall be similar to the initial stellar mass distribution (Tan et al. 2014). In addition, in this scenario cores are expected to be virialized (McKee & Tan 2002; Krumholz & Bonnell 2009).

We found that the number of cores detected in both clumps is considerably smaller than the number of thermal Jeans masses contained in the clumps ($M/M_J \sim 160$) showing that fragmentation is not efficient during the early stages of evolution. In addition, the fraction of total core mass to clump mass is 6% in the prestellar clump and rises to ∼23% in the protostellar clump. Since the number of cores in both clumps is similar, and the fact that the masses of the cores in the protostellar clump are typicaly higher than the masses of the cores in the prestellar clump, which are of the order of the clump Jeans mass, supports the hypothesis of a continuous increase in core masses due to accretion from the prestellar to the protostellar stage.

A large fraction of the cores within the prestellar clump (5 out of 10) are sub-virial ($\alpha < 0.7$), two are virialized ($0.7 < \alpha < 1.4$) and the remaining three (with $\alpha \geq 1.5$) are most likely transient features. On the other hand, five out of ten cores in the protostellar clump are virialized and two are in sub-virial states.

These results support the view of a globally collapsing turbulent clump undergoing gravitational fragmentation. In this scenario, during the early stages of evolution (AGAL333 clump) most of the formed cores should have masses typical of the thermal Jeans mass and be in sub-virial states. In a more advance stage (AGAL329 clump), the gas is funneled down to the center of the potential and the centrally located core continue to accrete gas at a high rate, becoming the most massive one.

5.6 Summary

We carried out ALMA band 3 observations of 3mm dust continuum and molecular emission, in lines of HCO^+, $H^{13}CO^+$, N_2H^+ and CH_3CN, towards two massive and dense clumps in early, but distinct, stages of evolution, one in a prestellar stage (AGAL333.014-0.521) and the other in a protostellar stage (AGAL329.184-0.314). The goal was to reveal the physical and dynamical characteristics of the small-scale structures (or cores) within these clumps. Table 5.11 summarizes the characteristics of the cores. The results are summarized as follows.

1) From the 3mm continuum images we identified, using the Clumpfind and Dendogram algorithms, about 10 cores within each clump. The cores in the prestellar clump, which are mainly distributed in a long filamentary structure running from NE to SW across the clump, have dust derived masses from 1.6 to 20 $M_\odot$, sizes from 0.006 to 0.022 pc (1200 to 4500 AU) and densities from 3.0×10^6 to 3.5 $\times10^7$ cm^{-3}. The cores in the protostellar clump have dust derived masses from 1.7 to 119 $M_\odot$, sizes from 0.005 to 0.030 pc (1000 to 6200 AU) and densities from 4.0×10^6 to 5.3 $\times10^7$ cm^{-3}. The fraction of total core mass relative to the clump mass is $\sim$6% in the prestellar clump and $\sim$23% in the protostellar clump. Most cores in the prestellar clump have masses within a factor of a few from the Jeans mass of the clump. However, the total number of cores is significanty smaller than the number of Jeans masses in the clump indicating that fragmentation is inefficient during the early stages of evolution of clumps.

2) Molecular emission was detected towards both clumps in all four observed species. Of these, the N_2H^+ emission is the brightest and most extended one and the one that best correlates with the continuum emission morphology.

Prestellar clump. The morphologies of the N_2H^+ and $H^{13}CO^+$ emission from AGAL333 are similar, delineating a complex network of filamentary structures across the whole region. The velocity field of the N_2H^+ emission shows a significant velocity gradient, of 4.7 km s^{-1} pc^{-1}, in a NE to SW direction, across the whole clump. The mass required to explain this as due to gravitationally bound rotation is 460 $M_\odot$ within a radius of 0.45 pc. CH_3CN emission is only detected towards the NE region of this clump.

Protostellar clump. The morphologies of the line emission from AGAL329 are noticeably different in the four observed transitions. The N_2H^+ emission arises from a bright central region, with three distinct condensations, and an extended envelope of emission which is highly correlated with the absorption feature seen in the 8 μm Spitzer image. The HCO^+ emission towards the central region, shows a banana-like morphology which is roughly coincident with the two westernmost N_2H^+ condensations, but no HCO^+ emission is seen from the eastern N_2H^+ condensation. In addition, the HCO^+ image shows two conspicuous features: a bright clumpy structure, located $\sim$18$''$ south of the central region, elongated in the NE-SW direction, (the South feature), and a weak V shaped feature located $\sim$ 10$''$ west from the central region (the West feature). The most prominent features in CH_3CN are a bright central region whose peak position coincides with the peak position of the central core mm-6, and a bright V shaped region coincident with the West feature seen in HCO^+.

3) Emission in the N_2H^+, HCO^+ and $H^{13}CO^+$ lines was detected towards all continuum cores within AGAL329 and all cores, except mm-9, in AGAL333. The line widths, determined from observations of the optically thin $H^{13}CO^+$ and N_2H^+ lines, are usually smaller for cores within the prestellar clump than for cores within the protostellar clump. The average line widths are 1.2 km s^{-1} and 2.0 km s^{-1} for AGAL333 and AGAL329 cores, respectively. The explanation for the large line widths in cores within the protostellar clump is not straightforward, it may reflect an increase in the level of turbulence due to the beginning of star formation activity, magnetic fields, or an increase in the gas velocities due to collapse motions. Emission in CH_3CN was detected from all continuum cores in the protostellar clump and only weak emission was detected towards five cores in the prestellar clump. The temperatures, derived from a rotational diagram analysis of the emission in the CH_3CN J=5_K - 4_K lines, range from 28 to 68 K for cores in protostellar clump and from 24 to 31 K for cores in the prestellar clump.

4) Five cores within AGAL333 exhibit inverse P-Cygni profiles in the HCO^+ line and five are sub-virial (virial parameters smaller than 0.7), indicating that most cores within the prestellar clump seem to be undergoing contracting motions. Within AGAL329, most cores exhibit double peak profiles in HCO^+, with a stronger blueshifted peak, and single peaked profiles in $H^{13}CO^+$, with a velocity in between those of the HCO^+ peaks. These pair of profiles in optically thick (HCO^+) and optically thin ($H^{13}CO^+$) lines are signature of infalling gas, which we suggest is associated to the global collapse of the protostellar clump.

5) The core at the center of the protostellar clump is the most massive one, has a Plummer-like intensity profile and exhibits line profiles which are characteristic of infalling gas, indicating an infall velocity of 1.6 km s^{-1} and a mass infall rate of 1.9×10^{-2} M$_\odot$/yr. These results convey the idea that this core is still acquiring mass via the gravitational focusing of gas from a globally collapsing clump towards its large potential well. In addition, this core is associated with a bipolar outflow in HCO^+ possibly driven by a recently formed high-mass protostar at its center.

6) The core mass function for the combined sample of cores within three clumps (AGAL329, AGAL333 and AGAL305 from Servajean et al. 2019) has a power law index of -1.33 ± 0.15, much flatter than that of the IMF for stars with masses greater than 1 M$_\odot$. The top-heavy nature of the CMF suggests that at an early stage of clump fragmentation, high mass cores

are more efficiently formed than low mass cores.

In summary, we conclude that we are witnessing the evolution of the dense gas in globally collapsing MDCs, with AGAL333 showing the initial stage of fragmentation, producing cores that are individually collapsing, while in AGAL329 we are seeing a later stage in which a considerable fraction of the gas has been gravitationally focused into the central region.

Acknowledgments: G.G. and S.N. gratefully acknowledge support from CONICYT projects PFB-06 and AFB170002. This paper makes use of the following ALMA data: ADS/-JAO.ALMA#2016.1.00645.S. ALMA is a partnership of ESO (representing its member states), NSF (USA) and NINS (Japan), together with NRC (Canada), MOST and ASIAA (Taiwan), and KASI (Republic of Korea), in cooperation with the Republic of Chile. The Joint ALMA Observatory is operated by ESO, AUI/NRAO and NAOJ.

Chapter 6

Summary

In this thesis, I investigated physical, chemical and fragmentation characteristics of massive and dense clumps (MDCs), which are the maternities of high-mass stars, in different evolutionary stages (from quiescent to protostellar to H II) to provide a better observational perspective about the process of formation of high-mass stars. First, I observed at the clump scale (angular resolution of 17-24″; $\sim$ 0.3 pc at 3.5 kpc) the emission in high-excitation ($J = 3 \rightarrow 2$ and $J = 4 \rightarrow 3$) molecular lines of HCO^+, HCN, HNC and N_2H^+ and $H^{13}CO^+$ $J = 3 \rightarrow 2$ line toward 73 MALT90 clumps in different evolutionary stages. Second, I observed the 350 μm continuum emission towards 23 MDCs in different evolutionary stages using the Artemis camera mounted at the APEX telescope in order to investigate their fragmentation properties at the $\sim$ 0.1 pc scale. Finally, I made ALMA 3 mm continuum and molecular lines (HCO^+, $H^{13}CO^+$, N_2H^+ $J = 1 \rightarrow 0$ and CH_3CN $5 \rightarrow 4$) observations towards two MDC, one in a prestellar stage and the other in a protostellar stage, to study the fragmentation properties and gas kinematics at the scale of 0.02 pc. The results from each project, presented in separate chapters in this thesis, are summarized here.

6.0.1 SuperMALT: physical and chemical properties of massive and dense clumps

In chapter 3, I presented the SuperMALT project, a survey of the emission in high excitation ($J = 3 \rightarrow 2$ and $J = 4 \rightarrow 3$) lines of HCO^+, HCN, HNC and N_2H^+ and $H^{13}CO^+$ ($J = 3 \rightarrow 2$), towards 73 MDCs in different evolutionary stages (prestellar, protostellar and H II phase). The objective of the survey was to investigate the bulk physical and kinematical properties of the clumps (spatial resolution of $\sim$ 20″; $\sim$ 0.3 pc at $\sim$3.5 kpc) and look for possible dependences with clump evolutionary stage. The main results and take aways from this project are listed here.

Line detection and profiles: Emission in the $J = 3 \rightarrow 2$ and $J = 4 \rightarrow 3$ lines was detected from all observed species in most clumps. The line profiles show a variety of shapes such as Gaussian, asymmetric/skewed and wings. The profiles of the $H^{13}CO^+$ ($J = 3 \rightarrow 2$) emission are Gaussian for all clumps. The profiles of the HNC emission in the $J = 3 \rightarrow 2$

and $J = 4 \rightarrow 3$ lines from most clumps are also Gaussian. On the other hand, the profiles of the HCO^+ and HCN lines are considerably broader than the $H^{13}CO^+$ profiles and typically show line asymmetric features.

Line emission morphology and sizes: The morphologies of the emission in the $J = 3 \rightarrow 2$ lines are similar to the 870μm continuum ATLASGAL emission. Among the four main species, N_2H^+ is the one that best traces the cold dust emission, exhibiting sizes very similar to the 870μm sizes. On the other hand, the HCO^+ sizes are typically 1.5 times larger than the N_2H^+ size , most likely due to the larger optical depths of the HCO^+ emission. The average size of the clumps in different evolutionary stages are similar. The morphologies of $J = 4 \rightarrow 3$ emission are more compact than those in the $J = 3 \rightarrow 2$ lines in all molecular species. Since the $J = 4 \rightarrow 3$ lines have higher critical densities, they maybe probing more denser regions within the clump.

Line widths: The line widths determined from the optically thin $H^{13}CO^+$ $J = 3 \rightarrow 2$ transition, as well as those determined from the HNC $J = 3 \rightarrow 2$ line, increase from prestellar to protostellar to H II clumps. This result suggests that non-thermal motions in evolved clumps are larger, possibly due to star formation activity or due to the globally collapsing gas motions. In general, the line widths of HNC are larger than those in $H^{13}CO^+$, indicating that HNC is only relatively optically thin despite its near Gaussian line profile.

Line intensity and ratios: For all observed lines, the intensity increases from prestellar to protostellar to H II clumps. This reflects the increase in temperature with clump evolution, the later stage clumps being hotter due to the formation of stars within them.

We computed ratios of velocity integrated line intensities in different species and analized them as a function of clump evolutionary stage. In general the ratios are similar, except for HCN/HNC which shows an increasing trend with evolutionary stage. We find that for a given pair of species, the ratios are different when using lines with different excitation (i.e. different Js).

Infall and expansion motions: We investigated large scale motions of the gas within the clumps, by analyzing asymmetries in the line profiles of optically thick lines (HCO^+ and HCN) in comparison with the optically thin $H^{13}CO^+$ profile. We found that blueshifted asymmetries, indicative of infall motions, are more common in the prestellar stage, while redshifted asymmetries, indicative of expansion motions, are more common in evolved clumps.

6.0.2 Fragmentation properties of MDCs at 0.1 pc scale

In chapter 4, I presented observations of the 350 μm continuum emission towards 23 MDCs in different evolutionary stages. This project, called the Artemis survey, focused on studying the fragmentation properties of the clumps at the 0.1 pc scale and investigate possible differences with clump evolutionary stage. The main results are summarized as follows.

Fragmentation level: At the scale of the observations ($\sim$0.1 pc), 66% of the clumps exhibit more than one substructure. The number of substructures (or cores) per clump ranges

from 1 to 4 for prestellar clumps, 1 to 5 for protostellar clumps, and 1 to 6 for H II clumps. On average clumps exhibit 2-3 substructures at the scale of 0.1 pc.

Fragmentation level versus clump physical properties: We investigated the level of fragmentation (or number of cores) per clump versus the clumps physical properties derived from molecular lines and dust emission. We did not find clear correlation between number of fragments per clump and their average molecular hydrogen density, virial parameter and line widths. We find that clumps with more fragments have larger line widths and lower densities than the average density of the sample.

Mass distribution Considering together the total number of cores extracted from the 23 MDCs, we find that the mass distribution of the cores is bimodal. There is a large population of cores with masses close to the Jean mass of the clump. The second population consists of more massive cores located near the center of the clump.

6.0.3 ALMA observations of two MDCs at the 0.02 pc scale

In chapter 5, I presented ALMA band 3 observations of 3mm dust continuum and molecular line emission, in HCO^+, $H^{13}CO^+$, N_2H^+ and CH_3CN, towards two massive and dense clumps in early, but distinct, stages of evolution, one in a prestellar stage (AGAL333.014-0.521) and the other in a protostellar stage (AGAL329.184-0.314). Both clumps have masses of $\sim$ 1000 $M_\odot$ and densities of $\sim 10^5$ cm^{-3}. The goal was to reveal the physical and dynamical characteristics of the small-scale structures (or cores) within these clumps. The results are summarized as follows.

Level of fragmentation: We found a similar number of cores ($\sim$10) within the prestellar and protostellar clumps. However, the mass of the cores in the protostellar clump are larger. In addition, the protostellar clump harbours a massive dense core at its center.

Molecular line emission: Emission was detected in all the observed lines towards most cores, except CH_3CN in which emision was only detected from the lower excitation rotational lines, K = 0, 1 and 2 toward about half of the cores in the prestellar clump. The morphology of the N_2H^+ emission best traces the cold dust emission in both clumps. Emission morphologies in HCO^+, $H^{13}CO^+$ and N_2H^+ show differences, however, the former two show relatively similar morphologies exhibiting clumpy emission around the central cores. CH_3CN probes warm and hot regions around the cores allowing us to derive core temperatures. These results illustrate the complex chemical changes that take place as the clumps evolve.

Line widths: The line widths of the cores in the prestellar clump, determined from the optically thin $H^{13}CO^+$ transition, are smaller than those of the protostellar cores.

Core temperatures: Core temperatures were determined from a rotational diagram analisis using the observed lines of CH_3CN. Cores in the prestellar clump have smaller temperatures than cores in the protostellar clump. The temperature of the central massive core in the protostellar clump exhibits a strong dependence with radius, with a peak value of 131 K and a power law slope of -0.8 ± 0.2.

Core kinematics: The profiles of the HCO^+ emission from most cores, in both the prestellar and protostellar clumps, are asymmetric and show self-absorption and/or wing features. Inverse P Cygni profiles are commonly seen in prestellar cores. Self-absorption profiles in HCO^+ are observed toward all protostellar cores. Using the line widths determined from the optically thin $H^{13}CO^+$ line and temperatures derived from CH_3CN rotational lines, we computed the virial mass and virial parameters of the cores. Most cores in the prestellar clump are sub-virial while most cores in the protostellar clump are virialized. The central massive core of the protostellar clump exhibits large scale infall motions as well as outflow features.

Mass distribution of the cores: The cores in the prestellar and protostellar clumps have, respectively, masses ranging from 1.6 to 20 $M_\odot$ and from 1.7 to 119 $M_\odot$. For the clump average density and temperature, Jeans mass for prestellar clump and protostellar clumps are 5.5 and 6.8 $M_\odot$, respectively. While the masses of the most cores are close to Jeans mass (within a factor of few), the number of cores observed is much lower than the "expected" Jeans number. The combined sample of cores follow core mass function of the form ($dN/dM \propto M^\alpha$) with a power law index of -1.33±0.15. The results suggest high-mass core formation efficiency is higher in the MDCs at early stages.

We also estimated the mass in the form of cores, which we defined as core mass fraction, toward the prestellar and protostellar clump. In prestellar clump, the core mass fraction is 6%. In protostellar clump, the core mass fraction is 23%. In addition, most massive core in the clump have 33% and 55% of total mass of the clump. Our findings demonstrate that fragmented cores continue to accrete more mass from the clump environment as the clump evolves.

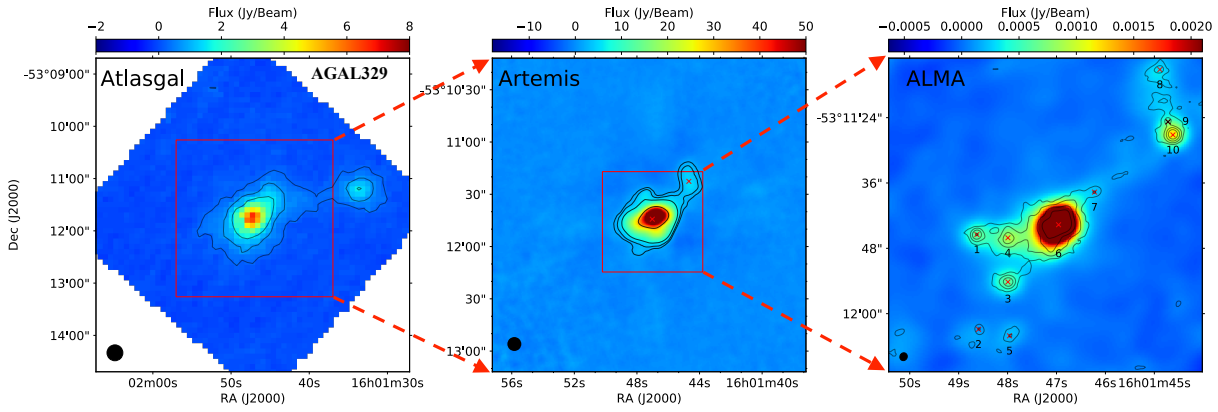

Figure 6.1: Maps of AGAL329 from ATLASGAL (left), Artemis (middle) and ALMA 3mm (right). Red box in left maps show regions zoomed in the maps shown in the right. Cores identified in ALMA maps are numbered in black color and marked in red crosses.

6.0.4 Conclusions

In this thesis, I investigated the physical, kinematical and fragmentation properties of massive and dense clumps, which are the sites of the formation of high-mass stars, in different stages

Table 6.1: Properties of clumps, and their cores, in different evolutionary stages.

SuperMALT survey: ∼0.3 pc scale			
	Prestellar	Protostellar	H II clump
Mass ($M_\odot$)	0.2 - 1.1 $\times 10^3$	0.2 - 42 $\times 10^3$	0.2 - 6.3 $\times 10^3$
Mean size [a] (R_{eff} pc)	0.83	0.92	0.83
Dust emission	IR-dark	IR bright	IR bright
		$\Rightarrow$ 24 μm and 4.5	$\Rightarrow$ 3.5, 4.6, 8, 24 μm
Dust temperature (K)	13-20	15-28	15-31
Line widths [b] (km s^{-1})	2.04±0.82	2.67±0.87	2.42±0.71
Kinematics [c]	Blue or red-shifted line asymmetry		
	Infall motions dominate		
		Expansion motions dominate	
Artemis survey: ∼0.1 pc scale			
Fragmentation per clump	1-4 cores	1-5 cores	1-6 cores
Core mass range ($M_\odot$)	5 - 110	7 - 1500	2 - 990
Mean core size (pc)	0.03-0.12	0.03-0.14	0.03-0.14
Core mass fraction	8%	22%	21%
ALMA study: ∼0.02 pc scale			
	AGAL333	AGAL329	
Clump mass ($M_\odot$)	1080	940	
Clump temperature (K)	22	28	
Fragmentation per clump	∼10 cores	∼10 cores	
Core mass range ($M_\odot$)	1.6 - 20	1.7 - 119	
Mean core size (pc)	0.012	0.014	
Core temperature (K)	24 - 31	28 - 68	
Average line widths (km s^{-1})	1.2	2.0	
Core mass fraction	∼6%	∼23%	

[a] Sizes from N_2H^+ $J = 3 \rightarrow 2$.
[b] Line widths of $H^{13}CO^+$ $J = 3 \rightarrow 2$.
[c] Kinematic signature of optically thick HCO^+ $J = 3 \rightarrow 2$.

of evolution from prestellar stage to protostellar and H II stages. For this, I performed dust and molecular line observations at millimeter wavelengths using the APEX telescope and ALMA interferometer, providing spatial resolutions from 0.3 pc to 0.02 pc, (i.e. clump to core scales). A summary of the results is presented in Table 6.1.

From the observations of 73 massive and dense clumps in different evolutionary stages in the high-excitation molecular lines of multiple species we characterized properties of molecular line emission for each phases.

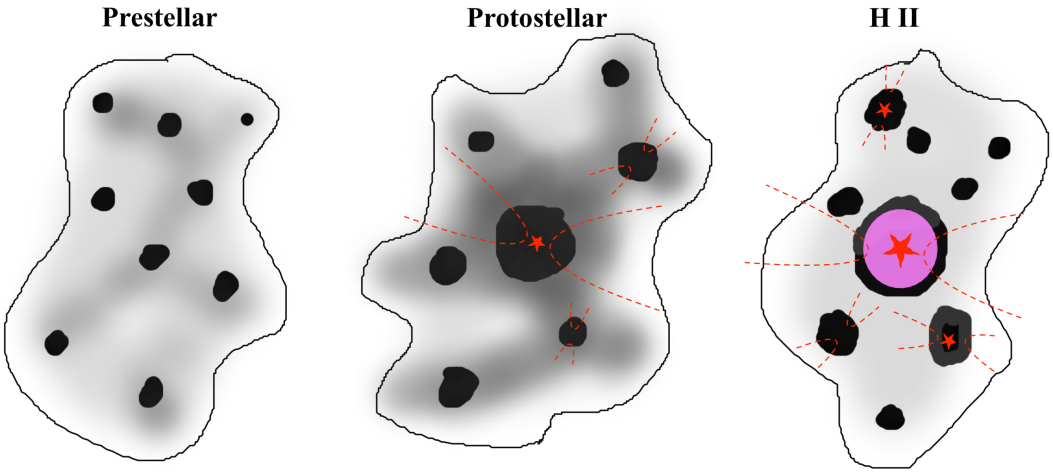

Figure 6.2: Schematic model of clump evolution from prestellar phase to protostellar phase. Prestellar stage clumps have fragmented substructures, relatively less massive and they are still in the process of gathering more mass from the Clump environment. At protostellar stage, cores have gathered more mass and some cores have already begun active phase of star formation. The central protostar in this phase accrete more mass from the globally collapsing gas. Signature of infall and outflows (shown in dotted lines) are common toward the cores and also at clump scale driven by the central massive core at this stage. Following this stage compact H II regions are formed around the protostar that is forming a high-mass star, consequently that becomes an extended H II region and bubble like H II region.

To explore the fragmentation processes of massive and dense clumps we observed them in three different spatial scales, from ~ 0.3 *pc* to ~ 0.1 *pc* to ~ 0.02 *pc*, the later achieved using the state of art facility ALMA interferometer. At the scale of ~ 0.3 *pc* the Supermalt clumps typically exhibits a single structure. When observed with ~ 0.1 *pc* resolution (the Artemis observations) we find that the clump fragments into two to three substructures. When looked at higher resolution of ~ 0.02 *pc* scale, we observed more substructures (of the order of 10) (see Figure 6.1), the findings consistent with a few other recent works reported in the literature. The key insights from the results are that clump fragmentation is hierarchical and fragmentation happens at very early stages.

Finally, combining the results presented in this work, I propose the following scenario (sketched in Figure 6.2) for the evolution of MDCs and their fragmentation processes. Our 20" angular resolution observations show that the formation of high mass stars takes place

in clumps with sizes of 0.5 - 1 pc and densities of $\gtrsim 10^4$ cm^3. We envision that these clumps are being feed by the filaments in which they form. Clumps in early stages of evolution usually exhibit large scale infalling motions, strongly supporting a global collapse model. The observations with 8" angular resolution shows two type of substructures within the clumps, first a population of fragments with masses of typically the clump Jean's mass (of 10 $M_\odot$) and central structures with larger masses (200 $M_\odot$). The number of observed fragments in a given clump is considerable smaller than the number of Jean's fragments expected from the Jeans criteria, showing that fragmentation is not a very efficient process during the early phases of evolution of clumps. As the clump evolves, the cores become more massive as they accrete mass from the surroundings. Cores near the center of the clump gravitational potential accretes mass at a higher rate to become massive and finally give birth to a high-mass star/s. Our observational results favor the view of a simultaneous evolution of large scale (clumps) and small scale (cores) structures and do not support a static model of a clump that fragments to form stars and give rise to the stellar mass distribution.

A clear shortcoming of this work is that we have not considered the role of magnetic field nor the role of filaments in the formation of the clump. A handful of studies reported in the literature have emphasised the role of the magnetic field in the fragmentation process (eg. Fontani et al. 2016) and role of filaments in the formation and evolution of clumps (eg., André et al. 2014, Contreras et al. 2017, Lu et al. 2018.). This work sets the stage for a more quantitative investigation of the role of magnetic field, turbulence, filamentary accretion and global collapse in the evolution of MDCs.

Bibliography

Ahrens, V., Lewen, F., Takano, S., et al. 2002, Zeitschrift Naturforschung Teil A, 57, 669

André, P., Di Francesco, J., Ward-Thompson, D., et al. 2014, in Protostars and Planets VI, ed. H. Beuther, R. S. Klessen, C. P. Dullemond, & T. Henning, 27

Andre, P., Ward-Thompson, D., & Barsony, M. 2000, in Protostars and Planets IV, ed. V. Mannings, A. P. Boss, & S. S. Russell, 59

André, P., Men'shchikov, A., Bontemps, S., et al. 2010, A&A, 518, L102

André, P., Revéret, V., Könyves, V., et al. 2016, A&A, 592, A54

Anglada, G., Rodríguez, L. F., Cantó, J., Estalella, R., & López, R. 1987, A&A, 186, 280

Araya, E., Hofner, P., Kurtz, S., Bronfman, L., & DeDeo, S. 2005, ApJS, 157, 279

Armstrong, J. T., Ho, P. T. P., & Barrett, A. H. 1985, ApJ, 288, 159

Beltrán, M. T., Brand, J., Cesaroni, R., et al. 2006, A&A, 447, 221

Bergin, E. A., & Langer, W. D. 1997, ApJ, 486, 316

Bertoldi, F., & McKee, C. F. 1992, ApJ, 395, 140

Beuther, H., Schilke, P., Menten, K. M., et al. 2002, ApJ, 566, 945

Blake, G. A., Sutton, E. C., Masson, C. R., & Phillips, T. G. 1987, ApJ, 315, 621

Bonnell, I. A. 2002, in Astronomical Society of the Pacific Conference Series, Vol. 267, Hot Star Workshop III: The Earliest Phases of Massive Star Birth, ed. P. Crowther, 193

Bonnell, I. A., & Bate, M. R. 2006, MNRAS, 370, 488

Carey, S. J., Noriega-Crespo, A., Mizuno, D. R., et al. 2009, PASP, 121, 76

Caselli, P., Myers, P. C., & Thaddeus, P. 1995, ApJL, 455, L77

Caselli, P., Walmsley, C. M., Zucconi, A., et al. 2002, ApJ, 565, 344

Churchwell, E., Babler, B. L., Meade, M. R., et al. 2009, PASP, 121, 213

Contreras, Y., Garay, G., Rathborne, J. M., & Sanhueza, P. 2016, MNRAS, 456, 2041

Contreras, Y., Rathborne, J. M., Guzman, A., et al. 2017, MNRAS, 466, 340

Contreras, Y., Schuller, F., Urquhart, J. S., et al. 2013, A&A, 549, A45

Contreras, Y., Sanhueza, P., Jackson, J. M., et al. 2018, ApJ, 861, 14

Cornwell, T. J. 2008, IEEE Journal of Selected Topics in Signal Processing, 2, 793

Csengeri, T., Bontemps, S., Wyrowski, F., et al. 2017, A&A, 600, L10

Cyganowski, C. J., Whitney, B. A., Holden, E., et al. 2008, AJ, 136, 2391

De Vries, C. H., & Myers, P. C. 2005, ApJ, 620, 800

Dunham, M. K., Rosolowsky, E., Evans, II, N. J., et al. 2010, ApJ, 717, 1157

Faúndez, S., Bronfman, L., Garay, G., et al. 2004, A&A, 426, 97

Fazio, G. G., Hora, J. L., Allen, L. E., et al. 2004, ApJS, 154, 10

Fontani, F., Commerçon, B., Giannetti, A., et al. 2016, A&A, 593, L14

Foreman-Mackey, D., Agol, E., Ambikasaran, S., & Angus, R. 2017, AJ, 154, 220

Foreman-Mackey, D., Hogg, D. W., Lang, D., & Goodman, J. 2013, PASP, 125, 306

Foster, J. B., Jackson, J. M., Barnes, P. J., et al. 2011, ApJS, 197, 25

Garay, G., Brooks, K. J., Mardones, D., Norris, R. P., & Burton, M. G. 2002, ApJ, 579, 678

Garay, G., Faúndez, S., Mardones, D., et al. 2004, ApJ, 610, 313

Garden, R. P., Hayashi, M., Gatley, I., Hasegawa, T., & Kaifu, N. 1991, ApJ, 374, 540

Gildas Team. 2013, GILDAS: Grenoble Image and Line Data Analysis Software, Astrophysics Source Code Library, , , ascl:1305.010

Ginsburg, A., & Mirocha, J. 2011, Astrophysics Source Code Library, ascl:1109.001

Goldsmith, P. F., Irvine, W. M., Hjalmarson, A., & Ellder, J. 1986, ApJ, 310, 383

Goldsmith, P. F., & Langer, W. D. 1999, ApJ, 517, 209

Güsten, R., Walmsley, C. M., Ungerechts, H., & Churchwell, E. 1985, A&A, 142, 381

Guzmán, A. E., Sanhueza, P., Contreras, Y., et al. 2015, ApJ, 815, 130

Hacar, A., Bosman, A. D., & van Dishoeck, E. F. 2020, A&A, 635, A4

He, Y.-X., Zhou, J.-J., Esimbek, J., et al. 2015, MNRAS, 450, 1926

—. 2016, MNRAS, 461, 2288

Heitsch, F., Slyz, A. D., Devriendt, J. E. G., Hartmann, L. W., & Burkert, A. 2007, ApJ, 665, 445

Hernández-Hernández, V., Zapata, L., Kurtz, S., & Garay, G. 2014, ApJ, 786, 38

Herschel, W. 1785, Royal Society of London Philosophical Transactions Series I, 75, 213

Heyer, M., Krawczyk, C., Duval, J., & Jackson, J. M. 2009, ApJ, 699, 1092

Hirota, T., Yamamoto, S., Mikami, H., & Ohishi, M. 1998, ApJ, 503, 717

Hoq, S., Jackson, J. M., Foster, J. B., et al. 2013, ApJ, 777, 157

Jackson, J. M., Rathborne, J. M., Foster, J. B., et al. 2013, PASA, 30, 57

Jackson, J. M., Whitaker, J. S., Rathborne, J. M., et al. 2019, ApJ, 870, 5

Jin, M., Lee, J.-E., & Kim, K.-T. 2015, ApJS, 219, 2

Jones, P. A., Burton, M. G., Cunningham, M. R., et al. 2008, MNRAS, 386, 117

Kauffmann, J., Pillai, T., Shetty, R., Myers, P. C., & Goodman, A. A. 2010, The Astrophysical Journal, 716, 433

Keto, E., & Wood, K. 2006, ApJ, 637, 850

König, C., Urquhart, J. S., Csengeri, T., et al. 2017, A&A, 599, A139

Kroupa, P. 2001, MNRAS, 322, 231

Krumholz, M. R., & Bonnell, I. A. 2009, Models for the formation of massive stars, ed. G. Chabrier (Cambridge University Press), 288–320

Lada, C. J. 1987, in IAU Symposium, Vol. 115, Star Forming Regions, ed. M. Peimbert & J. Jugaku, 1

Larson, R. B. 1981, MNRAS, 194, 809

Liu, M., Tan, J. C., Cheng, Y., & Kong, S. 2018, ApJ, 862, 105

Loughnane, R. M., Redman, M. P., Thompson, M. A., et al. 2012, MNRAS, 420, 1367

Louvet, F., Neupane, S., Garay, G., et al. 2019, A&A, 622, A99

Lu, X., Zhang, Q., Liu, H. B., et al. 2018, ApJ, 855, 9

Magalhães, V. S., Hily-Blant, P., Faure, A., Hernand ez-Vera, M., & Lique, F. 2018, A&A,

615, A52

Mangum, J. G., & Shirley, Y. L. 2015, PASP, 127, 266

Mardones, D., Myers, P. C., Tafalla, M., et al. 1997, ApJ, 489, 719

Martin-Pintado, J., Bachiller, R., & Fuente, A. 1992, A&A, 254, 315

McDowell, R. S. 1988, JChPh, 88, 356

McKee, C. F., & Tan, J. C. 2002, Nature, 416, 59

—. 2003, ApJ, 585, 850

McMullin, J. P., Waters, B., Schiebel, D., Young, W., & Golap, K. 2007, in Astronomical Society of the Pacific Conference Series, Vol. 376, Astronomical Data Analysis Software and Systems XVI, ed. R. A. Shaw, F. Hill, & D. J. Bell, 127

Miville-Deschênes, M.-A., Murray, N., & Lee, E. J. 2017, ApJ, 834, 57

Molinari, S., Swinyard, B., Bally, J., et al. 2010, PASP, 122, 314

Motte, F., Bontemps, S., & Louvet, F. 2018a, ARA&A, 56, 41

Motte, F., Nony, T., Louvet, F., et al. 2018b, Nature Astronomy, 2, 478

Myers, P. C. 2009, ApJ, 700, 1609

Neupane, S., Garay, G., Contreras, Y., Guzmán, A. E., & Rodríguez, L. F. 2020, ApJ, 890, 76

Neupane, S., Garay, G., Contreras, Y., & SuperMALT Team. 2018, in IAU Symposium, ed. M. Cunningham, T. Millar, & Y. Aikawa, Vol. 332, 254–260

Ossenkopf, V., & Henning, T. 1994, A&A, 291, 943

Padoan, P., & Nordlund, Å. 2002, ApJ, 576, 870

Palau, A., Ballesteros-Paredes, J., Vázquez-Semadeni, E., et al. 2015, MNRAS, 453, 3785

Palau, A., Zapata, L. A., Román-Zúñiga, C. G., et al. 2018, ApJ, 855, 24

Peretto, N., Fuller, G. A., Duarte-Cabral, A., et al. 2013, A&A, 555, A112

Pety, J. 2005, in SF2A-2005: Semaine de l'Astrophysique Francaise, ed. F. Casoli, T. Contini, J. M. Hameury, & L. Pagani, 721

Pineda, J. E., Rosolowsky, E. W., & Goodman, A. A. 2009, ApJL, 699, L134

Pokhrel, R., Myers, P. C., Dunham, M. M., et al. 2018, ApJ, 853, 5

Rathborne, J. M., Whitaker, J. S., Jackson, J. M., et al. 2016, PASA, 33, e030

Remijan, A., Sutton, E. C., Snyder, L. E., et al. 2004, ApJ, 606, 917

Rieke, G. H., Young, E. T., Engelbracht, C. W., et al. 2004, ApJS, 154, 25

Robitaille, T., Rice, T., Beaumont, C., et al. 2019, astrodendro: Astronomical data dendrogram creator, , , ascl:1907.016

Robitaille, T. P., Meade, M. R., Babler, B. L., et al. 2008, AJ, 136, 2413

Rosolowsky, E., Dunham, M. K., Ginsburg, A., et al. 2010, ApJS, 188, 123

Rosolowsky, E. W., Pineda, J. E., Kauffmann, J., & Goodman, A. A. 2008, ApJ, 679, 1338

Roussel, H. 2013, PASP, 125, 1126

Sana, H., de Koter, A., de Mink, S. E., et al. 2013, A&A, 550, A107

Sánchez-Monge, Á., Beltrán, M. T., Cesaroni, R., et al. 2013, A&A, 550, A21

Sanhueza, P., Jackson, J. M., Foster, J. B., et al. 2012, ApJ, 756, 60

Sanhueza, P., Jackson, J. M., Zhang, Q., et al. 2017, ApJ, 841, 97

Sault, R. J., Teuben, P. J., & Wright, M. C. H. 1995, in Astronomical Data Analysis Software and Systems IV, ed. R. A. Shaw, H. E. Payne, & J. J. E. Hayes, Vol. 77, 433

Savage, C., Apponi, A. J., Ziurys, L. M., & Wyckoff, S. 2002, ApJ, 578, 211

Schilke, P., Walmsley, C. M., Pineau Des Forets, G., et al. 1992, A&A, 256, 595

Schneider, S., & Elmegreen, B. G. 1979, ApJS, 41, 87

Schöier, F. L., van der Tak, F. F. S., van Dishoeck, E. F., & Black, J. H. 2005, A&A, 432, 369

Schuller, F., Menten, K. M., Contreras, Y., et al. 2009, A&A, 504, 415

Servajean, E., Garay, G., Rathborne, J., Contreras, Y., & Gómez, L. 2019, ApJ, 878, 146

Shirley, Y. L. 2015, PASP, 127, 299

Shu, F. H., Lizano, S., & Adams, F. C. 1987, in IAU Symposium, Vol. 115, Star Forming Regions, ed. M. Peimbert & J. Jugaku, 417–433

Stutz, A. M., & Kainulainen, J. 2015, A&A, 577, L6

Sutton, E. C., Peng, R., Danchi, W. C., et al. 1995, ApJS, 97, 455

Takahashi, S., Ho, P. T. P., Teixeira, P. S., Zapata, L. A., & Su, Y.-N. 2013, ApJ, 763, 57

Tan, J. C., Beltrán, M. T., Caselli, P., et al. 2014, Protostars and Planets VI, 149

Teixeira, P. S., Takahashi, S., Zapata, L. A., & Ho, P. T. P. 2016, A&A, 587, A47

Turner, B. E. 1991, ApJS, 76, 617

Urquhart, J. S., Csengeri, T., Wyrowski, F., et al. 2014, A&A, 568, A41

van der Tak, F. F. S., Black, J. H., Schöier, F. L., Jansen, D. J., & van Dishoeck, E. F. 2007, A&A, 468, 627

Vázquez-Semadeni, E., Gómez, G. C., Jappsen, A. K., Ballesteros-Paredes, J., & Klessen, R. S. 2009, ApJ, 707, 1023

Vázquez-Semadeni, E., González-Samaniego, A., & Colín, P. 2017, MNRAS, 467, 1313

Vázquez-Semadeni, E., Palau, A., Ballesteros-Paredes, J., Gómez, G. C., & Zamora-Avilés, M. 2019, MNRAS, 490, 3061

Virtanen, P., Gommers, R., Oliphant, T. E., et al. 2019, arXiv e-prints, arXiv:1907.10121

Whitaker, J. S., Jackson, J. M., Rathborne, J. M., et al. 2017, AJ, 154, 140

Whitworth, A. P., & Ward-Thompson, D. 2001, ApJ, 547, 317

Wilking, B. A., Lada, C. J., & Young, E. T. 1989, ApJ, 340, 823

Williams, J. P., de Geus, E. J., & Blitz, L. 1994, ApJ, 428, 693

Zhang, Q., Wang, K., Lu, X., & Jiménez-Serra, I. 2015, ApJ, 804, 141